Improving the mechanical properties of metallic materials via combined structural and compositional gradients

Shunyao Du

A thesis submitted in fulfilment of the requirements for the degree of Doctor of Philosophy

School of Aerospace, Mechanical & Mechatronic Engineering

Faculty of Engineering

The University of Sydney

2025

To my family

Declaration of Originality

I affirm that this submission represents my original work and, to the best of my understanding and belief, it does not include content previously published or authored by another individual. Furthermore, it does not contain material that has been submitted for the attainment of any degree or diploma at any university or institution of higher education, except where proper acknowledgment is provided within the text.

Signed:

Date: 31/08/2025

Acknowledgements

This thesis is not only a summary and discussion of scientific research findings but also a testimony to my PhD research career.

Firstly, I would like to thank my supervisor, Professor Xiaozhou Liao. During my PhD studies, he provided professional guidance and long-lasting encouragement and support. Due to the outbreak of COVID-19, I was forced into lockdown at home, unable to conduct any research experiments. However, during this time, my supervisor promptly provided me with very practical advice and recommended many useful online academic seminars to help me successfully navigate this difficult period. His expertise and rigorous academic attitude have been immensely beneficial to me, and I express my deepest respect and gratitude.

I would also like to thank my co-supervisor, Professor Simon P. Ringer, who provided me with valuable academic resources and a platform for academic exchanges.

I would like to thank Professor Huijun Li, Dr. Bosheng Dong, and Dr. Yangfan Wang from the University of Wollongong, who prepared compositional gradient structures using wire arc additive manufacturing technology, and the subsequent cold rolling treatment.

I would like to express my sincere gratitude to Mr George Faulkner from Aviation Component Services Pty Ltd (https://aviationcomponents.com.au/) for his generous support of my research. His provision of shot peening services was instrumental in enabling key experimental components of this work. His professionalism, technical expertise, and willingness to assist were greatly appreciated and contributed significantly to the successful completion of this study.

I would like to thank Dr. Mehdi Eizadjou from the Sydney Manufacturing Hub, who provided significant support in the annealing process of the samples.

I am deeply grateful to Dr. Hongjian Wang from the School of Aerospace, Mechanical and Mechatronic Engineering at the University of Sydney for his valuable assistance with the tensile testing. His technical support and hands-on help were essential to the successful execution of this part of my research.

I would like to thank Dr. Ziyuan Wang and his supervisor Seyed A. Hadigheh from the School of Civil Engineering at the University of Sydney for their professional support in digital image correlation theory and data processing. Their expertise and guidance were crucial in ensuring the accuracy and reliability of this aspect of my research.

I am grateful to Dr. Ying Liu from Professor Xiaozhou Liao's research group for her assistance with acquiring TEM and STEM images. Her technical skill and support greatly facilitated the microstructural characterisation central to this study.

I am also grateful to Dr. Hongwei Liu, Dr. Magnus Garbrecht, Dr. Vijay Bhatia, Mr. Jacob Byrnes, and Dr. Huma Bilal from the Australian Centre for Microscopy & Microanalysis for their professional teaching on microscopy techniques and sample preparation.

I also want to thank my friends and every member of our research group for their companionship and assistance during my PhD studies.

I also gratefully acknowledge the assistance of ChatGPT in polishing the language of this thesis and ensuring grammatical accuracy.

Most importantly, I would like to thank my parents for their love and support during my studies in Australia. Their understanding, encouragement, and selfless love have been the strong backbone of my academic journey.

Abstract

Overcoming the strength–ductility trade-off is a central challenge in the design of structural materials. We propose and validate a scalable dual gradient architecture in Cu–Al alloys. Wire arc additive manufacturing constructs a centimetre scale compositional gradient. Cold rolling, annealing and rotationally accelerated shot peening then introduce a near-surface nano and ultrafine-grained structural gradient, so that compositional and structural gradients act in concert within a single component. Systematic characterisation and modelling show that the gradient sequence governs layer morphology and compositional step formation through melt pool fields of heat, flow and solute. This control yields a narrow and deep geometry in Cu-rich layers and a shallow and wide geometry in Al-rich layers. Along the build direction, a columnar-to-equiaxed transition emerges. The Al-rich domain undergoes intermittent discontinuous dynamic recrystallisation, while the Cu-rich domain exhibits continuous dynamic recrystallisation. The <100> fibre texture first strengthens and then weakens. Hardness is most sensitive to Al solid solution strengthening, with grain size and residual stress acting as secondary modifiers.

During cold rolling, low SFE promotes shear bands and twinning. After subsequent annealing, grain size decreases with increasing Al content along the compositional gradient. The compositional transition regions display a bimodal grain size distribution. A crystallographic orientation gradient persists along the full compositional gradient direction.

Full-field digital image correlation together with finite element analysis shows that a single structural gradient maintains a stable strain gradient, while a single compositional gradient transfers load bearing from the surface to the core during loading. The dual gradient supplies parallel plasticity channels and interface pinning and forms a two-dimensional crack deflection network, which markedly suppresses localisation and increases fracture energy dissipation. Accordingly, the dual gradient specimen achieves at room temperature $\sigma_y \approx 385$ MPa, $\sigma_{UTS} \approx 495$ MPa, $\varepsilon_u \approx 38\%$ and $\varepsilon_f \approx 49\%$, and a strength–ductility index greater than 140 MJ m^{-3}, significantly outperforming homogeneous and single gradient counterparts of the same composition. This work establishes a cross-scale gradient–interface co-design guideline and provides a general route for engineering breakthroughs beyond the strength–ductility trade-off.

Plan for future publications

Journal Papers directly related to this thesis:

(1) Shunyao Du, Xiaozhou Liao. Compositional gradient structures in metallic materials: a review.

(2) Shunyao Du, Bosheng Dong, Yangfan Wang, Simon P. Ringer, Huijun Li, Xiaozhou Liao. Microstructure and hardness evolution in wire arc additively manufactured compositionally graded Cu–Al alloys.

(3) Shunyao Du, Bosheng Dong, Zenxi Pan, Jian Wang, Simon P. Ringer, Huijun Li, Xiaozhou Liao. Cold rolling texture in heterostructured materials.

(4) Shunyao Du, Bosheng Dong, Ziyuan Wang, S. Ali Hadigheh, Zenxi Pan, Yuntian Zhu, Simon P. Ringer, Huijun Li, Xiaozhou Liao. Simultaneous improvement of strength and ductility of metallic materials via combined structural and compositional gradients.

Thesis Authorship Attribution Statement

In **Chapter 4** of this thesis,

The gradient structures prepared through wire arc additive manufacturing were completed by Dr. Bosheng Dong and Dr. Yangfan Wang from the University of Wollongong.

In **Chapter 5** and **Chapter 6** of this thesis,

Data collection and processing in digital image correlation were completed by Dr. Ziyuan Wang from the School of Civil Engineering at the University of Sydney. The TEM images were taken by Dr. Ying Liu from Professor Xiaozhou Liao's research group.

Table of Contents

List of Figures

List of Tables

Chapter 1. Introduction

Background and context. Mechanical properties are an important aspect of the engineering design of metallic materials, for they govern ultimately the operational safety and functionality of load-bearing components [1–5]. Under service conditions, structural components need to resist high stresses without excessive deformation and failing, subjecting mechanical properties such as strength and ductility to high demands [2,4–6]. Strength is the ability of materials to resist plastic deformation and rupture under load, conveyed using measures such as the yield strength or ultimate tensile strength, while ductility is the ability for tensile plastic deformation prior to rupture, generally measured using elongation to failure or reduction of area [5,7]. Under structural application, high strength and enough ductility are equally important: strong but brittle members can undergo sudden catastrophic failure, whereas those having high ductility but low strength may exhibit unacceptable distortion and even collapse under load [4,6–9]. Achieving the optimum compromise between strength and ductility has therefore long been the focus of the science and engineering of structural materials [5,8–10].

Typically, strength and ductility have had an inverse relationship in metallic materials [11–14]. This conventional strength–ductility trade-off suggests strength-increasing techniques such as alloying, cold-working, and grain refinement to have the accompanying effect of loss of ductility, and vice versa, as represented by Fig. 1-1, where higher strength is accompanied by lower ductility values [12,13,15–18]. The strength–ductility trade-off has been the central conundrum of materials science and engineering, basically constraining the creation of structural metallic materials capable of being strong and absorbing high deformation energy [12–16,19]. The biggest challenge is to overcome this empirical limitation and achieve strong yet ductile materials [14,16,17,20–22].

In the past two decades, a paradigm shift has occurred with the emergence of gradient structured (GS) materials that defy the long-standing strength–ductility trade-off [23–25]. It has been shown that introducing structural heterogeneity in a material can produce synergistic mechanical responses unattainable in uniform microstructures [24,26–28]. Notably, materials with spatial gradients in microstructure, for example a surface layer of ultrafine grains gradually transitioning to a coarse-grained (CG) core, have delivered unprecedented combinations of high strength and high ductility [27,29,30]. Numerous

studies have since confirmed that gradient structures can produce a strength–ductility synergy: the integrated mechanical performance exceeds the rule-of-mixtures predictions and lies outside the trade-off envelope of conventional materials [26,29,31–34]. This exciting breakthrough has spurred a new design strategy for structural metallic materials, centred on tailoring internal gradients (in grain size, dislocation density, twin density, etc.) to amplify strength and ductility in tandem [28,30–35].

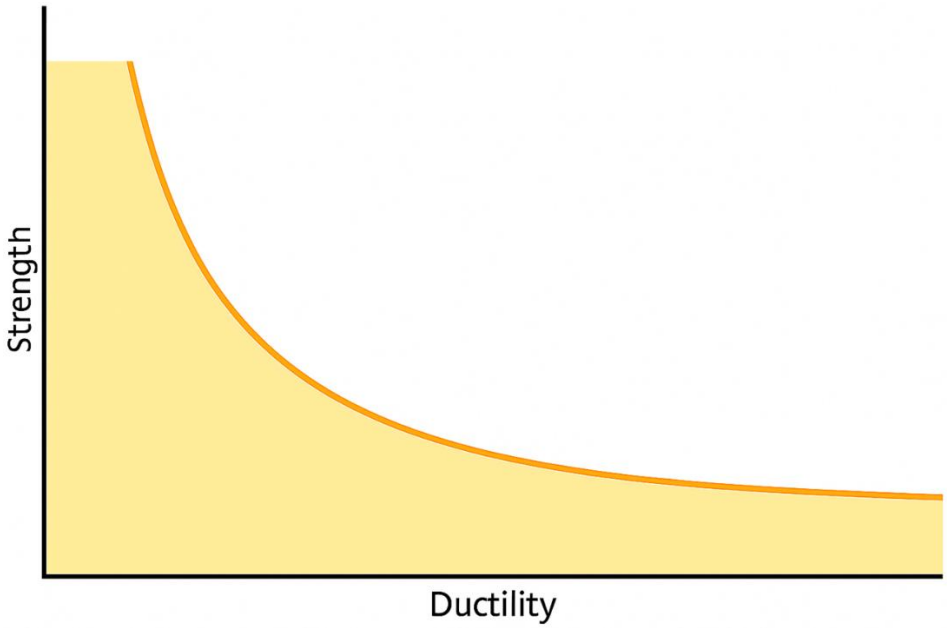

Figure 1-1 Schematic diagram illustrating the strength–ductility trade-off envelope for metallic materials, with typical values of strength and ductility falling within the shaded area.

The preceding heterogeneous or gradient architectures have structural heterogeneity [36]. A compositional gradient, in comparison, provides an extra parameter of freedom to tailor mechanical properties since modification of local composition changes the microstructure, the phases and stability, and the stacking fault energy (SFE) and hence the deformation mechanisms and mechanical characteristics in the area [37–39]. Essentially, parts of a compositionally graded material (CGM) are different metals or alloys, smoothly combined in one piece [38,39]. Hard phases or solute-rich regions are added where the requirement is hardening, whereas solute-depleted or ductile phases are in areas where plasticity is necessary [39]. In contrast with a composite with a sharp boundary, a gradient alloy varies in a gradual fashion in terms of composition, thus eliminating property step-downs and stress concentrations [40]. It allows for the optimisation of the properties (e.g. hardness,

yield strength, or toughness) in different positions, with structural continuity in total [37,39,41]. The compositional gradient controls the local microstructure: by adjusting fractions of phases, content of precipitates, or solid solution strength, it designs the work hardening behaviour and the yield strength in function of position [37–39,42].

Traditionally, the fabrication of compositional gradient structures (CGSs) has been arduous; modern processing technologies, most notably additive manufacturing (AM), have now rendered it practicable [43–45]. By sequentially varying the feedstock or the processing parameters, AM can deposit layers of differing composition, thereby establishing a continuously varying compositional gradient along the build direction [46–48]. Wire-arc additive manufacturing (WAAM), an arc-welding-based variant of AM, is particularly suitable for producing large-scale gradient components on account of its high deposition rate and low cost [49–52].

Concurrently, conventional mechanical processing techniques remain indispensable for creating structural gradients. Severe plastic deformation (SPD) methods, such as surface mechanical attrition treatment (SMAT), shot peening, and laser shock peening, can generate a nanocrystalline (NC) surface layer in which the grain size increases gradually towards the interior [53–56]. GSs may likewise be obtained via cold rolling followed by partial annealing [25,57].

In light of these developments, it is now feasible to combine structural and compositional gradients within a single material; for example, a compositionally graded preform produced by AM can subsequently acquire a structural gradient through mechanical treatment. Such dual gradient architectures are expected to exploit the advantages of both gradients, thereby maximising the strength–ductility synergy. Recent investigations indicate that multiple or hierarchical gradients can further augment material performance [58–60]. For instance, a dual gradient in grain size and precipitate density in high-entropy alloys has been demonstrated to surpass the properties of a single grain size gradient [58].

Problem statement. Whilst proof-of-principle studies [23–33] have demonstrated the promise of GS materials, controllable fabrication of dual gradient architectures in bulk components and mechanistic understanding of their deformation behaviour remain elusive. The key open questions are: (i) How does the directionality of a compositional gradient (increasing versus decreasing solute content) influence solidification microstructure,

texture and hardness? (ii) How do subsequent cold rolling and annealing treatments interact with the spatially varying SFE to modify microstructure and texture? (iii) Can a surface nano-/ultrafine-grained layer generated by shot peening cooperate with the underlying compositional gradient to deliver simultaneous gains in strength and ductility?

Resolving these issues would markedly advance research into gradient structures.

Research aims and objectives. The overarching aim of this thesis is to develop and validate a processing route, combining WAAM, cold rolling, annealing, and shot peening, for constructing controllable dual gradient architectures within a single Cu–Al system, and to elucidate the mechanisms by which such architectures enhance mechanical performance. The specific objectives are:

1. To design and fabricate two distinct variants of compositional gradient Cu–Al WAAM samples, and to systematically characterise the evolution of composition, microstructure, and hardness along the build direction.
2. Through cold rolling and subsequent annealing, to investigate the evolution of deformation texture and microstructure, as well as recrystallisation texture and microstructure, across regions of differing Al content.
3. By means of rotationally accelerated shot peening (RASP), to introduce a nano-/ultrafine-grained structural gradient at the surface and couple it with the internal compositional gradient, thereby realising a dual gradient structure.
4. To evaluate the room-temperature tensile properties, hardness gradient, and fracture behaviour of the dual gradient structures, and to reveal the mechanisms underpinning the synergy between strength and ductility.
5. To establish a multiscale correlation model linking composition, microstructure, and properties, thereby furnishing guidance for the design of GSs.

Scope and limitations. This thesis focuses on a specific materials system and set of processes to investigate the dual gradient concept. In scope are the following aspects: the material of interest is a Cu-based alloy with Al additions (Cu–Al), which will be used to create a gradient in composition. The choice is motivated by the significant effect of Al on Cu's stacking fault energy and mechanical behaviour, as well as practical considerations in WAAM processing of Cu alloys. The study encompasses WAAM to produce the initial compositional gradient, followed by cold rolling, annealing, and shot peening to introduce structural gradients. Characterisation techniques covered include optical microscopy,

scanning electron microscopy, electron backscatter diffraction, transmission electron microscopy, energy-dispersive X-ray spectroscopy, X-ray diffraction, hardness testing, and tensile mechanical testing with digital image correlation strain measurement. The mechanical characterisations are primarily quasi-static (room-temperature tensile tests and hardness); creep, fatigue, or high-rate behaviour are beyond the scope of this work. Additionally, some finite element modelling may be performed to support interpretations, but the core of the thesis is experimental.

Several limitations must be acknowledged. This study is confined to the Cu–Al system. Specifically, to ensure that the engineered compositional gradients remain a single face-centred cubic solid solution, the Al content has been limited to a gradient ranging from approximately 0 at.% to 15 at.% over a certain build height. Accordingly, the findings may not be directly transferable to alloys with markedly different phase diagrams or to compositions that are susceptible to cracking during the WAAM process. The scale of the produced gradient samples is constrained by the laboratory equipment; while WAAM allows larger samples than many lab processes, our samples (tens of centimetres in height) are still modest compared to industrial components. The gradient profile (both compositional and microstructural) will not be perfectly continuous; there may be layer-wise steps in composition inherent to the WAAM process and certain non-uniformities in deformation and recrystallisation, which we will characterise as faithfully as possible. Another limitation is that the analysis of texture evolution with changing composition is complex; while we attempt to deconvolve the effects, isolating the influence of composition versus deformation history may be difficult. Finally, due to time constraints, the optimisation of processing parameters (e.g. degrees of deformation, annealing temperature) will be done to a reasonable extent but may not be exhaustive – we aim for representative conditions rather than an exhaustive parametric study.

Within these boundaries, the thesis provides a detailed case study of a dual gradient material. The focus is on fundamental understanding of microstructure–property relations in the gradient, rather than on producing an immediately application-ready component. Nevertheless, the insights should be valuable for guiding future developments in GS materials in other contexts.

Significance of the study. This study contributes to materials science and engineering in three ways. First, it proposes a practical WAAM-based route for tailoring centimetre-scale

compositional gradients and couples it to surface nanocrystallisation, offering a scalable methodology for architectured metallic materials. Second, it clarifies the multiscale deformation mechanisms activated within a dual gradient Cu–Al material, enriching current theories of heterogeneous plasticity. Third, the Cu–Al dual gradient samples developed in this work exhibit an ultimate tensile strength of approximately 500 MPa coupled with an outstanding elongation to failure of 49 %, thereby providing concrete guidance for the design of high-performance Cu alloys.

Thesis structure. The remainder of the thesis is arranged as follows:

Chapter 2 – Literature review surveys mechanical behaviour of metallic materials, gradient structure classifications, fabrication methods, deformation mechanisms and mechanical properties, as well as texture evolution during cold rolling and annealing.

Chapter 3 – Experimental techniques and procedures details materials fabrication, post-processing, characterisation, mechanical testing and finite element simulations.

Chapter 4 – Microstructure and hardness of the as-printed materials presents composition, microstructure, texture and hardness profiles of FCG and RCG samples, and analyses composition–microstructure–property relationships.

Chapter 5 – Microstructure and texture induced by post-printing processes examines microstructural and textural evolution resulting from cold rolling and annealing, emphasising SFE effects.

Chapter 6 – Impact of gradient structures on mechanical properties evaluate the mechanical performance and deformation mechanisms of the dual gradient samples, and, in conjunction with numerical simulation, elucidate the stress–strain distribution and the underlying micromechanisms.

Chapter 7 – Conclusions and future perspectives summarises the principal findings and outlines avenues for future research.

Chapter 2. Literature review

Chapter 2 offers a comprehensive literature review that sets the scientific context for the subsequent experimental chapters. It commences with an overview of the mechanical behaviour of metallic materials, detailing tensile stress–strain characteristics, dominant strengthening mechanisms and prevailing strategies for enhancing ductility (Section 2.1). The review then progresses to gradient structures in metallic materials, outlining their taxonomy, the mechanistic origins of the strength–ductility synergy and representative property data (Section 2.2). Section 2.3 surveys state-of-the-art techniques for generating structural and compositional gradients, while Section 2.4 summarises texture evolution in face-centred cubic metallic materials under cold rolling and annealing. Readers who wish to focus on content that directly informs this thesis should prioritise Sections 2.1 to 2.3. These sections underpin the design of composition windows, the selection of WAAM processing routes and the interpretation of deformation mechanisms in the present work. Besides, because the evolution of texture in compositional gradient materials after cold rolling and annealing differs from that in conventional homogeneous materials, Section 2.4 first introduces the typical textures of homogeneous face-centred cubic metallic materials. This provides a clear baseline for the later discussion of gradient systems. The remaining material is retained to preserve completeness and narrative coherence and to offer a wider perspective. It draws on a companion review prepared by the author.

2.1 Mechanical behaviour of metallic materials

Metallic materials are valued in engineering for their strength and ductility. Strength is the ability of materials to resist plastic deformation and rupture under load, conveyed using measures such as the yield strength or ultimate tensile strength, while ductility is the ability for tensile plastic deformation prior to rupture, generally measured using elongation to failure or reduction of area [61–63]. These two properties are critical for structural applications: a material must be strong enough to carry loads, yet sufficiently ductile to avoid sudden brittle failure [61–63]. Section 2.1 defines the tensile metrics and strengthening concepts used throughout this thesis. Readers who already know these fundamentals may proceed directly to Section 2.2.

2.1.1 Tensile stress–strain curves

In practice, strength and ductility are quantified by standard tensile tests, from which a stress–strain curve is obtained, as shown in Fig. 2-1.

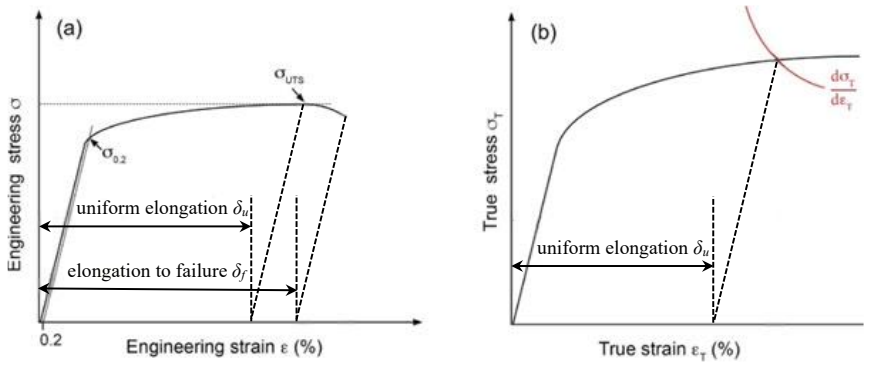

Figure 2-1 Typical tensile stress–strain curves for metallic materials. (a) Engineering stress–strain curve; (b) true stress–strain curve derived from the experimentally measured engineering counterpart.

As illustrated in Fig. 2-1(a), the specimen initially undergoes linear (elastic) deformation as the tensile strain increases; the slope of this linear segment defines the Young's modulus [61,64]. Plastic deformation commences at the elastic limit. Because the transition from elastic to plastic deformation is generally progressive, the exact yield point at which plasticity begins is difficult to pinpoint [61,64]. To facilitate determination, an offset of 0.2 % plastic strain is routinely adopted, the corresponding yield strength being $\sigma_{0.2}$. This parameter is intrinsic to the material and is widely employed in the design of mechanical components and structures [61,64]. A second strength parameter available from the tensile test is the ultimate strength, σ_{UTS}, i.e. the peak engineering stress on the stress–strain curve; it is also referred to as the tensile strength [61,64].

One of the most important properties obtainable from the engineering stress–strain curve is ductility, which for standard, large-scale specimens is usually quantified by the elongation to failure, δ_f [61,63]. Another measure is the uniform elongation, δ_u (see Fig. 2-1a) [61,65,66].

Fig. 2-1(b) presents the true stress–strain curve calculated from the engineering data. The uniform elongation can likewise be extracted from the true curve (Fig. 2-1b). According to the Considère criterion [61,67], necking instability, manifested by the development of a

localised deformation region, occurs when the strain hardening rate falls to a value equal to the flow stress, as shown below [61,67,68]:

$$\frac{d\sigma_T}{d\varepsilon_T} = \sigma_T \tag{2.1}$$

where true stress and true strain are denoted by σ_T and ε_T, respectively [61,67,68]. As shown in Fig. 2-1(b), the true uniform elongation, $\delta_{T,u}$, is identified at the intersection of the true stress–strain curve (σ_T–ε_T) and the strain hardening rate curve ($d\sigma_T/d\varepsilon_T$–ε_T) [61,67,68]. However, $\delta_{T,u}$ so determined typically underestimates the uniform elongation [1]. The correct value should be taken from the engineering stress–strain curve and may be calculated from $\delta_{T,u}$ using [61]:

$$\delta_u = e^{\delta_{T,u}} - 1 \tag{2.2}$$

For standard large tensile specimens, the fracture elongation δ_f is usually very close to the uniform elongation δ_u, as shown in Fig. 2-1(a). The measured δ_f, however, is markedly influenced by the gauge length, particularly when that length is very short [61,65], whereas δ_u is considerably less sensitive [61,65,69,70].

2.1.2 Strengthening mechanisms

In crystalline materials, plastic deformation occurs primarily by dislocation motion. Therefore, the most fundamental way to strengthen a metallic material is to impede dislocation motion [61,71,72]. Any microstructural feature that makes it more difficult for dislocations to move or multiply will increase the stress required for yielding. In essence, stronger materials are those with internal barriers that resist dislocation glide – these can be solute atoms, other dislocations, grain boundaries, second phase particles, etc. All classical strengthening mechanisms derive from this principle: they create obstacles or resistance to slip, thereby raising the yield and tensile strength of the materials [61,71,72]. Common strengthening mechanisms in metallic materials include solid solution strengthening, dislocation strengthening, grain boundary strengthening, second phase strengthening, and composite reinforcement [61,73]. Each mechanism operates via a different microstructural strategy, though all ultimately increase the critical resolved shear stress needed for dislocations to move. However, it is noteworthy that any strategy adopted to strengthen a material will, to some extent, compromise its ductility. Below we describe each mechanism in detail, along with relevant theoretical equations that quantify their

strengthening effects.

Solid solution strengthening. The incorporation of solute atoms into the metallic matrix enhances strength through solid solution strengthening [61,71]. Whether the solute atoms occupy substitutional lattice sites or interstitial positions, thereby forming substitutional or interstitial solid solutions, the mismatch in atomic size or elastic modulus relative to the solvent atoms introduces local lattice distortions [61,71]. These strain fields interact with dislocations, impeding their motion. Smaller solute atoms generate tensile strain fields in the lattice, whereas larger solute atoms create compressive fields; both types of fields obstruct the glide of nearby dislocations [61,71].

Quantitatively, the increase in yield stress ($\Delta\sigma$) from a solid solution is often modelled as proportional to the square root of solute concentration or to a solute-dislocation interaction parameter, though precise formulas come from empirical or semi-empirical models specific to each alloy system. One empirical relation is [73]:

$$\Delta\sigma \propto G \cdot \varepsilon_{solute}^{m} \cdot c^{n} \tag{2.3}$$

where G is shear modulus, ε_{solute} is the misfit strain, c is solute concentration, and m, n are fitting exponents. The exact form varies, but the trend is clear: more solute or larger size misfit yields greater strength [74].

Dislocation strengthening. When a metallic material is plastically deformed, its dislocation density increases dramatically. Newly generated dislocations interact and entangle with existing ones, making further dislocation motion more difficult [61,75–78]. This phenomenon, known as work hardening or strain hardening, is a key mechanism by which materials become stronger upon deformation [61,75–78]. Each dislocation carries a stress field, and dislocation-dislocation interactions (whether repulsive or attractive) create a "forest" of obstacles that inhibit movement of additional dislocations [61,75–78]. As deformation proceeds, dislocations can form tangles and substructures (e.g. cell walls) that further impede slip [61,75–78]. The classic Taylor relation quantifies the contribution of dislocations to flow stress. In its form [61,75–77]:

$$\sigma = \alpha M G b \sqrt{\rho} \tag{2.4}$$

where σ is the flow stress, α is a constant, M is the Taylor factor, G is the shear modulus,

b is the Burgers vector, and ρ is the dislocation density. This relation captures the observation that strength increases with the square root of dislocation density [61,75–78].

Grain boundary strengthening. Grain boundary strengthening derives from the impediment that grain boundaries impose on dislocation slip, and is reflected in the variation of yield strength with average grain size. The classical Hall–Petch relation can be used to describe this mechanism [61,67,71,79]:

$$\sigma_{0.2} = \sigma_0 + kd^{-1/2} \tag{2.5}$$

where σ_0 is a constant, k is the Hall–Petch slope, d is the average grain size. This equation demonstrates that, as the grains become finer, the increased boundary density intensifies dislocation blocking, thereby raising the material's strength. When the grain size is reduced to roughly 100 nm or below, this empirical law may fail because the dominant plasticity mechanism changes [61,67,80–84]. It is noteworthy that twin boundaries, as a special type of grain boundary, also act as potent barriers to dislocation motion [61,85].

Second phase strengthening. This mechanism comprises precipitation strengthening and dispersion strengthening. Fundamentally, it arises from the interaction between mobile dislocations and second phase particles [61], and its efficacy depends chiefly on the inter-particle spacing, l. The critical shear stress required for a dislocation to bow out between two particles and form a closed loop is [61]:

$$\tau = \frac{Gb}{l} \tag{2.6}$$

where G is the shear modulus and b is the magnitude of the Burgers vector. This expression is identical to that needed to activate a Frank–Read dislocation source [61].

Precipitation strengthening is achieved by the precipitation of a second phase from a supersaturated solid solution. When the precipitate is coherent or semi-coherent with the matrix [61,86], a dislocation may either circumvent the particle or shear directly through the coherent precipitate [61,71,86]. Dispersion strengthening is typically realised via mechanical alloying, whereby thermally stable particles are introduced into the matrix [71,86–88]. Both routes strengthen the materials by shortening the effective dislocation slip path and increasing the resistance to dislocation motion.

Metal–matrix composite strengthening. Strengthening in metal–matrix composites is

afforded by reinforcements such as fibres or whiskers [71,89]. Because these reinforcements possess a higher intrinsic strength, the external load is transferred from the more compliant matrix to the reinforcement, thereby increasing the overall load-bearing capacity [89]. When the reinforcement is particulate, the mechanism is directly analogous to dispersion strengthening; that is, the dispersed hard particles impede dislocation motion, thereby raising the material's strength [61].

2.1.3 Strategies to improve ductility

While high strength is desirable, a metallic material must also have adequate ductility to deform without fracturing under unexpected loads or stress concentrations. Ductility in tensile loading (often synonymous with tensile plasticity) is fundamentally about the material's capacity to sustain plastic deformation under tension, which is linked to how it stores and hardens from that deformation. The most fundamental principle for enhancing ductility is to delay the onset of instability (necking) during tensile deformation. In practical terms, this means maintaining a high work hardening rate so that the material keeps getting stronger as it elongates, thereby distributing strain more uniformly [90,91]. According to the Considère criterion, necking commences once the incremental strain hardening can no longer compensate for the reduction in cross-sectional area, i.e. when Eq. (2.1) is satisfied [61,67,68,92,93]. A high initial work hardening rate and a sustained hardening capacity at large strains will push this condition to higher strains, resulting in greater uniform elongation [94,95]. In essence, anything that promotes continuous strain hardening will enhance ductility by postponing localisation of deformation. The corollary is that materials with higher strength inherently require higher work hardening rates to achieve the same ductility as a softer material [96,97]. This is precisely why reliance on the aforementioned strengthening strategies alone, while conferring very high strength, often leads to reduced ductility: many such mechanisms curtail the material's capacity for further hardening. For instance, a high initial dislocation density leaves limited room for subsequent work hardening, and the introduction of a secondary phase may concomitantly stimulate the formation of brittle constituents [98,99]. This inverse relationship is the classic strength–ductility trade-off [61].

Over decades, metallurgists have sought ways to break this trade-off and obtain materials that are both strong and ductile [61]. Below, we outline mechanisms and microstructural design strategies aimed at improving ductility, each relying on boosting or preserving work

hardening and plastic deformation capacity.

To enhance the strength of metallic materials without sacrificing ductility, a range of approaches has been pursued. The earliest successful strategy involves distributing nanoscale precipitates within individual grains so that dislocations are compelled to accumulate in the grain interior [61,100]. Using an Al 7075 alloy as a model system, Zhao et al. verified the efficacy of this method [100]. After cryogenic rolling, the alloy exhibited a yield strength of 550 MPa while retaining a uniform elongation of approximately 3.3 %. Subsequent ageing of the cryo-rolled nanostructure generated a high density of intragranular precipitates, whereupon the ductility was augmented by roughly 1.25-fold to 7.4 %. More importantly, the strength rose by 12 % to 615 MPa (Fig. 2-2), thereby transcending the conventional strength–ductility trade-off [100]. TEM confirmed extensive dislocation accumulation around the precipitates, attesting to the effectiveness of this strategy [100].

A second, equally effective route is the introduction of nanotwins. Twin boundaries (TBs) likewise act as potent barriers to, and reservoirs for, dislocations, thereby improving strength and ductility in tandem [67,81]. Coherent TBs can be regarded as a special class of low energy grain boundary [86]. As obstacles to dislocation glide, they provide a strengthening effect analogous to that of conventional grain boundaries [85, 101]. Their advantage lies in their high degree of coherency [61], which renders it difficult for dislocations to penetrate the boundary [102]. In other words, unlike ordinary grain boundaries, TBs are less prone to absorb dislocations, making them highly effective sites for dislocation storage, raising the strain hardening rate and thus enhancing ductility. Prior investigations have demonstrated that preexisting deformation twins can improve both the strength and ductility of a material [103]. Moreover, because deformation twinning is strongly influenced by the stacking fault energy (SFE), the SFE itself plays a pivotal role in governing strength and ductility [104–106]. When the SFE is sufficiently low, deformation twins can be activated in situ during tensile loading, thereby promoting strain hardening and ductility [104].

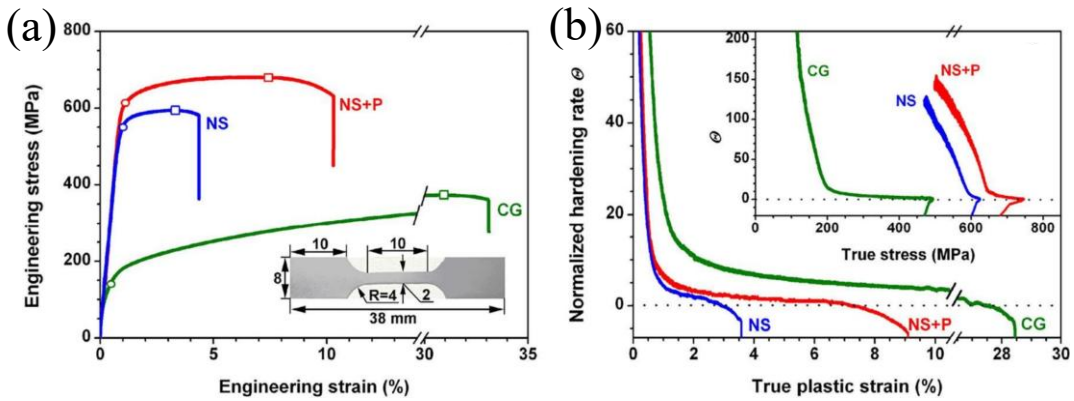

Figure 2-2 (a) Introducing finely dispersed precipitates into a nanostructured Al 7075 alloy yielded a concurrent increase in strength and ductility. (b) The same precipitation process markedly enhanced the alloy's work hardening capacity [100].

Additional strategies that elevate the strength of materials without undermining ductility include the introduction of high angle grain boundaries coupled with a low initial dislocation density [107,108], the deliberate formation of stacking faults (SFs) [109,110], hierarchical clustering of solute atoms [111], and bimodal grain size distributions [112,113], etc.

2.2 Gradient structures in metallic materials

Metallic materials in service commonly confront an intrinsic contradiction between high strength and high ductility, and substantial effort has therefore been devoted to resolving this dilemma [114,115]. Inspired by the graded architectures observed in biological materials, researchers over the past 40 years have explored compositional and structural gradients as a means of enhancing metallic performance [114]. The synthesis of a wide variety of gradient-structured materials has provided fresh opportunities to elucidate the mechanical behaviour associated with such architectures [116]. These emergent gradient materials frequently display unprecedented mechanical properties, most notably a strength–ductility synergy that has hitherto eluded materials with homogeneous or randomly distributed microstructures [61]. In this section, we systematically review recent advances in gradient-structured metallic materials, with particular emphasis on their classification, fundamental deformation mechanisms, and mechanical performance.

2.2.1 Classification of gradient structures

GS materials are bulk materials that possess a microstructural gradient along one or more

dimensions [117–119]. Such gradients may originate from variations in grain size [120,121], lamellar thickness [122–124], twin thickness [125–130], a combined gradient in grain size and twinning [131], or from changes in the volume fraction of constituent phases, precipitate density [114,132,133], and solute atom concentration [134]. Collectively, GS materials can be broadly classified into two principal categories: structural gradients and compositional gradients.

2.2.1.1 Structural gradient

The structural gradients most reported in the literature principally encompass grain size gradients, lamellar thickness gradients and twin thickness gradients. Certain gradient architectures may simultaneously exhibit multiple structural gradient characteristics [135]. Several representative structural gradients are illustrated in Fig. 2-3 [135].

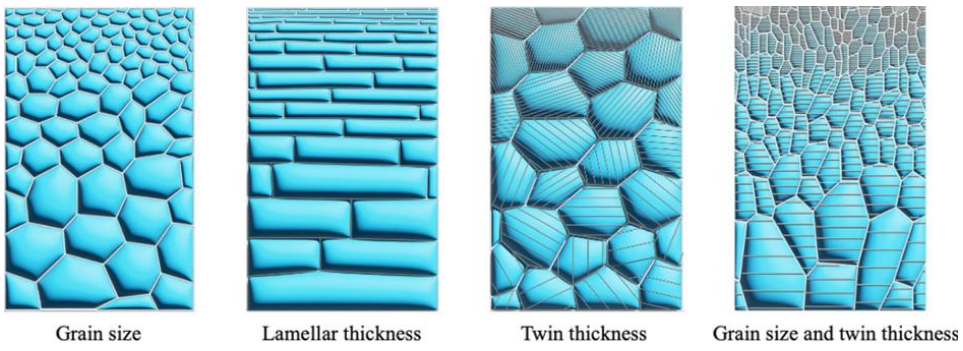

Figure 2-3 Typical types of structural gradients in metallic materials [135].

Grain size gradient. Fang et al. [121] first reported a grain size gradient architecture in Cu, comprising a CG matrix overlaid by a NC surface layer and an intermediate gradient transition zone. This pioneering work sparked extensive research, and grain size gradient structures have since been realised in numerous metallic materials, including Cu [136–138], Ni [139,140], interstitial-free (IF) steels [141,142], twinning-induced plasticity (TWIP) steels [143,144], and NiTi shape-memory alloys [145].

A typical grain size gradient structure contains a NC layer adjacent to a deformed CG layer, the grain size progressively increasing from the former to the latter [135]. Two gradient orientations can be distinguished: a forward gradient, in which the grain size increases from the surface towards the interior, and a reverse gradient, which displays the opposite trend [135,146]. By tailoring structural parameters, such as gradient orientation, the spatial

distribution of grain size, and the volume fraction of the gradient transition zone, material properties can be customised for specific engineering requirements [135]. To quantify these features, the hardness increment per unit thickness has been proposed as a convenient metric [147].

Lamellar thickness gradient. Liu et al. [122] were the first to fabricate a lamellar thickness gradient structure in Ni, characterised by low-angle lamellar boundaries. In this gradient lamellar architecture, the lamellar thickness increases progressively with depth along the thickness direction of the material. So far, lamellar thickness gradient structures have been realised in a range of alloy systems, including Ni [122], Al [123], Al–Cu alloys [124], Fe–Cr–Al alloys [148] and stainless steels [149–151].

Twin thickness gradient. Wei et al. [125] engineered a twin thickness gradient structure in TWIP steel by means of pre-torsion, whereby the thickness of deformation twins diminishes progressively from the material surface towards the centre, and the twin boundaries within each grain remain mutually parallel. To date, twin-thickness-gradient architectures have been identified in several low-stacking-fault-energy alloys, including Fe–Mn–C TWIP steels [125], stainless steels [126–128], Ti–Al alloys [129] and magnesium alloys [130].

Dual gradient in grain size and twin thickness. Cheng et al. [152] were the first to report a dual gradient structure in Cu, characterised by simultaneous gradients in both grain size and twin thickness, each decreasing from the surface towards the centre of the material. This pioneering study has since inspired the successful fabrication of dual gradient architectures in other metallic materials, such as Cu [152–155], Mg [156], stainless steel [157] and Mg alloys [158].

2.2.1.2 Compositional gradient

Compositional gradient denotes the spatial variation in composition within a component [159]. Unlike compositionally homogeneous materials, whose bulk composition is uniform, CGMs exhibit a gradual change in composition from one location to another [159]. This gradient may be continuous or realised through discrete steps or layers and is commonly accompanied by concomitant gradients in phase or other microstructural constituents [159,160]. Fig. 2-4 presents schematics of several CGSs. Three principal categories of compositional gradient can be distinguished [135]:

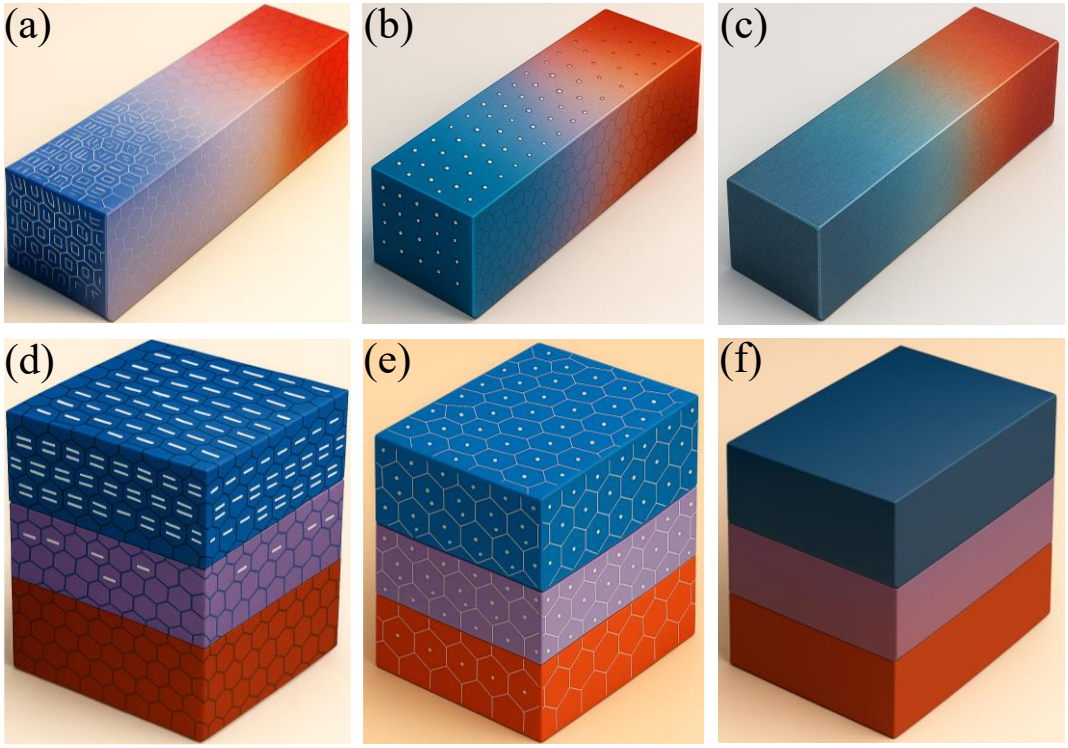

Figure 2-4 Schematic illustration of typical CGSs. (a) A continuous phase gradient; (b) a continuous precipitation gradient; (c) a continuous chemical composition gradient; (d) a discrete layer phase gradient; (e) a discrete layer precipitation gradient; (f) a discrete layer chemical composition gradient.

Phase gradient. A phase gradient arises when spatial changes in composition induce variations in the phase constitution of the material [159,161,162]. Distinct phases, or differing volume fractions of the same phases, therefore, appear in different regions, giving rise to a microstructural gradient. A phase gradient thus signifies that either the types or the proportions of phases present vary with position [162,163].

Precipitation gradient. A precipitation gradient occurs within a single matrix phase when the spatial distribution, size or volume fraction of a secondary phase (precipitates) varies [164]. In this situation the overall matrix composition may remain within the single-phase field, yet the number density of strengthening precipitates or particles changes with position [165]. Such gradients may be continuous or layered and are usually associated with corresponding gradients in mechanical strength [166].

Solid solution gradient. This category concerns spatial variations in solute-element concentration, irrespective of whether any accompanying phase transformation occurs [167–169]; a quintessential example is the compositional gradient within a continuous

solid solution.

In practical applications many graded materials simultaneously incorporate several of these gradient types. Gradients may be continuous, varying smoothly at the atomic scale to yield a seamless compositional profile, or stepwise, consisting of a sequence of discrete layers or zones, each compositionally uniform with abrupt changes between them [170–173]. It is also important to note that compositional gradients are frequently accompanied by microstructural gradients. Rigorous characterisation is therefore essential to isolate and quantify the specific effects attributable to the compositional gradient itself [170–173].

2.2.2 Reasons leading to strength–ductility synergy

This section summarises the fundamental mechanisms governing strengthening, strain hardening and ductility in materials possessing gradient structures.

2.2.2.1 Hetero-deformation induced (HDI) stress and multiaxial stress states

Metallic materials with gradient structures exhibit spatial variations in yield strength and ductility due to differences in local compositions and microstructures across the material. When such a gradient structured material is loaded, the stronger (harder) regions and weaker (softer) regions do not deform uniformly, which is known as mechanical incompatibility. The softer zones begin to yield and plastically deform at lower applied stresses, while adjacent harder zones remain elastic or deform less. As a result, a gradient in plastic strain develops across the interface between zones [61,116,135,174–178]. This non-uniform plastic deformation gives rise to a high density of geometrically necessary dislocations (GNDs) near the interfaces, as the material must accommodate the mismatch in strain to maintain continuity [61,114,135]. The GNDs accumulate into tangles or pile-ups at or near the boundaries between regions of different strength. In essence, any compositional gradient that produces a gradient in flow stress will inherently induce strain gradients, and a lattice curvature that necessitates GNDs to preserve lattice compatibility across the gradient [61,116,174–176].

The pile-up of GNDs at zone interfaces generates long-range internal stresses. Specifically, as GNDs build up on the interface within a softer region, they impose a back stress onto the dislocations in that soft region, opposing further plastic flow [23,32]. Conversely, the

same GND pile-up exerts a forward stress on the adjacent harder region, essentially assisting or "pushing" the harder zone towards yielding [61]. Hetero-deformation in a gradient structure thus produces a coupled internal stress state: the soft zones experience a back stress, and the hard zones experience a forward stress. These internal stresses are collectively termed hetero-deformation induced (HDI) stress.

Fig. 2-5(a) illustrates the origin of back stress in a gradient material. In the softer region, a Frank–Read source activates once the applied shear stress τ_a, exceeds its critical value τ_0, emitting n number of GNDs. These GNDs accumulate against the boundary, their identical Burgers vectors generating a long-range internal stress that opposes the external shear [23,61,135]. The long-range internal stress directly opposes the applied shear and, therefore, lowers the local stress at the source below τ_0, thereby inhibiting plastic deformation in the softer region and preventing further dislocation emission [61]. This stress is hence termed the back stress (τ_b). To enable further dislocation emission from the Frank–Read source, the applied shear stress must exceed both the back stress τ_b and the critical shear stress τ_0, thereby defining the threshold stress required for additional dislocation emission as follows [61,174–176]:

$$\tau_a = \tau_0 + \tau_b \tag{2.7}$$

Here, τ_0 defines the threshold shear stress required to activate the Frank–Read source, while τ_b denotes the back stress. Consequently, τ_b effectively increases the apparent strength of the softer region.

At the leading edge of a dislocation accumulation, a localised stress arises, scaling with the number of dislocations as $n\tau_a$. This intensified stress acts from the softer region towards the interface with the harder region, necessitating a corresponding equilibrating stress on the hard region's side. Such a balancing stress inherently facilitates plastic deformation within the harder region, effectively mirroring the role of externally imposed stress in activating dislocation slip [61,114,135]. Consequently, this internal stress in the harder region, originating from GND accumulations in the adjacent softer region, is termed the forward stress. At the boundary, the forward stress precisely counterbalances the back stress, having equal magnitudes but oriented oppositely [23,32,61,135].

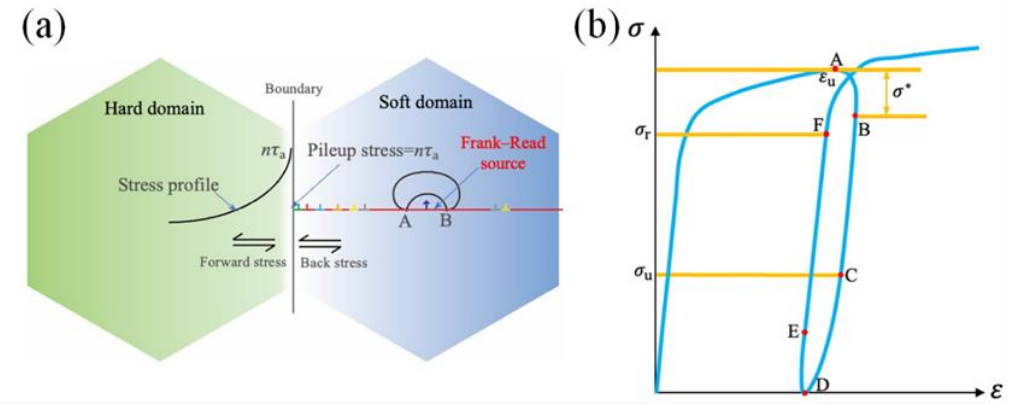

Figure 2-5 Illustrations depicting the mechanisms underlying back stress formation. (a) Representation of GND arrays, illustrating their contribution to internal stress fields [61,135]. Here, τ_a denotes the externally applied shear stress, and n represents the quantity of GNDs. (b) Illustration of typical unloading–reloading behaviour [61,135].

The interplay of back and forward stresses is more complex than a simple balancing act. Although these stresses negate one another precisely at the interface due to their equal magnitude and opposite orientation, their spatial distributions diverge significantly with increasing distance from the boundary. It is this discrepancy in spatial profiles that generates the HDI stress observed experimentally [135].

One of the most striking consequences of HDI stress in gradient materials is the simultaneous improvement of strength often far exceeding the rule-of-mixtures prediction, and ductility [179–200]. This enhancement is enabled by two related effects: HDI strengthening, which elevates the initial yield strength through internal stress, and HDI strain hardening, which sustains work hardening as HDI stress increases with plastic strain [61,135]. The back stress in the softer zones raises the apparent yield stress of the overall material since these regions can sustain a higher applied stress before yielding owing to the opposing internal back stress. This increase in yield strength attributable to the heterostructure is the HDI strengthening component [174–178]. Meanwhile, as deformation progresses, the continued accumulation of GNDs (and possibly progressive activation of new interfaces as initially elastic hard zones begin to yield) causes the internal HDI stress to build up further. The slope of the HDI stress–strain curve, which indicates the rate at which internal stress increases for a given increment of applied strain, defines HDI strain hardening [114,174–181]. Because HDI stress rises with strain especially during the early stages of plastic deformation, it provides an extra work-hardening

contribution beyond conventional mechanisms such as forest dislocation hardening [135]. This HDI strain hardening tends to be quite potent in gradient structures, manifesting as a high strain-hardening rate that delays necking and improves uniform elongation [61].

The HDI stress can be quantified through analysis of a hysteresis loop observed during cyclic unloading and reloading, assuming the reversibility of GND pile-ups under these conditions [61,114,116,135]. Fig. 2-5(b) illustrates this cyclic unloading–reloading behaviour schematically. The unloading phase commences at point A, defined by an unloading strain ε_u, and continues through a linear elastic region BC, characterised by an effective modulus E_u. The initial stress reduction along segment AB, denoted σ^*, arises from stress relaxation effects and is typically identified as the thermal component of the overall flow stress [61,135]. Complete unloading subsequently occurs at point D, where stress returns to zero. Upon reloading, the material follows another linear elastic path EF, with an associated modulus E_r. The stress magnitudes corresponding to points C and F represent the unloading yield stress σ_u and the reloading yield stress σ_r, respectively, facilitating calculation of the HDI stress via these measured quantities [23,32,61,135]. Consequently, the HDI stress can be determined using the following expression [23,32,174–178]:

$$\sigma_h = \frac{\sigma_r + \sigma_u}{2} \tag{2.8}$$

It is important to recognise that the validity of Eq. (2.8) for evaluating the HDI stress depends critically on the assumption that the GND configuration remains reversible throughout unloading–reloading cycles [135]. Nevertheless, under conditions of exceptionally high HDI stress, full unloading to zero stress followed by reloading may violate this reversibility assumption [61,135]. A notable consequence is the non-physical outcome where the measured σ_r value is less than σ_u. To mitigate this issue, unloading should be terminated and reloading initiated at a stress level sufficiently high to preserve the assumption underlying Eq. (2.8) [61,135]. Further investigation into this phenomenon is warranted [61].

Another unique aspect of deformation in gradient materials is the development of multiaxial stress states within the material under nominal uniaxial loading [61,135]. The heterogeneity and mutual constraints between hard and soft regions cause local deviations from purely uniaxial stress [174–178]. As one region tries to deform more than its

neighbour, internal lateral stresses arise to enforce compatibility. Subsequently, a configuration comprising a soft, CG layer sandwiched between two hard nanostructured layers is employed to elucidate the generation and evolution of multiaxial stress states, as shown in Fig. 2-6 [61].

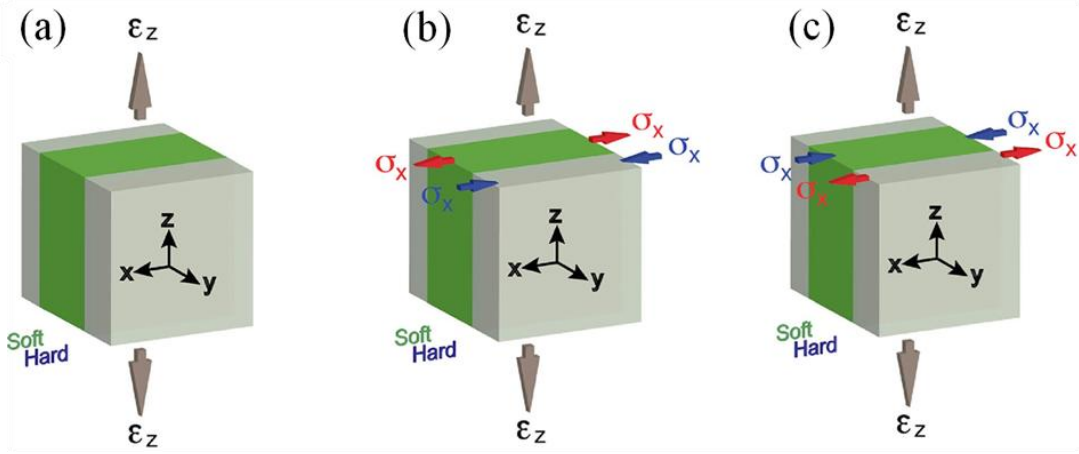

Figure 2-6 Schematic illustration of a layered heterostructure comprising a central CG soft layer enclosed by two harder, nanostructured outer layers, all possessing identical elastic modulus [61]. (a) Elastic-elastic stage; (b) elastic–plastic stage; (c) plastic-plastic stage [61,174–177].

Under the assumption of identical elastic modulus for both the soft and hard layers, application of a tensile strain ε_z along the z-axis initially produces compatible elastic deformation in these layers (Fig. 2-6(a)). Consequently, the specimen will experience contraction in both the lateral x-axis and the transverse y-axis directions, in accordance with the material's Poisson's ratio, ν. Specifically, the lateral and transverse contractions are given by [61]:

$$\varepsilon_x = \varepsilon_y = -\nu\varepsilon_z \tag{2.9}$$

As deformation continues and stress progressively increases, the structure transitions into an elastic–plastic regime, characterised by initial plastic yielding within the softer layer while the harder layers remain elastic (illustrated in Fig. 2-6(b)). Due to volume constancy in ideal plastic deformation, the effective Poisson's ratio for the deforming soft layer approaches $\nu = 0.5$, significantly exceeding the typical elastic Poisson's ratio for metallic materials, which generally ranges from 0.27 to 0.44, averaging around 0.33 [201,202]. Consequently, the lateral contraction rate of the softer layer surpasses that of the harder

elastic layers, inducing tensile stress within the softer layer and compressive stress within the harder layers, as depicted schematically in Fig. 2-6(b). Hence, the inherent mechanical incompatibility in such layered configurations transforms the externally applied uniaxial tensile stress into a complex, two-dimensional internal stress state [61].

Upon yielding of the nanostructured hard layers, the system enters the plastic–plastic regime (Fig. 2-6(c)). Owing to their limited work-hardening capacity, the hard phase rapidly localises deformation and nears necking, whereas the CG soft layer, with its greater strain hardening rate, stabilises the overall deformation to higher strains. Consequently, during this stage but before global necking, the hard layer contracts laterally more than the soft layer, reversing the x-direction normal stress such that σ_x is tensile in the hard constituents and compressive in the soft constituents (Fig. 2-6(c)) [23,32,61].

As illustrated by the model described above, variations in mechanical properties and deformation behaviours among different layers transform the externally applied uniaxial tensile stress into complex, interdependent two-dimensional stress states within the softer and harder regions [61,323]. Although the axial strain (ε_z) remains consistent throughout all layers, lateral strains (ε_x and ε_y) diverge between hard and soft regions, reflecting a strain partitioning phenomenon arising directly from mechanical incompatibility [323]. This partitioning of strain consequently generates the observed two-dimensional stress fields. While the simplified scenario presented in Fig. 2-6 addresses a two-dimensional case, actual gradient structures typically exhibit three-dimensional variations, resulting in correspondingly more complex three-dimensional patterns of strain and internal stress partitioning [61,188–190].

This multiaxial state has beneficial consequences for ductility. Firstly, the presence of lateral stresses means that the material's deformation is no longer confined to a single principal slip direction. The multiaxial stress state can activate multiple slip systems in the crystals, because the local resolved shear stresses occur on different planes due to the complex stress field [23,32,61,135]. Activating more slip systems leads to greater dislocation interactions including cross-slip, junction formation, Lomer-Cottrell locks, etc., thereby enhancing the work-hardening rate [61,135].

Secondly, multiaxial internal stresses help to delay strain localisation. Under purely uniaxial tension in a homogeneous material, once necking begins, the triaxial state at the

neck accelerates failure. In a gradient structure, however, the internal triaxial stresses develop early and spread over the material, effectively distributing plastic strain more uniformly [61,135]. The formation of dispersed strain bands, which are narrow regions of intense shear that traverse zone boundaries, is frequently observed in heterostructures and contrasts with the catastrophic single necking seen in homogeneous materials [61]. These strain bands can propagate and redistribute strain without causing immediate failure, thus delocalising deformation. In essence, the internal constraint creates a more stable plastic flow and increases the material's resistance to localisation, thereby enhancing uniform elongation and even improving toughness in some cases [135].

The above deformation mechanisms, specifically GND-driven HDI stresses and multiaxial constraint, are inherently tied to the presence of pronounced internal heterogeneity. Homogeneous materials, characterised by uniform composition and microstructure, cannot easily achieve these effects and consequently lie on the lower bound of the "strength–ductility trade-off" curve. In a uniform material under uniaxial load, deformation is uniform at the macroscale, so there are no internal boundaries to generate GND pile-ups on a large scale. While homogeneous materials do produce dislocation cellular structures or gradients in dislocation density (e.g. near grain boundaries or at sample surfaces), those internal features are much more subtle. The small misorientations across dislocation cell walls or incidental gradients in dislocation density can induce some short-range stress, but this is very weak compared to HDI stresses in a deliberately gradient-structured material [61]. In a uniform metallic material, the strength difference across any internal substructure is minimal, so any HDI hardening remains modest [61]. In short, the powerful back/forward stress coupling seen in gradient materials requires a significant contrast in flow stress between adjacent regions, a condition that homogeneous materials inherently lack. Moreover, a homogeneous material subjected to uniaxial tensile loading sustains a uniform uniaxial stress state throughout until the onset of necking, except for minor localised stress elevations potentially arising near microscopic inclusions or at grain boundaries. There is no mechanism to generate beneficial multiaxial stresses broadly throughout the gauge section. By contrast, gradient structures internally create a web of multiaxial stresses from the onset of plasticity, which as discussed promotes higher hardening [174–200]. However, introducing a soft region, such as embedding coarse grains within the UFG matrix, generates the HDI stress that continues to elevate flow stress with increasing strain, thereby producing kinematic hardening that prevents the rapid reduction

in work hardening typical of homogeneous UFG materials [61].

By contrast, homogeneous materials cannot generate significant HDI stresses or multiaxial constraint effects because they deform uniformly. They lack the internal soft–hard juxtaposition needed for GND pile-ups and back stress development. Any strengthening mechanism in a homogeneous metallic material (solid solution, precipitation, grain refinement, etc.) inevitably uses up some of the material's ductility, since all regions of the material flow together and there is no internal source of extra hardening once yielding starts. This contrasts starkly with compositional gradient materials, where the internal heterogeneity provides a dynamic hardening mechanism that kicks in during deformation, allowing strength and ductility to rise in tandem [23,32,61,114,135,174]. Essentially, gradient structures introduce a structural internal stress mechanism that homogeneous materials inherently lack.

In summary, gradient structured materials, whether their gradients are structural or compositional, share a fundamental suite of heterogeneous deformation mechanisms: mechanical incompatibility, GND pile-ups, HDI stresses, multiaxial stress and strain states, and an enhanced work hardening response [23,32,114,135,174–178]. Compositional gradients, however, constitute an even more versatile class of heterogeneous architecture, as compositional variations can modulate multiple deformation modes within the material, including slip, twinning, and phase transformation [61,144,198,203,204]. The specific deformation mechanisms associated with compositional gradients are discussed in the following sections.

2.2.2.2 Twinning and dislocation interactions

Gradient hierarchical twin network. Gradient hierarchical twin (GHT) networks represent a distinct type of structural gradient that significantly improves strength and strain hardening behaviour, primarily due to intricate twin interactions within their hierarchical structure [125]. The formation of these GHT networks occurs in two distinct stages, beginning with pre-torsion and continuing through subsequent tensile loading. During pre-torsion, initial (primary) twins emerge, establishing a gradient pattern aligned along specific crystallographic planes within individual grains [125,135]. The subsequent tensile loading induces the development of secondary and tertiary twins, oriented differently relative to the primary set (Fig. 2-7(a,b)). Importantly, primary twins impose

constraints on secondary twin propagation, while secondary twins similarly impede tertiary twin formation. These sequential and hierarchical constraints notably enhance strength and resistance to plastic deformation [125,135,205].

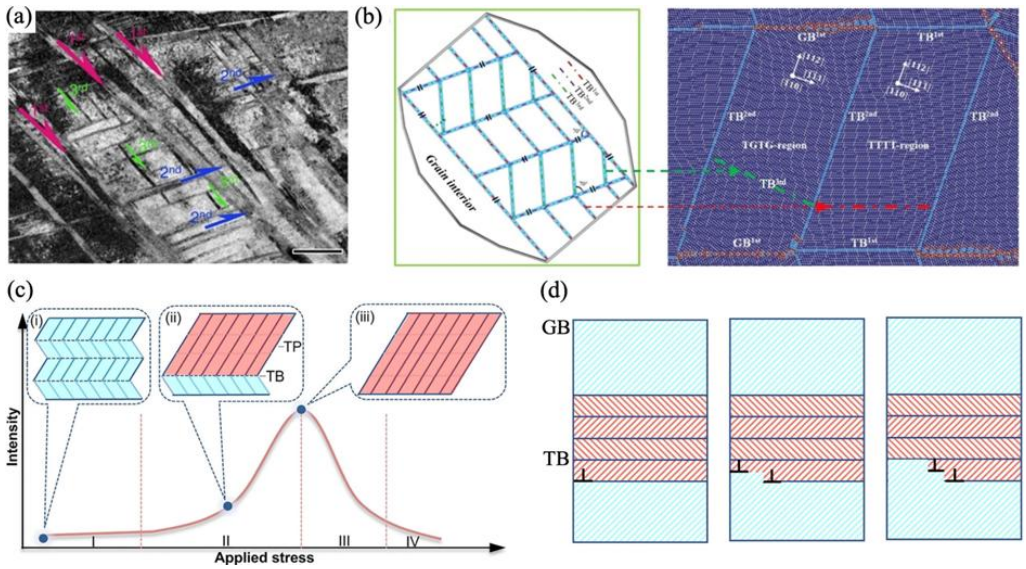

Figure 2-7 Nanotwin network within a gradient nanotwinned architecture. (a) Transmission electron micrograph image taken after uniaxial tension, revealing a three-tier twin network; primary, secondary, and tertiary twins are marked by pink, blue, and green arrows, respectively [125]. (b) Schematic and atomistic renderings of the hierarchical arrangement [205]. (c) Conceptual sketch of detwinning driven by the shear stress [208]. (d) Conceptual sketch of detwinning governed by the Eshelby stress [209].

Twin–dislocation interactions. A recently identified phenomenon emerges in gradient materials exhibiting simultaneous gradients in grain size and twin thickness [152,154,211,212]. In such systems, dislocations congregate into aligned bundles that traverse multiple twin boundaries within each grain and run parallel to one another. These aggregates, termed bundles of concentrated dislocations (BCDs), consist predominantly of mode II dislocations, with a smaller yet significant mode I fraction. Indeed, the mode II dislocation density within BCDs can reach up to eight times that found in homogeneous nanotwinned structures [135]. Arranged perpendicular to the twin planes and aligned with the structural gradient, these dispersed BCDs impart additional strengthening and work hardening.

Atomistic simulations via molecular dynamics have clarified the BCD formation mechanism (Fig. 2-8). To replicate experimental conditions, two nanotwinned building

blocks, NT-A (30 nm grain size, 0.83 nm twin thickness) and NT-B (50 nm grain size, 6.23 nm twin thickness), were alternately stacked to create gradient nanotwinned (GNT) architectures: GNT-AB (6.2 MPa nm^{-1} gradient) and GNT-ABAB (12.4 MPa nm^{-1} gradient) [152] (Fig. 2-8(a)). Tensile stress–strain data demonstrate a clear enhancement in strength with increasing gradient magnitude (Fig. 2-8(b)). Fig 2-8(c,d) depicts the schematic of the BCD dislocation architecture: Mode I dislocations pass through twin boundaries, whereas Mode II dislocations remain confined between adjacent twin boundaries. Shockley partials in Modes I and II can react to form stair-rod dislocations [213]. At low strains, mode I dislocations nucleate at the NT-A/NT-B interfaces and propagate towards neighbouring twin boundaries, whilst mode II dislocations emanate from lateral grain boundaries (Fig. 2-8(e–h)). With further deformation, a high-density network of BCDs develops within the grains (Fig. 2-8(i)), in which a minor fraction of stair-rod dislocations forms through interactions between Shockley partials γD and δB from modes I and II [213] (Fig. 2-8(j)).

The BCD structure represents a category of GND. Its population is governed not only by the plastic strain gradient but also, conspicuously, by the grain size [214,215]. Larger grains tend to harbour more BCDs, presumably because the likelihood of Mode I–Mode II interactions, and hence BCD formation, increases with grain size. This observation suggests new avenues for gradient structure design: simultaneous enlargement of grain size and enhancement of the structural gradient could greatly amplify the additional strengthening and work hardening imparted by BCDs [211].

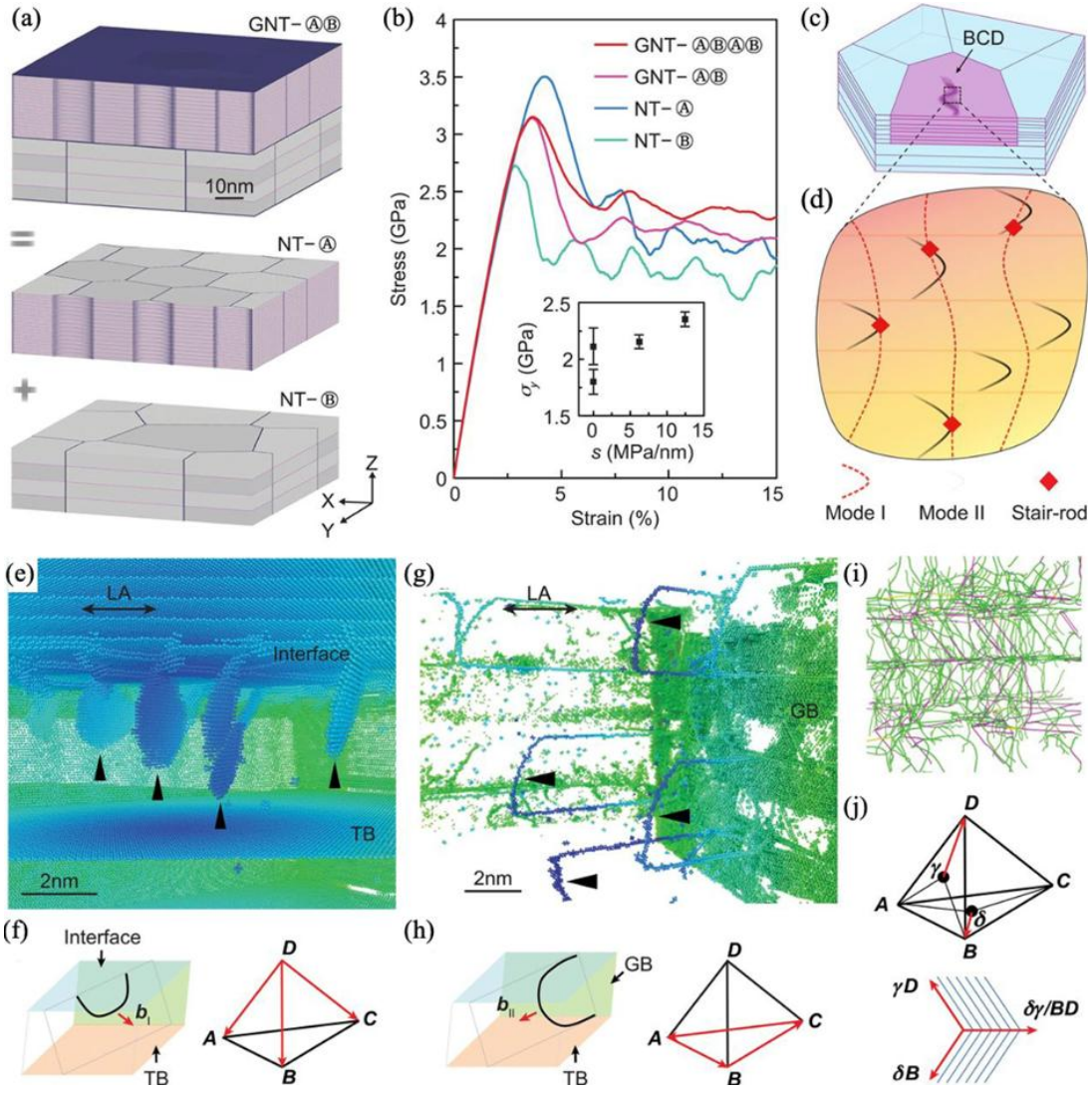

Figure 2-8 Molecular dynamics simulation analysis of twin–dislocation interactions in GNT structures exhibiting dual gradients in grain size and twin thickness [152]. (a) Constructed atomic configurations of GNT structures from two uniform twin thickness blocks, NT-A and NT-B. (b) Tensile stress–strain response. (c) Initiation of a BCD within a nanotwinned grain. (d) Magnified illustration of the BCD dislocation configuration. (e) Mode I dislocation generation at block interfaces, propagating towards adjacent twin boundaries. (f) Representation of mode I dislocation Burgers vectors (*DA, DB, DC*). (g) Mode II dislocation nucleation from lateral grain boundaries. (h) Illustration of mode II dislocation Burgers vectors (*AB, AC, BC*). (i) Detailed dislocation arrangement of the BCD region, with green lines depicting Shockley partials and red lines indicating stair-rod dislocations. (j) Mechanistic schematic demonstrating the formation of stair-rod dislocation *δγ/BD* through interactions between Shockley partials *γD* and *δB*.

2.2.2.3 Grain coarsening

A grain size gradient, characteristically manifested as a NC surface layer, is a prototypical structural gradient. During plastic deformation, this NC layer may undergo mechanically induced grain coarsening. A critical grain size threshold exists within the layer that governs whether coarsening is triggered [140,216]. When the grain size lies below this threshold, tensile straining initiates coarsening. The threshold is closely linked to a change in the dominant deformation mechanism, from localised dislocation glide to grain growth-controlled plasticity, and can be shifted by tuning the material's SFE [217].

In gradient structured materials, grain coarsening generally proceeds homogeneously across layers of differing grain size, potentially giving rise to numerous dispersed shear bands. Owing to their variety of propagation directions, these bands inhibit further localisation, thereby delocalising shear and enhancing structural stability [218]. Under uniaxial tension, the NC surface layer experiences a uniform, extensive increase in grain size, producing a broad grain size distribution [216].

Early observations of NC layer coarsening were interpreted using the curvature-driven migration model [219,220], in which grain boundary motion underlies coarsening. The velocity of grain boundary migration, v, can be estimated by the following expression [220]:

$$v = \frac{\omega\lambda^4}{k_B T}\exp\left(-\frac{Q^{GB}}{k_B T}\right)\Delta P \tag{2.10}$$

where ω is the atomic jumping frequency, k_B is the Boltzmann's constant, T is the temperature, Q^{GB} is the activation energy for grain boundary migration, and ΔP is the thermodynamic driving force. The latter is proportional to the ratio of grain boundary energy (γ) to grain size (d). Consequently, a reduction in grain size amplifies the driving force, facilitating grain boundary migration and thus promoting grain coarsening. Nevertheless, below a critical grain size, migration velocity diminishes significantly [221].

Grain boundary migration during coarsening entails cooperative atomic rearrangements along specific paths and movement through low energy boundary structures. Direct atomic-scale images of such migration have recently been obtained (Fig. 2-9) [222]. Migration may be regarded as comprising atomic detachment from, and attachment to, the grain boundary. The activation energy therefore contains contributions from both

processes: detachment is thermally activated, whereas attachment is influenced by the terminating structure of the grains [223]. Shear stress can also drive grain boundary migration, incorporating a normal grain boundary displacement and a lateral translation of the neighbouring grains [224]. Shear-coupled grain boundary migration has been widely confirmed experimentally and by molecular dynamics simulations [224–228]. In polycrystals, however, triple junctions constrain the motion, so growth soon stagnates [225].

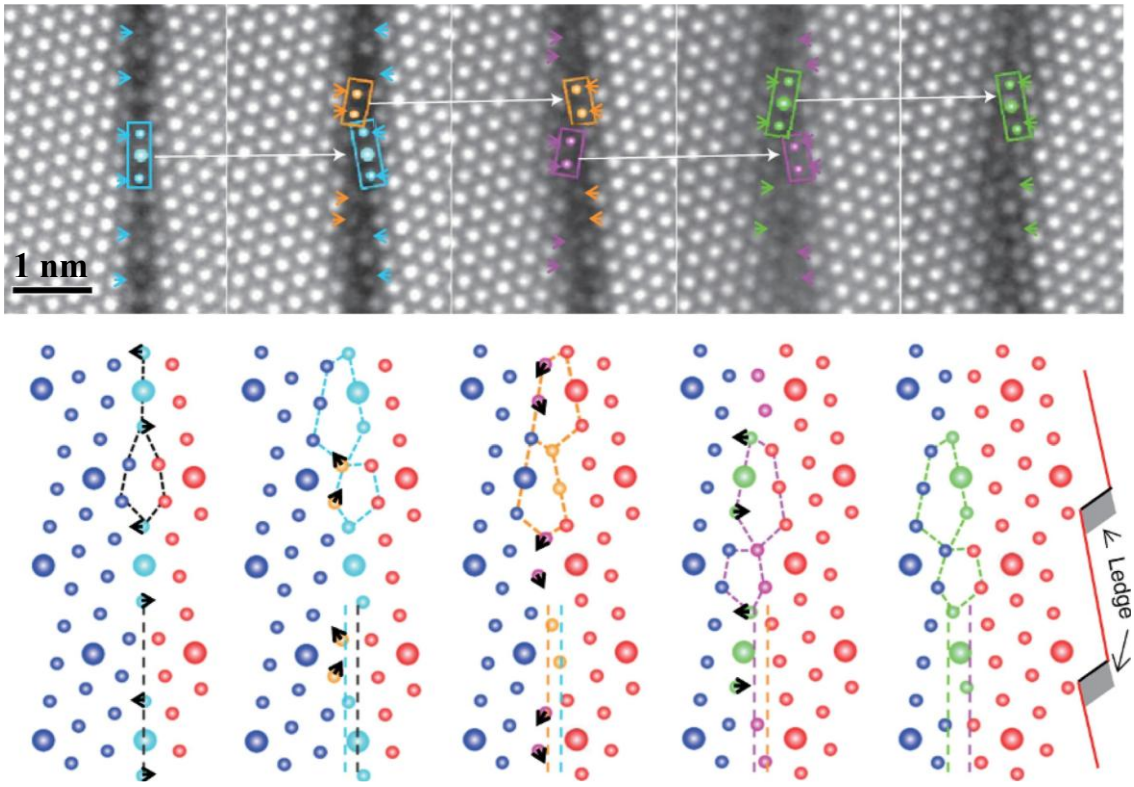

Figure 2-9 High-resolution high-angle annular dark-field (HAADF) scanning transmission electron microscopy (STEM) image illustrating grain boundary migration via coordinated atomic rearrangement [222]. The dotted polygons highlight structural units within the migrating boundary. Atomic columns, indicated in different colours (light blue, orange, pink, and green), progressively shift stepwise from the left-hand grain into the adjacent right-hand grain.

Mechanically induced grain coarsening is strain rate and temperature sensitive, becoming more pronounced at elevated temperatures or lower strain rates [136]. Its kinetics can be expressed as [136]:

$$v(\sigma, T) = v_0 \exp\left(-\frac{Q^{GB}(\sigma)}{k_B T}\right) \tag{2.11}$$

here, σ denotes the external stress, v_0 represents the intrinsic grain boundary migration velocity under stress-free conditions, and $Q^{GB}(\sigma)$ signifies the activation free energy for migration, which varies as a function of the applied stress and is given by the following expression [135]:

$$Q^{GB}(\sigma) = Q_0\left(1 - \frac{\sigma}{\sigma_0}\right)^P \tag{2.12}$$

In this context, Q_0 represents the intrinsic activation energy when stress is absent ($\sigma=0$), σ_0 denotes the threshold stress necessary for spontaneous boundary migration, and P is a dimensionless exponent. From these relationships, it follows that elevation of temperature or lowering of strain rate enhances grain boundary migration velocities.

The HDI stresses and multiaxial stress and strain states outlined earlier are universal mechanisms common to all gradient structured materials. By contrast, GHT networks, BCDs structures and grain coarsening phenomena arise predominantly in structural gradients, because they are generally linked to nanoscale grain sizes and their gradient distributions. The following sections address the deformation mechanisms that are encountered more commonly in compositional gradients.

2.2.2.4 Solute redistribution

Metallic materials with CGSs exhibit unique deformation mechanisms due to their spatially varying compositions. A key phenomenon is stress-driven solute redistribution during plastic deformation [229,230]. In CGSs, differences in composition between regions create chemical potential gradients that, under an applied stress, can drive diffusion of solute atoms from higher-concentration areas to lower-concentration areas [229,230]. This effect, which is essentially a mechanically induced diffusion analogous to the Gorsky effect in metallurgy, is negligible in homogeneous alloys with uniform composition but becomes significant in alloys exhibiting a compositional gradient [229,230]. This behaviour can be described by extended diffusion laws. Fick's first law for solute flux **J** can include a stress term [231–233]:

$$\mathbf{J}(\mathbf{r}, t) = -\frac{D_0}{R\theta} c(\mathbf{r}, t) \nabla \mu(\mathbf{r}, t) \tag{2.13}$$

In this expression, **J** (**r**, *t*) denotes the particle flux vector; **r** = $\langle x_1,\ldots,x_n\rangle \in \mathbb{R}^n$ specifies the spatial coordinate in n dimensions, and *t* represents time. Here, *R* is the universal gas constant, θ the absolute temperature, D_0 the diffusion coefficient and μ (**r**, *t*) the chemical potential, as prescribed by the constitutive relation [234]:

$$\mu(\mathbf{r},t) = R\theta \ln c(\mathbf{r},t) - \Omega\sigma_H(\mathbf{r},t) \tag{2.14}$$

Here, Ω denotes the partial molar volume ($m^3\ mol^{-1}$), and σ_H (**r**, *t*) represents the hydrostatic stress, defined as the arithmetic mean of the normal stress components, namely [231]:

$$\sigma_H = \frac{\sigma_{xx}+\sigma_{yy}+\sigma_{zz}}{3} \tag{2.15}$$

Under conditions of isothermal thermodynamic equilibrium, the generalised form of Fick's law (Eq. (2.13)), incorporating the chemical potential expression given by Eq. (2.14), can be expressed as follows [231]:

$$\mathbf{J}(\mathbf{r},t) = -D_0\left[\nabla c(\mathbf{r},t) - \frac{\Omega}{R\theta}c(\mathbf{r},t)\nabla\sigma_H(\mathbf{r},t)\right] \tag{2.16}$$

This indicates that solute atoms will redistribute in response to both concentration gradients and stress gradients [235]. In gradient alloys, plastic deformation often produces a heterogeneous stress and strain distribution, with softer lower-alloy regions deforming first while harder higher-alloy regions sustain greater elastic stress [61,135]. This internal stress mismatch provides a driving force for solute atoms to diffuse from the harder zones into softer zones to reduce the free energy [235]. In practice, such stress-assisted solute flow is usually limited at low temperatures due to slow lattice diffusion, but high dislocation densities and defects generated during deformation greatly accelerate redistribution [236–239]. Dislocations act as fast diffusion pipes and also as conveyors that drag atmospheres of solute atoms [236–239]. As dislocations move under load, they can carry solute atmospheres and leave behind enriched or depleted zones, effectively “pumping” solute from one place to another on a microscopic scale [236–239]. Over large strains, this can lead to a net relocation of solute along the gradient direction [236–240].

The deformation-induced solute redistribution in CGSs contributes to a remarkable synergy of strength and ductility [229,230]. A critical mechanism arising from solute redistribution is the interaction between moving dislocations and the spatially varying solute field, specifically the dislocation–solute interactions occurring across the gradient

[235–240]. As dislocations move from one compositional zone to another, they experience changing solute atmospheres and precipitate distributions. Heterogeneous precipitation or solute clustering often occurs, for instance, fine precipitates in solute-rich regions, which act as potent pinning sites [235–240]. Dislocation motion is thus impeded to varying degrees across the gradient, leading to increased dislocation entanglement and storage [235–240]. This phenomenon is analogous to dynamic strain ageing or Cottrell-atmosphere formation [235–240], but here it is spatially modulated by the gradient: dislocations accumulate and tangle in solute-rich regions, elevating work hardening rates [235–240]. One of recent studies has confirmed that compositional heterogeneity amplifies dislocation interactions, inducing more frequent pinning and depinning events that hinder dislocation motion and thereby increase strength without sacrificing ductility [241]. This mechanism parallels cluster strengthening observed in alloys containing nanoscale solute clusters [241].

2.2.2.5 Crack path deflection, crack tip blunting, and crack bridging

Three key micro-mechanisms have been identified by recent studies as responsible for the enhanced damage tolerance of CGMs: crack path deflection, crack tip blunting, and crack bridging [242–253]. These mechanisms, often working in concert, impede crack initiation and growth by altering the crack's trajectory or crack-tip conditions [242–245,247]. Compositional gradients can induce heterogeneous microstructures (such as ductile vs. hard phases, or variations in lattice stability) that locally toughen the material and divert or arrest cracks. In classical terms, crack deflection and bridging are extrinsic toughening mechanisms acting behind or along the crack wake, while crack-tip blunting is an intrinsic toughening mechanism operating ahead of the crack [250–253]. By leveraging these effects, graded alloys have demonstrated exceptional combinations of high strength, large tensile ductility, and high fracture resistance, thereby evading the traditional trade-off between strength and toughness [242–253].

Crack path deflection in gradient structures. A striking feature of fracture in CGMs is the tendency for cracks to deviate from a straight path (i.e. to deflect, twist or branch) as they propagate through regions of varying composition [242]. Crack path deflection refers to the crack's deviation from the principal stress plane, often resulting in a more tortuous route [243]. In graded structures, deflection is driven by spatial differences in local toughness and strength: the crack will seek out the path of least resistance, which

continually changes as the composition (and thus microstructure) varies [244]. This can lead to gradual curving of the crack trajectory or even crack branching within the graded zone [245].

Crack deflection in a gradient material is analogous to what occurs at interfaces in layered composites, but here it happens continuously [242]. In a homogeneous metallic material, the crack experiences the same resistance in all directions and thus typically propagates straight ahead. In a discretely layered heterogeneous material (e.g. a laminate), a crack may deflect along a bimaterial interface if that interface is weaker or if the adjoining layer has higher toughness [246]. However, once past the interface, the crack enters a new homogeneous layer and may propagate straight again [246]. In a compositional gradient, by contrast, there is no sharp interface, as the material resistance changes progressively. As a result, the crack path can continuously adjust, leading to a smoothly curved or zigzag trajectory through the gradient region [242–245].

Why does crack deflection increase toughness and ductility? Before addressing this question, certain fundamental concepts pertaining to cracks must first be elucidated. In linear elastic fracture mechanics, the three "modes" describe how a crack is loaded at its tip [247]: Mode I (Opening mode): The crack faces are pulled directly apart by a tensile stress acting perpendicular to the crack plane [247]. This is the most common and most critical fracture mode, in which the crack "opens" like a book. Mode II (Sliding or In-Plane Shear mode): Shear stresses act parallel to the crack plane and perpendicular to the crack front, causing the two faces to slide over one another in their own plane [247]. Imagine the crack faces sliding sideways against each other. Mode III (Tearing or Anti-Plane Shear mode): Shear stresses act parallel to the crack front (i.e. out of the crack plane), so the faces move in opposite directions out of the plane, like two pages being torn in opposite directions [247,248]. Each mode is associated with its own stress intensity factor, which quantifies the intensity of the corresponding crack-tip stress field [247]. Another pertinent concept is the resistance curve (R-curve), which characterises a material's fracture resistance [89,249]. A rising R-curve indicates stable crack growth, which means that a crack must extend by a finite amount before catastrophic failure [89,249]. Materials with steeply rising R-curves therefore exhibit enhanced damage tolerance and greater work-of-fracture than materials with flat (constant) resistance curves [89,249].

By making the crack path more tortuous, deflection increases the energy required for crack

advance in two ways [250–252]: (1) the crack must propagate over a larger area (a longer path) to achieve the same projection, consuming more energy in creating new surfaces, and (2) deflection often introduces mode II (shear) or mode III components at the crack tip, reducing the mode I stress intensity effective at driving opening. In essence, a deflected crack is less efficient at concentrating stress at its tip. This translates into a higher apparent fracture toughness [250–253]. Experiments confirm that crack deflection in graded materials contributes to R-curve behaviour, where the crack becomes harder to grow as it lengthens. Crack deflection also delays the onset of catastrophic failure in tension, giving the material extra ductility [253]. Rather than a single straight crack causing immediate rupture, a deflected crack may meander and require higher strains (or multiple microcracks) to coalesce into final failure [242,247,250–253].

Crack tip blunting and local plasticity. Another crucial mechanism is crack tip blunting, wherein a sharp crack is rendered effectively blunt by localised plastic yielding in a ductile heterogeneous zone [242–245,247,250–253]. Compositional gradients often create soft, ductile regions adjacent to harder phases. When a crack encounters such a ductile buffer, the high stress at the crack tip causes the soft material to yield and plastically deform, rounding off the crack tip [242–245]. This increases the crack tip radius and diminishes the stress concentration [243]. The outcome is a lower driving force for crack advance, as a blunted crack requires higher applied stress intensity to propagate than a sharp crack [244].

Sun et al. [254] demonstrated crack tip blunting in a chemically heterogeneous high-strength steel containing Mn-rich austenitic zones. In this medium-Mn steel, the bulk matrix would transform to hard martensite under stress, but the intentionally introduced Mn-rich islands remained stable austenite (Fig. 2-10) [254]. Cracks nucleating in the hard transformed regions were often arrested upon entering an austenite island [254]. The austenitic region, being more plastically compliant, yielded around the crack tip. Sun et al. observed that enhanced plastic compliance and flow of austenite at the crack tips result in crack blunting [254]. As a result, many H-induced microcracks in the heterogeneous steel were blunted and arrested in the Mn-rich zones instead of propagating (Fig. 2-11) [254]. Crucially, this crack tip blunting occurred even when all hydrogen traps were saturated, meaning it is an inherent mechanical toughening mechanism independent of hydrogen trapping [254]. The governing principle behind crack tip blunting is that the ductile zone increases the crack tip's plastic zone size and tip radius, thereby reducing the stress

intensity [254]. A simple fracture mechanics estimate of the plastic zone size r_p ahead of a crack in yield-controlled blunting is given by [247]:

$$r_p \approx \frac{1}{2\pi}\left(\frac{K_I}{\sigma_y}\right)^2 \tag{2.17}$$

where K_I is the stress intensity factor and σ_y is the yield strength of the crack tip material. A compositional gradient that provides a locally lower σ_y (more ductile phase) will produce a larger r_p for the same K_I, meaning the crack tip can undergo more plastic stretching and rounding. In essence, the crack tip becomes a notch of finite radius instead of an ideal crack. The stress concentration for a blunted crack of tip radius is far lower than for a sharp crack. For an elliptic crack/notch, one can approximate [255]:

$$\sigma_{max} \sim \sigma_{applied}\left(1 + \frac{2a}{\rho}\right) \tag{2.18}$$

where a denotes the semi-length of the elliptical notch and ρ represents the radius at the crack tip. Thus, blunting can halt crack growth until higher loads [250–253]. This was evidenced in the heterogeneous steel: blunted cracks surrounded by ductile austenite did not propagate further until new cracks eventually nucleated elsewhere in the harder regions [256]. Sun et al. noted that further crack propagation is no longer possible in a blunting/arrest event, requiring new cracks nucleate in other regions if loading continues [254].

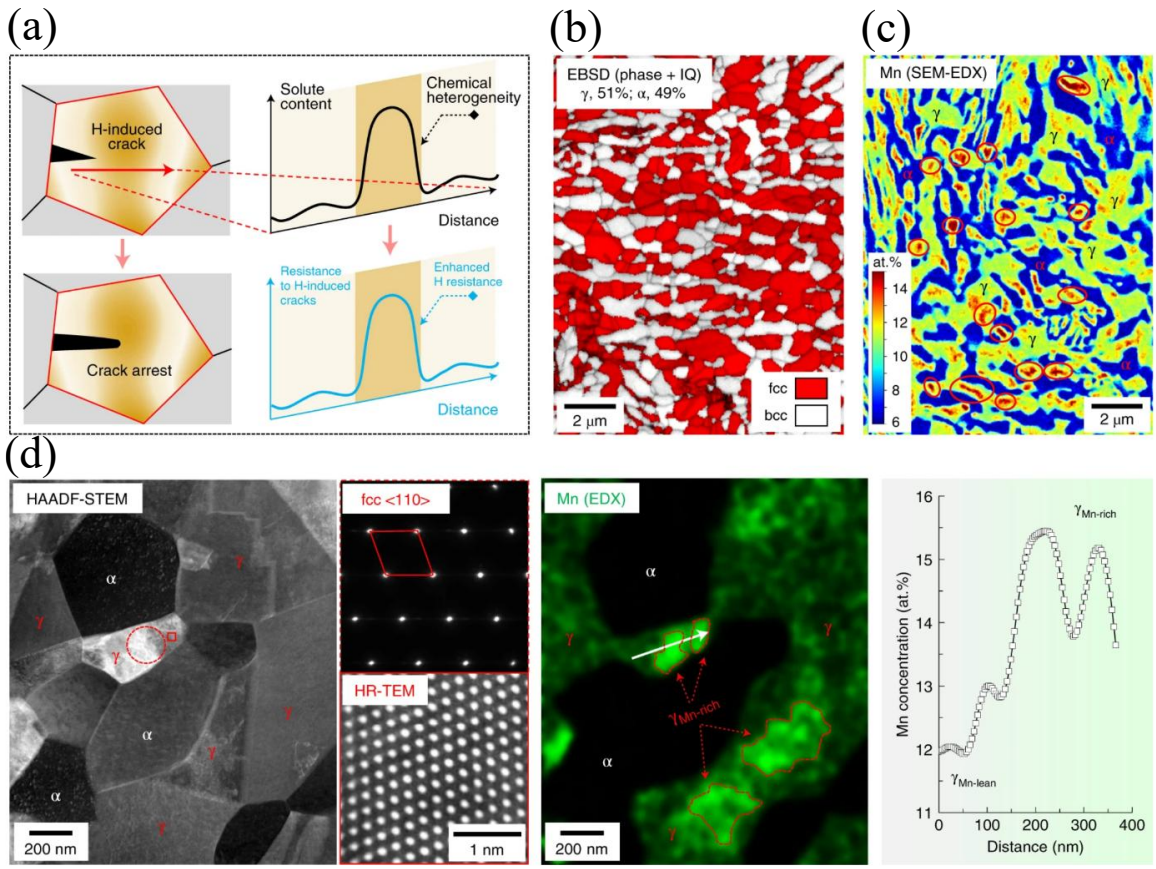

Figure 2-10 Conceptual and microstructural basis for crack arrest against hydrogen embrittlement by chemically induced heterogeneity: (a) schematic representation of the design concept, in which a hydrogen-induced crack propagates through a purpose-engineered solute-enriched buffer zone; the right-hand sketch schematically illustrates the solute-concentration profile together with the corresponding crack-resistance curve; (b) electron backscatter diffraction phase map, superimposed on an image quality map, revealing the dual-phase microstructure of fcc austenite and bcc ferrite; (c) scanning electron microscopy-based energy-dispersive X-ray spectroscopy (EDX) map showing the overall manganese distribution, in which chemically buffered zones, namely Mn-enriched regions within the austenite (~14 to 16 at.% Mn), are indicated by elliptical outlines; (d) HAADF-STEM image with accompanying EDX analysis demonstrating multiple Mn-rich domains within a single austenite cluster and even within individual grains; to the right of the STEM image are shown selected area electron diffraction patterns and high-resolution transmission electron microscopy images obtained from the circled and rectangular regions, respectively, whilst the EDX line scan is taken from the area marked by white arrows in the EDX map [254].

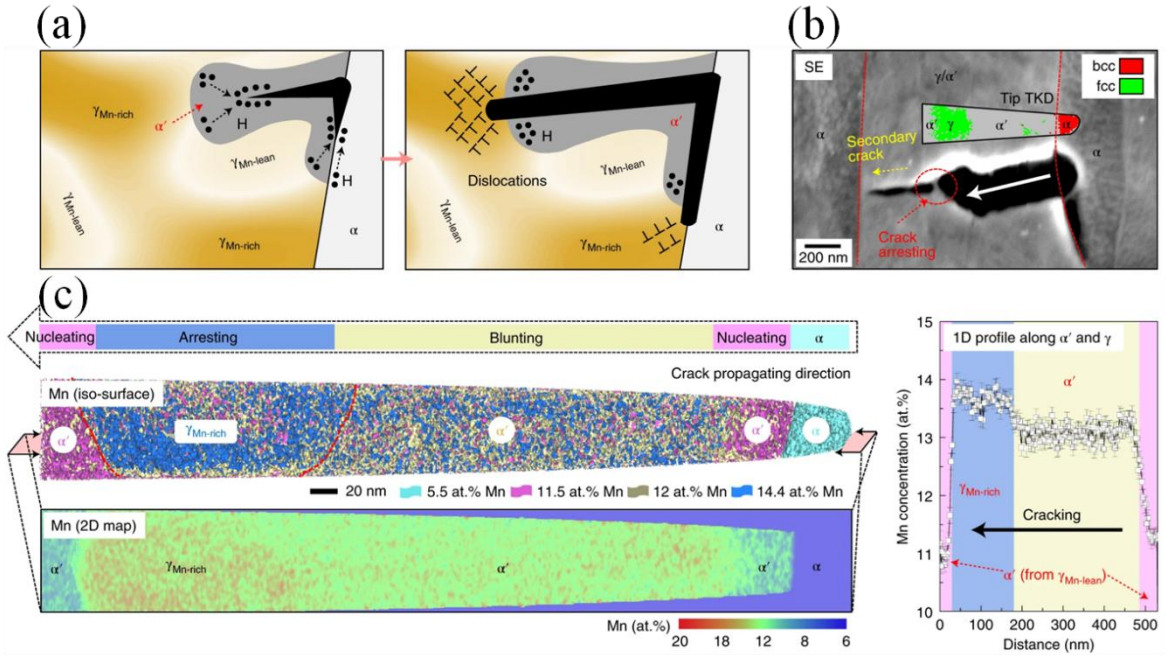

Figure 2-11 Hydrogen-induced crack arrest mediated by chemical heterogeneity: (a) schematic illustration of the arrest mechanism, wherein the strain-stable, Mn-enriched austenite ($\gamma_{Mn\text{-}rich}$) resists strain-induced transformation and, owing to its higher plastic compliance and lower hydrogen diffusivity, blunts and halts invading hydrogen-assisted microcracks; (b) representative passivated and arrested hydrogen-induced crack in the chemically heterogeneous steel after hydrogen charging and fracture, observed by secondary electron imaging near the fracture surface and specimen edge, where the hydrogen concentration approaches saturation; the inset shows a transmission Kikuchi diffraction phase map of the atom probe tomography tip extracted immediately beneath the crack tip, with the α/γ (ferrite/austenite–martensite) interface delineated by a red dashed line and the crack propagation direction indicated by a white arrow; (c) atom probe tomography analysis of the tip in (b), comprising a Mn iso-composition surface map, a two-dimensional Mn concentration map, and a one-dimensional Mn concentration profile traversing the α'–γ interface (error bars denote standard deviation); the colour coding (pink, yellow, blue) designates regions of differing Mn content [254].

Crack tip blunting by soft gradient zones not only arrests cracks but also increases the energy absorption at the tip [250–253,254]. Blunting is effectively a way to convert crack-driving energy into plastic deformation (a form of damage tolerance) [250–253,254]. A larger plastic zone means more energy is dissipated in plastic work rather than creating new crack surface [254]. In the Mn-graded steel, this was described via an energy argument

[254]: a larger Mn-rich buffer zone essentially requires a higher plastic energy for crack growth or opening. By Griffith's energy balance [257], the fracture resistance G_c rises when additional plastic work is needed to advance the crack [258]. Therefore, designing a compositional gradient to create ductile buffer regions increases the intrinsic toughness by crack tip blunting. Even in the absence of hydrogen, such heterostructures can be beneficial [254]. In comparison to conventional homogeneous transformation-induced plasticity (TRIP) steels, which suffer from autocatalytic crack propagation due to transformation-induced hydrogen release, the Mn-gradient structure interrupts this chain of damage evolution [254]. Consequently, the total crack length near the fracture surface in Mn-gradient samples is significantly reduced relative to the homogeneous counterpart [254]. Hence, this crack blunting mechanism constitutes one of the key factors underpinning the enhanced hydrogen embrittlement resistance of steels [254].

Crack bridging by ductile ligaments. The third major mechanism is crack bridging, wherein intact material ligaments span the faces of an opened crack, carrying load and "bridging" the crack behind the crack tip [242–245]. In CGMs, crack bridging often occurs when a tougher or more ductile region resists fracture even as an adjacent brittle region cracks, leaving unbroken segments that tie the crack flanks together [242]. These bridging ligaments provide closure stress on the crack and effectively shield the crack tip from the full applied driving force [247–253].

In the previously discussed high-strength steel featuring a Mn compositional gradient, Sun et al. [254] identified unequivocal microscale evidence of crack bridging. In about 21% of the examined microcracks, the Mn-rich austenite zones remained unfractured as the crack advanced into them, creating ductile ligaments that span across the crack wake [254]. As shown in their microscopy (Fig. 2-11(b)), an H-induced crack propagating in a martensitic region was arrested within the Mn-rich zone, and part of that austenitic region stayed intact bridging the crack faces [254]. The authors describe that these Mn-rich zones remain as ligaments that can bridge the crack wake, and this crack bridging effect will further reduce the crack tip stress intensity and continuously suppress or delay crack propagation [254]. In other words, the tough austenite bridges carry load after the crack has passed, effectively closing the crack and screening the crack tip from stress [254]. This is a powerful toughening mechanism because the crack cannot fully open or extend without additionally fracturing the bridging ligament, which requires extra energy [254]. The presence of

multiple small bridging zones (due to a high number density of Mn-rich islands) was noted to increase resistance, as it reduces the initial size of H-induced microcracks and demands higher energy for crack growth [254].

A governing description of crack bridging can be given in terms of stress intensity factors [253]. If a bridging ligament exerts a closing force on the crack surfaces, one can define a bridging stress intensity K_{bridge} that opposes the applied stress intensity $K_{applied}$. The effective crack tip driving force K_{eff} is then [253]:

$$K_{eff} = K_{applied} - K_{bridge} \tag{2.19}$$

The tougher the bridges (higher bridging stress or more numerous bridges), the larger K_{bridge} becomes, and thus K_{eff} seen at the crack tip is lower [253]. In practical terms, the crack will not propagate further until $K_{applied}$ increases enough that K_{eff} reaches the material's toughness [253,257]. In CGMs, the bridges are usually ductile phases which can sustain significant stress and plastic deformation, giving a substantial K_{bridge}. Sun et al. qualitatively confirmed this by noting the crack bridging ligaments reduce the crack tip stress intensity during hydrogen-assisted cracking [254]. This aligns with the general bridging equation above – the ligaments carry part of the load.

2.2.2.6 Integrated deformation mechanisms enabled by core–shell structures

Compositional gradients in alloys and composites can induce core–shell microstructures wherein one phase or region (the "core") is encased by another compositionally distinct phase (the "shell") [259–273]. Such architectures profoundly influence deformation by creating heterogeneities in crystal structure, strength, and stability between core and shell. A unifying theme from numerous studies [259–273] is that the core–shell design enables simultaneous strengthening and toughening by activating multiple deformation mechanisms. Dislocation motion is often strongly affected: hard cores can confine or accumulate dislocations, while softer shells act as sources or buffers for dislocations [259–261]. Phase transformations (e.g. TRIP) and mechanical twinning can be selectively triggered in the metastable regions due to local composition shifts [262–265]. Additionally, a mismatch in strength between core and shell leads to strain partitioning – the more compliant phase accommodates higher strain – which generates internal HDI stresses that

elevate work hardening capacity [266]. The interfaces between core and shell phases serve as potent barriers and facilitators: they can transfer loads between phases, block or redirect cracks, and promote hierarchical deformation (sequential activation of deformation modes across scales) [268].

2.2.3 Mechanical properties of gradient structured metallic materials

Having delineated the deformation mechanisms associated with gradient structures, this section reviews the mechanical properties of gradient structured metallic materials, with particular emphasis on the unique advantages these architectures confer in achieving a strength–ductility synergy. Several representative studies addressing the aforementioned deformation mechanisms will be examined in detail in the ensuing discussion.

Lu et al. [121] were the first to demonstrate the remarkable strength–ductility synergy attainable in gradient structured Cu. As illustrated in Fig. 2-12(a), the gradient material exhibits a yield strength double that of CG Cu, while maintaining comparable ductility, a striking outcome attributed to mechanically driven grain growth within the NC surface layer. Even in the absence of pronounced grain growth, diverse gradient structured metallic materials display excellent combinations of strength and ductility, including gradient IF steel (Fig. 2-12(b)) [120], Ni [274], TWIP steel (Fig. 2-12(c)) [125], and Cu [136]. Most recently, electrodeposition has been used to produce Cu possessing concurrent gradients in grain size and twin thickness [152]; this dual gradient architecture affords significant gains in both strength and ductility over a simple grain size gradient (Fig. 2-12(d)). Where TRIP [275] or TWIP [276–278] is activated within a gradient structure, ductility is further enhanced, chiefly because of the pronounced strain hardening response characteristic of heterogeneous architectures [23,120].

Several mechanisms have been proposed to account for the augmented strain hardening capacity. First, mechanically driven grain growth in the NC layer during tensile loading can partly restore the layer's strain hardening capability, reinstating a measure of forest hardening [121,216]. Studies on gradient IF steel confirm that such grain growth recovers some, though not all, of the hardening required to suppress necking; hence pure NC metals still tend to exhibit limited ductility [121,279].

Secondly, HDI strain hardening arises from mechanical incompatibility between adjacent layers, or within graded layers, which engenders strain gradients and hence GNDs that pile-

up at hetero-interfaces [23,174,176,280]. The resulting HDI stresses give rise to HDI strengthening and hardening, verified by unloading–reloading hysteresis loops [120] and direct measurements of HDI stress [174,177].

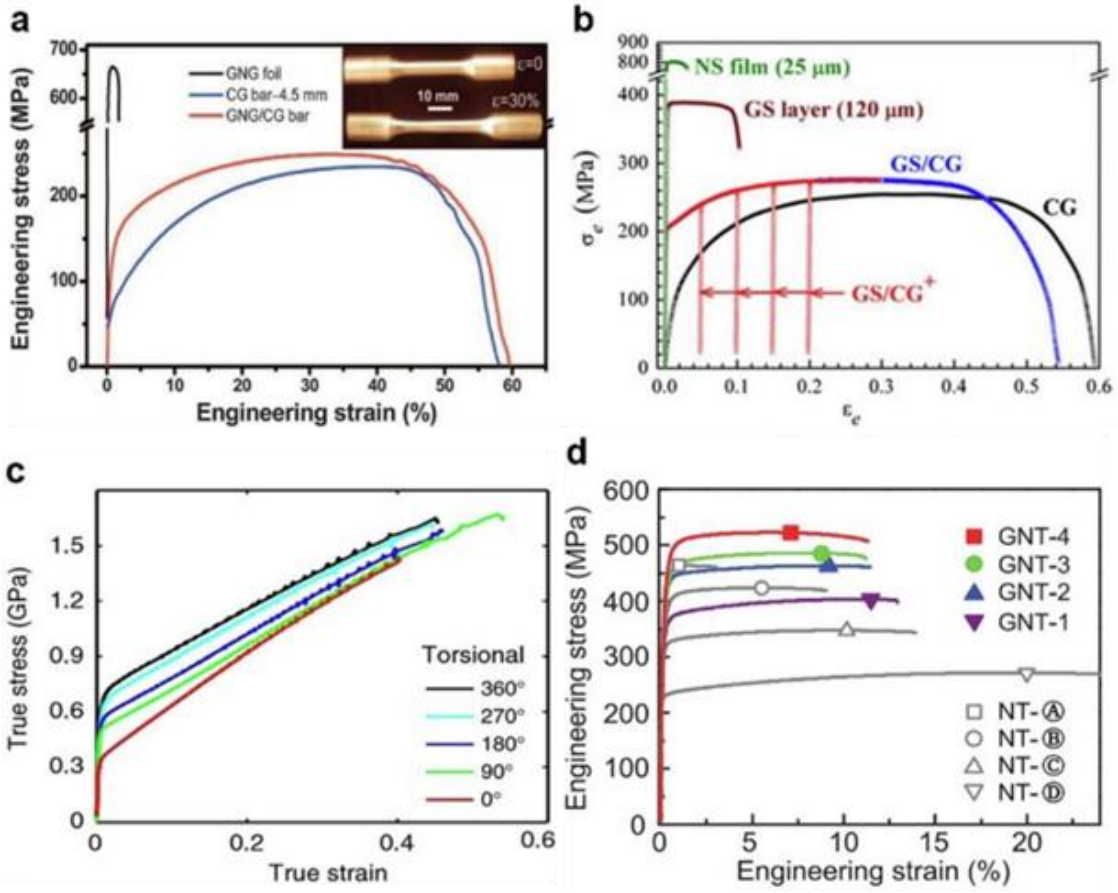

Figure 2-12 Tensile stress–strain responses observed across different heterogeneous structural materials: (a) GS Cu [121]; (b) GS IF steel [120]; (c) GS TWIP steel [125]; (d) GNT Cu [152]. Abbreviations: NS, nanostructure; GNG, gradient nanograin; NT, nanotwin.

Thirdly, additional hardening can be provided by residual stresses introduced via surface plastic deformation treatments [281]. Such processes generate a near-surface compressive stress layer. Synchrotron in-situ tensile measurements on IF steel (Fig. 2-13) reveal that a about 150 μm-deep compressive layer accommodates the greatest share of the external load (Fig. 2-13(b)). The compressive residual stress offsets the applied tensile stress, delaying local plastic flow and creating two elastic–plastic boundaries (Fig. 2-13(c)) at which GNDs accumulate, thereby intensifying HDI strengthening and hardening (Fig. 2-13(d)). With increasing strain, these boundaries migrate towards the centre of the

compressive layer, leaving high-density dislocation trails, both GNDs and statistically stored dislocations, that further boost work hardening.

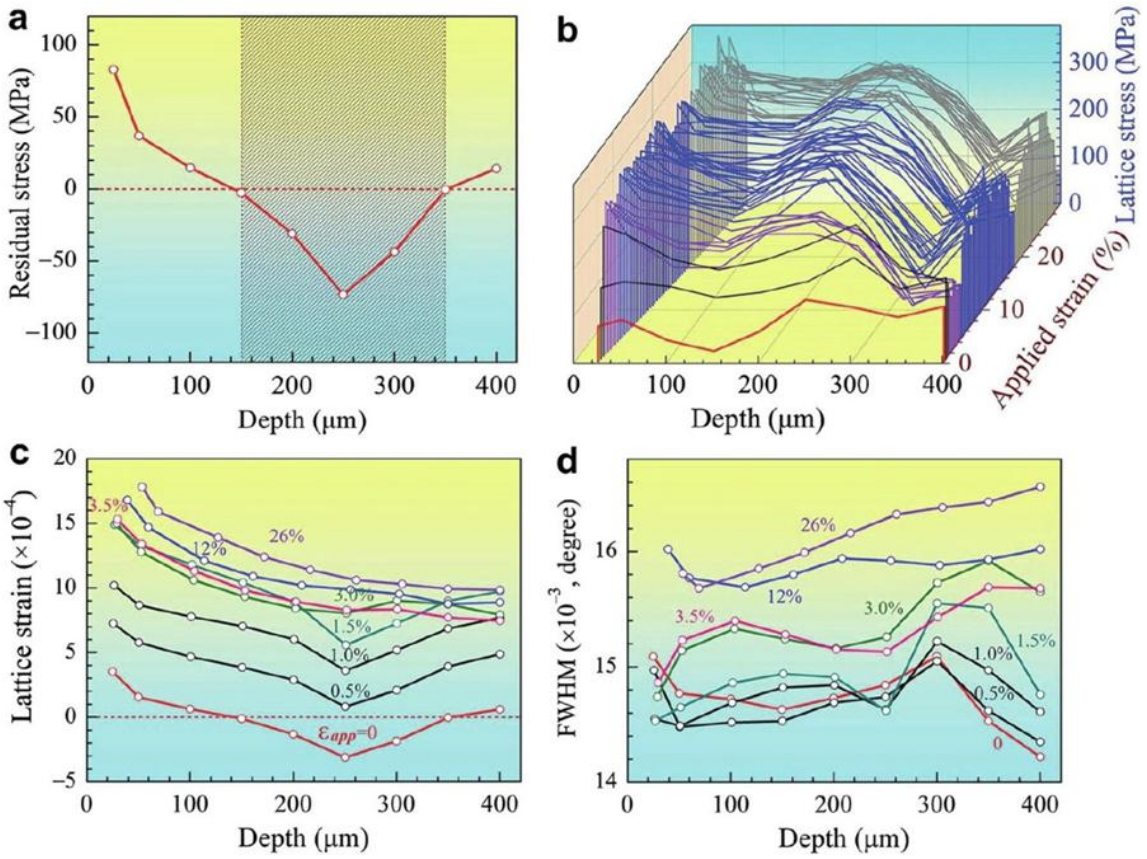

Figure 2-13 In-situ synchrotron X-ray diffraction measurements performed during tensile testing [281]: (a) initial distribution of residual stress as a function of depth before loading; (b) depth-dependent progression of axial lattice strain at various stages of applied tensile deformation; (c) variation in axial stress (strain) profile with increasing tensile strain along the depth; (d) evolution of full width at half maximum (FWHM), indicative of dislocation density, as a function of depth at different applied strains.

Fourthly, the overall constraint exerted by the gradient layers on a central CG core converts nominally uniaxial loading into a multiaxial stress state (Fig. 2-6), activating additional slip systems and fostering dislocation interactions that significantly enhance strain hardening [120]. Comparative tests on Cu samples with double-sided and single-sided constraints (Fig. 2-14) show that the former confer superior strength and ductility [282]. The volume fraction of the CG core therefore modulates the constraint effect, and an optimum fraction has been identified in gradient Cu [184].

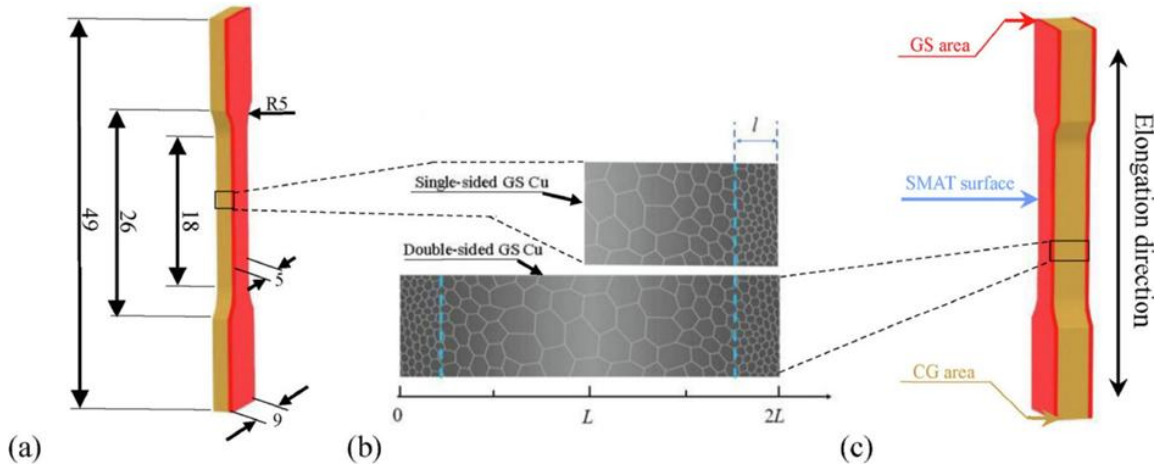

Figure 2-14 (a) Dimensions and geometry of a tensile sample exhibiting a single-sided GS; (b) illustrations comparing single- and double-sided GSs produced via SMAT; (c) geometry of the tensile sample with double-sided GS [282].

Recent investigations of GNT metals demonstrate that a twin thickness gradient confers supplementary strengthening relative to a uniform twin counterpart [233, 234]. The strain gradient between twin layers necessitates GND accommodation and generates back stresses within regions of larger twin thickness. Experimentally and computationally, a greater structural gradient produces a correspondingly larger strengthening increment, offering compelling evidence for the universal principles governing GS materials.

The preceding discussion elucidates how HDI stress and multiaxial stress and strain states arising from structural gradients enhance the strength and ductility of materials. Meanwhile, investigators have also introduced compositional gradients into numerous alloy systems to realise outstanding strength–ductility combinations [283–292]. A representative example that capitalises on HDI stress is presented below.

Dan et al. [290] took compositional grading to the realm of Ti alloys, fabricating a heterogeneous α-Ti alloy with in-situ Al concentration modulation via AM. They proposed an innovative in-situ compositional modulation strategy via laser engineered net shaping (LENS^{TM}), successfully fabricating a Ti/TiAl alloy with a heterogeneous multi-gradient structure [290]. This design involved the alternating deposition of CP-Ti and Ti-10 at.% Al powder layers, creating a gradual Al concentration gradient along the build direction [290]. At the microstructural level, this gradient resulted in a transition from fine basketweave grains in Al-rich regions to coarse lamellar and plate-like grains in Al-lean

regions [290]. Electron probe microanalysis analysis confirmed the continuity of aluminium distribution, while microstructural images clearly demonstrated the spatial gradient in grain morphology [290].

Fig. 2-15 shows the gradient material exhibited an exceptional synergy of strength and ductility, achieving a yield strength (σ_y) of approximately 760 MPa and an elongation to failure (ε_f) of 33.4% [290]. This performance not only surpassed that of homogeneous CP-Ti fabricated under the same conditions ($\sigma_y \approx 440$ MPa, $\varepsilon_f \approx 37.6\%$), but also maintained significantly enhanced ductility (almost six-fold) compared to homogeneous Ti-10 at.% Al ($\sigma_y \approx 910$ MPa, $\varepsilon_f \approx 6.1\%$), thereby breaking the conventional strength-ductility trade-off typically observed in Ti-based alloys [290]. Moreover, the gradient alloy exhibited an outstanding strain hardening capacity: the strain hardening rate curve exhibited a marked upward trend during deformation within the true strain interval of 0.02–0.05, as highlighted by the red arrow in Fig. 2-16, indicating effective suppression of localised deformation and delayed material failure [290].

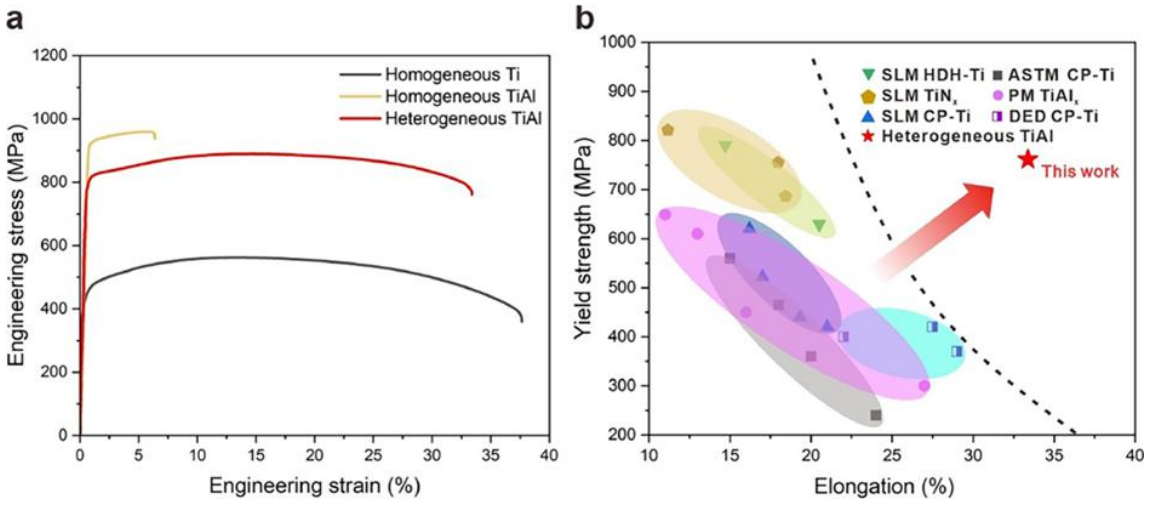

Figure 2-15 Room-temperature mechanical behaviour of as-fabricated homogeneous Ti, homogeneous TiAl, and heterogeneous TiAl samples [290]: (a) Engineering stress–strain relationships; (b) comparative assessment of yield strength and total elongation values obtained in this investigation relative to previously reported high-strength α-Ti alloys.

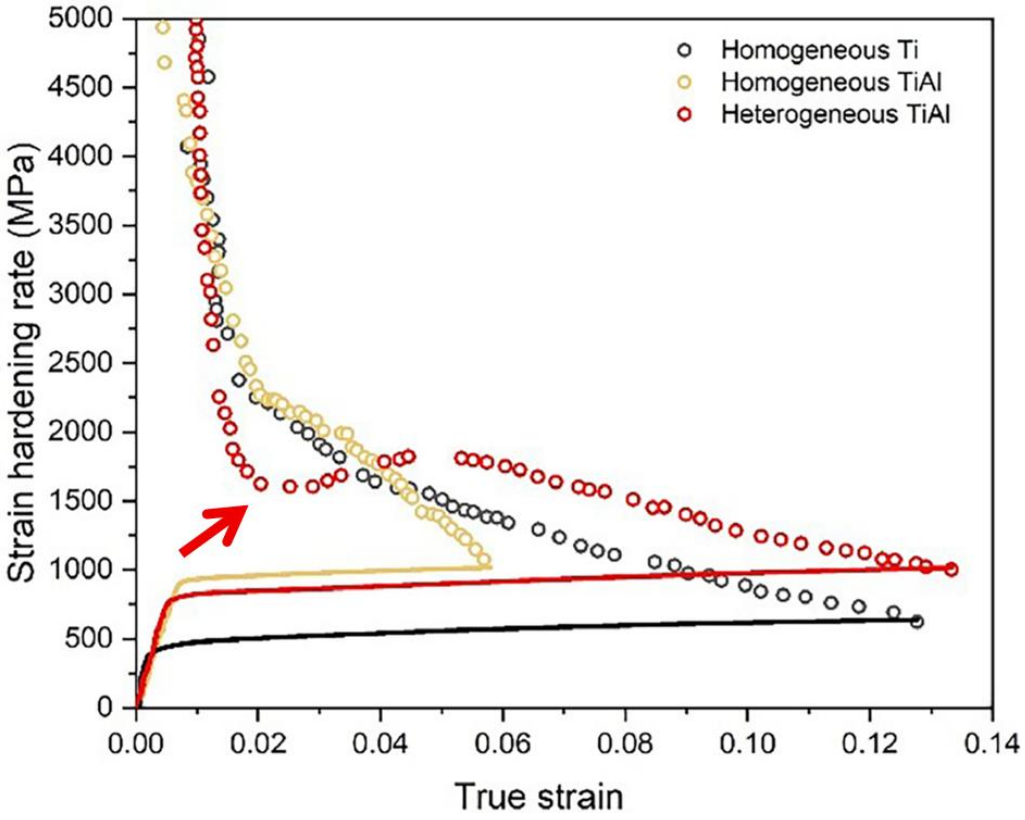

Figure 2-16 True stress–strain responses and associated strain hardening rate plots comparing homogeneous Ti, homogeneous TiAl, and heterogeneous TiAl alloys examined in the study [290].

The underlying mechanisms were attributed to gradient-induced stress and strain partitioning, as well as HDI strengthening derived from the gradient grain structure [290]. Digital image correlation and electron backscatter diffraction analyses revealed that initial strain localisation occurred within the harder TiAl layers and subsequently transferred to the softer Ti layers, enabling stress relaxation (Fig. 2-17) [290]. Concurrently, dislocation accumulation and grain refinement were observed in the Ti regions (Fig. 2-18), leading to the formation of "defect channels" that sustained high levels of deformation [290]. This coupled deformation mechanism, where soft zones accommodate strain and hard zones bear load, substantially enhanced both strength and ductility, providing a paradigm for the design of high-performance CGMs [290].

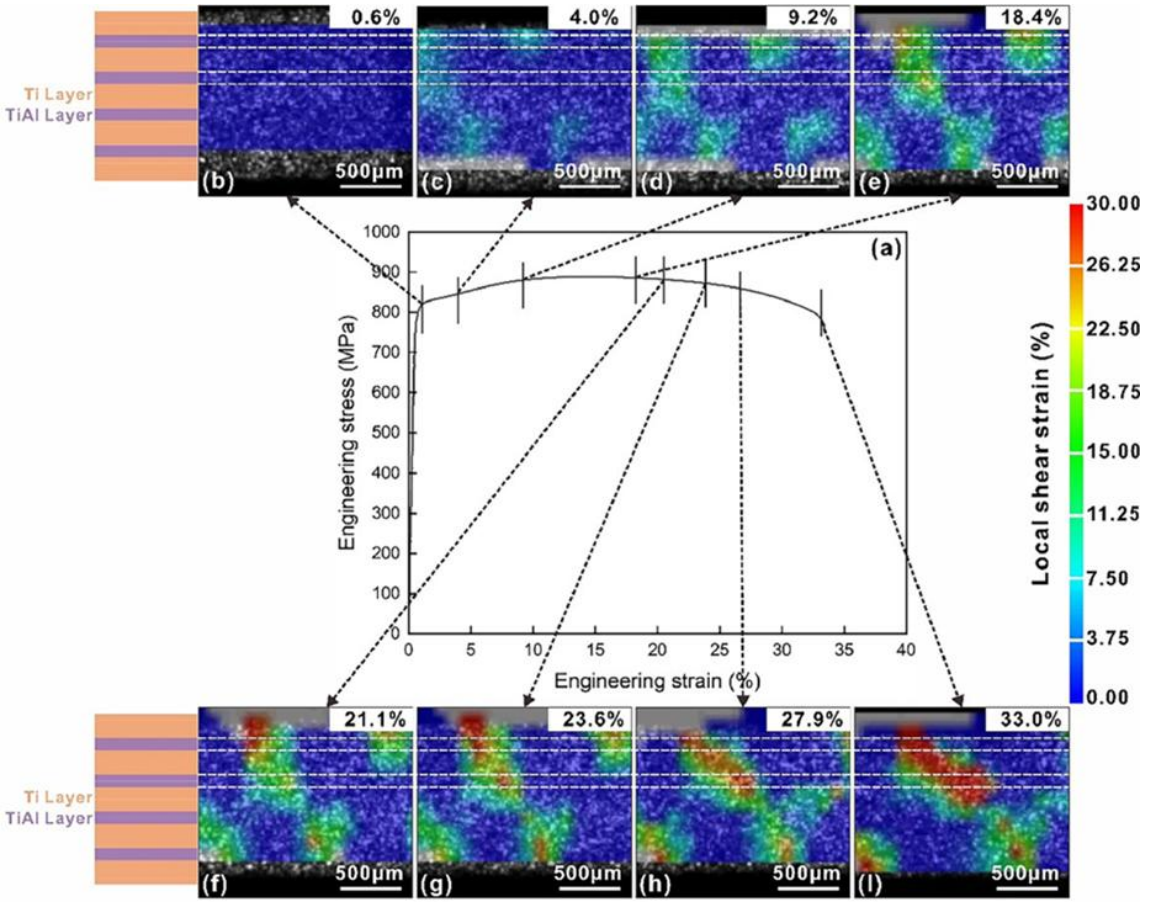

Figure 2-17 In-situ digital image correlation analyses illustrating progressive strain evolution along the tensile axis at various macroscopic deformation stages for the heterogeneous TiAl alloy [290]: (a) Corresponding stress–strain response highlighting selected deformation points; (b, c) initial deformation stage (Stage I) exhibiting minimal strain concentration; (d, e) intermediate deformation stage (Stage II) where heterogeneous strain regions begin emerging; (f) advanced deformation stage (Stage III) depicting enhanced strain localisation; (g, h) further deformation stage (Stage IV) displaying pronounced strain localisation expanding from the TiAl layer into adjacent Ti layers; and (i) final deformation stage (Stage V) indicating extensive strain localisation throughout the sample, ultimately leading to fracture.

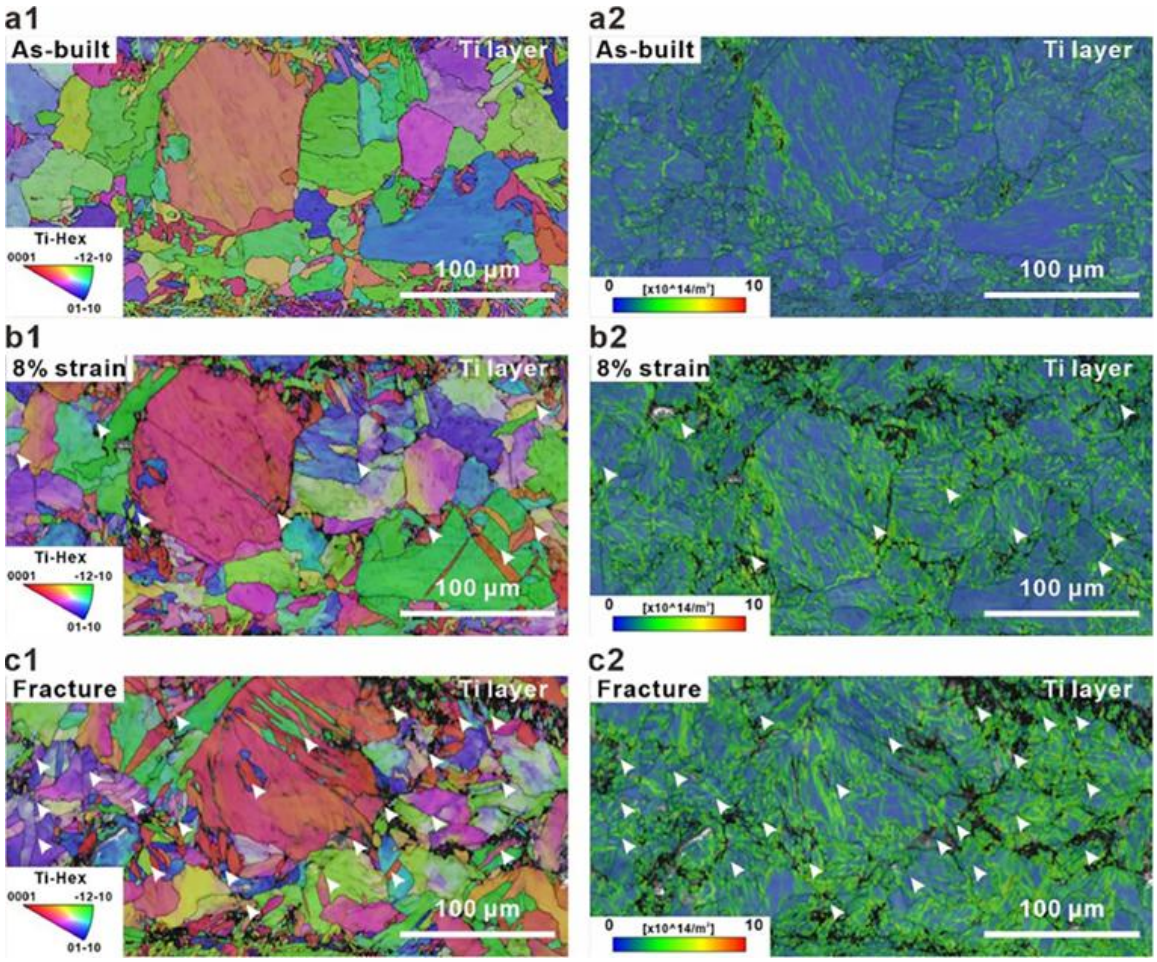

Figure 2-18 In-situ electron backscatter diffraction observations depicting the evolution of microstructural characteristics within the Ti layer of the heterogeneous TiAl specimen during progressive deformation [290]: (a1–c1) crystallographic orientation maps acquired at incremental strain stages, revealing significant grain refinement from the initial as-fabricated condition (a1), through intermediate deformation at approximately 8% strain (b1), and culminating at the point of fracture (c1); (a2–c2) corresponding maps illustrating the evolution of GND density, demonstrating a clear intensification and spatial expansion of dislocations within progressively refined grain structures from the initial undeformed state (a2), intermediate deformation (b2), to final fracture (c2).

The solute redistribution effect [229,230], which is intrinsic to compositional gradients, likewise contributes markedly to the synergy between strength and ductility. One representative example is provided by compositionally complex alloys (CCAs) [230]. A compositional gradient in the nanocrystalline $(TiZrNbHf)_{98}Ni_2$ alloy, characterised by ~3 nm Ni-rich local chemical order clusters dispersed within ~30 nm grains and Ni-enriched grain boundaries (~6.7 at %), a configuration absent in the Ni-free TiZrNbHf reference

[230]. Under 65 % compressive strain, atom probe tomography reveals Ni depletion from grain cores and enrichment along newly generated boundaries, confirming dislocation-mediated solute transport that refines grains to ~10 nm whilst preserving the interior-to-boundary gradient (Fig. 2-19) [230]. Density-functional-theory modelling yields a segregation energy of −1.919 eV and a boundary strengthening energy of −1.33 eV, demonstrating that the relocated Ni lowers grain boundary energy, enhances cohesion and arrests migration [230].

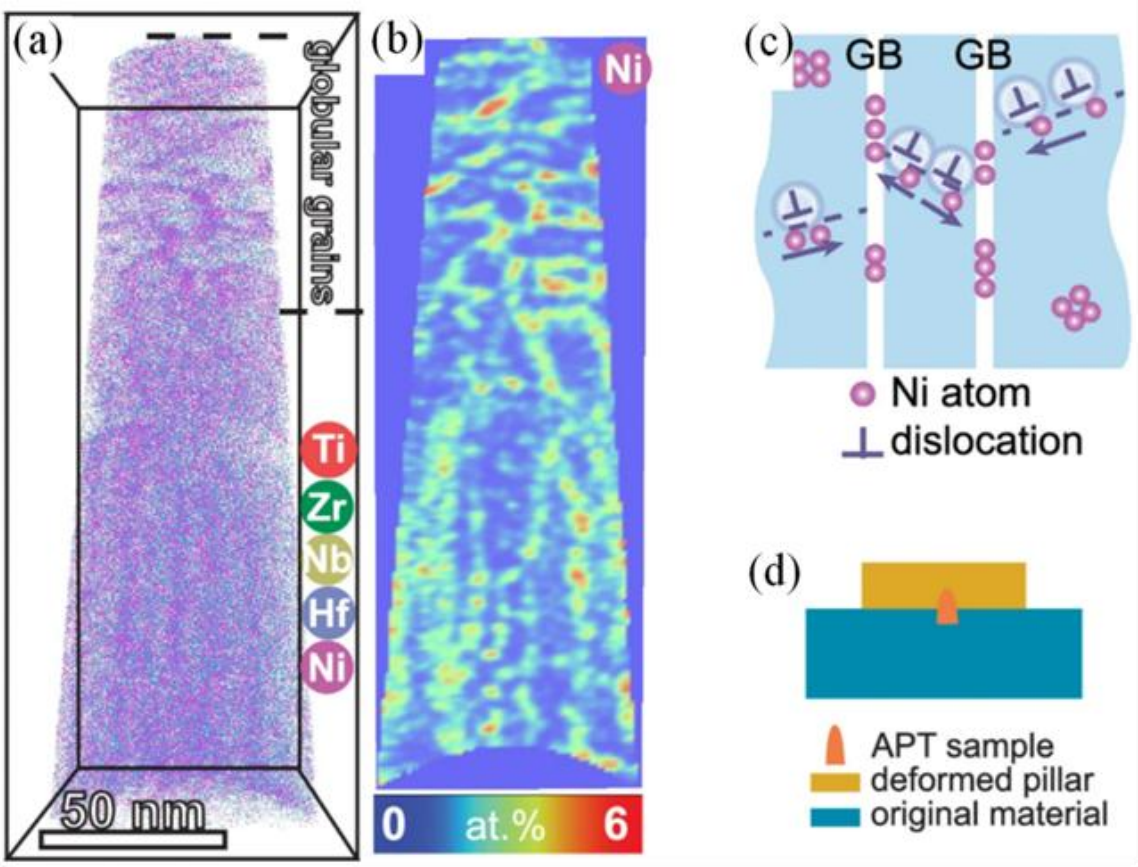

Figure 2-19 Post-compression chemical characterisation of the $(TiZrNbHf)_{98}Ni_2$ alloy [230]. (a) 3D atom probe tomography reconstruction from a micropillar that has undergone 65 % true strain. (b) Ni distribution map taken from a 2 nm-thick planar section of the dataset in (a). (c) Conceptual sketch illustrating how dislocation lines ferry Ni solute atoms from the grain interiors to grain boundaries during plastic flow. (d) Schematic pinpointing the area interrogated by atom probe tomography.

This solute redistribution elevates the yield strength from 1.3 GPa to 2.5 GPa through lattice distortion and cluster cutting that impede glide, Ni-decorated boundaries which raise the Hall–Petch slope by ~600 MPa, and stabilised nanograins that magnify these effects

[230]. Concurrently, Ni-rich clusters promote dislocation entanglement and accumulation, sustaining higher strain hardening rates than the reference throughout deformation [230]. As illustrated in Fig. 2-20, enhanced boundary cohesion suppresses crack initiation, extending homogeneous compressive strain from ~30 % to ~65 % and enabling crack-free micro-cantilever bending to 5.6 GPa at 11 % tensile strain, compared with 3.6 GPa and early cracking in the control alloy [230]. Accordingly, gradient-driven solute redistribution furnishes a unified mechanistic basis for the simultaneous enhancement of strength, ductility and work hardening in this nanocrystalline CCAs [230].

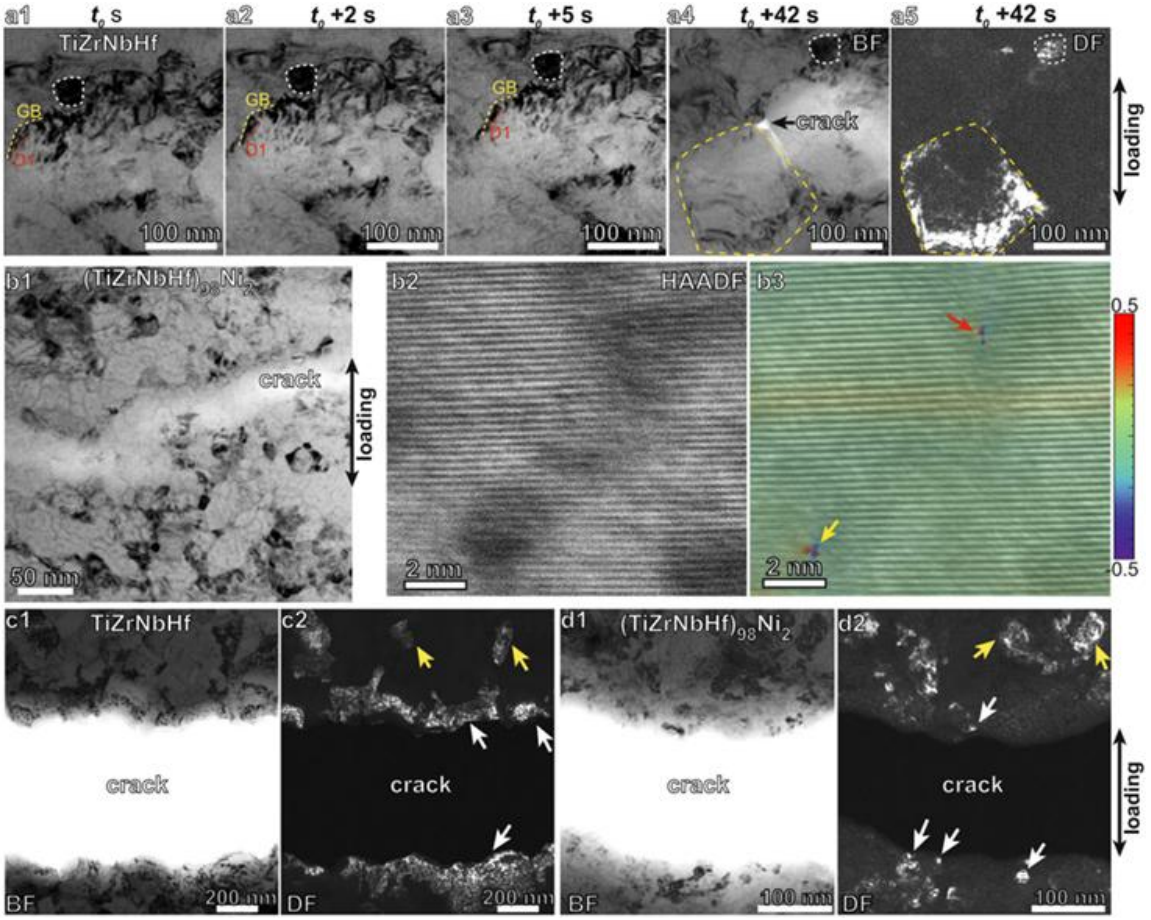

Figure 2-20 In-situ transmission electron microscopy (TEM) tensile testing of TiZrNbHf and $(TiZrNbHf)_{98}Ni_2$ alloys at room temperature [230]. (a1–a3) Successive TEM micrographs of the TiZrNbHf alloy illustrating dislocation motion (highlighted by red dashed lines) approaching and subsequently accumulating at a grain boundary (marked by yellow dashed lines). (a4, a5) Corresponding bright-field (BF) and dark-field (DF) TEM micrographs. A nanograin distinguished through DF imaging is enclosed by yellow dashed lines, while a reference nanograin is consistently indicated by white dashed lines in images (a1–a5). (b1) TEM image capturing crack progression in the $(TiZrNbHf)_{98}Ni_2$ alloy during

tensile loading. (b2) HAADF-STEM micrograph and (b3) corresponding overlay of atomic-scale strain mapping onto a BF-STEM image of the $(TiZrNbHf)_{98}Ni_2$ alloy taken adjacent to the propagating crack. (c1, c2) Post-fracture BF and DF TEM micrographs from the identical location within the TiZrNbHf alloy. (d1, d2) Corresponding BF and DF TEM images from the $(TiZrNbHf)_{98}Ni_2$ alloy post-fracture, captured from the same region. White arrows in (c2, d2) identify nanograins adjacent to the crack, whereas yellow arrows indicate grains positioned further away.

Recent investigations [254,293–298] have yielded direct observations indicating that compositional gradients can effectively deflect crack propagation paths, concomitant with crack tip blunting and bridging between adjacent cracks. Employing a scalable flake-powder metallurgy route, namely low-speed ball-milling of carbon nanotubes (CNTs)-decorated 6061Al to build an ultrafine-grained (UFG) nanoflake, followed by high-speed mixing with raw coarse 6061Al powder and 15 wt.% B4C microparticles, cold compaction, vacuum sintering and hot extrusion, Saba et al. [293] deliberately juxtaposed "soft" CG lamellae with a "hard" particle-strengthened UFG matrix to generate a well-dispersed compositional gradient architecture; the optimised 20:80 CG:UFG design yields CG bands ~5 μm wide that are fully embedded in the UFG matrix, thereby maximising hetero-deformation interactions [293].

This gradient composite exhibits an ultimate tensile strength of ≈ 550 MPa, elongation to failure of ≈ 7 % and a peak toughness index of ≈ 32.5 mJ mm^{-3}, while retaining the highest strain hardening rate in the series [293]. Compared with the homogeneous reference materials, it simultaneously outperforms the strength-dominated but brittle B_4C/UFG nanocomposite (yield strength ≈ 480 MPa, elongation to failure ≈ 1.4 %) and the ductile yet weak CG matrix (yield strength ≈ 180 MPa) [293].

Mechanistically, the experimental results revealed that [293]: (i) MgO nanoparticles and CG–UFG interfaces repeatedly deflect the crack path (Fig. 2-21(b,c) and Fig. 2-22(c)); (ii) the plastic zone ahead of the crack is blunted inside the soft CG domains once their width exceeds twice the interface affected zone (IAZ), providing space for dislocation emission (Fig. 2-21(d)); and (iii) multiple nano-voids around B_4C particles evolve into nanobridges that bridge the crack wake (Fig. 2-22(b)). Together with the high-density GND gradient as shown in Fig. 2-23, which supplies long-range HDI stress and extra work hardening, these

cooperative processes arrest and multiply cracks, thereby reconciling strength with ductility [293]. Overall, the study demonstrates that judicious tuning of compositional gradient parameters, especially CG fraction and bandwidth, can activate concurrent crack deflection, crack tip blunting and nanobridge formation, offering a robust strategy to transcend the long-standing strength–ductility trade-off in materials [293].

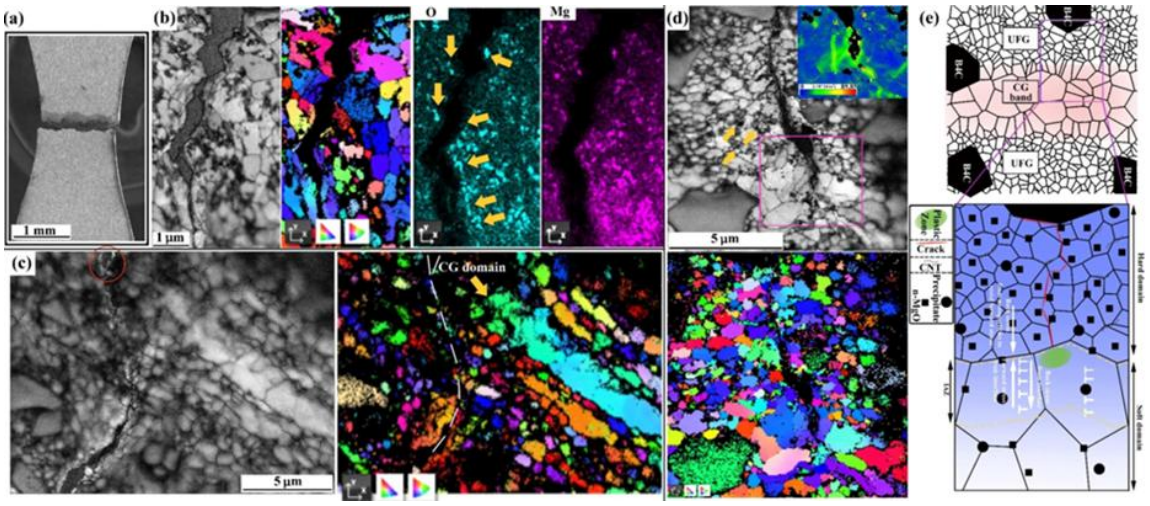

Figure 2-21 (a) In-situ tensile scanning electron microscopy observations combined with transmission Kikuchi diffraction analysis [293]. (b) Deflection of crack propagation induced by MgO nanoparticles. (c) Crack deflection in the vicinity of the CG band. (d) Crack blunting, with the inset revealing a high density of GNDs generated near the crack tip. (e) Schematic illustration of the fracture mechanism, delineating the crack-dominated failure process: crack initiation within hard regions, particularly at the interfaces of micrometre-sized particles; subsequent crack deflection by MgO nanoparticles dispersed in the UFG region surrounding B4C micrometre-sized particles; and final crack blunting at the UFG/CG interface.

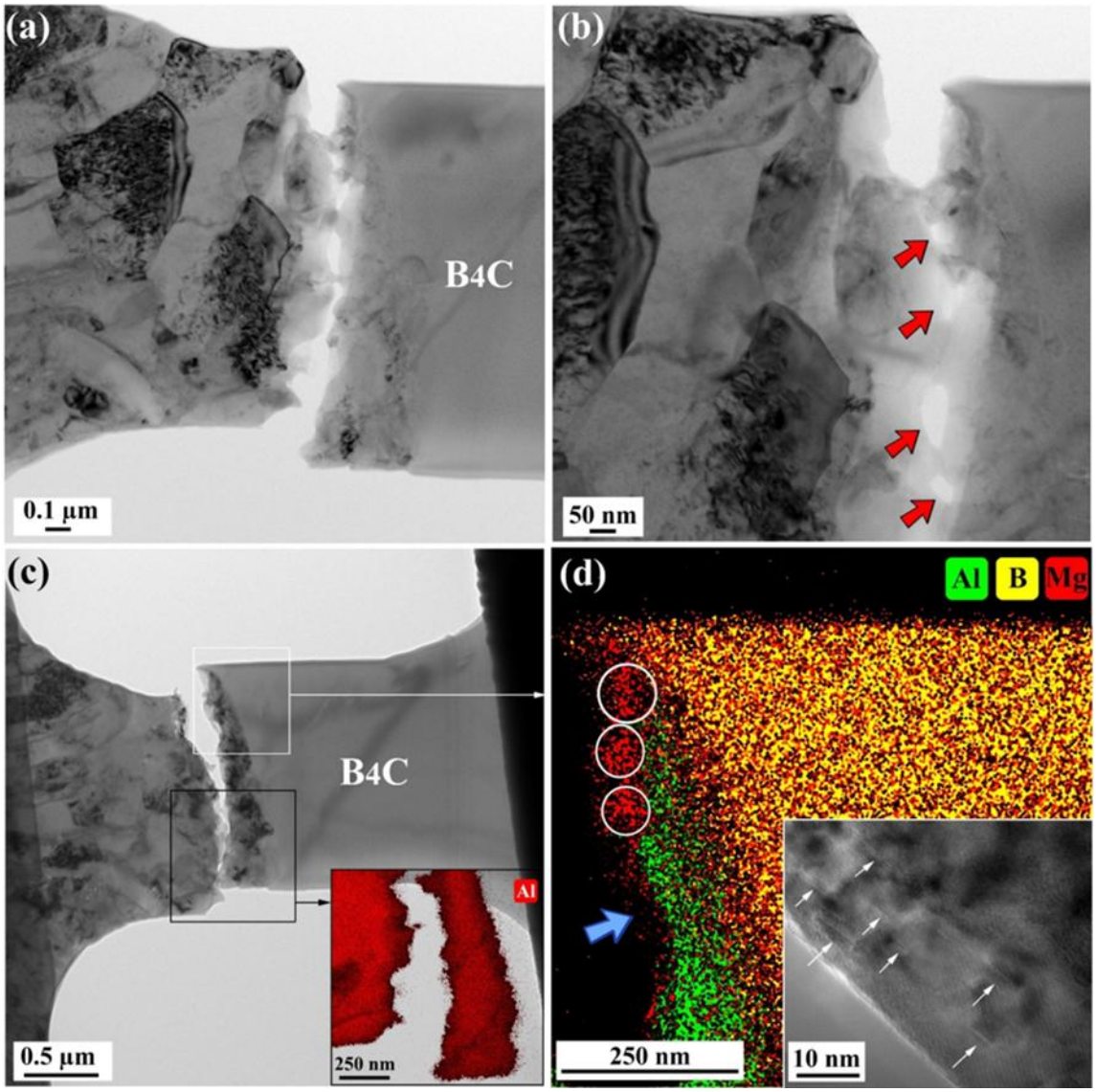

Figure 2-22 In situ tensile investigation of crack behaviour surrounding B_4C micrometre-sized particles within the UFG region [293]. (a, b) Transmission electron microscopy images capturing crack propagation. (c) Transmission electron microscopy micrograph of the fractured interfacial zone, whose inset presents an Al elemental distribution map indicating that nanoparticles deflect the crack around the B_4C particles, thereby generating a serrated crack path. (d) Al, B and Mg elemental maps of the upper fracture region highlighted in (c), corroborating the presence of MgO nanoparticles on the fracture surface (circled); the inset high-resolution transmission electron microscopy image in (d), acquired from the blue-arrowed area, reveals SFs on the fracture surface.

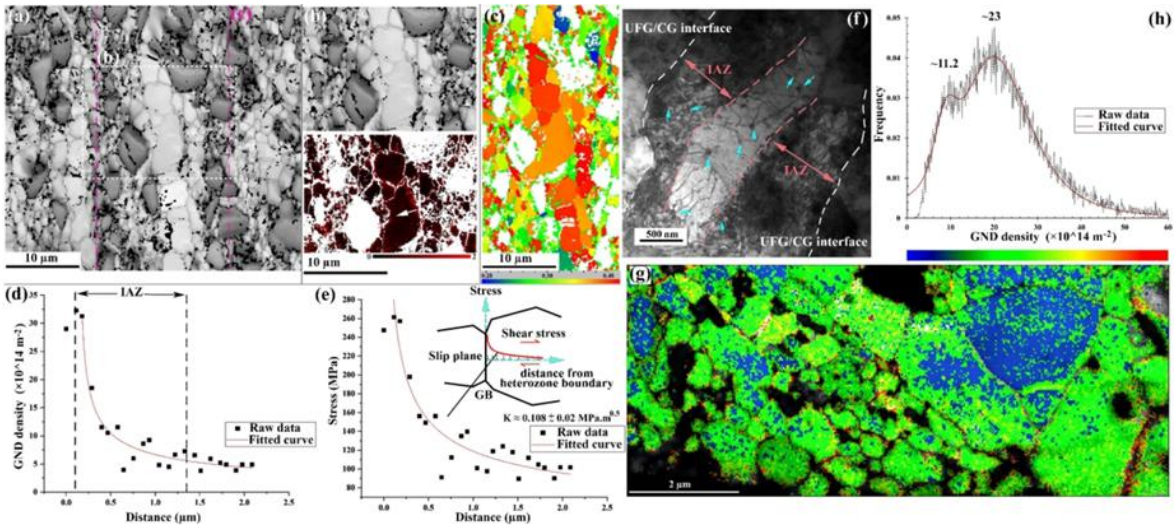

Figure 2-23 (a) Electron backscatter diffraction (EBSD) image quality (IQ) map of the 20:80 heterogeneous composite (HC), revealing CG bands embedded in UFG regions. (b) Enlarged IQ map combined with kernel average misorientation (KAM) analysis from the dashed rectangular region indicated in (a). (c) EBSD-based map depicting Schmid factor variations within the soft and hard domains. Experimental measurements with corresponding fitted profiles for (d) GND density and (e) stress distributions along the direction indicated by the white arrow in (b). A schematic representation of the gradient stress field formation at the interface between heterogeneous zones is provided in (e). The IAZ width in (d) is measured from the peak GND density region to the area showing negligible variation. (f) Transmission electron microscopy image of 20:80 HC strained to 3%, highlighting densely arranged dislocations within the soft domains adjacent to hetero-zone boundaries, confirming IAZ presence. Dashed lines delineate boundaries between soft and hard zones, and arrows indicate spherical nanoprecipitates pinning dislocations. (g) Transmission Kikuchi diffraction mapping of the same composite showing GND density distribution in soft and hard domains, accompanied by (h) corresponding frequency distribution of GND density [293].

Having elucidated the deformation mechanisms engendered by core–shell architectures, we now focus on a more specific configuration, namely core–shell systems with compositional gradients, and examine their attendant mechanical properties. A recurring observation is that core–shell structures significantly alter dislocation dynamics [259–261, 271]. Duan et al. [259] demonstrated this clearly in a nanocrystalline NiCoFeAlTiB alloy designed with an $L1_2$-type ordered core and a ~3 nm disordered FCC shell at each grain boundary [259].

The ordered core (a Ni_3Al-type superlattice) has a high anti-phase boundary (APB) energy, so dislocations are strongly impeded inside it and tend to accumulate and interact within the small grains [259]. In contrast, the thin disordered shell at the grain boundaries acts as a prolific dislocation source, allowing easy dislocation emission to sustain plastic flow [259]. As presented in Fig. 2-24, the undeformed sample exhibits a core–shell architecture and a low initial dislocation density, the broad yellow line indicating the disordered interfacial nanolayer (DINL). During the early stages of deformation, numerous dislocations nucleate at the grain boundaries and glide into the nanograins, and with increasing strain, dislocations on multiple slip systems (black dashed lines) are activated to accommodate the strain, intersecting within the grains and becoming immobilised within the nanocrystalline matrix. This core–shell synergy enabled extraordinary dislocation storage in a nanograined material that would otherwise suffer premature dislocation starvation [259].

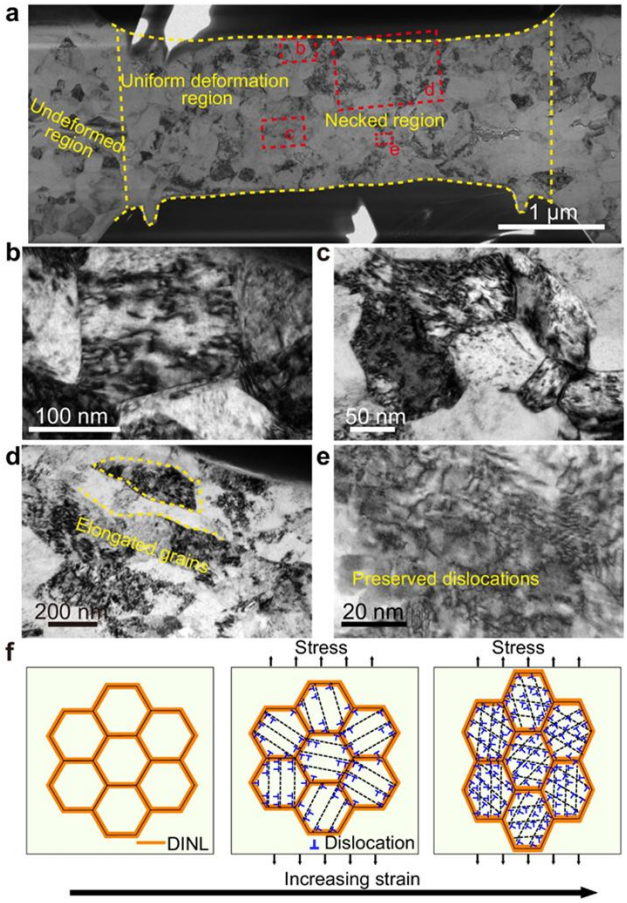

Figure 2-24 Plastic deformation mechanism of the nanocrystalline core – shell NiCoFeAlTiB specimen [259]: (a) Transmission electron micrograph mage of the sample after 25 % tensile strain at room temperature, displaying a pronounced necked region; (b,

c) activation of dislocations in the vicinity of the necked area (region bounded by the red dashed box in (a)); (d) conspicuous grain elongation within the neck, with grain boundaries delineated in yellow; (e) retention of a high density of dislocations in the nanograins of the necked region; (f) schematic illustration of the deformation mechanism in the nanocrystalline core–shell NiCoFeAlTiB alloy.

The result was a high work hardening rate at stresses ≥2 GPa and a delay in the onset of plastic instability [259]. Unlike conventional nanocrystalline materials which soften after ~5% strain, the core–shell NiCoFeAlTiB showed a plateau in the work hardening curve and maintained a positive hardening rate to large strains, as indicated by the black arrow in Fig. 2-25(a). By confining dislocations in the ordered core and continuously replenishing them from the shell, the structure prevents shear localisation and instead promotes uniform deformation [259]. Moreover, the ductile interfacial shell accommodated strain at grain boundaries, suppressing intergranular fracture [259]. This design resulted in record combinations of strength and ductility for a nanocrystalline alloy (Fig. 2-25(b,c)), confirming that dislocation accumulation and confinement within core–shell grains is a powerful strategy for overcoming the usual strength–ductility trade-off [259].

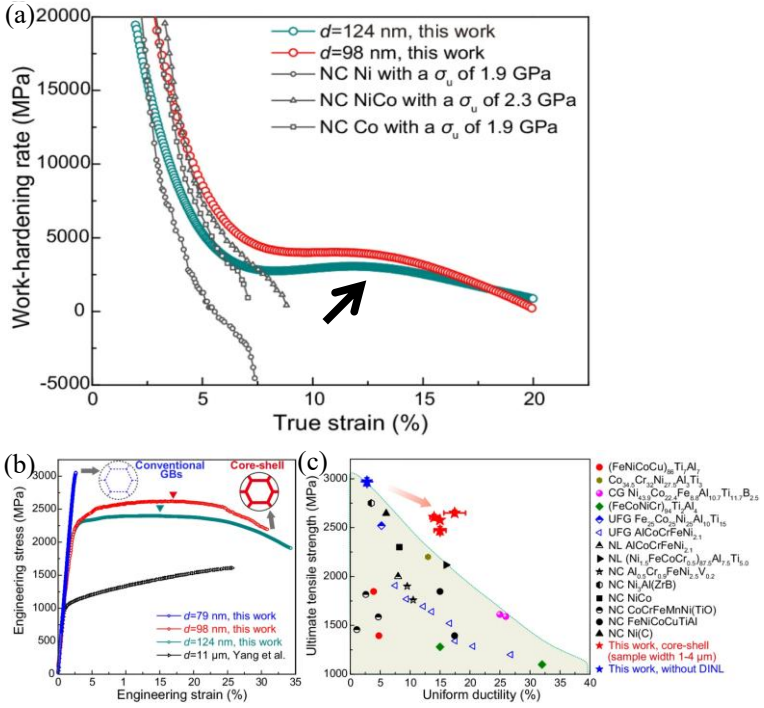

Figure 2-25 (a) Work hardening rate curves for the nanocrystalline core–shell samples with grain sizes *d*=98 nm (red curve) and *d*=124 nm (blue–green curve), together with the

corresponding curve for a nanocrystalline fcc alloy for comparative analysis. (b) Typical engineering stress–strain curves for the nanocrystalline core–shell samples; for comparison, curves are also presented for a bulk CG specimen and for a nanocrystalline sample without a core–shell architecture. (c) Correlation between ultimate tensile strength and uniform elongation of the nanocrystalline NiCoFeAlTiB alloy, benchmarked against comparable alloy systems [259].

Another critical deformation mechanism in core–shell systems is the activation of TRIP and TWIP in selected regions due to metastable phases created by compositional heterogeneity [262–265]. By locally adjusting composition via a core–shell design, one can introduce a metastable phase that will transform or twin under stress, thereby enhancing ductility through strain induced hardening [262–265].

Haftlang et al. [262] provided a clear case in a medium-entropy maraging steel (Fe–Ni–Mn–Co based) that was processed to contain a dual phase microstructure of martensite (ultra-high strength, but brittle) and reverted austenite (ductile, metastable) [262]. By a controlled reversion heat treatment, they obtained about 25% volume fraction of retained austenite dispersed in a martensitic matrix, which yielded a tensile strength ~1.6 GPa with ~25% total elongation, far exceeding the ductility of conventional maraging steels, typically <12% elongation at similar strength (Fig. 2-26) [262].

Crucially, the newly formed austenite exhibited a compositional core–shell structure: within each reverted austenite grain, there was compositional partitioning of Ni, Mn, Ti, and Si such that the regions near the interfaces had different stability than the grain core [262]. Atom probe analyses showed that Ni and Ti tended to segregate toward certain layers, assisting precipitate formation, while Mn partitioned differently, leading to multiple concentric compositional “shells” at the martensite/austenite interface [262]. This gradient in solute content produced a gradient in SFE and martensitic transformation temperature within each austenite region [262].

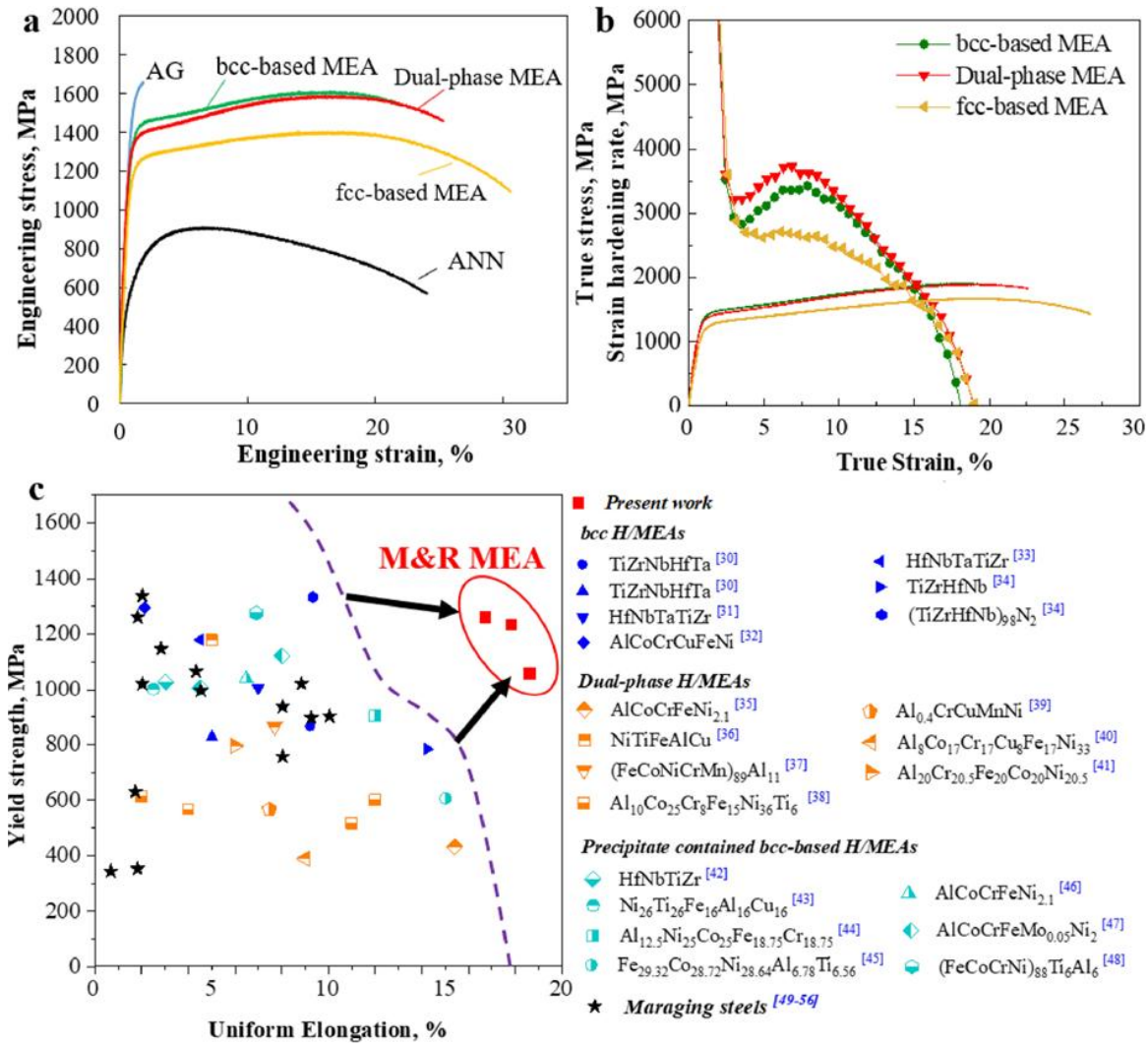

Figure 2-26 Room-temperature tensile properties of the Fe-based medium-entropy alloy [262]: (a) engineering stress–strain curve of the recovery treated $Fe_{68}Ni_{10}Mn_{10}Co_{10}Ti_{1.5}Si_{0.5}$ alloy; (b) corresponding work hardening rate curve plotted against true strain; (c) comparison of yield strength versus uniform elongation.

As a result, upon straining, the austenite did not transform all at once. Instead, the deformation induced martensitic transformation ($\gamma \rightarrow \alpha'$) nucleated preferentially in certain parts of the austenite grains (Fig. 2-27). The gradual change in SFE across the austenite effectively distributed the TRIP effect over a range of strains, rather than a sudden burst, providing a sustained source of hardening [262]. The authors noted that the core–shell austenite regions acted as strong barriers to dislocations and as reservoirs of strain due to the progressive martensitic transformation [262].

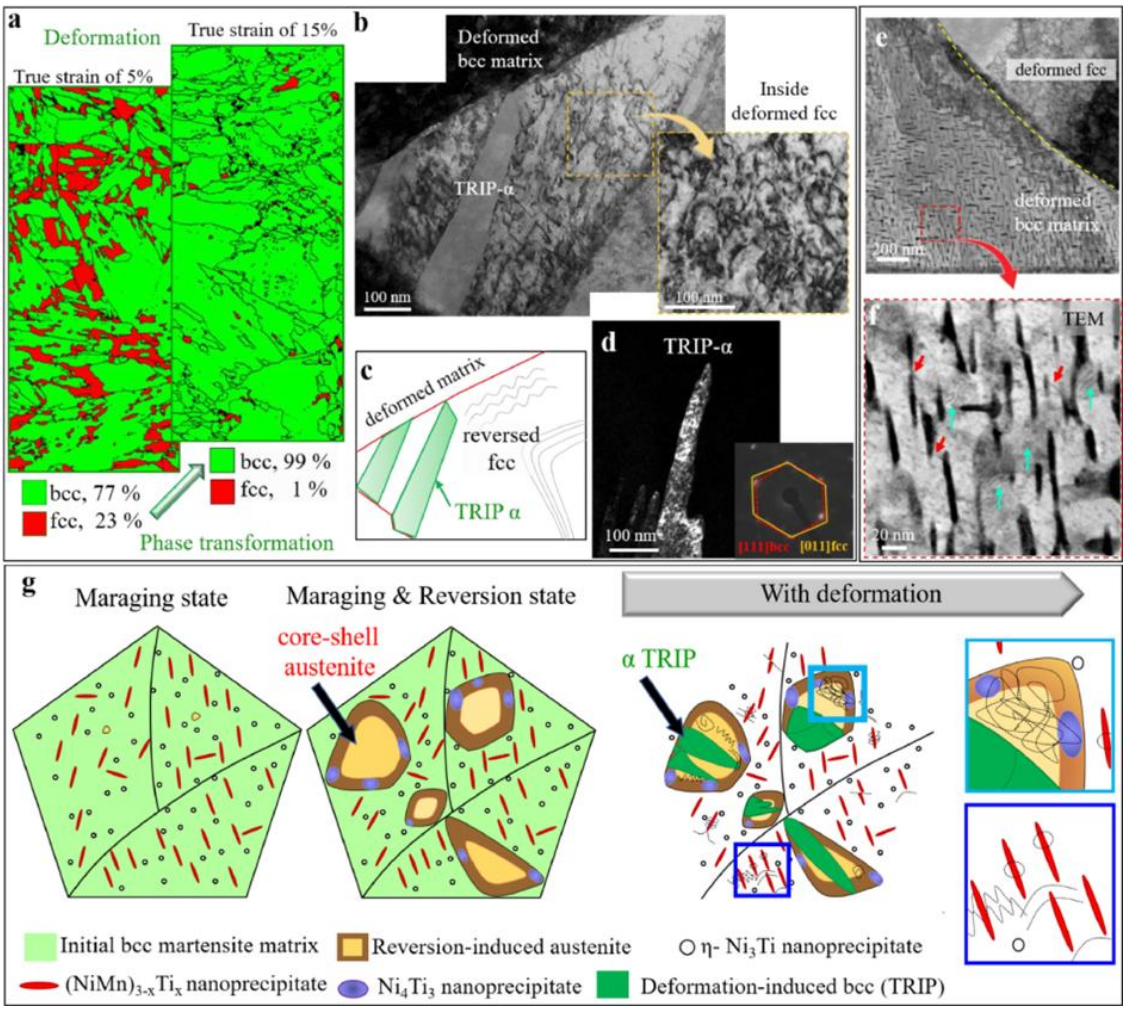

Figure 2-27 Microscale deformation mechanisms of the dual phase medium-entropy alloy at room temperature [262]: (a) Electron backscatter diffraction phase maps acquired at true strains of 5 % and 15 %; (b, d) bright- and dark-field transmission electron microscopy images of the deformed specimens, together with the corresponding selected area electron diffraction patterns, highlighting the contributions of the various microstructural features during deformation; (c) schematic depiction of the TRIP effect operating in the reverted austenite grains; (f) pinning (red arrows) and shearing (cyan arrows) actions of $(NiMn)_{3-x}Ti_x$ precipitates within the martensite grains, the transmission electron microscopy foil being extracted from a specimen deformed to a true strain of 10 %; (g) schematic illustration of the microstructural evolution in the alloy.

This TRIP-assisted heterostructure accounted for a multistage strain hardening behaviour [262]: the strain hardening rate curve showed three distinct stages corresponding to elastic–plastic transition, gradual TRIP onset, and eventual saturation, as shown in Fig. 2-26(b). During the second stage, the transformation of austenite, with attendant volume expansion

and new dislocations, compensated for strain softening and maintained a high work hardening rate [262]. Notably, the formation of martensite laths from the austenite shells also generated additional interfaces and obstacles, which is much like a dynamic precipitation, further boosting strength [262].

In essence, the compositional core–shell design in this alloy enabled the simultaneous operation of precipitation strengthening (from nanoscopic intermetallic precipitates in the martensitic matrix) and TRIP toughening (from metastable austenite shells) [262] – a potent combination for achieving high strength and ductility.

Apart from TRIP, TWIP can also be harnessed via core–shell designs [264,265]. An example can be seen in the $L1_2$-type high-entropy intermetallic (HEI) of Liu et al [265]. Due to a low SFE in the disordered FCC shell regions, abundant SFs and micro-twins form during deformation [265]. These faults effectively subdivide the FCC regions into finer "plates," imparting a dynamic Hall–Petch effect that raises strength and postpones necking [265]. The formation of intrinsic SFs and Lomer–Cottrell locks in later stages further resists dislocation motion (Fig. 2-28). Although not a classical TWIP alloy, the core–shell HEI leveraged a similar concept: tailoring local SFE via composition to encourage planar deformation mechanisms that boost ductility [265].

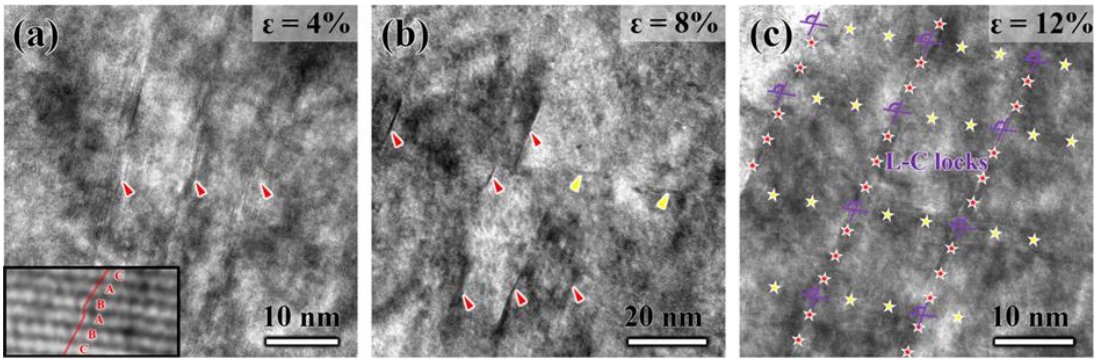

Figure 2-28 Microstructural evolution of the as-cast $L1_2$-type HEI compound during plastic deformation with increasing tensile strain [265]: (a) parallel arrays of SFs on the {111} planes observed at a true strain of 4 %, with the inset illustrating the stacking sequence of a single fault; (b) intersecting SFs on different {111} slip planes at a true strain of 8 %; (c) development of a pronounced multilevel SF network together with V-shaped Lomer–Cottrell (L-C) lock structures on the {100} planes at a true strain of 12 %.

In summary, metastable shells that undergo phase transformation or twinning under stress

provide an on-demand source of hardening via new martensite or twin boundaries and contribute significantly to the strain hardening capacity of core–shell materials [262–265].

The interaction between a strong core and a ductile shell invariably leads to non-synchronous deformation of the two constituents [266]. This mismatch can be advantageous: the stronger phase bears more load initially, while the more ductile phase yields and accommodates strain, thus delaying catastrophic failure of the strong phase [266]. The geometrically necessary condition of strain compatibility between core and shell gives rise to HDI stresses that elevate the overall flow stress and work hardening rate of the core–shell system [61,135,266]. Moreover, the interfaces intrinsic to core–shell architectures themselves frequently serve to deflect or even arrest crack propagation [266,268].

A striking example is the TiAl/Nb core–shell composite developed by Shen et al. [266] to address the brittleness of γ-TiAl intermetallics. In this powder-metallurgy composite, ductile β-Nb forms a continuous honeycomb shell network surrounding TiAl-rich cores (lamellar γ-TiAl colonies) [266]. In compression tests, the composite achieved a fracture strain of ~33% and an ultra-high strength of ~2.4 GPa (Fig. 2-29).

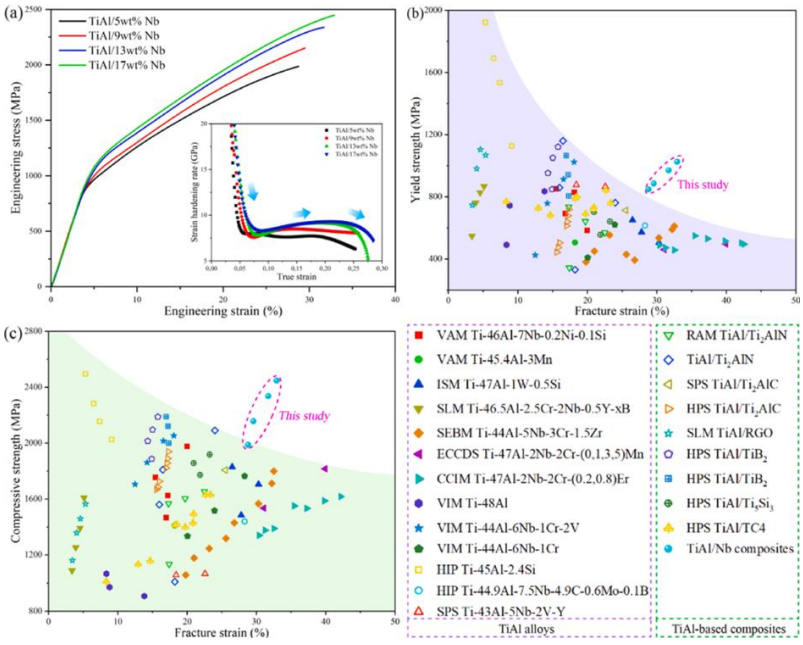

Figure 2-29 Room-temperature compressive performance of the core–shell TiAl/Nb composites [266]: (a) Engineering stress–strain curves; (b, c) relationships between yield strength/ultimate compressive strength and fracture strain for the composites developed herein, benchmarked against data reported in the literature.

The authors attribute the high strength to an unremitting increase of HDI stress arising from the core–shell architecture [266]. Initially, the ductile Nb network yields at a lower stress, allowing the TiAl cores to remain elastic and carry increasing load [266]. This produces a kinematic hardening: as the Nb plastically flows, it imposes a restraining back stress on the TiAl, effectively increasing the stress needed to deform the TiAl cores [266]. As strain continues, the TiAl eventually yields or micro-yields via fine slip or phase transformation at colony boundaries, but by then the Nb has work hardened considerably [266]. This asynchronous yielding ensures that there is always a fraction of the material carrying higher stress (TiAl) and another fraction accommodating more strain (Nb), which is the hallmark of strain partitioning [266]. The internal stress gradients between hard core and soft shell translate into a sustained strain hardening rate. The flow curve did not reach a clear saturation within the tested range because the hard phase kept being engaged at higher and higher stresses. This "prolonged cooperative deformation" mechanism is essentially the HDI hardening concept reported in other heterostructured materials [61,135,266]. Shen et al. also emphasise the toughening role of the Nb shell: it enables relative sliding between TiAl colonies in the early stage, preventing brittle grain boundary fractures, and later, bridges cracks and blunts them, thanks to its ductility and the presence of multiple constituents (some Nb-rich B2 phases formed at interfaces) [266]. Cracks that initiate in the TiAl core are arrested or deflected by the surrounding Nb network, resulting in a significantly higher fracture strain than monolithic TiAl (Fig. 2-30). In essence, the load transfer from the failing brittle phase to the ductile phase and the crack bridging by the ductile phase are crucial for the enhanced toughness [266].

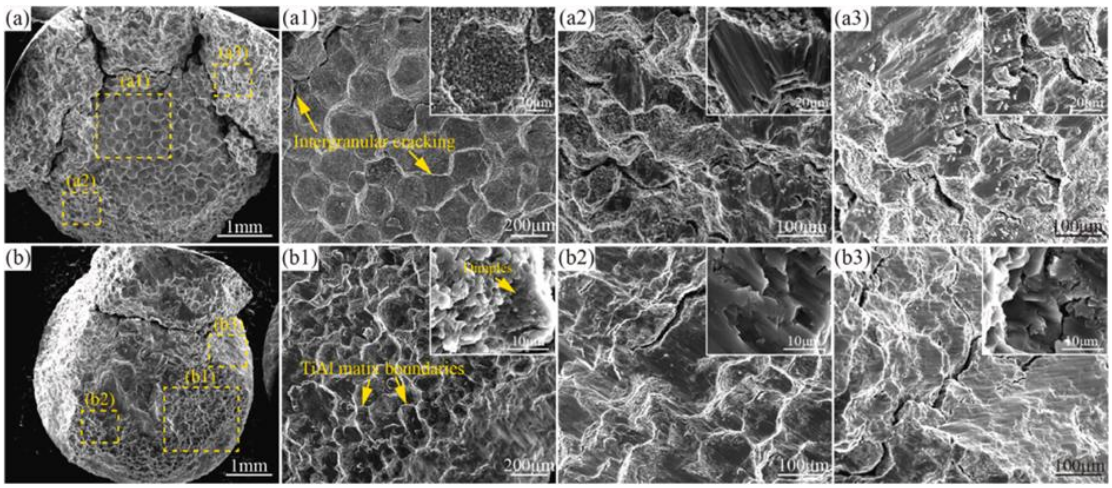

Figure 2-30 Fracture surface morphology of the TiAl/Nb specimens following room-temperature compression [266]: (a) TiAl/9 wt.% Nb; (b) TiAl/13 wt.% Nb.

Having delineated how individual gradients, whether structural or compositional, ameliorate the classical strength–ductility trade-off by promoting heterogeneous deformation and auxiliary toughening mechanisms, the spotlight now shifts to materials endowed with dual gradient architectures. Such bifurcated gradients engender more intricate strain partitioning phenomena, GNDs interactions and localised stress states, thereby furnishing new avenues for tailoring mechanical performance [58–60,152–158].

Employing arc-melting followed by SMAT, a rapid 900 °C anneal and 700 °C ageing, Qin et al. [58] engineered an $Al_{0.5}Cr_{0.9}FeNi_{2.5}V_{0.2}$ high-entropy alloy with two superposed gradients: a grain size gradient that tapers from ~100 nm dislocation-cell structures in the top-100 μm layer to ~15 μm equiaxed grains in the core, and a precipitation gradient in which coherent $L1_2$ and semi-coherent B2 nanoparticle fractions fall from 69 %/≈35 % at the surface to 34 %/≲5 % centrally [58]. This "SMAT-Aged" dual gradient architecture delivers a yield strength of ≈ 960 MPa, an ultimate tensile strength of ≈ 1.25 GPa, a uniform elongation of ≈ 16 % and a peak strain-hardening rate of ~4 GPa at $\varepsilon \approx 2$ %, decisively outperforming the single gradient as-SMATed alloy ($\sigma_y \approx 890$ MPa, uniform elongation ≈ 10 %) and the CG annealed control ($\sigma_y \approx 340$ MPa, UE ≈ 43 %) (Fig. 2-31). Kernel average misorientation (KAM) analysis reveals a three-fold larger build-up of GNDs at layer and phase boundaries (Fig. 2-32(b,d)), while loading–unloading–reloading tests register higher HDI stress and HDI hardening throughout deformation [58]. Transmission electron microscopy (TEM) confirms that hundreds-nanometre B2 particles induce Orowan bowing and dislocation pile-ups (Fig. 2-33(c,d)), whereas 7 nm $L1_2$ precipitates are shearable, trapping dislocations inside and around themselves (Fig. 2-33(e,f)); together with the ultrafine surface grains, these features sustain work hardening, deflect crack paths and delay localisation [58].

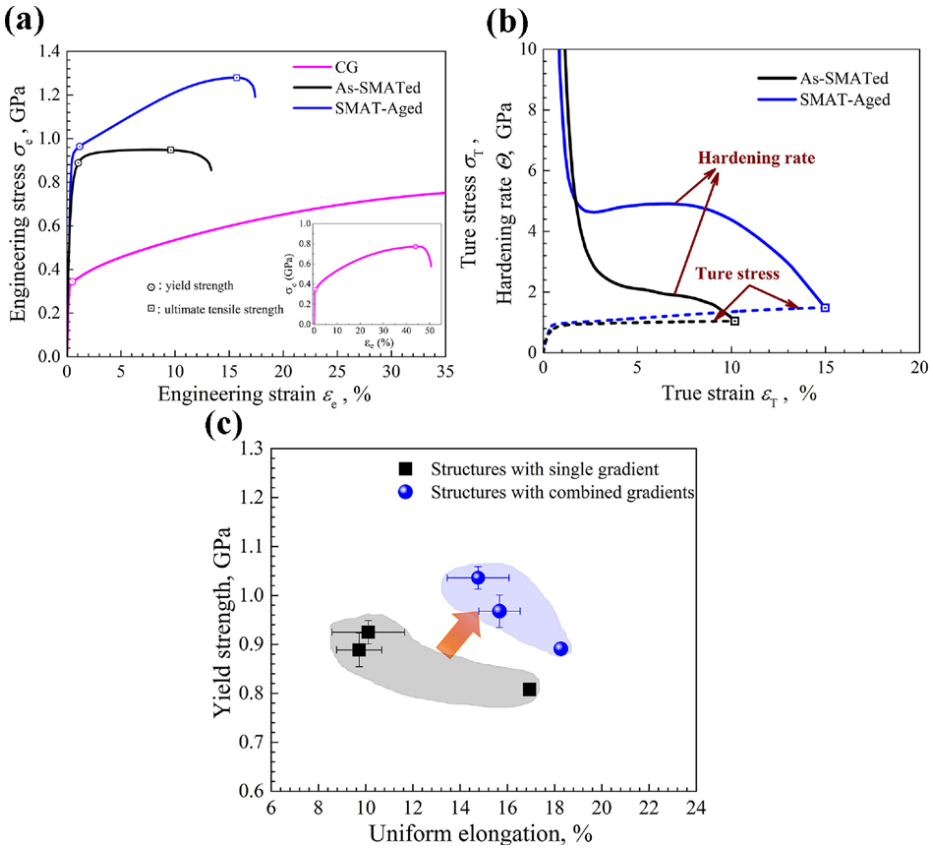

Figure 2-31 Tensile performance comparison among different samples [58]: (a) Engineering stress–strain relationships; (b) variation of true stress and corresponding strain hardening rate against true strain; (c) correlation between yield strength and uniform elongation across all examined samples.

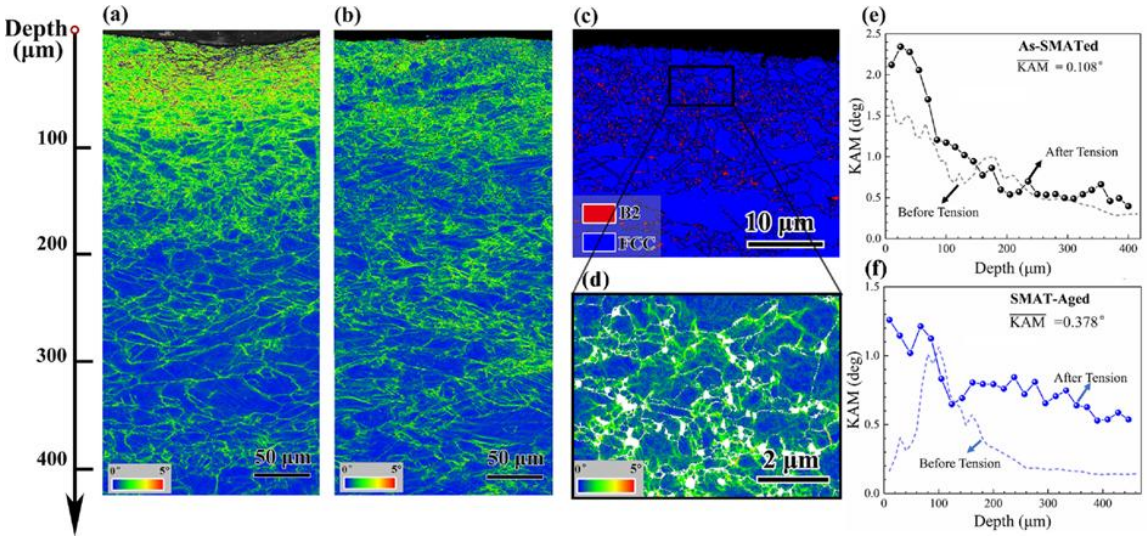

Figure 2-32 KAM maps illustrating microstructural variations [58]: (a) Sample after surface mechanical attrition treatment (as-SMATed); (b) sample subjected to SMAT followed by ageing (SMAT-Aged). Enlarged images of the uppermost surface layer of the

SMAT-Aged sample showing (c) phase distribution and (d) corresponding KAM analysis. Variation profiles of the mean KAM values as a function of depth, comparing states before and after tensile deformation: (e) as-SMATed; (f) SMAT-Aged samples.

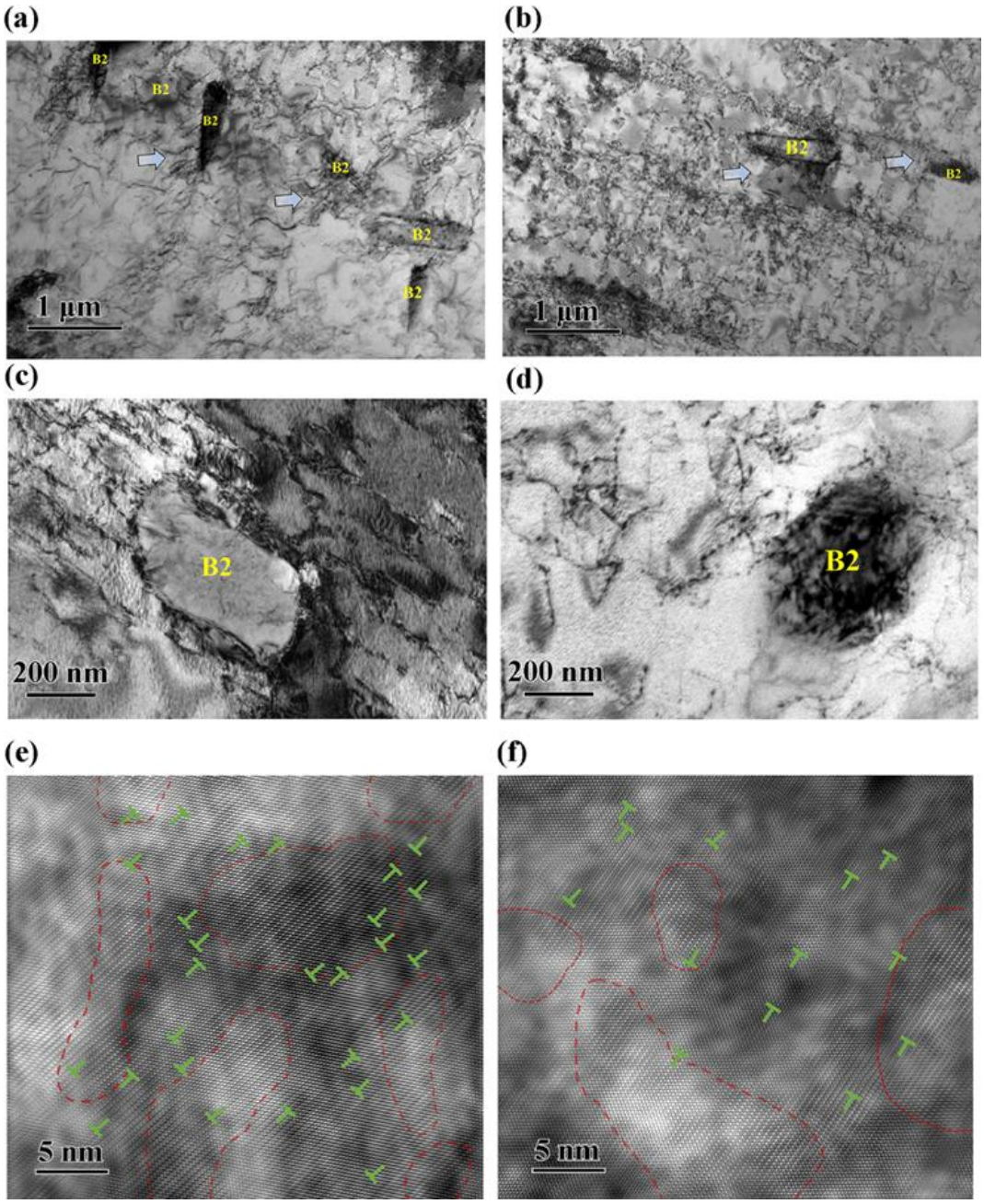

Figure 2-33 TEM and high-resolution TEM (HRTEM) micrographs of the SMAT-Aged specimen following tensile deformation [58]: Bright-field TEM images of (a, c) the surface region and (b, d) the central region. Corresponding HRTEM images highlighting dislocation interactions and pile-ups around $L1_2$ nanoprecipitates in (e) the surface layer and (f) central region; both (e) and (f) were processed via fast Fourier transformation (FFT) and inverse FFT, with $L1_2$ nanoparticles indicated by red circles.

2.3 Techniques to produce gradient structures

This section surveys the processing routes that enable precise, and often scalable, control over gradient formation. For clarity, the discussion is divided into two categories. Section 2.3.1 focuses on methods that engineer structural gradients, where the principal variable is the microstructural length-scale or defect density while composition remains nominally uniform. Section 2.3.2 then examines techniques that impose compositional gradients, intentionally varying the elemental or phase constitution to generate property partitions.

2.3.1 Methods for preparing structural gradients

2.3.1.1 Physical post-processing

Physical post-processing routes chiefly encompass surface mechanical treatments, pre-torsional processing and the accumulative roll bonding (ARB) technique. By imposing severe plastic deformation at the surface and progressively attenuating the shear strain towards the interior, these methods engender gradient microstructures [135].

Surface mechanical treatment. Over the past few decades, surface mechanical processing has become a routine route for creating gradient microstructures in metallic materials. The principal variants include surface mechanical attrition treatment (SMAT), surface mechanical grinding treatment (SMGT), surface mechanical rolling treatment (SMRT) and peening. Schematic illustrations of these techniques are provided in Fig. 2-34 [135].

As depicted in Fig. 2-34(a), SMAT employs ultrasonic vibrations with frequencies of ≈ 50 Hz–20 kHz inside a reflection chamber to propel hard spheres against the sample surface at velocities of 1–20 m s^{-1}, thereby imposing severe plastic deformation [299]. During treatment the near-surface strain rate approaches ~ 10^4 s^{-1} and diminishes gradually with depth [300]. This method preserves the substrate's original composition and secures good interfacial integrity between the gradient layer and the core, but the attainable gradient layer thickness is limited, making SMAT most suited to thin sheet samples.

The SMGT workflow is illustrated in Fig. 2-34(b). A cylindrical sample is clamped beneath a hemispherical hard head (typically WC/Co) at a preset depth. The head slides axially along the cylinder at speed v_1, while the specimen rotates at speed v_2. Sliding induces intense plastic deformation in the surface layer, generating material pile-up ahead of the head and forming a plastic zone. The surface strain rate in SMGT likewise reaches ~ 10^4

s^{-1}. A key advantage of SMGT lies in its ability to tailor grain morphology, producing either equiaxed or lamellar structures, and to refine surface grains to < 10 nm [135].

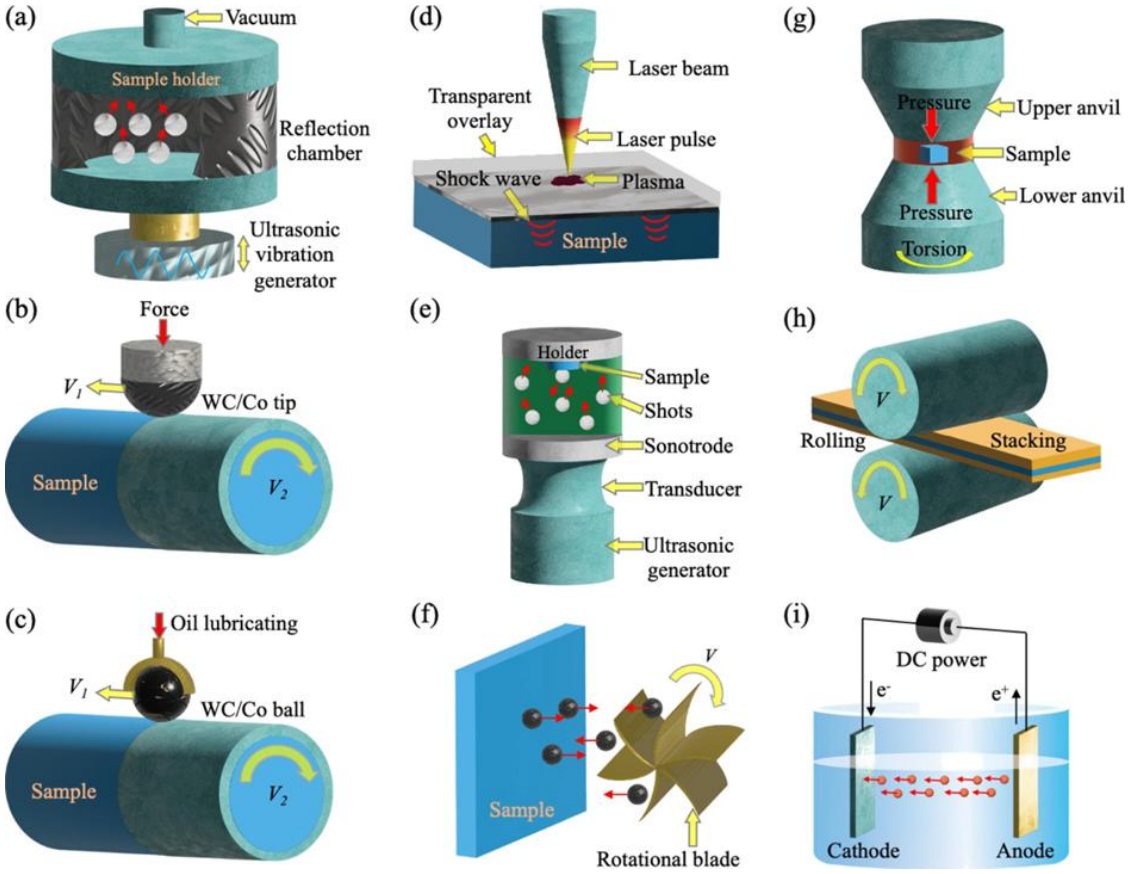

Figure 2-34 Schematic overview of physical post-processing methods and chemical electrodeposition approaches for generating gradient structured metallic materials [135]: Physical post-processing methods comprise (a) SMAT, (b) SMGT, (c) SMRT, (d) laser shock peening, (e) ultrasonic shock peening, (f) rotationally accelerated shock peening, (g) pre-torsion, and (h) ARB. (i) Direct-current electrodeposition is presented as a chemical fabrication technique.

As shown in Fig. 2-34(c), the SMRT apparatus resembles that for SMGT except that the hemispherical head is replaced by a hard spherical roller. The roller traverses the cylinder axis under lubrication, and the surface strain rate can also attain ~ 10^4 s^{-1} [122]. SMRT yields a more uniform and smoother surface finish than either SMAT or SMGT. Furthermore, both SMGT and SMRT permit repeated passes to thicken the gradient layer, although they are generally restricted to cylindrical rod specimens and necessitate auxiliary cooling to control the temperature rise during processing [123].

Peening utilises high-energy media to impose severe plastic deformation at the surface and may be classified, according to the peening source, into laser shock peening (LSP), ultrasonic shot peening (USP) and rotationally accelerated shot peening (RASP).

The workflow of LSP is illustrated in Fig. 2-34(d). A high-energy laser beam generates a pulsed shock wave at the surface. After traversing a transparent confinement layer and an ablative coating, the laser energy is absorbed and constrained within the ablation layer, which continuously vaporises to form a high-pressure plasma. The resulting compressive shock wave, with a surface strain rate of up to 10^6 s^{-1}, propagates into the substrate and gradually attenuates with depth, thereby producing a graded microstructure and introducing residual stresses extending several millimetres beneath the surface [301,302]. The advantages of LSP include localised treatment capability, improved interfacial bonding and suitability for complex geometries; its drawbacks are high energy consumption, the potential for unfavourable surface roughness and a risk of contamination.

In USP, an ultrasonic generator propels spherical media to impact the surface at velocities of up to ~ 20 m s^{-1} (Fig. 2-34(e)). The ultrasonic signal is converted by a transducer into mechanical vibration, accelerating the media and inducing intense plastic deformation; the surface strain rate reaches ~ 10^5 s^{-1} and decreases with depth [303]. Compared with LSP, USP consumes less energy, can produce a thicker gradient layer and yields lower surface roughness, although partial material removal may occur, thereby affecting the sample volume.

As depicted in Fig. 2-34(f), a rotating system propels steel balls against the surface at velocities of up to ~ 80 m s^{-1}, generating a plastic strain gradient. Relative to USP, the kinetic energy of the balls in RASP is roughly twenty-fold higher, and contamination is reduced because debris can be removed by the dust-extraction system. However, the method is limited to thin sheet samples when fabricating gradient structures [304].

Pre-torsion. Pre-torsional processing induces severe plastic deformation by applying a torsional moment to the sample. One end of the sample is rigidly clamped, whilst the other is rotated about its longitudinal axis (Fig. 2-34(g)). During twisting, the plastic strain decreases progressively from the periphery towards the core, thereby generating a gradient microstructure [125]. As the twist angle increases, the grain size in the edge region is incrementally refined. Pre-torsional processing offers procedural simplicity and low cost;

however, excessive deformation may bring about material degradation.

Accumulative roll bonding. The ARB technique employs two rolling mills to consolidate multilayer metal sheets [305]. Before processing, the sheet surfaces are cleaned and stacked. During rolling, intense compression bonds the sheets into an integral laminate, as illustrated in Fig. 2-34(h). With each successive pass the specimen thickness is progressively reduced, thereby imposing severe plastic deformation throughout the material. Subsequent annealing is usually undertaken to promote partial recrystallisation. By varying the stacking sequence of the constituent sheets, distinct gradient architectures can be obtained [306]. ARB offers the advantages of straightforward scale-up, applicability to diverse geometries and low cost; its chief limitation lies in the difficulty of refining surface grains to below ~ 100 nm.

2.3.1.2 Electrodeposition

Electrodeposition deposits metallic material onto a substrate by means of an electric current and is regarded as one of the most promising routes for generating gradient architectures in metals [135]. A typical set-up comprises an anode, a cathode and an electrolyte containing soluble salts of the metal to be deposited. The anode is usually fashioned from a high-purity electrochemical plate, while the cathode is a polished substrate. During processing, the applied current drives metal ions to plate out on the cathode surface (Fig. 2-34(i)). By adjusting the current density and the composition of the electrolyte, a variety of gradient microstructures can be produced [152]. After deposition, the gradient layer is detached from the cathode.

Electrodeposition is technologically mature, allows precise tailoring of gradient profiles and is widely adopted in both research and industrial arenas [135]. However, beyond its relatively high energy demand, diffusion limitations within the electrolyte can restrict the deposition rate; these constraints become especially significant when thick gradient layers are required, markedly prolonging the processing time [135].

2.3.1.3 Additive manufacturing

Additive manufacturing (AM) is an emergent technology that affords high design freedom and minimal material wastage, and is now widely deployed for the fabrication of metallic components [43–48]. At present, the principal AM routes for generating gradient

architectures in materials comprise directed energy deposition (DED), electron beam melting (EBM) and laser powder bed fusion (LPBF) [[43–48]].

Directed energy deposition. DED is widely used to fabricate structurally graded metallic materials. The process employs either an electric arc or a laser to melt metallic wire or powder feedstock [307–310], thereby enabling precise control over the microstructure, including structural gradients. DED is particularly suited to the manufacture of large-format components, offering high deposition rates and favourable cost efficiency.

Wire-arc additive manufacturing (WAAM) is one of the variants of DED that employ wire feedstock and an electric arc as the energy source, rather than a laser. WAAM encompasses several welding processes, including gas metal arc welding, plasma arc welding and, most commonly, gas tungsten arc welding (GTAW) [311]. As illustrated in Fig. 2-35(a), a non-consumable tungsten electrode melts a metallic wire beneath a shielding gas, and the molten metal is deposited layer by layer onto the substrate. The cooling rate typically lies in the range 100–300 K s^{-1} [312]. Structural gradients can be induced by using alternating current; for example, in Ti alloys the β-grain size decreases progressively with increasing alternating current density [309]. By adjusting the current density at successive layers, a grain size gradient can thus be engineered within the build.

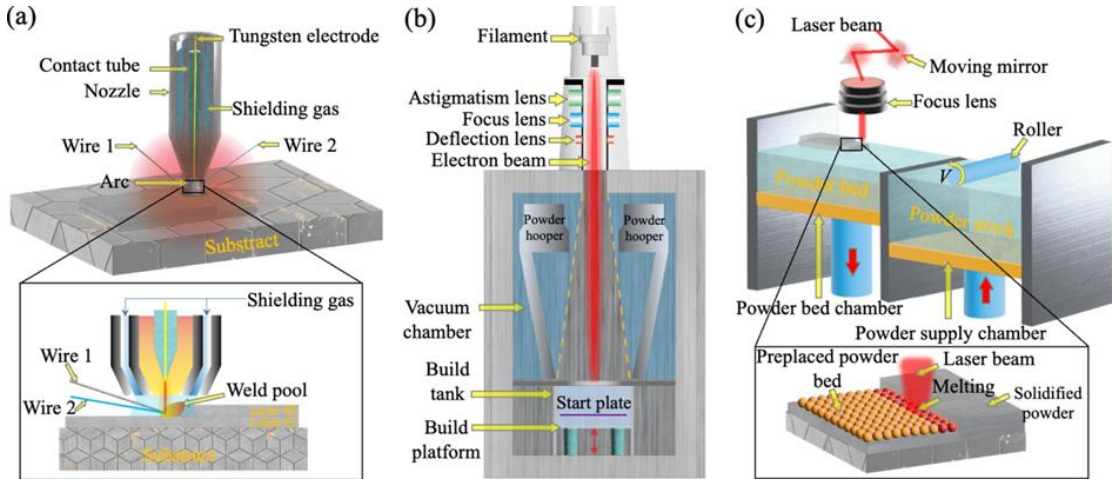

Figure 2-35 Illustrations of AM methods employed to produce structural gradients for metallic materials [135]: (a) DED; (b) EBM; and (c) LPBF.

Laser-based DED progressively builds components by sequentially melting and solidifying metal powders using a focused laser [313]. Powders are supplied directly into a melt pool created by the laser beam, subsequently bonding to the underlying substrate and solidifying

rapidly. Typical cooling rates in this process range from 10^3–10^5 K s^{-1} [314]. By selectively adjusting processing conditions throughout the deposition height, various structural gradients can be precisely engineered.

Electron beam melting. EBM employs a focused electron beam under high vacuum to fuse metal powders, as illustrated in Fig. 2-35(b). The vacuum environment effectively prevents oxidation, preserving material integrity. During fabrication, metallic powder layers spread within a build chamber are selectively melted by an electron beam, typically reaching temperatures near 1100 ℃ [313]. Characteristic cooling rates range from 10^2–10^3 K s^{-1} [315], facilitating precise management of solidification kinetics. Adjustments to beam parameters, such as location, current intensity, and scanning velocity, modulate cooling conditions, enabling controlled formation of gradient grain structures via heterogeneous nucleation at the advancing solidification interface [316]. Additionally, the EBM process yields minimal residual stress and negligible oxidation.

Laser powder bed fusion. LPBF, depicted schematically in Fig. 2-35(c), selectively melts metallic powders distributed uniformly on a build platform using a precisely focused laser [313]. Each powder layer is sequentially deposited and melted following the designated component geometry. Unmelted powders surrounding the part provide mechanical support. Following solidification of a layer, the platform is incrementally lowered, and the powder deposition-melting cycle is repeated. Characteristically high cooling rates between 10^3–10^8 K s^{-1} [317] induce rapid solidification conditions. Such rapid cooling notably generates a gradient in grain size, exemplified at the interface of 316L stainless steel and CuCrZr alloys, primarily due to phase segregation and intrinsic thermal treatments during processing [318]. LPBF efficiently fabricates complex-shaped components, supports a diverse range of materials, and typically requires limited additional structural supports.

In summary, AM furnishes a convenient route for introducing structural gradients into components of complex geometry and holds great promise for the large-scale production of gradient metallic materials. Nevertheless, process-induced defects may arise, and the grain size within the gradient region is often relatively coarse (> 100 nm). These challenges can be mitigated by optimising parameters such as energy density, powder feed rate, scan speed and hatch spacing for each alloy system. It should also be emphasised that, although the techniques described here focus on structural gradients, AM is equally capable of generating compositional gradients and this capability will be discussed in Section 2.3.2.

2.3.2 Methods for preparing compositional gradients

The fabrication of controllable CGSs in metallic materials remains a formidable manufacturing challenge [319]. A wide array of processing routes has therefore been devised and refined, each possessing distinct advantages, limitations and realms of applicability [320]. In broad terms these routes fall into two classes [321–323]: (i) conventional manufacturing processes, comprising principally forming techniques long employed in powder metallurgy and coating deposition; and (ii) modern AM technologies, wherein components are built by the layer-wise accumulation of materials.

2.3.2.1 Conventional fabrication methods

Conventional methods for fabricating metallic CGSs stem chiefly from advances in powder metallurgy and surface coating technology [324–326]. Typically, discrete material batches are placed in a prescribed gradient to form a pre-assembly, which is subsequently consolidated or joined [327]. Established techniques include layered powder metallurgy (pressing followed by sintering), thermal spray, spark plasma sintering, casting or liquid-phase infiltration, together with solid-state processes such as friction welding and extrusion [327]. Collectively, these routes have proved effective for producing both bulk graded components and compositionally graded surface coatings.

Powder metallurgy. Powder metallurgy (PM) is one of the earliest and most direct routes for producing CGSs. The method begins with the preparation of distinct metallic (or metal–ceramic) powders whose compositions match the specified locations within the component. These powders are then placed sequentially in a die to create a “green compact” possessing position-dependent composition. The stack may be arranged in discrete layers to form a stepwise gradient, or a continuous gradient can be obtained by progressively feeding or gradually blending the powders during deposition [328]. Consolidation follows by pressing and sintering [329–332]. The powder assembly is usually compacted by cold uniaxial pressing or cold isostatic pressing and subsequently sintered at high temperature to densify the body and metallurgically bond the layers [328]. During sintering, interdiffusion at the composition interfaces is critical to achieving a smooth transition. At sufficient temperature and dwell time, diffusion will eliminate sharp discontinuities and broaden the transition zone [333]. If thermal cycling is inadequate, sharp composition boundaries may remain, separated only by a narrow diffusion layer. Accurate control of sintering temperature, time and atmosphere is therefore essential for

tailoring the gradient profile [332]. Fig. 2-36 depicts a typical PM processing workflow and the associated formation mechanism for CGSs.

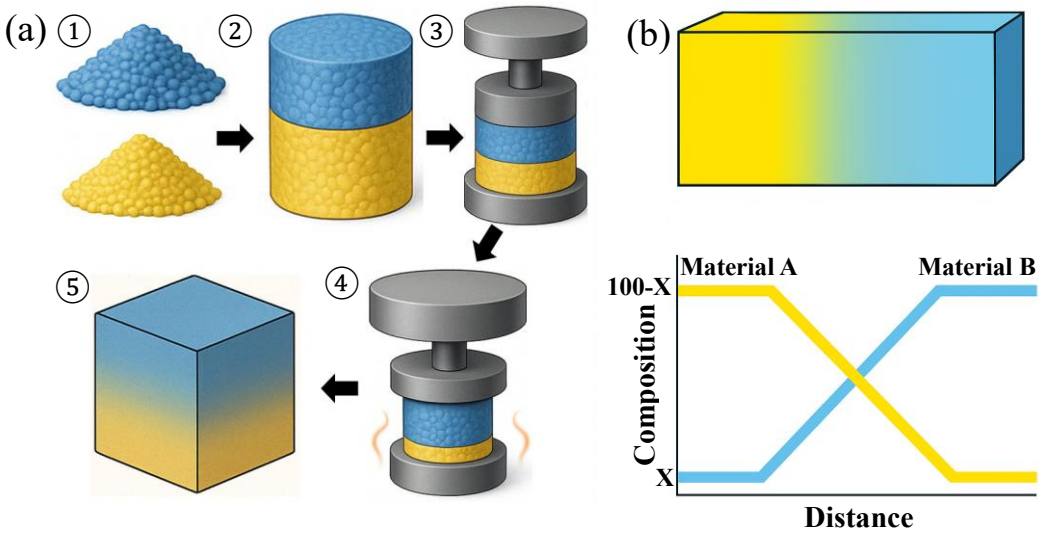

Figure 2-36 (a) Schematic workflow of PM preparation of CGSs: ① Powder preparation (yellow = Powder 1, blue = Powder 2); ② Stacking in die; ③ Cold uniaxial or cold isostatic pressing; ④ Sintering; ⑤ Graded material billet. (b) Schematic of the interdiffusion mechanism during sintering. The billet (top) shows a continuous compositional gradient from material A (yellow) to material B (blue). The plot (bottom) charts the corresponding variation in composition with distance, where the declining material A curve intersects the rising material B curve at the centre, delineating a smooth transition zone formed by bidirectional atomic diffusion. X denotes a specific composition content.

The flexibility of PM in material selection and composition control makes it very attractive. The method can freely combine metals with ceramics or other additives [330]. The equipment is relatively simple and easy to scale up [333]. However, it is difficult to achieve defect-free and fully dense parts, especially for high melting point phases or large-sized components [333]. Residual porosity and imperfect interlayer bonding may reduce mechanical properties [333]. Despite this, PM remains a basic technology for the preparation of CGSs and is often combined with advanced sintering auxiliary processes, such as spark plasma sintering, to improve the preparation quality [332].

Thermal spray. Thermal spray includes techniques such as plasma spray and high velocity oxygen fuel (HVOF) spray, whereby coatings are produced by ejecting molten or semi-

molten particles onto a substrate surface. By gradually changing the compositions of the feed powders during the spray process, coatings with compositional gradients through the thickness can be formed. In a typical method, two feed powders or suspensions, such as material powder A and material powder B, are used, and their relative feed rates are continuously adjusted from 100:0 to 0:100 to achieve a compositional gradient from 100% material A at one end to 100% material B at the other end [334,335]. The thermal spray process is carried out under high temperature conditions, such as atmospheric plasma spray (APS), where the plasma jet temperature is about 10,000 K, which can completely or partially melt the particles. These particles deform upon impact with the substrate and rapidly solidify to form flat particles, which form a layered microstructure [334]. To achieve gradient coatings, multiple layers are usually deposited, and the powder ratio is gradually adjusted after each deposition or during the deposition process [336]. Fig. 2-37 shows the plasma spray process for preparing CGSs In the APS process, a plasma spray gun equipped with a cathode-anode structure generates a high temperature plasma jet, and the powder feedstock enters the plasma jet under the propulsion of a carrier gas. The molten particles are sprayed onto the substrate to form a coating (Fig. 2-37(a)) [335]. By connecting multiple powder feeders or using a sequential feeding method, a gradual transition between powders can be achieved, such as mixing two material powders in different proportions. Suspension plasma spray (SPS) or solution precursor plasma spray (SPPS) technology can also prepare gradient coatings by changing the suspension or solution compositions (Fig. 2-37(b)) [337–339].

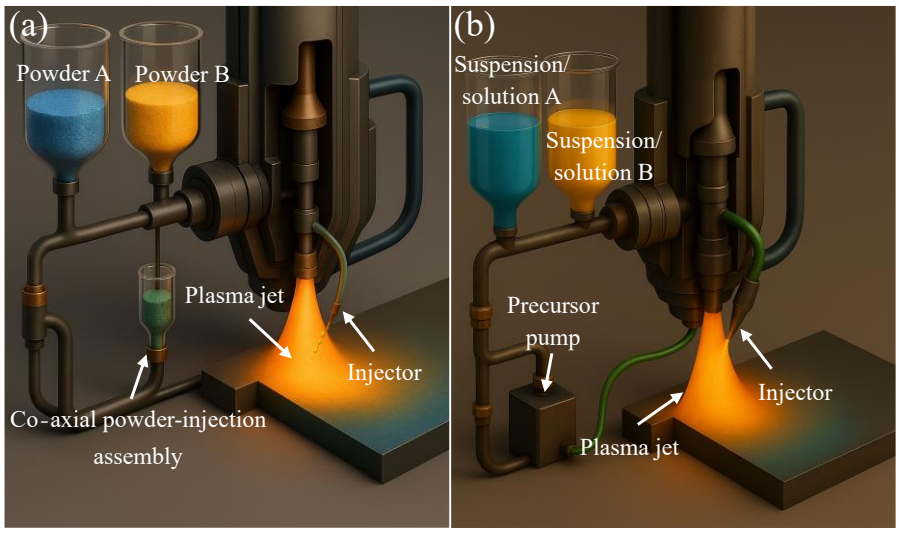

Figure 2-37 Workflow and mechanistic schematics of thermal spray techniques for fabricating compositionally graded metallic coatings. (a) APS; (b) SPPS.

Thermal spray methods can coat large areas and complex shapes of parts at a fast speed and have been proven in industry. Composition control can be achieved by adjusting the feed rate in real time, thereby forming a continuous gradient [340,341]. Coatings of materials with extremely high melting points can be sprayed without melting a large area of the substrate. Gradient coatings produced using APS/HVOF techniques have been shown to reduce delamination and residual stresses in coatings because the gradual change in composition mitigates the sudden change in properties [342]. However, thermal spray has some limitations. Thermal spray is generally used to produce coatings rather than bulk parts. Coating thicknesses are typically less than 1 mm, although thicker coatings can be achieved through multiple spray passes [343]. The microstructure is inherently layered and has some porosity, and post-processing may be required to achieve full density. Gradient control at the microscale may not be precise, and some mixing zones may exist due to particle mixing [344]. Oxidation or degradation of the material may also occur in the high temperature spray environment unless a vacuum plasma spray system is used. In addition, this method is limited in that at least one material must be sprayable (meltable) and stable in the molten state [341,344]. Despite this, gradient thermal spray coatings have been successfully applied to applications such as biomedical implants and cutting tools [345].

Casting and melt infiltration methods. Casting techniques can produce CGSs by controlled solidification or by infiltration of one material into another. One approach is sequential casting, where two or more alloys are poured one after another in a mould such that they partially mix at the interfaces, creating a gradient [346]. For instance, a bimetal rod with a gradient can be cast by first pouring metal/alloy A, then metal/alloy B on top before A fully solidifies, and the result after solidification is a graded transition region due to melt interdiffusion (Fig. 2-38(a)). A more controlled variant is gravity or centrifugal casting with an applied thermal gradient, which can drive segregation of alloying elements in a deliberate way [347].

Infiltration-based methods are very effective for certain metal–metal CGSs. The general process is first to create a porous preform of one material with a gradient in porosity or phase, then infiltrate it with a second material in liquid form (Fig. 2-38(b)) [348]. The classic example is making a W–Cu graded material [349]. W and Cu are immiscible in solid state, so traditional melting won't mix them. Instead, a graded porous W structure can be formed by packing and lightly sintering W powder with a designed density gradient

and then molten Cu is infiltrated into it. The Cu fills the pores, resulting in a fully dense CGS where the Cu/W ratio varies according to the initial porosity gradient of the W preform. Wang et al. used such an approach, first sintering a W body with a porosity gradient and then infiltrating Cu to obtain a W–Cu CGS [350].

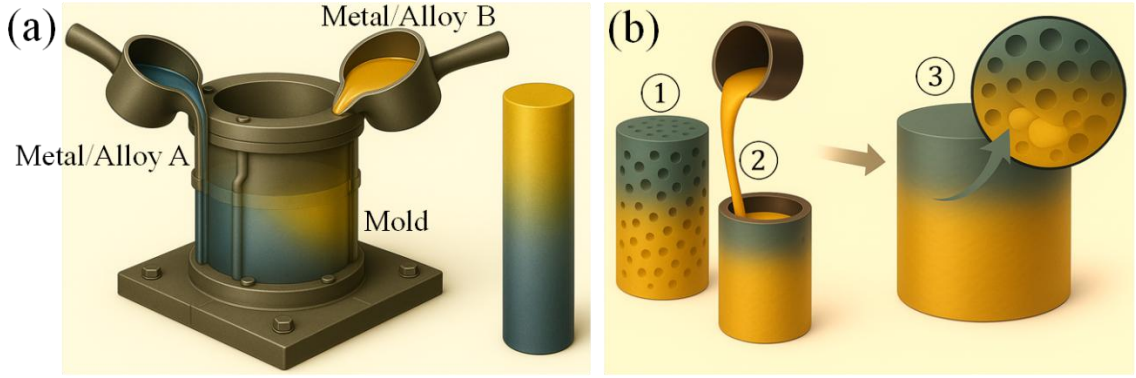

Figure 2-38 (a) Sequential casting for CGSs: Metal/Alloy A is poured first and partially solidifies before Metal/Alloy B is introduced, creating a liquid–liquid interface that solidifies under an imposed thermal gradient. (b) Infiltration-based fabrication of CGSs: ① Preparation of a porosity-graded cylindrical preform of Metal/Alloy A (blue, grading to yellow); ② Infiltration with molten Metal/Alloy B (yellow) inside a cylindrical mould; ③ Solidification and extraction of the fully dense graded cylinder exhibiting a continuous axial A→B composition gradient. Mechanistic inset: liquid Metal/Alloy B fills the pore network, wets Metal/Alloy A and, on solidification with short-range diffusion, produces a seamless gradient.

Casting and infiltration can produce near-net-shape gradient components that are fully dense. They are well-suited for metal–metal combinations that are otherwise not easy to join continuous gradient if the preform porosity is continuous. The resulting microstructure often has excellent bonding since one material solidifies within the other's pores (mechanical interlock and sometimes metallurgical bonds if soluble) [351]. Nonetheless, controlling the distribution of the gradient relies on preparing a suitable preform, which often involves its own complex manufacturing process, such as by 3D printing or precisely layering powders to form a porosity gradient preform. During the infiltration process, if not properly managed, gravity and capillary forces can lead to uneven material distribution, such as more material infiltrating one area. During the casting process, convective mixing can blur the gradient boundaries or lead to compositional instabilities, such as macro

segregation [352]. In addition, if the composition gradient changes too sharply, thermal stress problems may occur during cooling. In some cases, if the two materials are reactive, brittle intermetallic compounds may form at the interface, although ideally, a combination of non-reactive materials is usually selected for infiltration. Despite these challenges, casting and infiltration techniques have been successfully used to manufacture CGSs, such as armour materials with compositional gradients and gear components with hard surfaces and high-toughness cores [353].

Chemical and physical vapour deposition. Vapour deposition techniques are capable of producing compositional gradients, especially as thin films or surface coatings on bulk substrates. In chemical vapour deposition (CVD), gaseous precursors react on a substrate to deposit material, and by varying the gas composition or process parameters over time, one can gradually change the deposited film's composition (Fig. 2-39(a)) [354–357]. Similarly, physical vapour deposition (PVD) processes (sputtering, evaporation) can achieve gradients by, e.g., co-sputtering from multiple targets and changing power on each target to shift the film composition from one material to another continuously (Fig. 2-39(b)) [358–361].

CVD/PVD-produced CGSs are usually thin (microns to a few millimetres), but they offer extremely fine control over composition profiles. However, the limitation of vapour deposition for CGSs is primarily thickness and deposition rate, since building a large bulk part via vapour methods would be prohibitively slow and costly. Thus, these techniques are mostly used to create surface CGSs or thin-film multilayers rather than bulk gradient components [355,359]. Nonetheless, they play a crucial role in certain high-performance systems.

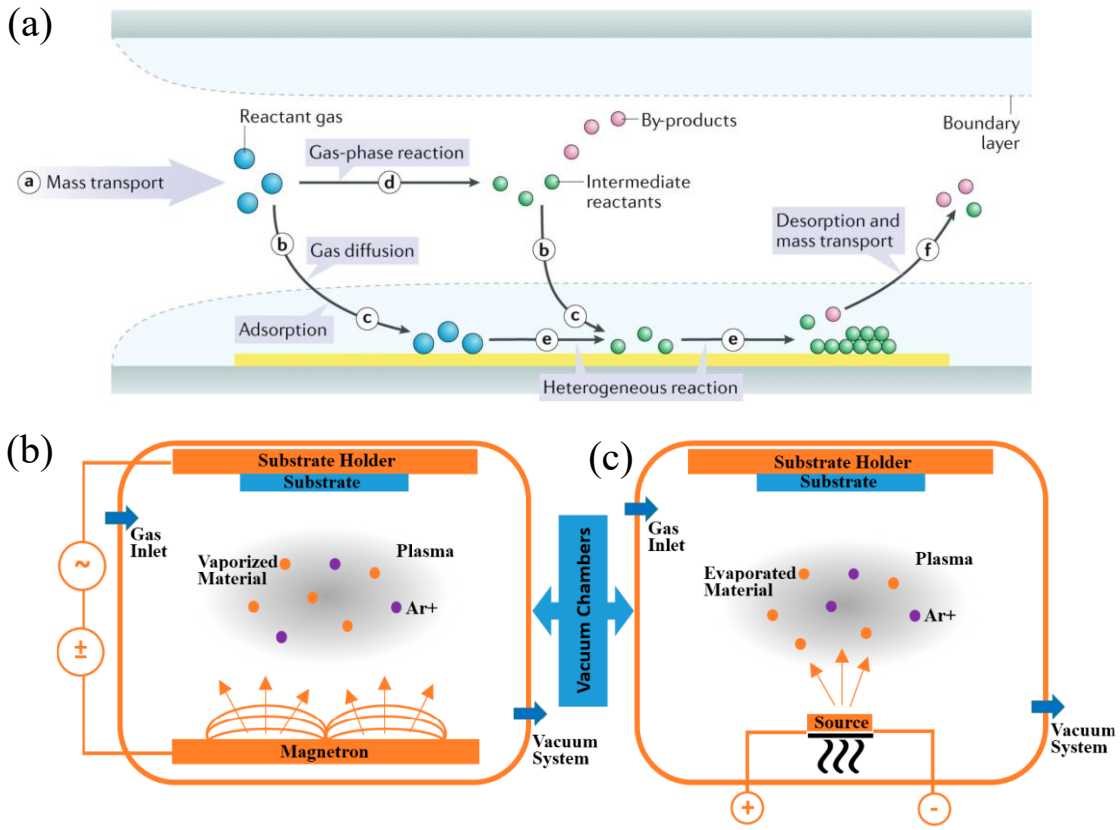

Figure 2-39 (a) Schematic illustration of the fundamental stages in a generic CVD process. (b, c) Schematic representations of two conventional PVD techniques: (b) sputtering; (c) evaporation employing ionised argon (Ar^+) [354,358].

Self-propagating high-temperature synthesis. Self-propagating high-temperature synthesis (SHS), also referred to as combustion synthesis, exploits highly exothermic reactions that are locally ignited and subsequently propagate through the reactant mixture as a combustion wave, thereby forming new phases (Fig. 2-40) [362–364]. By judiciously arranging the reactants such that the extent of reaction, or the phases synthesised, varies spatially, SHS can be harnessed to fabricate CGSs [365]. A representative approach involves stacking reactive powder beds of differing composition; as the combustion wave traverses the stack, products with lamellar or continuous gradients are generated. SHS is particularly attractive for CGS production because it supplies its own internal heat source, obviating prolonged external heating, and the rapid solidification of the products yields a refined microstructure [366].

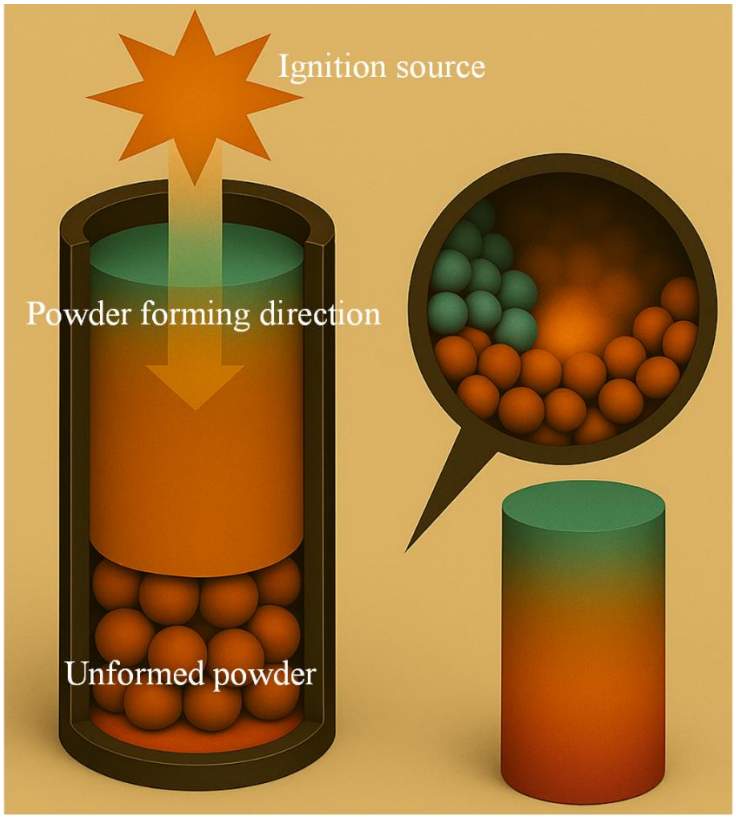

Figure 2-40 Schematic workflow for the fabrication of CGSs by SHS. Reactive powder layers are stacked inside a cylindrical die, and a local ignition source at the top launches a self-sustaining combustion wave that traverses the compact and converts it into a dense bar exhibiting a smooth axial compositional gradient. The inset zooms into the advancing reaction front, illustrating intense local heat release, melting and diffusion of reactant particles (spheres).

Accurately controlling the combustion front to achieve a smooth gradient is, however, inherently challenging. Reaction kinetics and heat-flux transport may render the compositional transition excessively steep rather than gradual. Moreover, SHS generally requires a sealed vessel to enable applied pressure or atmospheric control, and the violent nature of the reaction can induce cracking, complicating the maintenance of structural integrity in the final component. In practice, SHS is frequently combined with subsequent techniques, such as post-SHS hot pressing or casting, to manufacture compositionally graded materials [366,367].

In summary, SHS is a specialised route for fabricating graded materials, predominantly employed for refractory metals or ceramic-rich gradients that are difficult to achieve via conventional melting or sintering. Owing to the difficulties in controlling the combustion

front and ensuring dimensional precision, its application in metallic CGMs remains limited and largely confined to exploratory studies.

Other techniques. Several additional strategies merit consideration. Friction stir processing/welding (FSP/FSW) can generate graded architectures by surface alloying. A groove is first machined into the surface of a metallic plate and packed with a dissimilar metallic powder; subsequent FSP plasticises and intimately mixes the materials, thereby establishing a gradient that extends from the surface into the substrate [368]. This route affords a fine-scale gradient and sound interfacial bonding because the entire operation occurs in the solid state, although the resulting gradient layer is generally restricted to the near-surface region [369].

Diffusion bonding likewise enables compositional grading. Here, foils or plates of distinct composition are stacked and diffusion-bonded to yield a laminated gradient structure; further heat treatment promotes interfacial diffusion, producing a continuous gradient [370,371].

Electrophoretic deposition (EPD), outlined in Section 2.3.1.2, can likewise be employed to fabricate compositionally graded coatings. By modulating the deposition voltage or duration, a gradient in particle concentration is induced; sintering of the deposit then consolidates a graded coating [372–374]. At present, however, these techniques for metallic CGSs remain chiefly at the investigative stage.

2.3.2.2 AM techniques

AM affords spatial control over composition during the layer-by-layer construction of a component, thereby opening new avenues for the fabrication of metallic CGSs. Unlike conventional routes, which typically require discrete layering and consolidation stages, AM, guided by computer-aided design (CAD), can synthesise and solidify layers of differing composition in situ throughout the build. The metal-based AM techniques best suited to CGSs fall into two principal categories: DED and LPBF, both of which can be adapted for multimaterial fabrication [43–48,375–380].

It should be emphasised that AM fabricates a component through the same layer-by-layer deposition principle irrespective of whether a structural or a compositional gradient is desired: a digital toolpath slices the part into lamellae and precisely controls the energy

input and feedstock delivery in each voxel, so that every deposited layer can be tailored independently of its neighbours [43–48]. The distinction lies in which variables are modulated during deposition. To generate a structural gradient, the machine keeps the feedstock composition constant but varies processing parameters, such as laser power, scan speed, hatch spacing or interlayer cooling time, to impose localised thermal histories that refine or coarsen the microstructure along the build direction [375–380]. Conversely, to create a compositional gradient the thermal schedule remains nominally uniform, while the feedstock itself is altered in real time, for example by switching powder hoppers, blending powders in programmable ratios or toggling wire feeds in DED [43–48,375–380]. In short, structural gradients exploit spatial control over heat flow and solidification kinetics, whereas compositional gradients exploit spatial control over material compositions, yet both rely on AM's common capacity for voxel-scale process customisation [43–48,375–380].

Moreover, emerging multimaterial AM strategies, such as binder jetting [381–383] and material jetting employing multiple binders [384–386], can also been used for fabricating compositional gradients, although they remain uncommon for structural metallic materials.

2.4 Texture evolution of face-centred cubic metallic materials

Nearly all structural metallic materials are polycrystalline aggregates of grains with various orientations. During processing, these grains tend to develop preferred crystallographic orientations, known as a texture, rather than remaining randomly oriented [387]. Texture is crucial because it strongly influences anisotropic properties, such as yielding and formability, in metallic materials [387]. Understanding how textures form and evolve can therefore guide the design of processes and alloys to achieve desirable properties. In face-centred cubic (FCC) metallic materials, texture development occurs predominantly during two stages of manufacturing: (i) plastic deformation (e.g. cold rolling), which produces a deformation texture, and (ii) annealing (recovery and recrystallisation), which produces an annealing or recrystallisation texture [387]. This section surveys texture evolution in FCC materials, focusing on the mechanisms, transitions, and key factors governing texture during cold rolling and subsequent annealing.

2.4.1 Texture evolution induced by cold rolling

Cold rolling imposes severe shape change on FCC polycrystals and produces characteristic

deformation textures. Mechanistically, plastic deformation in FCC materials occurs by dislocation slip on {111}<110> glide systems and, in many cases, by deformation twinning on {111}<112> systems (especially in low-SFE materials) [387]. The balance between these mechanisms – slip vs. twinning – largely dictates the resulting texture. High-SFE materials (e.g. Al, Cu, Ni) deform predominantly via dislocation slip; many dislocations cross-slip and form dense cell or subgrain structures, gradually rotating grains toward stable orientations predicted by slip-based models (e.g. Taylor theory) [388]. The result is the classical copper-type rolling texture: a spectrum of orientations along the β-fibre connecting Copper {112}<111> and Brass {110}<112>, with a notable S {123}<634> in between [389]. The typical rolling texture components in FCC metallic materials are shown in Fig. 2-41 [387]. In fact, in high-purity Cu or Al rolled to high reductions (~90%), the Copper and S orientations often dominate, with Brass and others present to lesser degrees [387]. Low-SFE materials (e.g. α-brass, certain stainless steels, high-Mn alloys) also accommodate strain by slip, but concurrently activate deformation twinning at relatively low strains, as the reduced SFE makes twin nucleation energetically easier. These materials develop a distinct brass-type rolling texture marked by a strong Brass component and frequently a Goss component, while the Copper and S components are comparatively weaker [390]. For example, heavily rolled 70/30 brass exhibits Brass {110}<112> as the predominant orientation (intensity about three times higher than Copper in some cases), plus a secondary Goss {110}<001> component [391]. Such differences are understood as a consequence of twinning and shear banding altering the orientation trajectories during deformation [392].

In quantitative texture terms, cold rolling textures in FCC materials can be described by orientation distribution functions (ODFs) or pole figures. A well-known feature is the strengthening of certain ideal orientations with strain. For instance, in high-SFE materials, the β-fibre intensifies continuously: with higher rolling reduction, orientations along {111}⟨110⟩ and approaching {110}⟨112⟩ gain in volume fraction [387–392]. Experiments on pure Cu sheets show that as rolling reduction increases from ~20% to ~87%, the deformation texture components {112}<111> (Copper), {123}<634> (S), and {110}<112> (Brass) all become sharper and more prominent [387–392]. The Brass orientation in particular often strengthens at very high strains (e.g. >60% reduction), as lower-strain components rotate toward Brass along the fibre [387–392]. Concurrently, the spread of orientations around these ideal positions typically narrows – signifying a more

ordered texture – when deformation is predominantly by slip [387–392]. By contrast, in low-SFE FCC materials where twinning occurs, the evolution can be more complex [387–394]. Twinning introduces new orientations that are twin-related variants of the parent orientation (typically a 60° rotation about ⟨111⟩). These twin orientations can correspond to known components; for example, a primary Copper-oriented grain ({112}<111>) will produce twin lamellae that are approximately Goss oriented ({110}<001>) [387–394]. Indeed, Kaushik et al. report that in a CoCrFeMnNi HEA, one variant of a Copper orientation grain twinned into Goss orientation [395]. Likewise, twinning of S-oriented grains tends to generate Brass-oriented twins [395]. The net effect is that twinning can redirect orientation trajectories: grains that might otherwise stay around Copper or S (if only slip occurred) are partially rotated toward Brass or Goss due to twin formation [395]. This accelerates the texture's shift to a brass-type character. At the same time, because twinning creates additional orientation spread (the matrix vs. twin orientations), it often weakens the overall texture intensity relative to a pure slip scenario [395]. In other words, deformation twinning tends to scatter orientation density into twin-related orientations, preventing any single component from becoming overwhelmingly strong at intermediate strains [395]. Consistent with this, experiments on twinning-prone alloys (e.g. brass, low-SFE steels) show that their rolling textures, while brass-type, are generally less sharply peaked (more diffuse) than those of high-SFE metals at the same reduction [387–395].

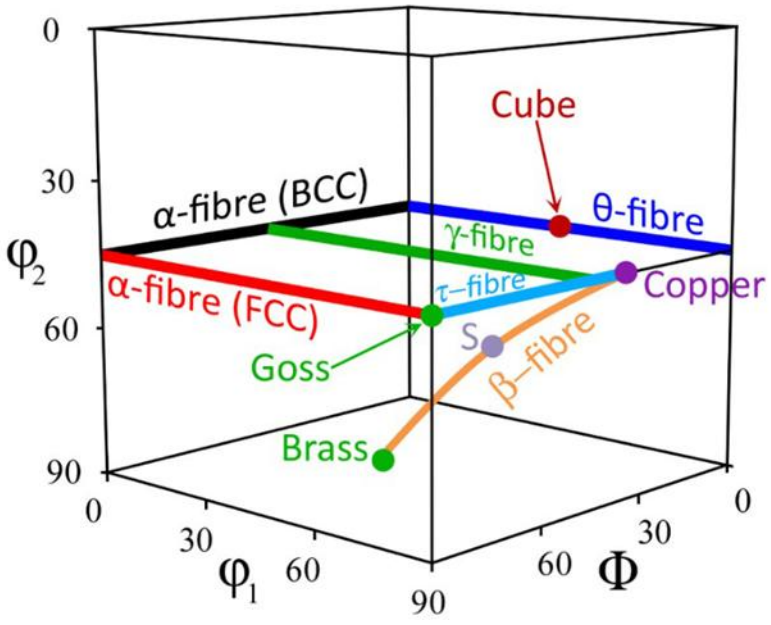

Figure 2-41 The typical rolling texture components in FCC metallic materials [387].

Another hallmark of heavy rolling is the formation of shear bands in some materials, especially once a critical strain is exceeded. Shear bands are narrow zones of intense shear strain that cut through the prevailing deformation substructure, often at a moderate angle to the rolling plane. They are commonly observed in brass-type materials (e.g. in Cu–Zn, Cu–Ni–Si alloys, high-entropy alloys) at high reductions [395–398]. Shear bands create a new set of orientations inside them, often lying between Brass and Goss on the φ_1-Φ sections of the ODF (sometimes termed "intermediate" orientations) [395–398]. These bands can facilitate a texture transition by consuming areas of the material and replacing their orientation with a different one. For instance, in copper and 70/30 brass, the onset of shear banding has been linked to a transition in the dominant texture – more so than twinning alone – with Goss and other components surging once shear bands proliferate [395–398]. Generally, shear banding contributes to stabilising the brass-type end orientations at extreme strains, as orientations within shear bands often evolve toward Brass or between Brass and Goss [395–398]. Thus, slip, twinning, and shear banding all interplay during intense deformation to produce the observed texture.

It should be noted that initial texture and deformation conditions also influence the rolling texture outcome. If the starting material has a strong texture, deformation will rotate those grains and might yield a somewhat different path than a random-start material (orientation path "memory"). However, after high strains (e.g. >50%), the effect of initial texture is often diminished, and the material tends toward its characteristic rolling texture [387–394]. Deformation temperature is another factor: lower temperatures reduce SFE effectively and promote twinning. A classic example is copper rolled at liquid-nitrogen temperature (−196 °C), which develops a brass-like deformation texture instead of the usual copper-type and correspondingly fails to produce a cube recrystallisation texture upon annealing [387–394]. Higher strain rates or certain rolling techniques (e.g. asymmetric rolling) can also alter textures slightly by introducing additional shear or rotation components, but the core slip/twin behaviour remains governed by SFE and crystal symmetry [387–394].

In summary, cold rolling textures in FCC metallic materials evolve via a competition between dislocation slip and deformation twinning. High-SFE materials follow the classic Copper→Brass rotation paths, resulting in Copper/S/Brass mixtures (copper-type texture). Low-SFE materials activate extensive twinning which shifts textures toward Brass/Goss (brass-type texture) and broadens the orientation spread. At very high strains, shear

banding further influences texture, often reinforcing Brass-like components [387–399]. Key factors that influence the deformation texture include: (i) SFE: Higher SFE favours dislocation slip and sharper copper-type textures; lower SFE promotes twinning, yielding brass-type textures [387–399]. (ii) Deformation strain (reduction): Greater rolling reductions sharpen and stabilise certain texture components, though extreme strain can introduce shear band orientations [387–399]. (iii) Initial grain orientation/textures: A strong initial texture may bias the evolution, but with sufficient strain the texture typically converges to the material's characteristic rolling texture [387–399]. (iv) Deformation temperature/rate: Lower temperatures (or higher rates) promote twinning and hence a transition toward brass-type textures. Warm rolling (higher temperature) in low-SFE materials can suppress some twinning, resulting in a texture closer to that of high-SFE materials [387–399]. (v) Alloying and second phase particles: Solute elements can alter SFE and dislocation behaviour; for instance, adding Co to Ni lowers SFE and gradually transforms Ni's rolling texture from copper-type to brass-type as Co content increases [400]. Likewise, microalloy precipitates can pin dislocations or promote localised shear, indirectly affecting texture development [387–392].

These factors mean that while general trends exist, the exact rolling texture of a given FCC material may vary in intensity and minor components. Nonetheless, the copper-type vs. brass-type dichotomy – largely controlled by slip vs. twin activity – provides a useful framework for understanding FCC deformation textures across different materials.

2.4.2 Texture evolution induced by annealing

Following cold deformation, FCC materials are often annealed to restore ductility through recovery and recrystallisation. During annealing, the deformation microstructure (high dislocation density, subgrains, twins, shear bands) is replaced by new, strain-free grains that nucleate and grow. This process generates a recrystallisation texture, which can differ markedly from the prior deformation texture [401]. The mechanisms governing annealing texture development include oriented nucleation (certain orientations nucleate more readily from the deformed state) and oriented growth (certain orientations grow faster or consume others) [402], both of which are influenced by the stored energy distribution and boundary characteristics in the deformed microstructure.

In high-SFE, slip-dominated FCC materials, recrystallisation textures are typically

dominated by the cube orientation {001}<100> [394,403]. For example, heavily rolled pure Al and Ni sheets recrystallise into a very sharp cube texture – often over 75–90% of grains adopting {001}<100> [401,404]. The origin of this cube texture has been a subject of study for decades. It is generally thought that cube-oriented regions in the deformed microstructure either store lower energy and thus nucleate first – an "oriented nucleation" hypothesis – or that once any cube grain nucleates, it has a growth advantage (perhaps due to 45° misorientation relationships that promote high mobility of boundaries) – an "oriented growth" hypothesis [401,402]. In practice, both effects may play a role. Cube-oriented subgrains often exist already in the rolled state of high-SFE metals (sometimes retained fragments of a prior annealing texture or spontaneously formed during deformation), and upon annealing these can rapidly recrystallise into cube grains [405,406]. Additionally, cube grains can consume the surrounding deformed matrix efficiently, especially if that matrix has orientations like Copper or S that are near 40–50° away, which makes a special boundary with cube that migrates quickly, according to the "strain energy release maximisation" model [401]. The result is an unequivocally sharp cube recrystallisation texture in metals such as Al and Cu, provided the material is relatively pure and heavily rolled [401]. Minor components like Goss {110}<001> or R–{124}<211> (in Al) may appear, often as twins of the cube grains or due to oriented growth from specific deformation fragments [394,403]. For instance, in high-purity Cu, a small Goss component is sometimes observed after recrystallisation, which analysis suggests originates from Brass-oriented regions of the deformation texture transforming via twinning or boundary nucleation into Goss grains [401]. Overall, though, the cube component is by far the most prominent in recrystallised textures of high-SFE FCC materials [404,406].

In low-SFE FCC materials, recrystallisation textures are more varied and often significantly weaker (more diffuse) than in their high-SFE counterparts [401]. A striking example is 70/30 brass: whereas pure Cu gives a strong cube texture upon annealing, a Cu–30%Zn alloy with very low SFE, shows essentially no cube component after recrystallisation [394,403]. Instead, brass's recrystallisation texture is typically described by a component near {236}<385> (sometimes called the "Brass recrystallisation" orientation) [401]. This {236}<385> orientation is crystallographically related to the deformed Brass orientation – in fact it can be generated by a 60° ⟨111⟩ twin rotation from Brass, or by a small rotation from the Brass twin variant {122}<212> [394,403]. Thus, one

interpretation is that Brass-oriented regions recrystallise into grains of {236}<385> (and its twin {123}<374>, etc.), rather than into cube grains [394,401,403]. Consequently, the annealing texture retains a memory of the deformation texture (Brass) rather than resetting to cube. Similarly, in low-SFE material, which exhibits a brass-type rolling texture, recrystallisation does not produce cube grains, but instead orientations approximating {236}<385> and other variants [401]. Why does this happen in low-SFE materials? The explanation lies in how recovery and nucleation proceed. Low-SFE materials deform via planar, heterogeneous dislocation structures that recover quite rapidly upon annealing, even before new grains nucleate [401]. This means the stored energy differences between regions, which drive selective nucleation of certain orientations, are smaller – many regions are similarly "recovered." With the driving pressure for oriented nucleation diminished, recrystallisation tends to initiate in whatever sites are available (often stress concentrations at shear band intersections or grain boundaries) rather than selectively in cube subgrains [401]. Moreover, low-SFE materials form abundant annealing twins during grain growth – every new grain can quickly form Σ3 twins as it grows – which multiplies the number of distinct orientations present in the recrystallised aggregate [407]. This annealing twinning has a profound effect: it effectively randomises or at least weakens the texture, since each growing grain immediately generates one or more twin orientations (e.g. a cube grain would generate a {221}<310> twin, etc.), spreading intensity across related orientations. In brass, for example, recrystallised grains frequently form twins on {111}, which can produce orientations like Goss from cube, or {236}<385> from Brass, etc., thereby preventing any single component from dominating [401].

Another factor in low-SFE materials is solute drag and particle pinning, which can alter growth rates. Small impurity additions that lower SFE (e.g. 0.03% P in Cu) are known to completely suppress the cube texture, presumably by inhibiting the growth of cube nuclei and allowing other orientations to grow instead [394,403]. In brass, varying the annealing temperature can change the recrystallisation texture: at lower annealing temperatures, one might see more retention of deformation orientations due to sluggish nucleation and the need for growth through high angle boundaries, which may favour certain misorientations, whereas higher annealing temperature can sometimes lead to a slightly different texture (e.g. a mix of {236}<385> and others) as different nucleation sites activate [394,403]. Generally, however, the trend stands that cube texture strength diminishes with decreasing SFE. There appears to be a threshold SFE above which a strong cube recrystallisation

texture is obtained, and below which cube is absent and other orientations prevail [401].

It is important to note that the deformation texture heavily influences the recrystallisation texture, especially in medium-to-high SFE materials where oriented nucleation dominates. If the deformation texture is very strong, as in heavily rolled copper with a sharp Brass and S, the recrystallisation texture may include components derived from those orientations (e.g. Goss from Brass as mentioned) in addition to cube [394,401,403].

In summary, annealing transforms deformation textures in FCC materials through recovery, nucleation, and growth processes that are highly sensitive to SFE and prior deformation structures. High- and medium-SFE materials reliably produce a sharp cube recrystallisation texture with minor twins of cube, due to oriented nucleation/growth driving cube grains to dominate [394,401,403,404]. Low-SFE materials, on the other hand, show varied annealing textures – often retaining traces of the deformation texture or its twin variants – because recovery diminishes orientation differences and annealing twins introduce new orientations, leading to a weaker overall texture [401,407]. The presence of many twin boundaries in recrystallised low-SFE materials tends to further randomise the texture by dividing grains into twin-related orientations. In practical terms, this means low-SFE materials after annealing are more isotropic in properties (texture-softened) compared to high-SFE materials which may retain strong anisotropy due to a sharp cube texture [394,401,403,404,407].

Chapter 3. Experimental techniques and procedures

This chapter retains concise primers on the principles and workflow of the characterisation methods used in this work. Each primer is limited to what governs data quality and interpretation. Readers who already know these methods may proceed directly to the subsequent subsections that report the materials, the measurements and the results. The intent is to preserve completeness and accessibility while keeping the focus on information that underpins reproducible data. This chapter extensively describes electron microscopy methods relevant to this research. Firstly, Section 3.1 clearly elaborates the working principles behind the microscopy technique being employed here. Section 3.2 fully elaborates the concept-based design strategies, fabrication processes, and procedures for processes under which samples were prepared. Next, Section 3.3 clearly delineates procedures adopted for preparing specimens for electron microscopic analysis, whereas Section 3.4 puts forward all methods adopted in this research for probing mechanical performance.

3.1 Structural characterisation techniques

This section begins by summarising the various signals generated when an electron beam interacts with matter and then describes the advanced structural characterisation techniques and their principles employed in the present study, namely scanning electron microscopy (SEM), transmission electron microscopy (TEM), scanning transmission electron microscopy (STEM), X-ray energy-dispersive spectroscopy (XEDS) and X-ray diffraction (XRD).

3.1.1 Interactions between the electron beam and materials

Structural analysis in both SEM and TEM hinges on the manner in which high-energy electrons engage with a specimen [408,409]. These encounters are classified as elastic, in which the electrons suffer virtually no energy loss, or inelastic, wherein a portion of their energy and momentum is imparted to the material [408,409]. The interaction cascade yields a suite of signals, notably backscattered and forward scattered electrons, characteristic X-rays, visible-light photons, Auger electrons and secondary electrons, as depicted schematically in Fig. 3-1. Each signal conveys complementary crystallographic or chemical information that can be harvested with dedicated detectors [408–410]. The

subset of interaction products employed in the present investigation is outlined succinctly below.

Backscattered electrons (BSEs) constitute the energetic portion of the incident beam that is elastically redirected out of the interaction volume. Because the elastic scattering cross-section increases markedly with atomic number, domains enriched in heavier elements yield more intense BSE signals, appearing brighter in micrographs. Complementary

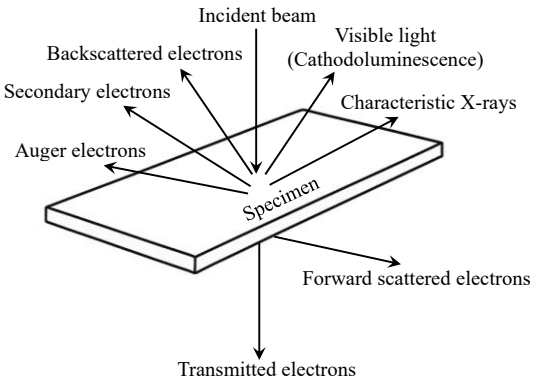

Figure 3-1 Schematic representation of the diverse interaction phenomena initiated when an electron beam interrogates a specimen.

chemical information is furnished by characteristic X-rays generated during electron-induced ionisation. The mechanism is sketched in Fig. 3-2. When a primary electron dislodges an electron from a core (K, L, M, N or O) subshell, a vacancy is left behind. Relaxation of an outer-shell electron into this vacancy liberates a photon whose energy equals the difference between the binding energies of the two levels, representing the minimum energy that must be transferred, referenced to the Fermi level [410].

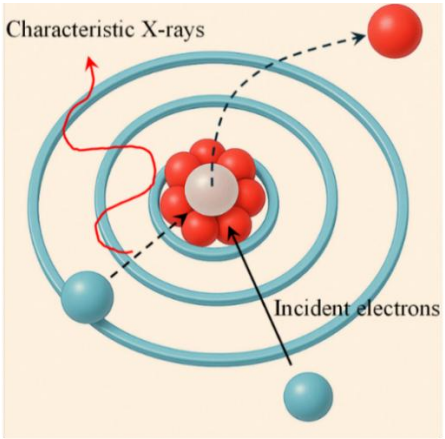

Figure 3-2 Schematic diagram illustrating the emission of characteristic X-rays.

The size of this energy gap is element-dependent and hence gives a characteristic spectroscopic fingerprint for compositional identification. Secondary electrons (SE2) are formed when loosely bound valence- or conduction-band electrons within the specimen are excited by the incident beam and are dislodged from the lattice. Their energy is low, normally less than 50 eV, and is such that much of this is retained within the first ≈50 nm of the surface upon reabsorption. Hence, just those SE2 which escape retain information related to the near-surface topography of the specimen [410].

3.1.2 Scanning electron microscopy

SEM derives microstructural and compositional insight from the spectrum of signals generated when the incident electron probe impinges upon the specimen [410,411]. Surface relief is visualised through the collection of low-energy secondary electrons, whereas crystallographic and atomic-number contrast is furnished by backscattered electrons [410,412]. Elemental composition is obtained by interrogating the characteristic X-ray emission spectrum [410,413].

A conventional SEM column comprises an ultra-high-vacuum chamber, an electron source, a suite of electromagnetic condenser and objective lenses, a motorised specimen stage and an array of signal detectors, including SE2, BSE, electron backscatter diffraction (EBSD) and energy-dispersive X-ray spectroscopy units [410–413]. The overall operating principle is outlined schematically in Fig. 3-3. Electrons emitted from either a thermionic or a field-emission cathode are accelerated towards the anode and subsequently converged into a finely focused beam by sequential magnetic lenses before being rastered across the specimen surface [408–413].

In a standard SEM, the BSE detector is mounted coaxially above the specimen, thereby maximising the solid angle for electron capture. SE2, which are low-energy carriers (< 50 eV) released from near-surface electronic states, are registered by a secondary electron detector. Because a significant fraction of SE2 is reabsorbed within the lattice, the detected yield is dominated by surface geometry: the escape probability scales with the tilt between the specimen normal and the incident probe. A larger tilt augments the collected signal, so local variations in orientation appear as brightness modulations that produce the familiar topographical contrast in SEM micrographs [410].

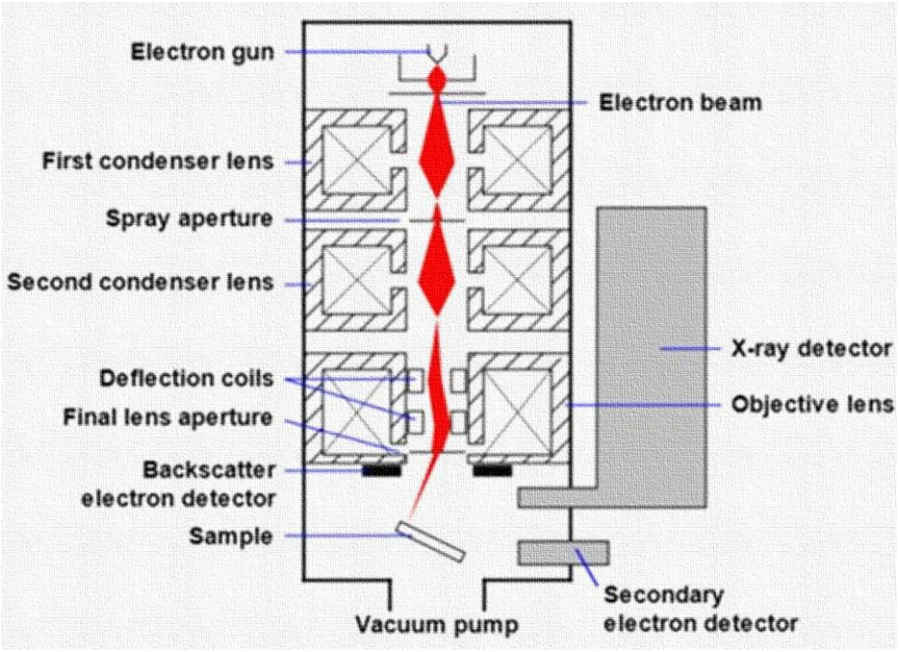

Figure 3-3 Schematic diagram of an SEM operating system [410,413].

EBSD augments scanning electron microscopy by enabling spatially resolved crystallographic analysis [410,414]. When the finely focused primary beam impinges upon a crystalline specimen, a subset of backscattered electrons escapes the surface at angles close to the Bragg condition. These electrons undergo diffraction within the lattice and generate Kikuchi bands that are recorded on a phosphor-coupled, high-sensitivity camera. The geometric arrangement of the bands embodies the local crystal orientation and permits unequivocal phase discrimination [410].

This study primarily employs five EBSD data products: inverse pole figure (IPF), pole figure (PF), image quality overlaid with grain boundaries (IQ + GBs), grain reference orientation deviation (GROD), and kernel average misorientation (KAM). IPF uses colour coding to represent per-pixel crystallographic orientation, links orientation to morphology, and reveals texture distributions. PF quantifies the strength and symmetry of preferred orientations in the sample reference frame and is used to describe the texture of the whole specimen and of orientation subgroups. IQ + GBs juxtaposes Kikuchi band clarity with an explicit grain boundary network, is sensitive to local defects and strain, and assists in identifying high and low angle boundaries, twin boundaries, and their connectivity. GROD maps the intragranular rotation field relative to a grain reference orientation, thereby characterising strain localisation and early signatures of recrystallisation. KAM measures the local orientation gradient through nearest-neighbour misorientation, provides a relative

indicator of dislocation density, and locates regions of stress concentration and substructure refinement. Together these maps constitute a multiscale information chain from orientation, texture, and interfacial networks through to dislocations and strain gradients, which enables quantitative reconstruction of microstructural evolution and elucidation of its intrinsic linkage to mechanical response.

3.1.3 Transmission electron microscopy

A TEM is composed of five principal subsystems: an ultra-high-vacuum column, a specimen holder, an electron source, a suite of electromagnetic lenses and a digital image-acquisition unit [409,410]. Functionally it parallels an optical microscope, substituting an electron beam for visible light and thereby achieving sub-angstrom resolution, making TEM the pre-eminent technique for elucidating atomic-scale structure in materials science.

Electrons originate at the gun, which may employ either thermionic or field-emission cathodes [409,410]. Accelerating potentials in the 100–1000 kV range impart sufficient energy for penetration of thin foils. After passage through the condenser assembly the probe is finely focused onto the specimen. For meaningful analysis the specimen must be electron-transparent, typically < 100 nm thick, although the critical thickness varies with both material density and the operating voltage: higher voltages enhance transmittance. Transmitted and forward scattered electrons provide the signal for image formation. Downstream of the specimen the objective lens produces the primary image, which is subsequently magnified by the intermediate lens set before being projected onto a fluorescent screen [409,410].

TEM provides complementary information from real space (imaging mode) and reciprocal space (diffraction mode) [409,410]. Fig. 3-4 illustrates schematically the electron trajectories in both modes. Two planes are key to its function: back focal plane, upon which the diffraction pattern occurs, and image plane, where amplified real-space image forms [409,410]. Placing apertures at the back focal plane selects certain diffracted beams, allowing for high-resolution phase contrast imaging (transmitted plus limited diffracted beams), bright-field image (transmitted beam alone) or dark-field image (sole diffracted beam). Image plane apertures demarcate unique regions for diffracting, leading to selected area electron diffraction (SAED) patterns, yielding information concerning lattice spacing, orientation, and symmetry [409,410].

Whereas TEM excels at structure characterisation, practical limitations are still in place. TEM preparation is a thickness-constrained time-consuming process; many oxides are chemically or mechanically damaged by conventional thinning methods [410]. Special preparation techniques are therefore required to preserve native chemistry and structure. Moreover, irradiation exposure for extended periods can cause beam-driven artefacts, necessitating dose control to preserve beam-sensitive phase integrity [410].

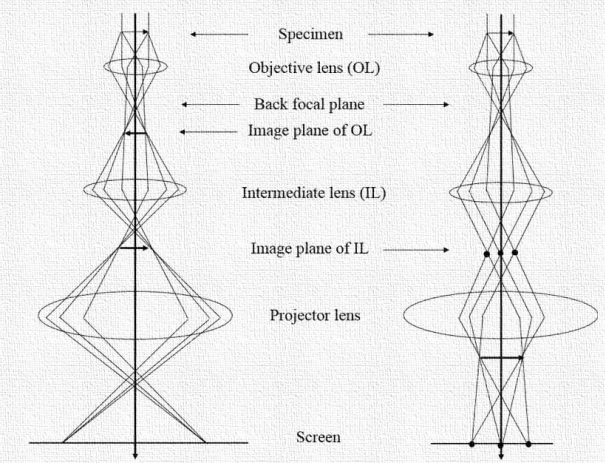

Figure 3-4 Electron trajectories in a TEM during imaging (left-hand panel) and diffraction (right-hand panel) modes [410].

3.1.4 Scanning transmission electron microscopy

A scanning transmission electron microscope (STEM) integrates the operational schemes of TEM and SEM [415]. Incorporation of aberration-correctors permits sub-angstrom investigation of elemental composition and electronic states, routinely resolving individual atoms [416]. STEM imaging employs a tightly converged probe rastered across a specimen thinned to conventional TEM dimensions, thereby ensuring electron transmission and ultimate lateral resolution [410]. A configurable detector suite enables the concurrent acquisition of complementary signals, so a single raster can provide an extensive data set. Whereas SEM customarily functions below 30 kV, STEM operates at 60–300 kV; the associated reduction in electron wavelength improves spatial resolution and allows direct imaging of atomic arrangements [410].

Fig. 3-5 outlines an aberration-corrected STEM column. Electrons emitted from the gun are accelerated and shaped by condenser optics, then focused by the objective lens into an Å-scale probe. Scan coils sweep this probe over the specimen, and an objective aperture

defines the maximum convergence angle. Downstream, an annular dark-field (ADF) detector intercepts the transmitted beam and records incoherently scattered electrons to produce dark-field contrast. Varying the detector's inner collection angle with post-specimen lenses heightens atomic-number sensitivity, yielding high-angle annular dark-field (HAADF) or 'Z-contrast' images whose intensity scales with the projected atomic number [410].

The pronounced Z-dependence of HAADF-STEM makes it the technique of choice for analysing crystal structures and nanoscale compositional variations in a wide spectrum of materials [410].

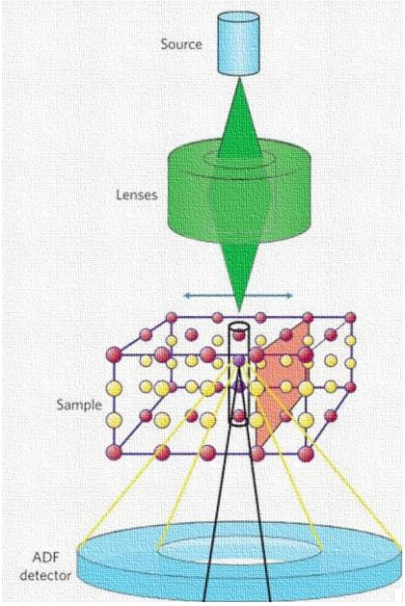

Figure 3-5 Schematic illustration of the fundamental operating principle of STEM [410,417].

3.1.5 X-ray energy-dispersive spectroscopy

X-ray energy-dispersive spectroscopy (EDXS) furnishes quantitative compositional analysis within both scanning and transmission electron microscopes. Because every characteristic X-ray possesses an energy uniquely associated with its parent element, a semiconductor detector can discriminate and register these photons. Incoming quanta are converted into voltage pulses whose amplitudes are proportional to photon energy; subsequent pulse counting yields an intensity–energy spectrum that may be rendered as a point analysis, a line profile or a two-dimensional compositional map. In the present work the mapping mode, implemented in STEM, was employed to visualise local chemistry with high spatial fidelity [410].

3.1.6 X-ray diffraction

X-ray diffraction (XRD) was employed to identify crystalline phases, evaluate preferred orientation (texture) and estimate dislocation densities. The technique is governed by Bragg diffraction, a specific manifestation of the broader Laue condition, illustrated schematically in Fig. 3-6. When the wavelength, λ, of the incident radiation is comparable with the interatomic spacing of a crystal, coherent scattering from successive lattice planes produces constructive interference at discrete angles θ that satisfy Bragg's law, $n\lambda = 2d\sin\theta$, where d is the interplanar spacing and n is an integer. Consequently, a material with a known crystal structure yields a characteristic diffraction pattern from which the phase assemblage can be inferred. Quantitative assessment of texture and the volume fraction of individual phases is achieved by comparing measured intensities with reference patterns in the Powder Diffraction File (PDF) database [409,410].

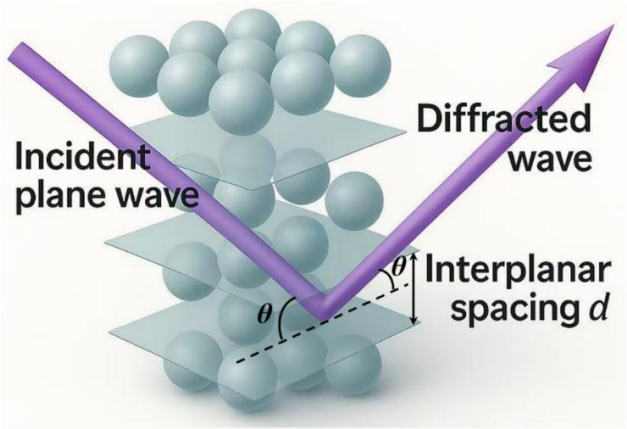

Figure 3-6 A schematic representation of Bragg diffraction.

3.2 Materials fabrication and processing

In the present thesis, Cu–Al alloys are employed as the model material. The alloys were fabricated via WAAM and subsequently subjected to cold rolling, annealing and RASP to obtain specimens for mechanical performance testing and microstructural characterisation. The ensuing section sets out the fabrication route and post-processing procedures in detail.

3.2.1 Design and fabrication of Cu–Al alloys

WAAM is used because it enables metre-scale builds, high deposition rates and precise in-situ composition control. Twin independent wire feeders allow continuous adjustment of the Cu-to-Al ratio during laydown, which is well suited to programmed single- and dual-

gradient structures. The process yields stable melt-pool conditions for high-thermal-conductivity metals, while current, voltage, travel speed and wire feed can be logged and held within tight tolerances. This transparency supports reproducibility and credible scale-up. The WAAM platform employed here integrates a GTAW torch, twin independent wire feeders, an auxiliary argon-shielding manifold and a pre-heating module, all synchronised by a programmable control console. The torch assembly is illustrated schematically in Fig. 3-7: discrete nozzles supply Cu and Al wires, inclined 30° to the substrate and offset by 60° from one another to stabilise the shared melt pool during simultaneous feeding. A 3.5 mm arc length was selected to generate a focused, high-energy plasma with adequate voltage and heat input. Beyond the intrinsic GTAW shield, an auxiliary argon curtain at 9 L min-1 trails the torch. It remains for about 60 s after the arc is turned off and prevents oxidation while the fresh layer cools [418,419].

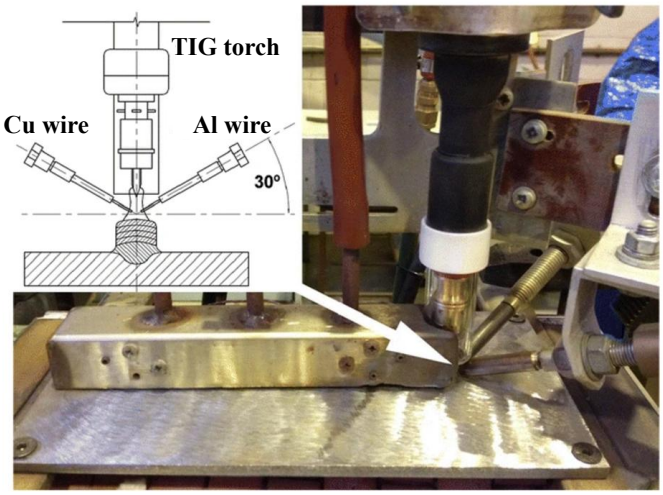

Figure 3-7 The WAAM system [418].

Two wire feeders deliver 0.9 mm-diameter high-purity Cu and Al wires into a shared weld pool. This enables in-situ alloying [418]. Each feeder has independent speed control to produce a continuous change in the Cu to Al ratio [418]. Thermal management is controlled at three levels. The preheating module brings the baseplate to a stable setpoint before deposition and maintains it during the build. The controller keeps the interpass temperature within a defined window by inserting a timed dwell while the argon curtain remains on. Power and motion channels are logged at high-frequency and held within tight tolerances, which keeps heat input per unit length consistent from layer to layer. Bead width and height are checked periodically, and the wire-feed ratio is adjusted in small steps when drift is

detected so that composition and geometry change in a controlled manner along the gradient. In this research, two distinct compositional gradients were produced. The first, designated the “forward compositional gradient (FCG)” sample, exhibited an Al content that increased along the build direction from 0 at.% in 5 at.% increments to 15 at.%, followed by a symmetric decrease in identical increments back to 0 at.%. The second, termed the “reverse compositional gradient (RCG)” sample, displayed the opposite trend: the Al fraction decreased from 15 at.% to 0 at.% and then increased symmetrically to 15 at.% along the build direction. The Cu–Al binary is used because Al content provides a strong lever on SFE. A through-thickness change in Al therefore creates a designed change in deformation mode. This is central to the goal of achieving a strength–ductility synergy in dual-gradient materials. Based on the Cu–Al binary phase diagram (Fig. 3-8) [420–422], the Al content was intentionally restricted to 0–15 at.% with a conservative upper bound of 16 at.% for phase stability and avoiding intermetallic formation. This range keeps the alloy in a single FCC phase across the relevant thermal cycle and suppresses brittle intermetallics that would undermine manufacturability and ductility. The approach is practical because high-purity Cu and Al wires are commercially available and can be alloyed in situ during deposition. Moreover, to eliminate substrate-induced influences on the deposited component and to minimise microstructural discrepancies between the uppermost and mid-build regions [418], four supplementary buffer layers were deposited at both the bottom and the top of each specimen. The composition of these buffer layers was dictated by the type of compositional gradient: in the FCG sample they contained 0 at.% Al, whereas in the RCG sample they contained 15 at.% Al. The processing parameters employed for fabricating the Cu–Al CGMs are summarised in Table 3-1, and the two gradient designs are illustrated schematically in Fig. 3-9.

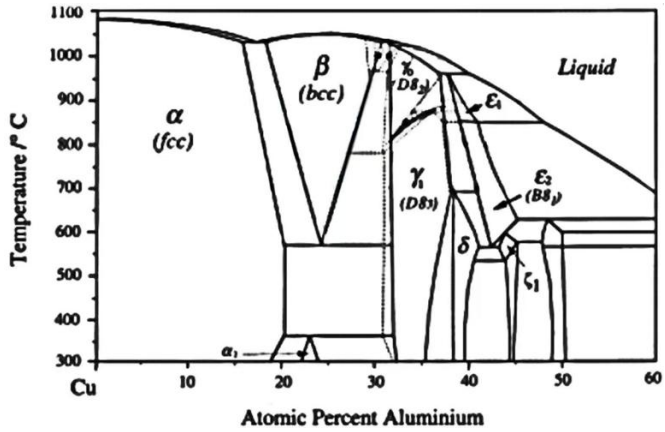

Figure 3-8 The Cu–Al binary diagram [420].

Table 3-1 Processing parameters for WAAM-fabricated Cu–Al CGMs in this study.

Nominally designed Al content (at%)	Current (A)	Travel Speed (mm/min)	Wire feed speed (mm/min)		Volume melting (mm^3/min)		Mass deposition rate (g/min)
			Cu	Al	Cu	Al	
0	160	95	1210	0	950	0	8.5
5	160	95	1130	103	887	66	8.1
10	160	95	1050	272	825	173	7.9
15	160	95	970	298	762	189	7.3

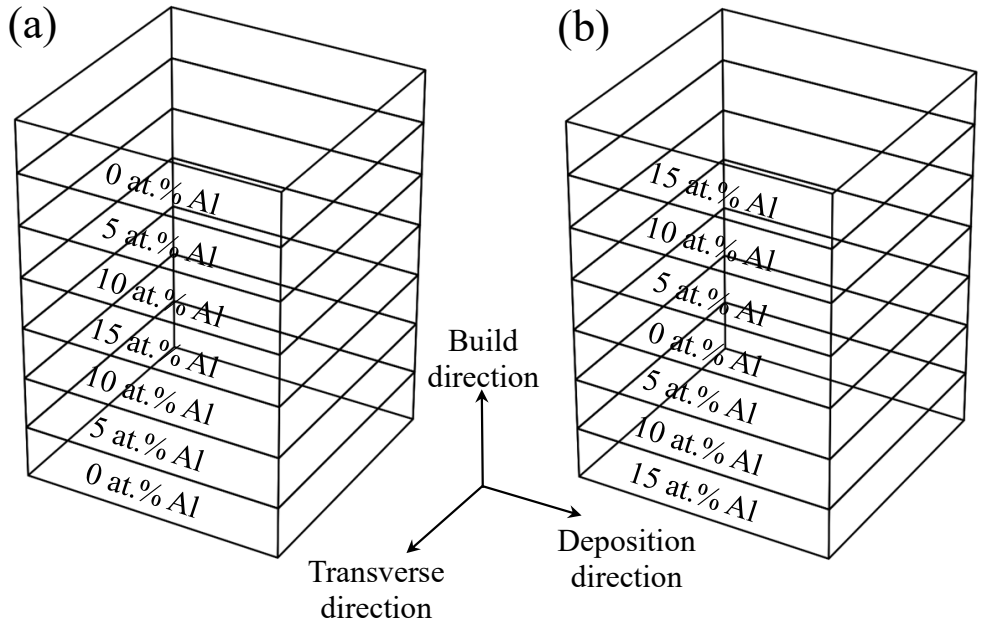

Figure 3-9 Schematic representation of the compositional gradient designs: (a) FCG; (b) RCG.

3.2.2 Cold rolling and annealing

The as-printed compositionally graded specimens were cold-rolled on a two-roller configuration fitted with rolls 100 mm in diameter. Rolling was conducted parallel to the deposition direction at a feed rate of 60 mm s^{-1}, with a total of seventeen passes. After each pass, the workpiece was allowed to cool fully to ambient temperature before the next pass, thereby eliminating temperature-induced artefacts that might otherwise detrimentally affect the alloy compositions and microstructures.

After cold rolling (CR), the samples were annealed under a range of temperature–time schedules. Annealing was performed at 300 ℃, 400 ℃ and 500 ℃ for holding periods of 30 min and 60 min, respectively. All samples were water-quenched immediately after annealing.

3.2.3 Rotationally accelerated shot peening

The operating principle and processing workflow of RASP have already been described in detail in Section 2.3.1.1. Prior to RASP, the upper and lower surfaces of the annealed samples were mechanically polished to achieve a flat, scratch-free surface while preserving the integrity of the compositional gradient. Polishing was performed on a TegraPol-25 machine (Struers, Netherlands) using a 1 μm diamond suspension, followed by chemo-mechanical polishing with a 0.05 μm colloidal silica suspension (OPS). Both surfaces of each graded sample were then subjected to RASP employing 0.5 mm ball diameter at a peening pressure of 200 KPa for 10 min.

Uniformity is ensured by process control. The toolpath uses a raster pattern with constant standoff and normal incidence. Track spacing yields a nominal 50% overlap, and successive passes reverse the scan direction to minimise bias. Head rotation speed and traverse feed are held constant. Air pressure is regulated at the nozzle and verified at the start and end of each run. Coverage is fixed at two passes per area.

3.3 Microscopy sample preparation

The following section provides a detailed account of the preparation of specimens for SEM and TEM.

3.3.1 Sample preparation for SEM

SEM specimens were prepared as follows.

(1) Sections were removed from the as-printed components, the as-rolled plates, as-annealed plates or the tensile-deformed samples using an Alumina (Al_2O_3) abrasive wheel mounted on an Accutom-50 precision diamond cutter (Struers, Netherlands).
(2) Depending on the subsequent characterisation route, the cutting samples were either mounted in epoxy resin or bonded to a sample holder with LOCTITE® 401 adhesive [410] to facilitate grinding and polishing.
(3) The exposed surface was ground on P1200 silicon-carbide (SiC) paper until a flat, uniform surface was obtained.
(4) Mechanical grinding is commonly assumed to disturb the material to a depth approximately three times the abrasive particle size. Given that P1200 SiC paper has an average grit size of ~15.3 μm [410], a further ~50 μm of material was removed with

P4000 SiC paper to eliminate the affected layer.

(5) Surface quality was checked under an optical microscope (OM) to confirm that scratches introduced by the P1200 paper had been completely eradicated.

(6) Mechanical polishing was carried out on a TegraPol-25 machine (Struers, Netherlands) using 3 μm and subsequently 1 μm diamond suspensions. Final chemo-mechanical polishing was performed for 5 min with a 0.05 μm OPS.

(7) The surface was re-examined by OM to ensure that all residual scratches had been removed.

(8) The polished surface was rinsed with distilled water followed by ethanol for 30 s.

(9) Any remaining liquid was removed with a rubber suction bulb to prevent possible corrosion or oxidation.

(10) Finally, the specimens were affixed to SEM stubs with conductive carbon tape and a thin layer of silver paint was applied to the underside to guarantee reliable electrical conductivity during examination.

3.3.2 Sample preparation for TEM

TEM requires electron-transparent foils, ideally < 100 nm thick, for high-resolution imaging. Because the compositionally graded specimens comprise multiple discrete layers and transitional zones, conventional electrolytic polishing would be both time-consuming and impractical, and the limited specimen size would hinder accurate localisation of the region of interest. Ion-beam thinning was therefore employed, using the following procedure:

(1) Rectangular pieces measuring 1.5 × 3 × 0.4 mm^3 were cut from the bulk using an Accutom-50 precision diamond saw (Struers, Netherlands) at a feeding rate of 0.03 mm s^{-1} and a rotation speed of 2000 r min^{-1}.

(2) The sections were ultrasonically cleaned in acetone and subsequently in ethanol to remove surface contaminants.

(3) A silicon wafer was scribed to the same dimensions as the tripod holder with a diamond scriber, then bonded to the holder with a high-strength adhesive and left for 30 min to cure. The tripod angle was adjusted and the wafer surface polished flat.

(4) The specimen was glued to the wafer, allowed to cure for 10 min, mounted in the tripod, and aligned so that its top surface was parallel to the polishing platen. Successively finer diamond lapping films (30 μm, 9 μm, 3 μm and 1 μm) with lubricant were used

until surface scratches were minimised.

(5) The polished sample was ultrasonically cleaned in acetone by a Branson 2510 Ultrasonic Cleaner, followed by a second ethanol rinse.

(6) The rear face of the specimen was bonded to a fresh silicon wafer with adhesive and left for 10 min to cure fully.

(7) With the tripod reset, the specimen was ground into a wedge, again using 30 μm → 9 μm → 3 μm → 1 μm diamond films. When part of the specimen edge disappeared, the sample was released with acetone and rinsed in ethanol. The thinnest edge of the wedge was < 1 μm.

(8) The wedge was affixed to a molybdenum support ring with epoxy resin and left for 30 min to harden.

(9) The mounted foil was placed in a model 695 Precision Ion Polishing System (PIPS II) (Fig. 3-10). Liquid nitrogen was fed to the cooling stage throughout to suppress ion-beam damage and contamination.

(10) Dual ion guns impinged on the specimen at ± 6° incidence with an accelerating voltage of 3 kV for 40 min.

(11) The incidence angle was reduced to ± 4° and the voltage to 1 kV for a further 20 min, yielding a flat electron-transparent area < 100 nm thick suitable for high-resolution TEM examination.

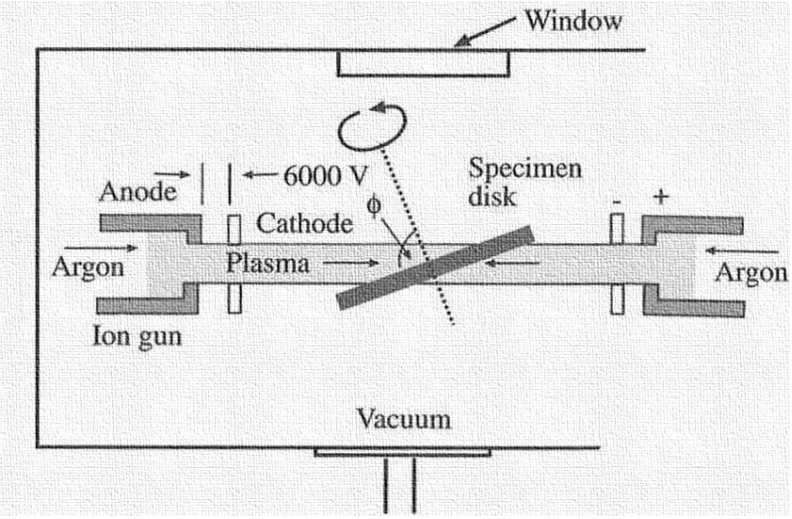

Figure 3-10 Schematic illustration of a precision ion-beam thinning system [410,423].

3.4 Mechanical testing

This section provides a detailed description of the mechanical property assessments and

the complementary image analysis technique employed in this study, namely Vickers hardness testing, uniaxial tensile testing and digital image correlation, together with the corresponding experimental parameters and settings.

3.4.1 Vickers hardness tests

Hardness expresses a material's ability to withstand localised plastic indentation [424,425]. Experimental determination entails driving an indenter into a polished surface and assessing the residual imprint. Four standard protocols exist, namely Brinell, Vickers, Rockwell and Knoop, but the Vickers test is generally preferred because its calculation does not depend on indenter size and the diamond pyramid is suitable for virtually all substances. Loads from 1 g to 1000 g are applied to the square-based diamond; once the load is removed, the mean diagonal length d of the impression is measured optically. The Vickers hardness number is then obtained from $HV = (1.854 * F)/d^2$, where F is the applied force in kilogram-force and d is expressed in millimetres. The complete procedure is illustrated schematically in Fig. 3-11.

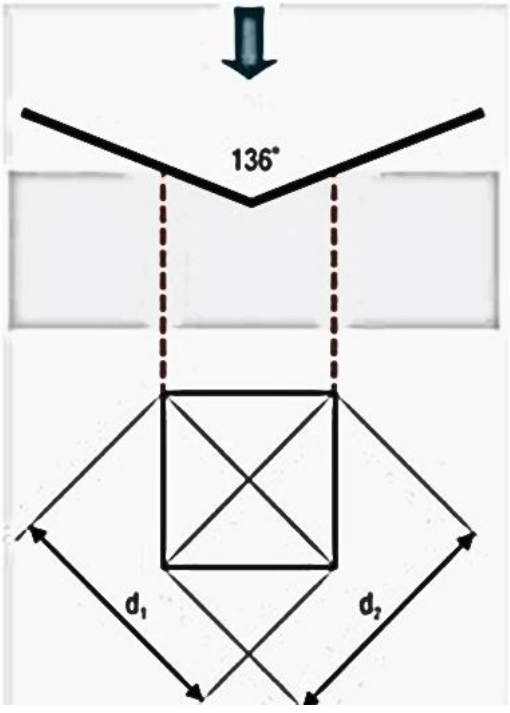

Figure 3-11 Schematic illustration of the Vickers hardness testing method [424].

In the present work, Vickers hardness profiles were obtained at 250 μm intervals along the build direction of the as-printed specimens, whereas for the post-printing specimens,

measurements were made at 25 μm intervals through the thickness. All tests were conducted on a Leco Vickers hardness tester (LV700AT) with a load of 0.1 kgf and a dwell time of 15 s. By adjusting the x- and y-stage coordinates, successive indents were placed diagonally through the section to maintain the prescribed spacing between adjacent impressions. Five identically spaced diagonal traverses were measured on each specimen to secure statistical robustness. Accordingly, the hardness at each height (as-printed) or depth (post-printing) was calculated as the mean of at least five indents made at that level. Error bars in the hardness profiles represent the standard deviation of all measurements at the corresponding height or depth.

3.4.2 Tensile tests

Engineering components routinely experience tensile, compressive, shear and torsional forces. When these loads are applied slowly and distributed uniformly across the section, a material's mechanical response is most evaluated by a uniaxial stress–strain experiment, with the tensile test serving as the benchmark. In this procedure a flat or round coupon machined into a dog-bone profile is gripped at each end and pulled under controlled displacement until fracture, the reduced waist ensuring that deformation and failure occur away from the grips. Fig. 3-12 defines the principal dimensions of the flat specimen: overall length L; gauge length G; gauge-section width W; reduced-section length A; grip length B; grip width C; fillet radius R; and thickness T.

Throughout the test, a load cell measures the axial force while an extensometer records elongation within the gauge. These signals are logged digitally as force versus extension. Dividing the instantaneous force by the original cross-sectional area and the extension by the gauge length converts the raw data to engineering stress and strain, respectively, from which a complete stress–strain curve is constructed. The curve provides the Young's modulus, yield strength, ultimate tensile strength and uniform elongation, parameters essential for assessing structural performance and for calibrating constitutive models.

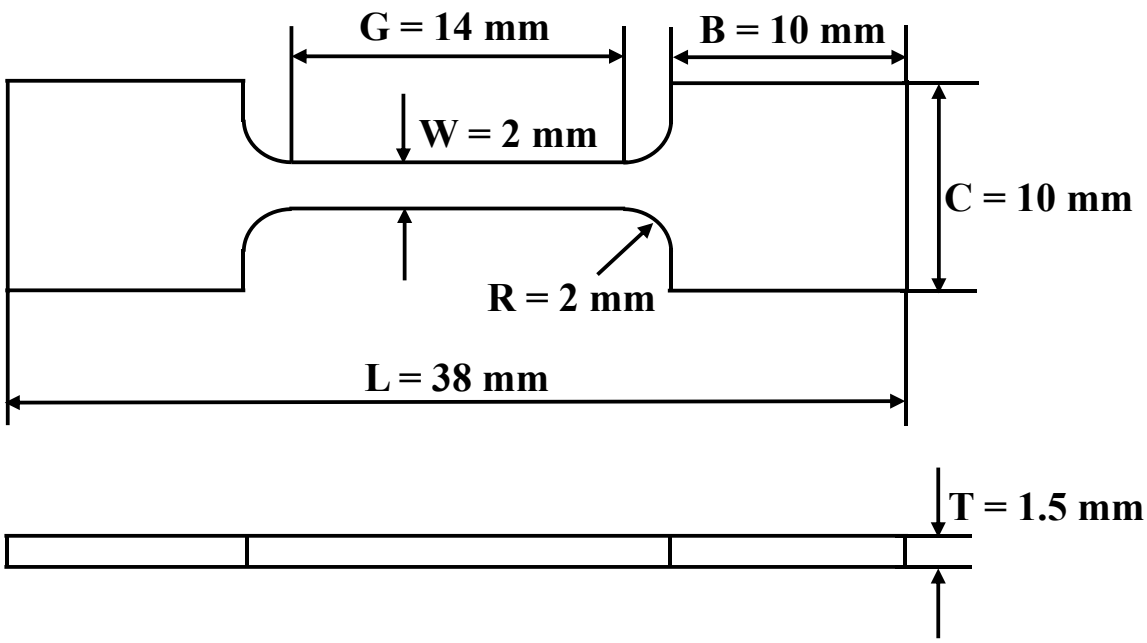

Figure 3-12 Schematic illustration of the rectangular tensile specimen.

Flat dog-bone specimens were machined with a gauge length of 14 mm, a width of 2 mm and a thickness of 1.5 mm. Quasi-static uniaxial tensile tests were carried out at room temperature on an MTS 810 universal testing machine equipped with a 100 kN load cell and a non-contact laser extensometer [410], using an initial strain rate of 5×10^{-4} s^{-1}. True stress values were calculated from the applied load and the instantaneous cross-sectional area at the specimen centre [410]. To guarantee the reproducibility of the stress–strain response, at least three specimens were tested for each post-printing treatment condition.

3.4.3 Digital image correlation technique

Digital image correlation (DIC) is a non-contact optical technique that provides full-field measurements of displacement and strain by tracking the motion of a random surface pattern between successive digital images. The method was pioneered in the early 1980s, when Peters, Ranson and co-workers demonstrated that grey-level correlation could be used to resolve in-plane displacements with sub-pixel accuracy [426,427]. At the heart of DIC lies the assumption of grey-level conservation: the grey value of a material point remains invariant during deformation provided that lighting and imaging conditions are unchanged. A region of interest (ROI) on the reference image is divided into small, square subsets. For each subset, the correlation algorithm seeks the subset in the deformed image that maximises a similarity metric, typically the zero-normalised cross-correlation or the

sum-of-squared differences. A least-squares optimiser refines the match to sub-pixel precision by fitting a shape function (usually an affine transformation) to describe the deformation of the subset [428]. DIC has become the de-facto optical extensometer for modern tensile experiments because it delivers full-field kinematic data while remaining entirely non-contact [429,430]. In a standard tensile test arrangement, the load frame supplies the force history, while one or two synchronised cameras image the speckled gauge section. The image sequence is then correlated in step with the force–time signal so that stress and strain share a common time-base [429]. For thin, flat coupons a single 2-D camera is usually sufficient [429,430].

In the thesis, during tensile testing, the strain distribution and its evolution on the specimen flank (length–thickness plane) of each graded structure were recorded in situ using a DIC system equipped with a short-focal-length optical lens. Prior to DIC imaging, a random speckle pattern was generated by spraying white paint onto a black background. A typical speckle image is presented in Fig. 3-13. A random black-on-white speckle pattern was air-brushed onto the 1.5 mm-thick gauge section of each coupon. The spatial resolution was 4.44 μm pixel^{-1}. The digital image correlation ROI encompassed 352 × 1060 pixel^{2}. Within this ROI the speckles exhibited an average equivalent diameter of 9.8 pixel and a median of 7.4 pixel, giving an effective speckle size distribution of 7–12 pixel. The mean intensity gradient reached 186, well above the accepted threshold of 20 for sub-pixel DIC, ensuring correlation coefficients in excess of 0.99 and a high signal-to-noise ratio [431].

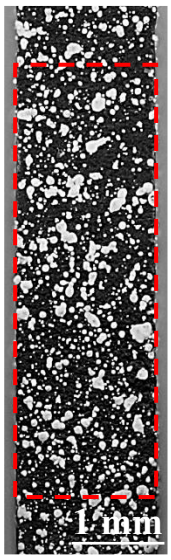

Figure 3-13 Typical speckle pattern. The red rectangle delineates the region selected for DIC analysis.

3.5 Finite element method simulations

The finite element method (FEM) is a numerical procedure for solving boundary-value problems that are expressed in terms of partial differential equations. The continuum domain is discretised into a mesh of finite elements, within which the unknown field variables (e.g. displacement) are approximated by interpolation (shape) functions. A weighted-residual (usually Galerkin) approach is employed to derive the weak form of the governing equations, transforming the continuous problem into a system of algebraic equations that is solved for the nodal values of the field variables [432,433].

Within solid mechanics the total potential energy (or its incremental counterpart) is minimised, ensuring equilibrium at the mesh nodes, compatibility inside each element and satisfaction of the natural boundary conditions. Material behaviour is introduced through a constitutive model that links stresses and strains. For metallic materials undergoing large plastic deformation, rate-dependent elasto-plastic laws such as Johnson–Cook are widely adopted [434]. Non-linearities arising from plasticity, contact and large strain kinematics are treated by incremental–iterative schemes (most commonly Newton–Raphson), and convergence is monitored via force or displacement norms [435].

In the present study, a three-dimensional finite element model was developed in Abaqus 6.14 to elucidate qualitatively the micromechanical mechanisms governing the CR and tensile deformation of the compositionally graded structure. Because graded and laminated architectures exhibit similar interfacial interactions arising from mechanical incompatibility during deformation [176,178,436,437], the graded structure was idealised as a multilayer symmetric model. The constitutive response of each layer was defined by the experimentally measured uniaxial true stress–strain curve. Plastic flow under complex stress states was simulated using an isotropic hardening model based on the von Mises yield criterion [436]. The mesh consisted of eight-node linear brick elements (C3D8) [436]. FEM models of the CR processes and the tensile tests are depicted in Fig. 3-14.

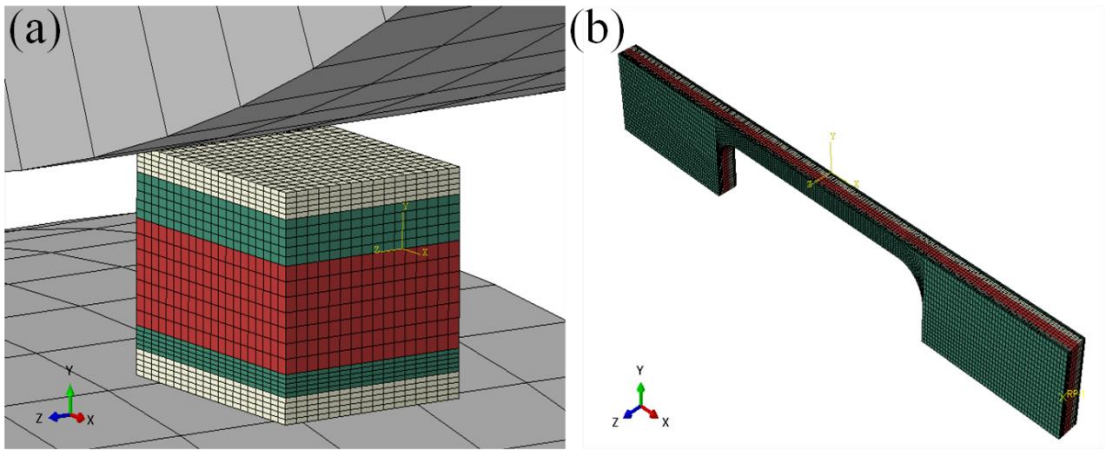

Figure 3-14 FEM models. (a) Samples for CR. (b) Samples for tensile tests.

3.6 Experimental apparatus and parameter settings

The experimental instrumentation and parameter settings employed in the present thesis are as follows.

The SEM characterisation was performed on a Zeiss Ultra+ field-emission SEM fitted with an EBSD detector [410]. EBSD maps were acquired at an accelerating voltage of 20 kV with a step size of 25 nm [410]. The data were processed and analysed using AZtecCrystal software.

Conventional TEM was undertaken on JEOL JEM-2100 and JEM-2200FS instruments, each operated at an accelerating voltage of 200 kV [410]. STEM was carried out on a double-aberration-corrected Titan Themis-Z fitted with ChemiSTEM (Super-X) energy-dispersive X-ray spectroscopy detectors and run at 300 kV [410]. High-angle annular dark-field (HAADF) images were acquired using a camera length of 115 mm [410]. Quantitative energy-dispersive X-ray spectroscopy in the Themis-Z employed a probe current of 200 pA, with acquisition times adjusted to accumulate in excess of 1×10^5 counts, thereby minimising statistical uncertainty in compositional maps [410].

Chapter 4. Microstructure and hardness of the as-printed materials

4.1 Introduction

In recent years, WAAM has attracted intense attention as a sustainable route for the fabrication of large and complex metallic components, owing to its high material utilisation, rapid deposition rate and virtually unconstrained build size [49,50]. Compared with powder based AM techniques, WAAM employs welding wire as the feedstock and dispenses with costly vacuum or inert gas chambers, thereby lowering equipment expenditure and enhancing production efficiency. It is thus suitable for the rapid manufacture of large-scale metallic structures required in the field of engineering [52].

CGMs enable a spatially continuous transition in composition and properties within a single component, thereby providing new design freedom for service under multi-field coupling environments [159]. In the present study, an additional motivation for adopting CGMs is to address the classical strength–ductility trade-off: by judiciously tailoring continuous compositional and attendant microstructural gradients, we promote heterogeneous deformation and enhanced strain hardening across the section, delivering a concurrent increase in strength and tensile ductility. WAAM, with its intrinsic capability for on-line wire switching and real-time adjustment of processing parameters, offers a practical technological route for the rapid and precise fabrication of large-scale metallic compositional gradients [49]. Recent studies on Ti–TiB [438], Al–Li [439] and Cu–Ni [440] gradient deposits produced in unidirectionally increasing or decreasing modes have yielded preliminary insights into the spatial evolution of microstructure and mechanical properties. Nevertheless, it remains unclear whether the gradient sequence itself (incremental versus decremental) triggers distinct grain morphology evolution and crystallographic orientation selection, or whether there exists a causal relationship between gradient sequence and asymmetry in hardness distribution. Systematic and directly comparable investigations are presently lacking. Most published work regards gradient direction as a single variable and does not undertake parallel contrasts between forward and reverse designs, thereby hindering fundamental understanding of the synergistic effects between thermal history and compositional gradient [441].

Building upon the scientific questions and knowledge gaps identified above, this chapter

employs WAAM to design and fabricate two gradient specimens exhibiting symmetrical compositional variations: (i) FCG specimens, in which the Al content rises from 0 at.% to 15 at.% along the build direction and then symmetrically falls back to 0 at.%; and (ii) RCG specimens, whose compositional trajectory is the mirror opposite of the FCG samples. Using a suite of multiscale characterisation techniques, including optical microscopy, EDS, EBSD with orientation mapping, XRD and Vickers hardness testing, this study systematically compares the grain morphology, orientation evolution and hardness distribution asymmetry produced by the two gradient sequences. The intrinsic mechanisms whereby the superimposed thermal history and the direction of the compositional gradient couple to dictate the microstructure–property relationship are elucidated. The resulting insights furnish a scientific basis for optimising the design of WAAM-fabricated gradient structures and for tailoring their properties across length scales, while also establishing a critical experimental baseline for the ensuing chapters on synergistic gradient strengthening.

4.2 Results and discussion

In this chapter, the macroscopic geometrical morphology of the two types of gradient samples is first subjected to quantitative assessment to verify the morphological stability of the deposition process (Section 4.2.1). Cross-sectional EDS scans are then employed to obtain the compositional profile along the build direction, thereby validating the fidelity of the imposed gradient design (Section 4.2.2). Building on this foundation, EBSD is used to compare the interlayer microstructural evolution of the FCG and RCG specimens (Section 4.2.3), while orientation pole figures elucidate the spatial variation in crystallographic orientation (Section 4.2.4). Finally, the distribution of Vickers hardness with deposition height (Section 4.2.5) is analysed to reveal how the coupling of thermal cycling and compositional gradient influences the hardness gradient and heterogeneity, thereby providing experimental evidence for constructing the gradient design–performance relationship.

4.2.1 Macroscopic geometry of as-printed samples

Both the FCG and RCG samples comprise twelve superimposed clad layers and display the characteristic “string-of-pearls” morphology, as shown in Fig. 4-1(a,b). The interfaces between adjacent layers are smooth and fully metallurgically bonded, indicating a stable

arc and favourable wetting during deposition. No macroscopic porosity, lack-of-fusion defects, or through-thickness cracks are detected. Notwithstanding these shared features, the two builds exhibit pronounced differences in their overall geometry.

The principal geometric attributes of an individual clad layer are briefly outlined. Fig. 4-1(c) depicts a schematic of a single bead, where *H* denotes the bead height, i.e. the layer thickness measured along the build direction (BD) [442]. This parameter governs the interlayer increment programme and influences the evolution of the thermal profile during fabrication [442,443]. *W* represents the bead width, defined as the maximum transverse dimension along the transverse direction (TD) [443]. In practice, this width is typically determined from macro-sectional micrographs [444].

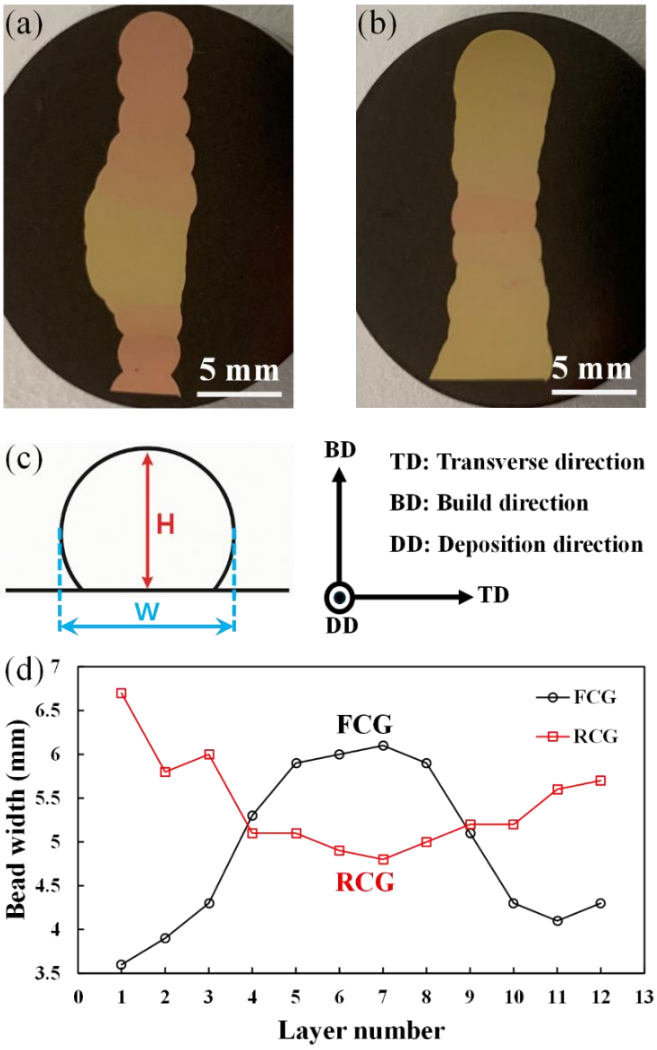

Figure 4-1 (a) Macroscopic cross-section of the FCG sample. (b) Macroscopic cross-section of the RCG sample. (c) Schematic of a hemispherical wire-arc bead. (d) Layer-resolved bead width evolution for the two samples.

Fig. 4-1(d) discloses the overall trajectory of the bead width–deposition height relationship and highlights the disparities between the gradient samples, which is indispensable for evaluating build stability and geometric precision. It reveals that the FCG sample exhibits a characteristic “S-shaped” geometric profile. The bead width increases sharply from the first to the sixth layer, attaining a maximum at the seventh layer, approximately 70% wider than the first, and this lateral spreading is accompanied by a reduction in bead height, meaning the bead becomes thinner. Thereafter, as the deposition height increases, the bead width progressively diminishes, and by the topmost layer it has contracted by about 30% relative to its peak value, with a concomitant increase in bead height, meaning the bead thickens.

In contrast, the RCG sample displays a pronounced “hourglass-shaped” profile: the beads are comparatively wide at both the base and apex, whereas a conspicuous constriction appears in the central region (layers 6–8). The narrowest layer, layer 7, is 28 % and 16 % narrower than the lowest and uppermost layers, respectively.

A further noteworthy feature is that although the basal and cap layers in each sample share the same nominal composition (Cu-rich for the FCG sample, Al-rich for the RCG sample), their bead widths differ appreciably. In the FCG sample, the topmost bead is roughly 19 % wider than the bottommost bead, whereas the RCG sample exhibits the opposite trend, the uppermost bead being about 15 % narrower than its counterpart at the base. The measured bead widths for each layer in both compositional gradient samples are summarised in Table 4-1. The underlying mechanisms responsible for these contrasting phenomena are elucidated in detail in the following section.

Table 4-1 Layer-resolved bead width (mm) of FCG and RCG samples.

Sample type \ Layer	1	2	3	4	5	6	7	8	9	10	11	12
FCG	3.6	3.9	4.3	5.3	5.9	6.0	6.1	5.9	5.1	4.3	4.1	4.3
RCG	6.7	5.8	6	5.1	5.1	4.9	4.8	5.0	5.2	5.2	5.6	5.7

A comparison of the two samples reveals a common characteristic: in each build, the Cu-rich clad tracks are invariably narrower than their Al-rich counterparts, irrespective of layer

position. This behaviour is attributed to intrinsic differences in the thermophysical properties of Al-enriched and Cu-enriched melts, which govern the redistribution of supplementary heat within the melt pool and, consequently, the extent of lateral spread of the liquid metal, which is manifested as the bead width *W*. The critical property differentials and their quantitative effects are analysed below.

Heat flow controlled melt pool size. In WAAM the arc may be idealised as a moving heat source. Adopting Rosenthal's steady-state solution for a three-dimensional point source, the instantaneous surface temperature distribution is [445,446]:

$$T(r) = T_0 + \frac{\eta Q}{2\pi k r} \tag{4.1}$$

where T_0 is the pre-deposition workpiece (ambient) temperature, η is the thermal efficiency, Q is the total arc power and k is the material thermal conductivity. The radial distance $r = \sqrt{y^2 + z^2}$ is the three-dimensional polar coordinate measuring the separation between the heat source and the observation point. The melt pool boundary occurs where the temperature attains the liquidus, T_L, taking $r = y_m$ (surface) therefore yields [445,446]:

$$y_m = \frac{\eta Q}{2\pi k (T_L - T_0)} \tag{4.2}$$

Given that the bead width $W \approx 2\ y_m$, expression (4.2) therefore predicts the following dependence of W on the thermal conductivity:

$$W \propto k^{-1/2} \tag{4.3}$$

Eq. (4.3) represents only a point source approximation. If the heat input is modelled instead by a Gaussian or Goldak double ellipsoidal distribution, the negative correlation between bead width W and thermal conductivity k is preserved, i.e. $W \propto k^{-1}$ or $W \propto k^{-1/2}$ [446]. Shah et al. [447] recently reported that, during WAAM of Cu alloys, high thermal conductivity promotes rapid heat dissipation. Macroscopically, this manifests as a reduced bead width and an elevated cooling rate, consistent with the inverse relationship predicted by Eq. (4.3). In summary, higher thermal conductivity accelerates heat dissipation, suppressing the lateral temperature rise in the melt pool under a constant heat input and thereby narrowing the deposited bead.

In metallic systems the bulk of conduction electrons originate from the near-Fermi-level

s/*p* bands, which may be treated as quasi-free. Electron–lattice interactions are described by the average free path l or the relaxation time τ. By Matthiessen's rule, the reciprocal addition of the individual scattering rates yields the total resistivity [448,449]:

$$\rho(T, C) = \rho_{ph}(T) + \rho_{imp}(C) + \rho_{s-d}(T, C) + \rho_{str} \tag{4.4}$$

where ρ_{ph} is phonon scattering, which increases with temperature; ρ_{imp} means scattering from impurity potentials, linearly proportional to solute concentration; ρ_{s-d} denotes additional scattering arising from *s*–*d* electron interactions [450]; and ρ_{str} represents scattering associated with structural defects such as dislocations and grain boundaries (negligible in the liquid state) [451]. In liquid Cu–Al between 1100 and 1500 °C, ρ_{ph} is essentially saturated, while ρ_{str} can be negligible. Hence the solute dependence is dominated by impurity scattering and *s*–*d* interactions. Introducing Al atoms into liquid Cu increases both mechanisms owing to disparities in valence electron count and atomic radius, thereby shortening the mean free path l and raising the macroscopic resistivity ρ [452].

Within the 5–15 at.% Al range, the resistivity of liquid Cu–Al alloys is experimentally observed to increase approximately linearly with Al content and may be expressed as:

$$\rho(C_{Al}, T) = \rho_0(T) + C \cdot C_{Al} \tag{4.5}$$

where $\rho_0(T)$ is the intrinsic resistivity of pure Cu at the constant temperature, C_{Al} is the atomic fraction of Al, and C is a constant. Near 1400 K the measured value is $C \approx (3–4) \times 10^{-8}$ Ω · m · at.%$^{-1}$ [452,453]. Physically, C quantifies the contribution of Al solute atoms to the electron scattering cross-section and depends on the pseudopotential difference between Cu and Al, the electron density, and the temperature [454].

According to the Wiedemann–Franz law, deviations of the Lorenz number (L) for liquid metals and their alloys from the classical value $L_0 = 2.44 \times 10^{-8}$ W · Ω · K^{-2} are only 3–5 % at high temperatures and may therefore be neglected [450]. Treating L as constant yields:

$$k(C_{Al}) = \frac{LT}{\rho(C_{Al})} \Longrightarrow k(C_{Al}) \propto \frac{1}{\rho(C_{Al})} \tag{4.6}$$

That is, a linear increase in resistivity ρ with Al content C_{Al} produces a correspondingly linear decrease in thermal conductivity k. Experimental data reported by Sun et al. [455] at

1380–1430 K, combined with the Wiedemann–Franz calculations of Thakore et al. [456], provide the resistivities and thermal conductivities for Cu–Al alloys listed in Table 4-2, which shows that each additional 1 at.% Al raises ρ by approximately (0.6–0.8) × 10^{-8} Ω · m and lowers k by roughly 8–10 W · m^{-1} · K^{-1}. At 15 at.% Al, the liquid thermal conductivity falls to about one quarter of that of pure Cu [455,456].

Consequently, in the single-phase Cu–Al binary alloy system an increase in Al content diminishes the thermal conductivity, thereby promoting a larger bead width. This intrinsic effect underlies the observation that, under identical processing conditions, Cu–Al alloys yield wider and flatter clad tracks than pure Cu.

Table 4-2 Resistivities and thermal conductivities for Cu–Al alloys with different Al content [455,456].

Al content (at.%)	ρ / 10^{-8} Ω · m	k / W · m^{-1} · K^{-1}
0	6.8	315
5	9.0	200
10	11.8	135
15	15.0	80

Marangoni spreading effect. The lateral motion of liquid within the melt pool is governed by the Marangoni number (*Ma*), which quantifies the competition between convection driven by surface tension gradients and diffusive (thermal or mass) transport. Spatial variations in surface tension with temperature or solute concentration generate tangential stresses at the free surface, thereby inducing thermocapillary (or solutocapillary) convection. The magnitude of *Ma* determines whether this convection can overcome viscous damping and diffusive smoothing to dominate the flow field [457–459].

During WAAM deposition of Cu–Al gradient samples, experimental measurements show that Cu-rich (Al-lean) layers are markedly narrower than Al-rich layers. This geometric disparity can be rationalised quantitatively in terms of the direction and intensity of thermo-solutal Marangoni convection. The tangential stress acting on the melt pool surface arises from coupled temperature and compositional gradients, and the combined driving force can be written as [458–460]:

$$Ma_{tot} = Ma_T + Ma_C = \frac{L}{\mu}\left(\frac{\partial\sigma}{\partial T}\frac{\Delta T}{\alpha} + \frac{\partial\sigma}{\partial C_{Al}}\frac{\Delta C_{Al}}{D}\right) \tag{4.7}$$

where, Ma_T and Ma_C are the thermal and solutal Marangoni numbers, respectively, L is characteristic horizontal length scale of the melt pool, μ is dynamic viscosity, α is thermal diffusivity, D is mass diffusivity of Al in liquid Cu–Al alloys, $\partial\sigma/\partial T$ is temperature coefficient of surface tension, $\partial\sigma/\partial C_{Al}$ is compositional coefficient of surface tension, ΔT is interfacial temperature difference, ΔC_{Al} is interfacial Al concentration difference.

To facilitate the discussion, the deposition modes of the FCG and RCG samples are idealised as two cases: (i) deposition of a Cu-rich layer upon an underlying Al-rich layer, and (ii) deposition of an Al-rich layer upon a Cu-rich layer. The former scenario is considered first. When a Cu-rich droplet spreads over the surface of an Al-richer melt, splatting occurs such that the droplet centre, which contacts the substrate melt last, preserves its original composition, whereas the rim touches the Al-rich liquid first and is rapidly diluted. This instantaneous compositional partition evolves during the WAAM dwell into a steady radial gradient in which the Al concentration is lowest at the centre and highest at the periphery, i.e. $\partial C_{Al}/\partial r > 0$, where C_{Al} denotes the Al content and r is the radial coordinate measured from the geometrical centre of the droplet ($r = 0$) to its rim ($r = R$).

The intrinsic surface tension of Al is markedly lower than that of Cu: in the range 1350–1400 K, $\sigma_{Cu} \approx 1.30$ N · m^{-1} [460], whereas $\sigma_{Al} \approx 0.90$ N · m^{-1} [461]. Increasing the Al content therefore decreases the droplet surface tension, giving $\partial\sigma/\partial C_{Al} < 0$, where σ is the surface tension of the liquid Cu–Al alloys [460]. Experimental data by Schmitz et al. [460] indicate $\partial\sigma/\partial C_{Al} \approx -(1.0–2.0) \times 10^{-2}$ N · m^{-1} · (at.%)$^{-1}$, the negative sign remaining essentially invariant between 1300 and 1500 K, thereby corroborating this deduction. By definition, the surface shear stress is [460]:

$$\tau_M = \frac{\partial\sigma}{\partial r} = \frac{\partial\sigma}{\partial C_{Al}}\frac{\partial C_{Al}}{\partial r} < 0 \tag{4.8}$$

This means τ_M acts in the negative r direction (from rim towards centre), thereby inducing an inward surface flow that drags the molten film centripetally.

To couple surface tension with the Al concentration and to quantify the attendant driving force, the solutal Marangoni number (Ma_C) is subsequently evaluated in accordance with Eq. (4.7). Using the measurements of Schmitz et al. [460] ($|\partial\sigma/\partial C_{Al}| = 1.5 \times 10^{-2}$ N · m^{-1} · (at.%)$^{-1}$), the gradient adopted in the present design ($\Delta C_{Al} = 5$ at.%). The characteristic length L is conventionally defined as the horizontal radius of the melt pool and is

commonly approximated as one-half of the observed bead width, i.e., $L \approx W/2$. Examination of Table 4-1 reveals that, for both FCG and RCG samples, deposition of a Cu-rich layer upon an Al-rich substrate produces bead widths of 4–6 mm. The corresponding L therefore falls in the range 2–3 mm. In the present analysis, L = 2.5 mm is adopted. The dynamic viscosity is taken as μ = 4 mPa · s [462], and the solutal diffusivity as $D = 1 \times 10^{-8}$ m^2 · s^{-1} [463,464]. Based on the foregoing data, the solutal Marangoni number is calculated as $Ma_C \approx 4.7 \times 10^6$. This value exceeds the classical critical Marangoni number, $Ma_{cr} \approx 10^2$ [465,466], by more than four orders of magnitude. Above this threshold, surface tension gradients overcome viscous damping and thermo-mass diffusion, instigating interfacial convection. For a clean, non-volatile liquid layer driven solely thermally, linear stability analyses and canonical experiments give $Ma_{cr} \approx$ 79–83. Inclusion of solutal or dual driving and surface deformation effects raises the limit slightly, so $Ma_{cr} \approx 10^2$ is widely adopted for engineering assessments [465,466]. The extraordinarily large Ma_C obtained here therefore indicates that the solutal surface tension gradient overwhelmingly dominates viscous–diffusive damping, generating turbulent-level centripetal thermocapillary flow. Under such conditions, large vortices fragment into multiscale eddies, velocity gradients steepen, and the efficiencies of heat and mass transfer increase by at least an order of magnitude [467].

Having examined the solutal Marangoni number, the second key parameter is the thermal Marangoni number (Ma_T). For all molten metals $\partial\sigma/\partial T$ is negative (≈ −0.10 to −0.30 mN · m^{-1} · K^{-1}); a value of −0.20 mN · m^{-1} · K^{-1} is adopted here [460,461]. This sign implies that, from the droplet centre to its rim, the decreasing temperature raises the surface tension, producing a gradient opposite in direction to that generated by solute. Hence, when a Cu-rich layer is deposited upon an Al-rich layer, the thermally driven Marangoni effect counteracts the solutally driven one [458].

Under typical WAAM arc parameters the power density follows a Gaussian distribution, and the arc centre temperature (T_c) exceeds the edge temperature (T_e) by 150–350 K [468]; ΔT = 250 K is therefore assumed. Taking $\alpha = 3.2 \times 10^{-5}$ · m^2 · s^{-1} [469], L = 2.5 mm, μ = 4 mPa · s and ΔT = 250 K yields $Ma_T \approx 9.8 \times 10^2$. With $Ma_T \approx 10^3$ vastly smaller than the solutal Marangoni number ($Ma_C \approx 10^6$), the solutally driven thermocapillary flow overwhelmingly dominates when depositing a Cu-rich layer onto an Al-rich one, and the opposing thermal contribution can be safely neglected [457,465,466].

In summary, when a Cu-rich layer is deposited upon an underlying Al-rich layer, the solutally driven Marangoni effect dominates, outweighing the thermally driven counterpart by roughly three orders of magnitude [457]. The resulting surface tension gradient generates a centripetal surface flow that draws the rim liquid towards the droplet centre [458]. Mass conservation then forces the converging stream to plunge downward at $r \rightarrow 0$, entraining the underlying melt and deepening the pool [460]. The displaced liquid returns radially outwards along the pool base and climbs the solid–liquid interface to close a characteristic twin-vortex toroidal circulation [458,470]. Such inward surface flow curtails lateral replenishment, suppressing pool width and, hence producing a narrow bead [458,459]. Simultaneously, the circulation elevates the central temperature and lowers the viscosity, further intensifying the downward jet and deepening the pool, so that the deposited bead appears taller [470].

In the reciprocal configuration, where an Al-rich layer is deposited upon a Cu-rich substrate, the droplet centre contains more Al than its periphery and therefore exhibits a solutal Marangoni effect opposite to that operating when a Cu-rich layer is laid over an Al-rich one. Because the temperature derivative of surface tension is negative for all metallic melts, the thermally driven Marangoni component acts in the same direction as before. In this case, however, the solutal and thermal contributions act synergistically, producing an outward (centrifugal) surface flow from the centre towards the rim [458,470]. This flow promotes lateral spreading of the droplet and increases the bead width. Momentum dissipation at the rim causes the surface liquid to descend, forming a pair of closed toroidal vortices that reduce the melt pool depth [470,471]. Hence, the Al-rich layer adopts a "shallow-and-wide" clad geometry, in stark contrast to the "narrow-and-deep" morphology characteristic of the Cu-rich layer [459,471]. A schematic of the overall Marangoni effects for the two deposition modes is provided in Fig. 4-2.

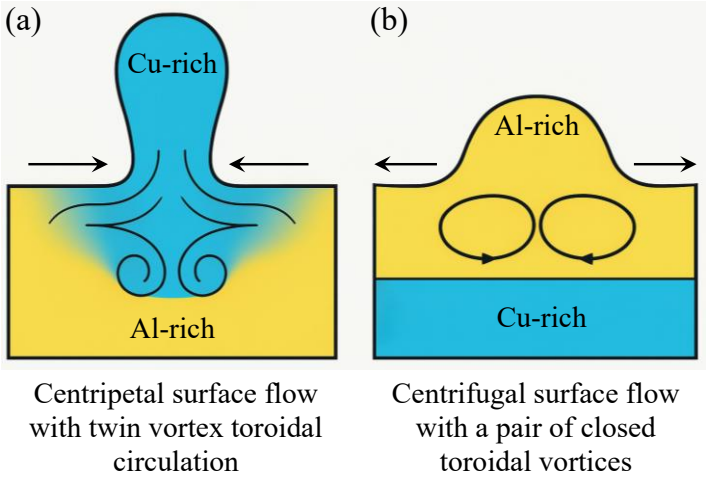

Figure 4-2 Schematic illustration of Marangoni-driven convection during dissimilar layer deposition in WAAM. (a) Deposition of a Cu-rich layer upon an Al-rich substrate. (b) Deposition of an Al-rich layer upon a Cu-rich substrate.

Influence of liquidus temperature, latent heat and melt pool superheat. The liquidus temperature of Cu-rich alloys is roughly 50 °C higher than that of Al-rich counterparts [472]. Under an identical arc temperature, therefore, a Cu-rich melt pool possesses a lower superheat, a shorter lifetime and a more restricted lateral spread. Another parameter governing pool geometry is the latent heat of fusion (L_f), defined as the energy absorbed per unit mass as a metallic material transforms from solid to liquid at its melting point [473,474]. Multiplication by the liquid density, ρ_{liq}, gives the volumetric energy required to generate the liquid phase, $q_v = \rho_{liq} \cdot L_f$. Although the latent heat of fusion of an Al-rich alloy exceeds that of a Cu-rich alloy, the difference in alloy density renders the two q_v values comparable [473,474]. Consequently, the higher liquidus temperature (≈ 1085 °C for Cu-rich versus ≈ 1042 °C for Al-rich compositions) constitutes the principal thermodynamic constraint dictating melt pool superheat and, ultimately, the final bead dimensions [471,472].

In WAAM, the markedly narrower bead width of Cu-rich tracks relative to their Al-rich counterparts arises from the synergistic action of three thermophysical factors. First, the higher thermal conductivity of Cu-rich melts accelerates lateral heat dissipation, curtailing the transient superheat and thereby limiting the radial spread of liquid metal. Second, the coupled thermo-solutal Marangoni flow imposed on Cu-rich droplets is dominated by an inward-directed, solutally driven surface current that draws rim liquid towards the centre; mass conservation forces this flow to plunge beneath the surface and close a twin-vortex

circulation, further constraining the pool's lateral dimensions. Third, the higher liquidus temperature of Cu-rich alloys (≈ 1085 °C versus ≈ 1042 °C for Al-rich alloys [472]) reduces the pool superheat under identical arc conditions, shortening its lifetime and impeding horizontal expansion. Collectively, these factors suppress bead widening in Cu-rich layers, yielding a "narrow-and-deep" clad geometry in stark contrast to the "shallow-and-wide" morphology characteristic of Al-rich deposits.

Examination of the bead width data in Table 4-1 shows that, in the FCG sample, both the bottom and top layers are Cu-rich, yet the top layer displays a markedly greater bead width despite their identical composition. Conversely, in the RCG sample, both extremities are Al-rich, but the top layer is appreciably narrower than the base layer. This antithetical behaviour can be explained by the intrinsic thermophysical disparities between Cu-rich and Al-rich melts and by their respective positions within the multilayer heat flow path.

Cu-rich layers exhibit a markedly higher thermal conductivity and a higher liquidus temperature than their Al-rich counterparts. When a Cu-rich layer is deposited directly on the highly conductive substrate at the start of the FCG build, the steep vertical heat gradient and rapid lateral conduction into both the substrate and the adjacent Cu-rich melt accelerate solidification, curtail the lifetime of the liquid melt pool, consequently, restrict lateral wetting [455,472]. The resulting track is therefore comparatively narrow (3.6 mm). In contrast, the terminal Cu-rich layer at the top of the same FCG deposit is underlain by multiple Al-rich strata of lower thermal conductivity. These intervening layers impede downward heat flux and, together with the elevated inter-pass temperature that typifies the upper part of a WAAM stack, establish a quasi-steady thermal plateau [475]. Under these conditions the Cu-rich melt cools more slowly, retains fluidity for longer and achieves a greater equilibrium spreading width [475,476], allowing W to grow to 4.3 mm.

The converse situation arises in the RCG sample. The basal Al-rich layer, although in direct contact with the cold substrate, is inherently insulated by its low thermal conductivity [455]. Its low liquidus temperature further prolongs melt superheat [472]. The melt therefore enjoys a longer residence time before solidification, permitting extensive lateral flow and a wide bead footprint. So, the melt attains a width of 6.7 mm, the broadest in either sample. At the opposite end of the build, the terminal Al-rich layer is supported by a column of Cu-rich material with high thermal conductivity [455]. This underlying heat sink removes enthalpy more efficiently than the Al-rich melt can conduct it away, and any

further rise in the mean stack temperature has already saturated by this stage of deposition [475]. The melt therefore solidifies rapidly, yielding a narrower track (5.7 mm) [476].

In summary, under the two gradient strategies the opposing variation in bead width between the basal and uppermost layers stems from: (i) the opposing thermal conductivities and liquidus temperatures of Cu-rich and Al-rich alloys, and (ii) the evolving vertical heat extraction path within the deposit, which sequentially places each alloy either in thermal contact with the substrate (dominant conduction) or atop a thermally resistive or conductive column (modified heat accumulation).

4.2.2 Compositional distribution along the build direction

A visual inspection of the macrographs (Fig. 4-1(a,b)) reveals pronounced layer-by-layer colour banding that directly reflects the intended Al gradient. The chromatic scale produced by chemical polishing is monotonic: deep reddish-brown hues correspond to Cu-rich (Al-lean) layers, whereas light yellow-ochre tones denote Al-rich (Cu-lean) layers. Variations in hue therefore provide a first-order indication of composition.

In the FCG sample, the clad track cross-sections are uniformly red at the substrate interface. The hue gradually lightens, reaching a distinct yellow in the mid-height region, before returning to red at the top. This colour evolution indicates that the Al concentration increases progressively within the initial six deposition layers and subsequently decreases in a symmetric manner throughout the upper six layers, consistent with the “forward” design philosophy.

By contrast, the RCG sample exhibits the opposite chromatic progression. The basal layers are light yellow (Al-rich), the intermediate layers display a reddish tint (Al-lean), and the uppermost layers again adopt the initial yellow hue. Consequently, the Al content exhibits an initial decline followed by a subsequent increase, in accordance with the “reverse” design concept.

To determine the Al distribution in the two compositional gradient samples with greater precision, EDS line scans were performed along the build direction from the substrate to the apex of both the FCG and RCG samples. The resulting profiles are presented in Fig. 4-3. For direct comparison, the nominally designed composition profiles are also plotted as red curves, whereas the experimentally measured profiles are shown as black curves. Based

on these EDS traces, each deposit can be partitioned into two categories of region: (i) steady-state composition zones, in which the Al gradient $\partial C_{Al}/\partial z \approx 0$, and (ii) transition zones exhibiting finite gradients. Here, C_{Al} denotes the Al content and z is the coordinate along the BD.

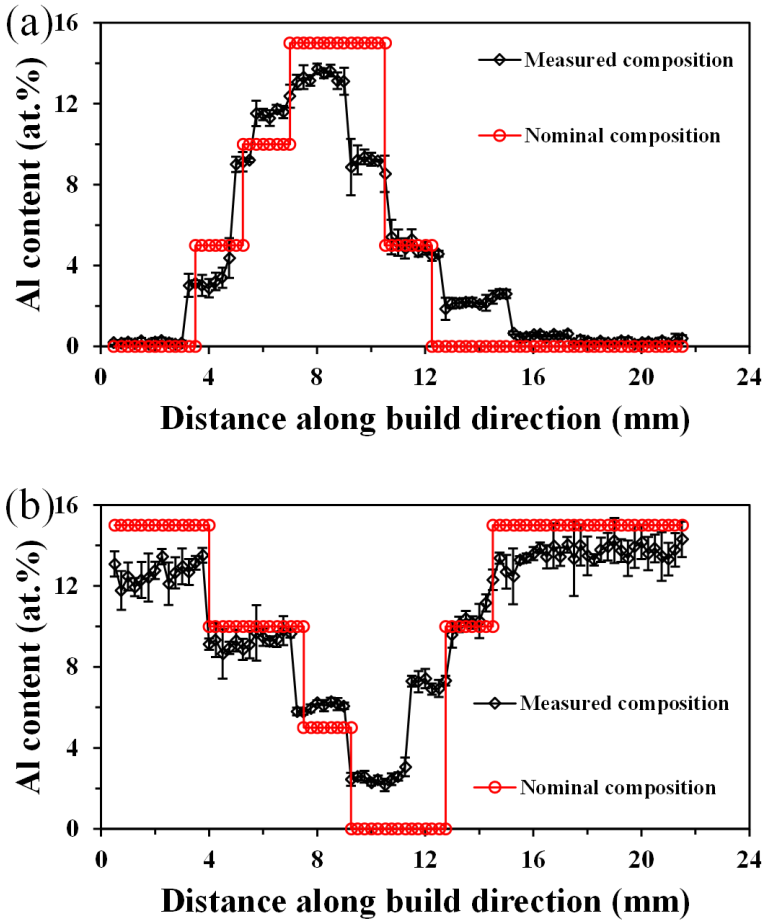

Figure 4-3 Al content profiles along the build direction of as-printed samples. (a) FCG sample. (b) RCG sample. The red lines indicate the nominal composition, and the black lines indicate the measured composition.

Fig. 4-3 illustrates that, in the FCG sample, the Al content is virtually zero at the substrate and then surges to ≈ 9.1 at.% at a height of 5.5 mm, forming a sharp, pinnacle-shaped high-Al "terrace" across 6.25–9.5 mm. Thereafter, the concentration declines steadily through 9.5–17.75 mm and returns to ≈ 0.2 at.% between 18 and 22 mm. The resulting profile rises steeply and falls gently, producing a bell-shaped curve. By contrast, In the RCG sample the basal layer already contains 12–13 at.% Al, and this high-Al plateau persists over 0–3.75 mm. With further progression along the BD, the Al content drops to 2.5 at.% in the

3.75–9.25 mm interval and remains at this mean level up to 11.25 mm. It then rises rapidly to 13–14 at.% between 11.25 mm and 14.75 mm. The resulting profile thus exhibits a gentle descent followed by an abrupt ascent, yielding a characteristic “basin-shaped” curve.

Both compositional gradient structures thus exhibit asymptotic, quasi-steady “staircase” structures: the Al content along the BD changes discontinuously, comprising a series of low fluctuation plateaux separated by steep steps. This morphology indicates that, within a given height interval, the supply-mixing-solidification cycle in the melt pool attains a stable regime. Moreover, the compositional variability within each plateau is minimal, with standard deviations below 1 at.% for both samples, confirming that the composition is effectively “locked” in the steady-state zones.

Further examination reveals that the FCG sample decomposes into ten discrete steady-state composition zones along the BD, with a mean zone height of 1.8 mm. Zone 1 (1–3.5 mm) and Zone 10 (18–22 mm) constitute the relatively long plateaux, whereas the high-Al region (Zones 3–6, 5.5–11 mm) is partitioned into four narrow steps, the shortest measuring only 0.5 mm. During the subsequent Al-decreasing segment (Zones 6–10, 9.75–22 mm) five steady-state regions are present; their lengths increase progressively with height, ranging from 1.25 to 4 mm.

By contrast, only seven steady-state intervals can be discerned in the RCG sample, yielding an average zone height of 2.7 mm, approximately 48 % greater than that of the FCG sample. A broad Al-rich basal plateau (Zone 1, 0.5–3.75 mm) is followed by two successively narrowing steps. The minimum-Al trough (Zone 4, 9.25–11.25 mm) is again comparatively wide. The composition then rebounds through two short plateaux before merging into an extensive terminal Al-rich zone (Zone 7, 14.75–21.5 mm) with a height of 6.75 mm. The statistical characteristics of the steady-state zones in the FCG and RCG samples are summarised in Tables 4-3 and 4-4, respectively.

Table 4-3 Steady-state composition zones of the FCG sample.

Steady-state zone	BD interval (mm)	Length (mm)	Average Al content (at.%)	Standard deviation (at.%)
1	1.00 – 3.50	2.50	0.2	0.06
2	3.75 – 5.00	1.25	3.1	0.18
3	5.50 – 6.00	0.50	9.1	0.10
4	6.25 – 7.25	1.00	11.5	0.16
5	7.75 – 9.50	1.75	13.3	0.26
6	9.75 – 11.00	1.25	9.1	0.31
7	11.25 – 13.00	1.75	4.9	0.34
8	13.25 – 15.50	2.25	2.2	0.24
9	15.75 – 17.75	2.00	0.6	0.08
10	18.00 – 22.00	4.00	0.2	0.08

Table 4-4 Steady-state composition zones of the RCG sample.

Steady-state zone	BD interval (mm)	Length (mm)	Average Al content (at.%)	Standard deviation (at.%)
1	0.50 – 3.75	3.25	12.7	0.54
2	4.00 – 7.00	3.00	9.3	0.34
3	7.25 – 9.00	1.75	6.1	0.19
4	9.25 – 11.25	2.00	2.5	0.25
5	11.50 – 12.75	1.25	7.2	0.21
6	13.00 – 14.00	1.00	10.1	0.31
7	14.75 – 21.50	6.75	13.6	0.42

A comparison of the compositional profile characteristics of the two gradient architectures indicates that, in both the FCG and RCG samples, the steady-state zones occurring during the Al-decreasing stage are invariably longer than the corresponding zones formed during the Al-increasing stage. Thus, the ascent segments are steeper, whereas the descent segments are comparatively gentle. Under an identical number of deposited layers, moreover, the FCG sample exhibits a greater total count of steady-state zones than its RCG counterpart. Finally, it is noteworthy that the RCG sample contains no interval in which the Al content falls below 1 at.%. The mechanisms underlying these distinctions are examined in the following section.

Comparison of solidification rates governed by thermal conductivity contrasts. As noted earlier, Cu-rich layers possess a markedly higher thermal conductivity than their Al-rich counterparts (Table 4-2) [455,471]. In both FCG and RCG samples, the Al-increasing segment invariably involves an Al-rich melt pool spreading over a Cu-rich substrate. The highly conductive substrate behaves as a “cooling fin”, extracting heat rapidly and causing the pool to solidify within a very short BD interval [471,475]. Its convective lifetime is

therefore minimal. Each compositional step is scarcely diluted by interlayer mixing, so the steady-state zones are “frozen in” as narrow plateaux with steep slopes, producing a dense array of crisp terraces.

Conversely, during the Al-decreasing segment a Cu-rich melt pool is deposited on a thermally resistive Al-rich substrate. The restricted heat removal path means that thermal flux is impeded, the pool cools more slowly, and the liquid phase persists over a greater distance [475,476]. The pool lifetime is correspondingly prolonged. Extensive thermo-solutal convection ensues between the top of the newly deposited layer and the underlying material, stirring adjacent terraces together and amalgamating them into broader plateaux [476,477]. Each steady-state region is thus elongated, its slope necessarily reduced, and the overall number of terraces diminishes accordingly.

Natural convection intensity triggered by density contrasts. Cu-rich liquid is denser than its Al-rich counterpart [478]. Hence, during the Al-decreasing stage a heavy Cu-rich melt overlies a lighter Al-rich substrate. This inverted density stratification intensifies the downward-sinking/upward-rolling convection loop, entraining Al from the previous layer and attenuating the compositional step, so that the terrace becomes progressively “flattened” [479]. When vigorous convection or an extended melt pool lifetime repeatedly stirs solute across the interlayer interface, the step amplitude is diminished. In the EDS profiles such gentle slopes no longer satisfy the “abrupt-change” criterion, and several anticipated steady-state zones may therefore be interpreted as a single plateau. In essence, “step attenuation” signifies a reduction in contrast between steps and plateaux, directly reducing the number of discernible terraces and slowing the rate of decline in Al content.

In gradient deposition, each programmed wire-feed increment should theoretically create a distinct compositional discontinuity between the new layer and its predecessor. If, prior to solidification, the melt pool does not entrain substantial volumes of the underlying liquid, it “remembers” its feed composition. After freezing, the layer retains almost the original average Al content. This ability to preserve the nominal feed ratio and avoid interlayer dilution is termed the solute memory effect [480]. During the Al-increasing stage, a lighter Al-rich melt overlies a denser Cu-rich substrate [478]. The high thermal conductivity of the Cu-rich base extracts heat rapidly, causing the pool to reach its liquidus temperature and solidify within 1–2 mm of travel [455]. As the light liquid rests upon a heavy substrate, no density inversion exists, suppressing large-scale natural convection.

Consequently, the solute memory is strong: circulation remains largely confined within the current layer, deep erosion of the underlying solid is minimal, and vertical solute transport across layers is negligible. Moreover, the high conductivity of the Cu-rich solid establishes a steep thermal gradient at the solid–liquid interface, accelerating the advancement of the solidification front. This “rapid freezing” locks the solute distribution, preventing macroscopic diffusion from smoothing the step further. The terraces are thus readily preserved, and the Al-increasing segment exhibits a steeper slope.

Deposition sequence and height-dependent heat accumulation. The FCG wall initially traverses a “rapid heat dissipation” regime, because the high-conductivity Cu-rich substrate extracts heat efficiently [455,469,480]. Pronounced thermal build-up is encountered only in the mid-to-upper portion, once an Al-rich substrate has been established. By that stage several compositional terraces have already been "locked in", so that even though later terraces expand slightly, the total count remains at ten [475,476]. In the RCG wall, by contrast, a thermal “insulation layer” is created at the base, and early heat accumulation smooths out several theoretically expected steps. When Al-rich melt is deposited higher up onto an already warmed, Cu-rich foundation, the low-conductivity liquid persists for an extended period, promoting inter-platform mixing and coalescence such that only seven plateaux survive [475,481].

In essence, the high-conductivity, high-density Cu-rich layers act as “freezing–isolating” agents in the FCG architecture but become “mixing–merging” triggers in the RCG arrangement, while the low-conductivity, low-density Al-rich layers play the opposite roles. The coupling of these layers with the substrate heat flow path and the evolving thermal accumulation explains why the Al-increasing segment exhibits a steeper slope than the Al-decreasing segment, and why the FCG structure contains a rich population of steady-state composition zones, whereas the RCG structure contains comparatively few.

Thermal–solute environment of the “minimum-Al” interval in the RCG build. In the RCG sequence, consisting of Al-rich to Cu-rich to Al-rich, the only portion theoretically capable of reaching an extremely low Al level lies midway up the wall, where a Cu-rich bead is deposited onto an existing Al-rich substrate. This “high-conductivity melt over low-conductivity base” configuration channels the heat flux vertically into the Al-rich layer, rapidly forming a deep, persistent remelt trough [480]. Entrainment of the underlying Al-rich solid elevates the lower limit of Al in the Cu-rich pool, preventing the composition

from falling below ≈ 1 at.% [480]. At the same time, the density inversion drives vigorous natural convection, further diluting the Cu-rich melt [478]. Because the Al-rich foundation is thermally resistive, heat accumulation begins at an early stage [476]. As the build height increases the average wall temperature rises, and the pool lifetime lengthens. Thus, when the Al content first starts to decline, the newly deposited, low-conductivity Al-rich melt flows for an extended period on an already warmed Cu-rich base in a "lukewarm bath" of reduced temperature difference, so that convection cannot be rapidly frozen out and any residual Al-lean zone is further homogenised [476].

The combined action of (i) deep remelting, (ii) density-driven strong convection and (iii) heat-accumulation-enhanced mixing inexorably admixes 1–3 at.% Al into every nominally Cu-rich layer [481]. Consequently, even though the wire-feed schedule nominally contains pure Cu passes, the solidified structure never drops below ~2.5 at.% Al, and no segment with < 1 at.% Al is observed throughout the wall [477,481]. In short, within the reverse gradient deposition order the high-conductivity, high-density Cu-rich melt couples strongly with the pre-existing Al-rich insulating layer. Convection and remelting lift the Al "floor", while heat accumulation prolongs mixing, ultimately erasing the theoretical ultra-low-Al step [477].

4.2.3 Microstructural evolution along the build direction

This section aims to systematically elucidate the microstructural evolution, along the BD, of two symmetrically compositional gradient components. Layer-by-layer cross-sections obtained via SEM–EBSD are employed to quantify the variation in grain size, morphology and boundary character with deposition height. Using these data, a segmented comparative analysis of the FCG sample (Section 4.2.3.1) and the RCG sample (Section 4.2.3.2) is conducted to uncover the intrinsic influence of gradient sequence on the regulation of microstructure.

4.2.3.1 FCG sample

Fig. 4-4 presents IPF maps parallel to the BD (IPF-BD) and corresponding Al EDS maps acquired at successive heights along the BD of the FCG wall. An accompanying Al content profile is included for clarity, and the EBSD sampling positions are marked (a)–(g). As BD increases from the substrate towards the wall apex, the microstructure displays a multiscale, composition-height-coupled gradient evolution.

Fig. 4-4 (a1),(a2) demonstrates that the Cu-rich steady-state composition region (SCR) adjacent to the substrate (BD ≈ 2–6 mm) contains only 0.2 at.% Al. This zone is hereafter denoted SCR-0.2-1, because the FCG wall exhibits a symmetrical compositional profile, the suffix “1” designates the ascending-Al segment, whereas the corresponding region in the descending-Al segment is labelled “2”. Driven by rapid quenching and a steep thermal gradient, SCR-0.2-1 develops slender columnar grains together with fine equiaxed grains, accompanied by residual cellular dendritic traces. Notably, within SCR-0.2-1 the columnar grains are situated nearer the substrate, whilst the equiaxed grains reside closer to the fusion line (indicated by a black dashed line in the figure), signifying that a columnar to equiaxed transition occurs along the BD in this region. For quantitative analysis, the area of every grain was measured and its equivalent circular diameter calculated to assess grain size, while the fractions of low-angle grain boundaries (LAGBs, 2–10°) and high-angle grain boundaries (HAGBs, > 10°) in each zone were determined.

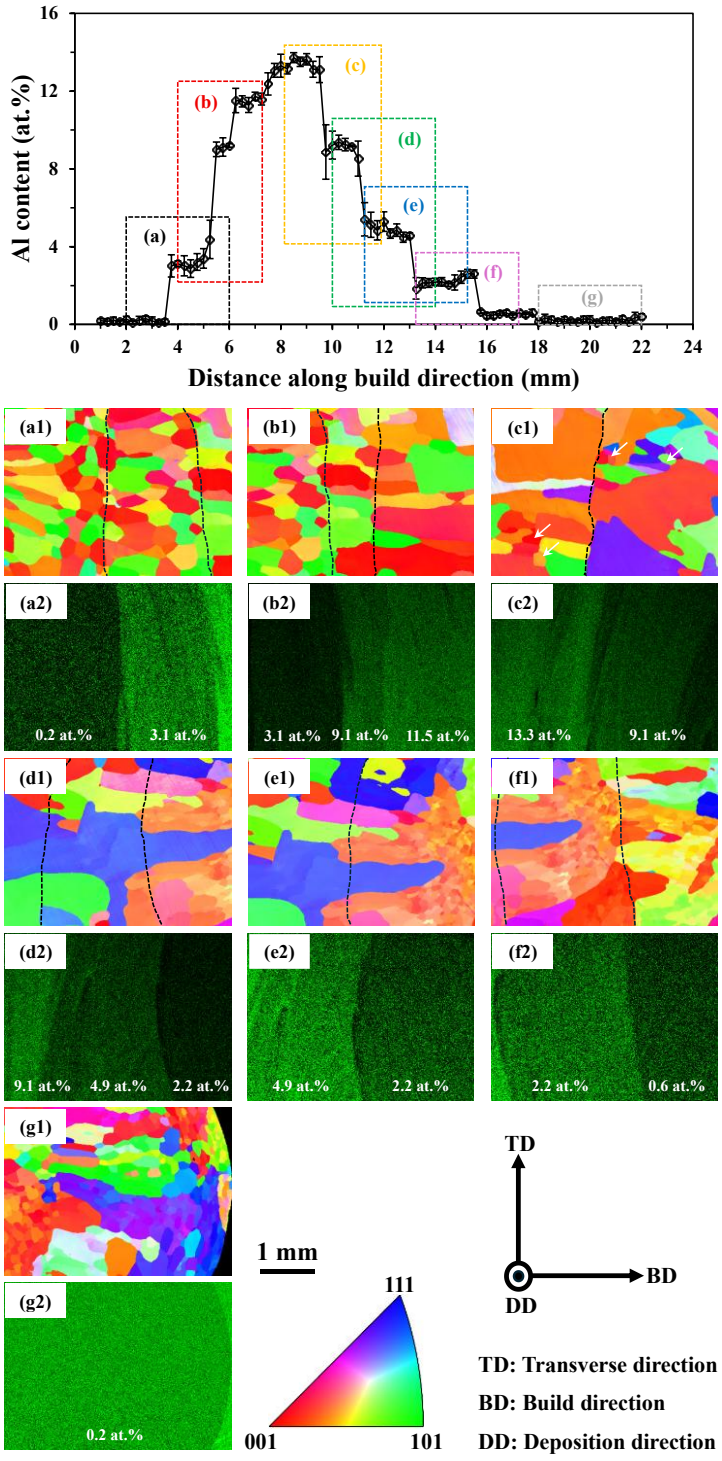

Figure 4-4 Al Microstructural evolution of the FCG sample. An accompanying Al content profile measured along the BD of the FCG wall. Dashed coloured boxes labelled (a)–(g) delineate the heights at which EBSD and EDS analyses were performed. (a1–g1) IPF-BD maps for the transverse section at each boxed position; the colour key corresponds to the stereographic triangle shown bottom-centre. The dashed black line marks the fusion line. (a2–g2) Corresponding Al EDS maps revealing compositional partitioning along the BD. Average Al contents (at.%) for the different regions in each field of view are annotated.

In the SCR-0.2-1 region the mean grain size (d) is 387 μm, with LAGBs accounting for 11.4 % and HAGBs predominating at 89.6 %. The Al distribution is comparatively uniform, and the compositional step across the fusion line remains sharp.

With increasing build height, the average Al content rises stepwise from 3.1 at.% to 11.5 at.%. Concomitantly, the columnar grains undergo pronounced epitaxial growth and marked coarsening, such that d increases from 528 μm to 942 μm. The LAGBs fraction initially falls and then rises, dropping to 20.8 % before increasing to 24.2 %. Throughout, the Al compositional step retains a sharp width of approximately 250 μm.

Traversing further into the 8–13 mm interval above the substrate, the Al content first rises to 13.3 at.% and then reverses to 4.9 at.%. On the left-hand side, the SCR-13.3 region develops coarse columnar grains aligned with the BD and containing a minor fraction of equiaxed grains. Here, the proportion of LAGBs increases to 23.3 %, while HAGBs decrease to 76.7 %. Conversely, on the right-hand side, the SCR-9.1-2 region, where the Al content has fallen to 9.1 at.%, exhibits a mixed microstructure of ultra coarse columnar grains and fine equiaxed grains, the d broadening to 1370 μm. This domain presents a pronounced single-crystal-island morphology, with the LAGBs fraction plummeting to 7.88 % and the HAGBs fraction rising to 92.1 %. Equiaxed grains in both SCR-13.3 and SCR-9.1-2 are highlighted by white arrows in Fig. 4-4 (c1). Progressing into SCR-4.9, multiple millimetre-scale columnar grains continue to grow epitaxially along the BD, and the equiaxed component disappears.

Within the height interval 13–18 mm above the substrate, the SCR-2.2 and SCR-0.6 of the FCG wall exhibit markedly different grain morphologies and boundary characteristics (Fig. 4-4 (f1),(f2)). The SCR-2.2 zone is dominated by an ultra-coarse equiaxed–columnar mixed microstructure, with a mean grain size of d = 1904 μm. LAGBs account for 77.5 %, whereas HAGBs constitute only 22.5 %. A dense honeycomb network of LAGBs subdivides the giant grains into sub-millimetre-scale subgrains. By contrast, in the SCR-0.6 zone the mean grain size precipitously decreases to d = 879 μm. The LAGBs fraction falls to 60.5 %, while the HAGBs fraction rises to 39.5 %. Moreover, a greater population of fine newly nucleated equiaxed grains is evident. Al EDS maps show uniform brightness within both regions, and the compositional step across the fusion line retains a sharp width, corroborating that, at this height, solute homogenisation remains governed by transient melt-pool convection, with solid-state diffusion contributing negligibly.

Within the uppermost segment (18–22 mm above the substrate), the SCR-0.2-2 region displays a multi-scale, composite microstructure: the matrix is dominated by fine equiaxed grains containing a few flattened columnar grains oriented parallel to the BD. The mean grain size is d = 869 μm, representing a substantial refinement compared with the 1904 μm giant grains in SCR-2.2. EBSD analysis shows that LAGBs constitute 51.9 %, whereas HAGBs account for 48.1 %. EDS mapping indicates a completely homogeneous Al distribution, with no residual compositional step through the region. The numerical data are summarised in Table 4-5 and the corresponding grain size distribution histogram is shown in Fig. 4-5.

Table 4-5 Quantitative statistics of the mean grain size and the fractions of grain boundaries in the different SCRs of the FCG sample.

Regions	Grain size (μm)	LAGBs (%)	HAGBs (%)
SCR-0.2-1	387 ± 137	11.4	88.6
SCR-3.1	528 ± 206	20.8	79.2
SCR-9.1-1	805 ± 315	18.8	81.2
SCR-11.5	942 ± 336	24.2	75.8
SCR-13.3	1100 ± 588	23.3	76.7
SCR-9.1-2	1370 ± 828	7.9	92.1
SCR-4.9	1298 ± 580	10.3	89.7
SCR-2.2	1904 ± 882	77.5	22.5
SCR-0.6	879 ± 270	60.5	39.5
SCR-0.2-2	869 ± 456	51.9	48.1

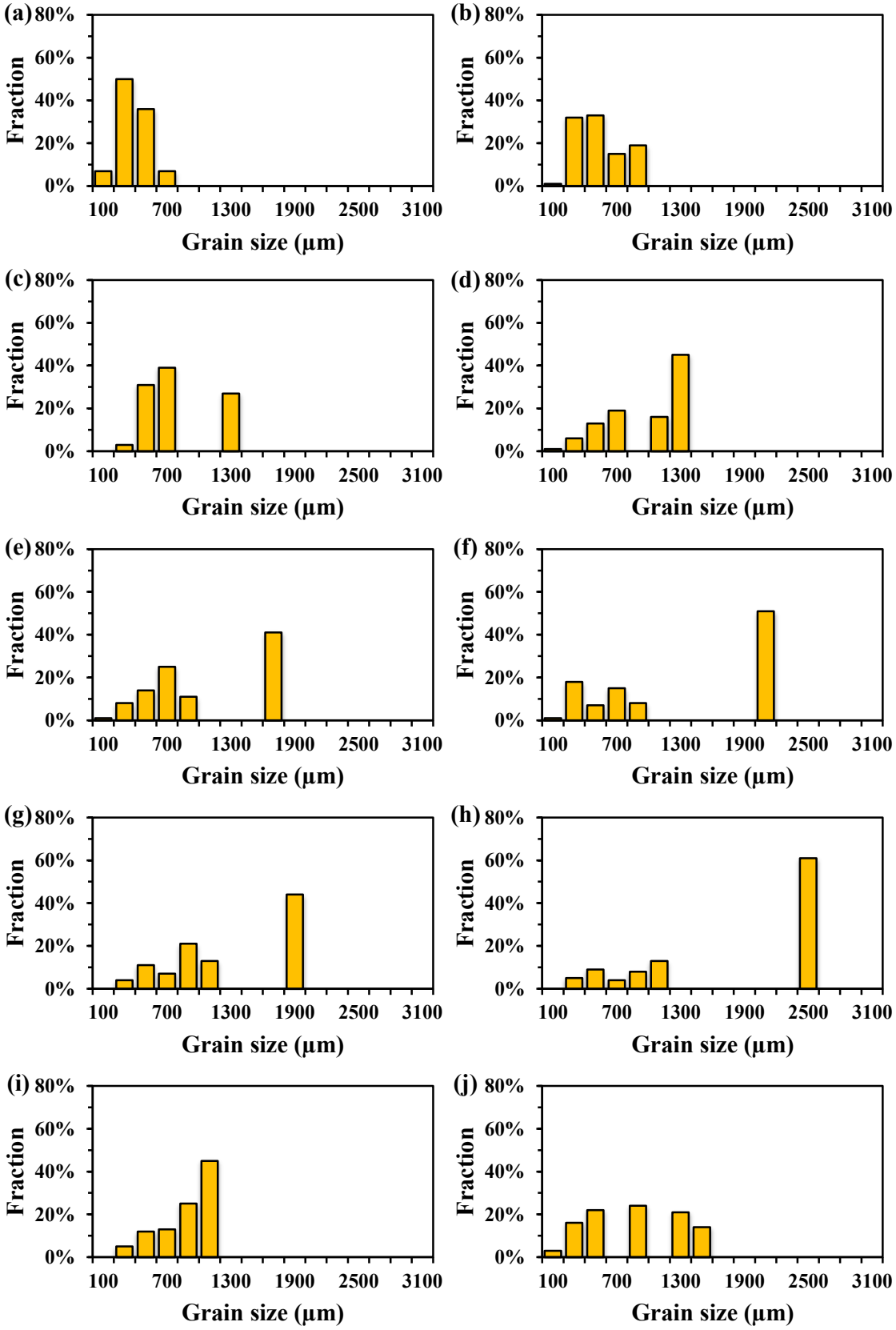

Figure 4-5 Histograms of the grain size distributions for the individual SCRs in the FCG sample: (a) SCR-0.2-1; (b) SCR-3.1; (c) SCR-9.1-1; (d) SCR-11.5; (e) SCR-13.3; (f) SCR-9.1-2; (g) SCR-4.9; (h) SCR-2.2; (i) SCR-0.6; and (j) SCR-0.2-2.

Columnar to equiaxed transition (CET) in the near-substrate region. In the substrate-adjacent portion of the FCG architecture (SCR-0.2-1 and SCR-3.1, BD ≈ 2–5 mm), IPF images reveal a pronounced CET on the left-hand side of the fusion line, namely at the crown of the underlying melt pool (see Fig. 4-4 (a1)). To elucidate this CET more clearly, Fig. 4-6 presents the image quality (IQ) plus grain boundaries (GBs) map corresponding to Fig. 4-4 (a1), in which HAGBs and LAGBs are highlighted by black and blue lines, respectively. The regions enclosed by white dashed rectangles delineate the melt pool crowns within SCR-0.2-1 and SCR-3.1. The profusion of equiaxed grains inside these rectangles confirms the occurrence of an appreciable CET.

During WAAM, the thermal gradient (G) and solidification rate (R) within the melt pool play pivotal roles in microstructural evolution [482,483]. The product $G \times R$ represents the cooling rate (C), which controls the characteristic length scale of the solidification structure. Higher cooling rates yield finer microstructures [484]. Whereas the ratio G/R determines the grain morphology: a high G/R ratio favours planar or cellular growth, while a low ratio promotes dendritic or equiaxed grain formation [485,486]. Within a representative WAAM processing window, thermo-fluid–solid coupled simulations of single-phase FCC Cu–Al binary alloys containing 0–15 at.% Al, together with in-situ thermometry, consistently demonstrate that the G decreases monotonically from the fusion line to the melt pool surface, by approximately 60–70 % along the BD [480,487]. Concurrently, the R follows $R = v \cdot \cos\alpha$, where v is the travel speed and α is the angle between the solid–liquid interface normal and the travel direction. Experimental and numerical studies show that, from the bottom to the top of the melt pool, α falls from ≈ 75° to < 20°, causing R to rise sharply [487]. Although the reduction in G diminishes the thermal driving force for directional growth, the stepwise increase in R elevates the instantaneous cooling rate $C = G \cdot R$. At the pool crown C attains 40–60 K · s^{-1}, roughly two- to three-times higher than the 10–25 K · s^{-1} recorded at the pool base [480,488]. Consequently, the high G/R ratio associated with large G and low R at the pool bottom favours the formation of columnar grains growing along the heat flow direction, whereas the combination of a low G/R ratio and high C at the pool top markedly enhances the nucleation rate, triggers a CET, and yields a fine equiaxed grain structure.

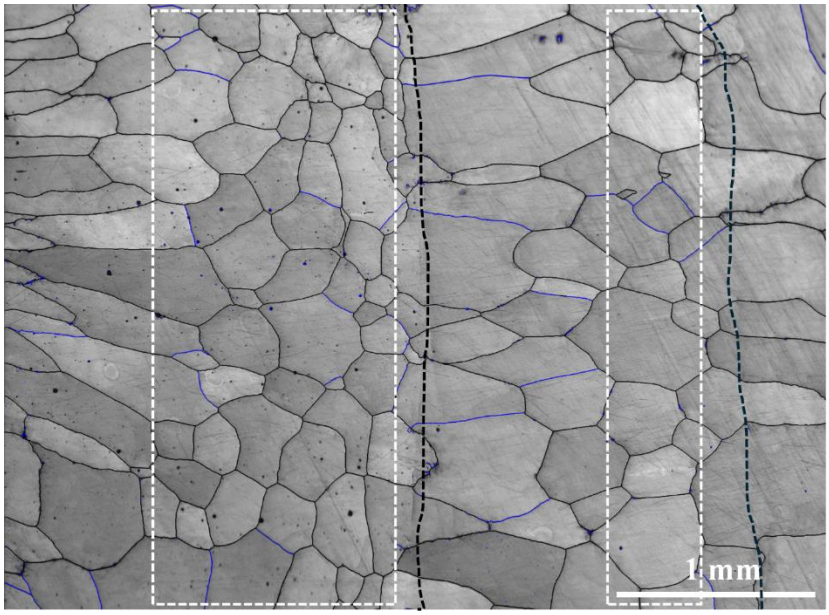

Figure 4-6 EBSD IQ + GBs map for the SCR-0.2-1 and SCR-3.1 regions. The black lines denote HAGBs, the blue lines indicate LAGBs, the white dashed rectangles delineate the tops of two consecutive melt pools, and the two black dashed lines represent the positions of the fusion lines.

As the wall height increases, cyclic interlayer heat accumulation markedly modifies the solidification conditions at the melt pool crown. Multisource in situ thermography finite element coupling shows that the cumulative heat input elevates the substrate temperature before arc reignition for the subsequent layer, thereby further reducing the G. Meanwhile, studies have shown that the cooling rate decreases from approximately 40 K · s^{-1} in the first layer to less than 20 K · s^{-1} [489,490]. The simultaneous decreases in G and C diminish the constitutional undercooling (ΔT_c) ahead of the solid–liquid interface, restoring a high G/R regime and favouring preferential growth of well-oriented columnar grains. Meanwhile, thermal buildup prolongs the melt pool lifetime, so that the fine equiaxed grains formed at the pool crown are partially dissolved or laterally "engulfed" by adjacent columnar grains during successive remelting–resolidification cycles, generating a multi-layer, "bamboo-joint" columnar-banded structure [490]. Experiments on Al alloys likewise record a progressive decline and eventual disappearance of the equiaxed volume fraction from the base to the top of the build, corroborating the dominance of the heat accumulation and grain competition mechanism [491]. In summary, the fading of equiaxed grains at the melt pool crown with increasing deposition height is principally attributable to: (i) concurrent reductions in G and C, together with a rise in G/R, that suppress the CET; and

(ii) the extended melt pool lifetime and remelting-induced dissolution or replacement of previously formed equiaxed grains.

Discontinuous dynamic recrystallisation (DDRX) in the mid-height Al-rich region of the deposit. Dynamic recrystallisation (DRX) is a kinetic softening mechanism that operates during high temperature plastic deformation, in which the continuous accumulation of dislocations is counterbalanced in situ by the nucleation and growth of new grains, thereby refreshing the grain structure and lowering the system's free energy [492]. According to the mode of nucleation and growth, DRX is commonly categorised into three basic types [492]: (i) discontinuous dynamic recrystallisation (DDRX), in which dislocation pile-ups cause the original HAGBs to bulge and form new nuclei, which subsequently grow by boundary migration; (ii) continuous dynamic recrystallisation (CDRX), in which intragrain low-angle subgrains progressively rotate and merge, eventually transforming into HAGBs; and (iii) geometric dynamic recrystallisation (GDRX), typically arising under severe plastic deformation, whereby elongated grains collide and become "segmented", producing nearly equiaxed fragments [493]. DRX is activated once the accumulated dislocation density exceeds a critical strain. The equiaxed grains indicated by the white arrows in Fig. 4-4 (c1) have developed via DDRX, and this phenomenon is repeatedly observed within the Al-rich zones of the mid-height section of the FCG deposit.

Table 4-6 provides a mechanistic comparison of the equiaxed grains observed in Cu–Al components fabricated by WAAM. The comparison synthesises classical solidification and CET theory, the fundamentals of DRX, and WAAM-specific observations for Cu-based and related alloys under directed energy deposition conditions. In the Cu–Al system, because the α-Cu matrix possesses a high SFE, once sufficient high-temperature strain accumulates during thermal cycling, CDRX is generally favoured over DDRX. By contrast, equiaxed grains generated directly by solidification are governed predominantly by CET rather than by solid-state evolution [494–498].

Table 4-6 Diagnostic criteria for equiaxed grain formation mechanisms in WAAM Cu–Al [494–500].

Aspect	CET	DDRX	CDRX
One-glance criterion	Equiaxed dendritic or cellular features are obvious; cell or dendrite arm spacing is visible	Fine equiaxed grains form a necklace along prior grain boundaries; boundary bulging is clear	Equiaxed grains are diffusely distributed; no continuous necklace band and no obvious bulging; subgrains progressively transform into grains
EBSD and KAM key signals	Low KAM and little internal substructure; GBs character distribution dominated by HAGBs; little residual LAGBs	A high HAGBs fraction in the necklace band; high KAM in unrecrystallised interiors; strong contrast between HAGBs and LAGBs and sharp interfaces	Abundant LAGBs and a continuous spectrum of misorientation; gradual conversion from LAGBs to HAGBs; low KAM inside the newly formed grains
Spatial location and thermal history	Often at the bead surface, at the trailing edge of the melt pool or in locally remelted and resolidified regions, controlled by reduced G over R and constitutional undercooling	Common at grain boundaries and triple junctions in the reheated layer beneath the active bead, requires thermo mechanical coupling	More prevalent in reheated layers that experience multiple high temperature cycles but only moderate strain, more likely in high SFE α-Cu
Strain requirement	No high-temperature strain required; the phenomenon is governed by solidification	Requires hot deformation above a critical level; strain is mostly localised at grain boundaries	Requires moderate accumulated strain plus repeated heating; no strong localisation required
Morphology and size	Size typically tens of micrometres, dendritic or cellular rosettes	New grains 2 to 10 μm, can grow with high-temperature dwell	Subgrains or cells start at 2 to 5 μm, final grains mostly 5 to 50 μm
Texture trend	Epitaxial columnar growth is interrupted; overall texture markedly weakens and tends towards random	Texture in the necklace band weakens markedly; boundary-related preferences may be retained	Progressive weakening and spread from the parent orientation; the ODF broadens but may not be fully random

Fig. 4-7 depicts the occurrence of DDRX within the Al-rich region of the FCG deposit (Al content 9–13 at.%). The abundance of LAGBs in Fig. 4-7 (a) indicates that the matrix columnar grains have undergone extensive dislocation activity and energy storage during repeated, intense thermo-mechanical cycles. Once the local stress–strain state exceeds a critical threshold, grain boundary bulging provides preferred sites for subsequent

nucleation [501]. Continued boundary migration then “shears” the nuclei from the matrix grain and allows rapid growth, producing fine equiaxed grains completely enclosed by HAGBs, as highlighted by the yellow arrows in Fig. 4-7 (a), which are hallmarks of a classic DDRX process [485,492].

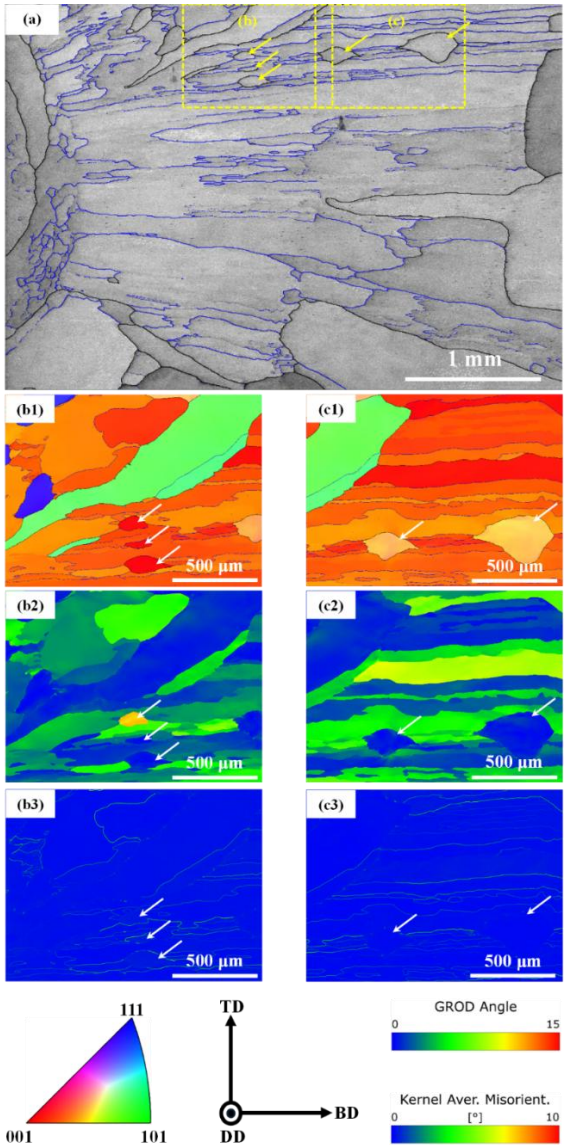

Figure 4-7 DDRX in the Al-rich mid-height region of the FCG wall (Al ≈ 9–13 at.%). (a) EBSD IQ + GBs map. Black lines denote HAGBs and blue lines mark LAGBs. Yellow arrows highlight representative DDRX equiaxed grains. (b1, c1) The magnified IPF-BD maps for the selected regions in (b) and (c), corresponding to the yellow dashed boxes in (a), display the crystallographic orientations (colour key shown bottom left). (b2, c2) GROD maps reveal intra-grain orientation gradients. Colour scale: 0–15°. (b3, c3) KAM maps indicate dislocation density. Colour scale: 0–10°. White arrows in (b1–b3) and (c1–c3) point to DDRX grains at different growth stages.

Fig. 4-7 (b1)–(b3) and (c1)–(c3) corresponds to the enlarged IPF-BD, grain reference orientation deviation (GROD) and kernel average misorientation (KAM) maps from the yellow dashed rectangles in Fig. 4-7 (a). In Fig. 4-7 (b1) the DDRX-derived equiaxed grains are rendered in pure red, signifying a <001> orientation nearly parallel to the BD, whereas the adjacent columnar parent grain appears orange, i.e. still close to <001> but noticeably misoriented. Fig. 4-8 (a),(b) presents the crystallographic orientations of the parent grain and the DDRX-derived equiaxed grain identified in Fig. 4-7 (b1). The black rectangles mark the precise positions of the respective grains on the pole figures. The <100> axis of the DDRX-derived equiaxed grain is aligned with the BD, whereas the parent grain's <100> axis is offset. The quantitative deviation is obtained from the red dashed ellipse in Fig. 4-8 (c), which shows that the maximum pole density is displaced from the BD by 10–15°, indicating a crystallographic misorientation of roughly 10–15° between the parent grain and the DDRX-derived grain, significantly well above the HAGBs threshold. Similarly, Fig. 4-7 (c1) displays another DDRX-derived equiaxed grain in the Al-rich region. Unlike the earlier case, the parent grain's <100> axis is parallel to the BD, whereas the <100> axis of the DDRX-derived equiaxed grain is tilted with respect to the BD, as shown in Fig. 4-9 (a),(b). Nevertheless, a crystallographic misorientation exceeding 10° persists between the parent and DDRX-derived grains (Fig. 4-9 (c)). This orientational contrast confirms that the new grain has adopted a preferred orientation aligned with the heat flow/growth direction [471]. These observations indicate that the grain nucleated independently rather than growing epitaxially from the parent grain [459]. During subsequent growth, it was preferentially retained and competitively engulfed neighbouring grain boundaries [502].

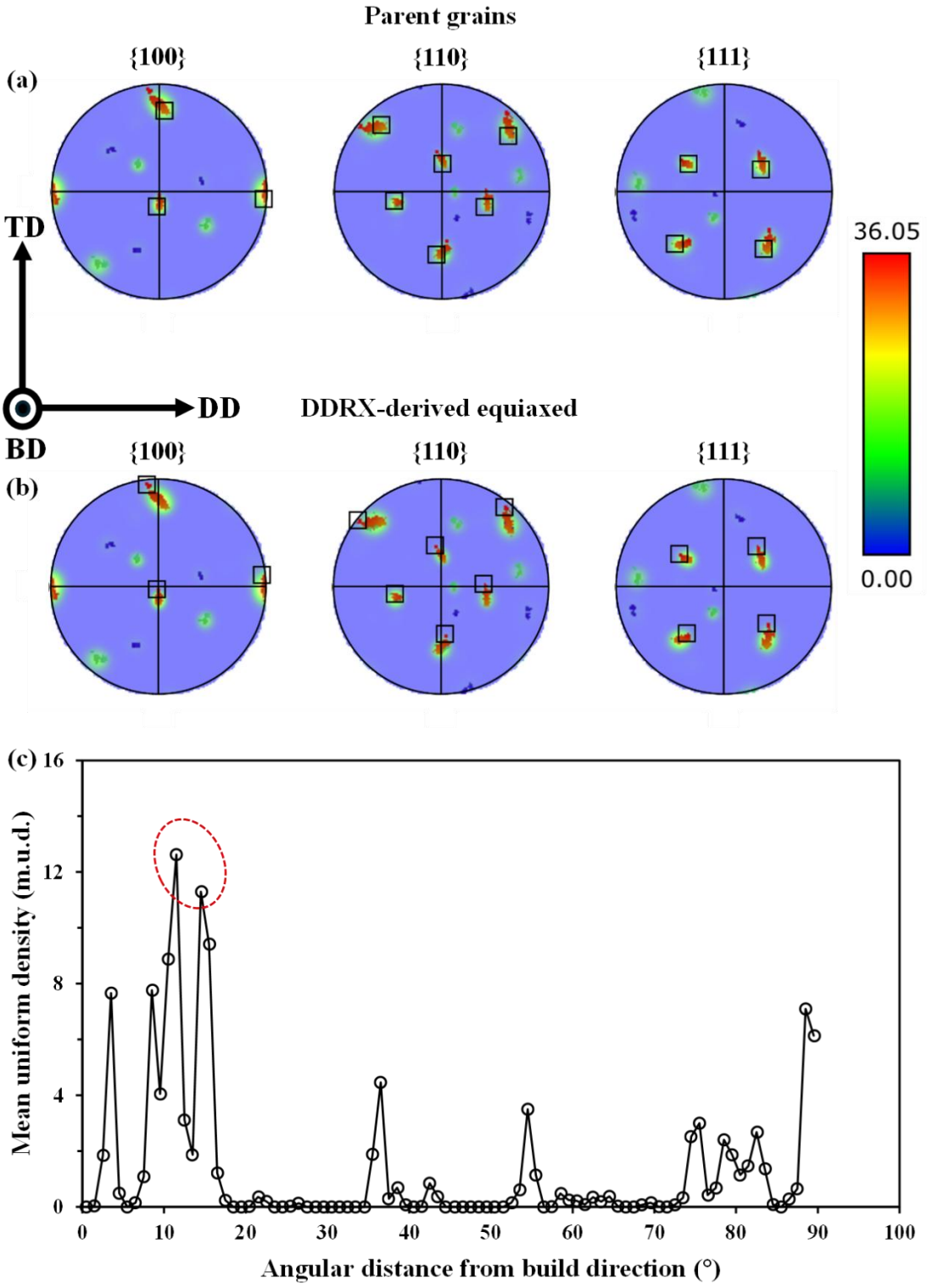

Figure 4-8 Crystallographic comparison between the parent columnar grain and the DDRX-derived equiaxed grain selected from Fig. 4-7 (b1). (a) {100}, {110} and {111} pole figures of the parent grain. The black rectangles indicate the precise pole positions of that grain. (b) Corresponding pole figures for the DDRX-derived equiaxed grain. The black rectangles mark the grain's poles. (c) Superposition of the two <100> pole clusters illustrates their relative misorientation. The red dashed ellipse encloses the maximum pole density locus.

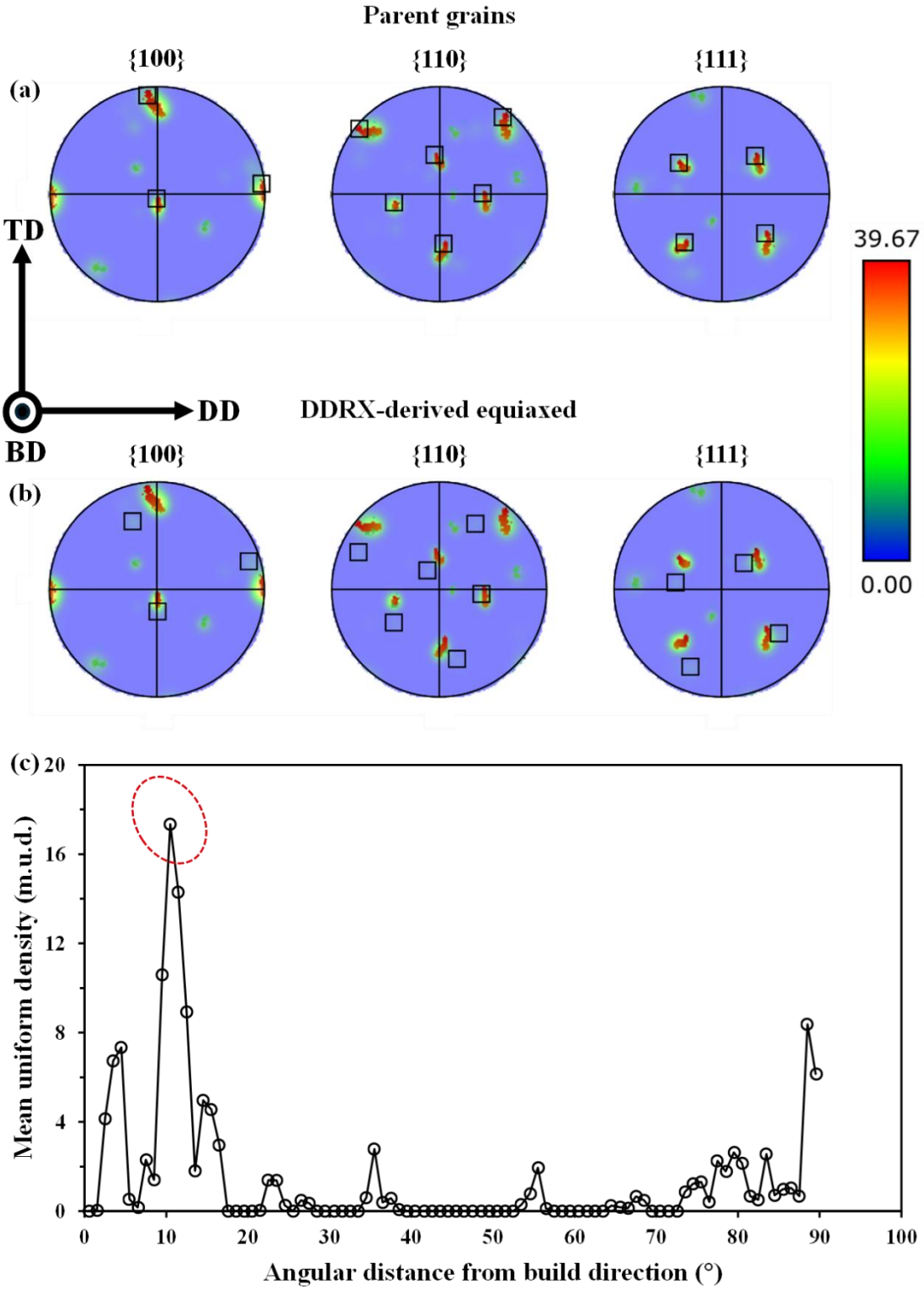

Figure 4-9 Crystallographic comparison between the parent columnar grain and the DDRX-derived equiaxed grain selected from Fig. 4-7 (c1). (a) {100}, {110} and {111} pole figures of the parent grain. The black rectangles indicate the precise pole positions of that grain. (b) Corresponding pole figures for the DDRX-derived equiaxed grain. The black rectangles mark the grain's poles. (c) Superposition of the two <100> pole clusters illustrates their relative misorientation. The red dashed ellipse encloses the maximum pole density locus.

Fig. 4-7 (b2),(c2) further discloses the recrystallisation kinetics: under cyclic thermo-strain loading, the parent columnar grain bulges to generate embryonic nuclei that initially inherit an orientation close to that of the matrix and undergo bulk lattice rotation during boundary migration [503]. Sustained stress and interface motion then impose a unidirectional, progressive orientation gradient along the growth direction, thereby increasing the average misorientation. As a result, the GROD assumes an orange–yellow hue (5–10°). Because the local misfit between neighbouring regions remains minimal, the KAM remains < 1° (see Fig. 4-7 (b3)). Hot compression experiments on 316LN steel by Liu et al [503]. showed that newly formed DDRX-derived grains in the bulging-to-early growth stage typically retain an internal orientation gradient of 5–12°, while their KAM decays rapidly. The concurrence of these two indicators is therefore a key criterion for identifying grains in the growth stage. As boundary migration proceeds, the newly formed grains detach completely from the parent matrix, their lattice rotation gradually ceases, and recovery-mediated dislocation annihilation almost exhausts the stored energy. Consequently, the internal orientation becomes highly uniform: the GROD falls below 2° and appears blue, while the KAM remains below 0.5°, indicating an extremely low density of dislocations (see Fig. 4-7 (b3),(c3)). Hadadzadeh et al. proposed that grain orientation spread (GOS)/GROD ≤ 5° combined with KAM ≤ 1° represents the lower bound for fully recrystallised grains [504]. A stricter criterion of GROD ≤ 2° is often adopted to define a "fully stabilised" dynamic-recrystallisation domain [504].

In summary, an orange GROD signifies that an equiaxed grain is in the transitional "bulging–orientation rotation–strain release" stage of DDRX, whereas a blue GROD indicates that the grain has completed orientation homogenisation and dislocation exhaustion, entering the steady-state competitive regime. The spatio-temporal evolution between these stages is governed by the dislocation accumulation rate, the driving force for boundary migration, and interlayer heat build-up. In the low SFE Cu–Al system, the bulging-to-early growth stage is protracted, and the GROD colour contrast is pronounced, in line with DDRX evolution in low- to medium-SFE alloys [503,505].

Taken together, the bulged grain boundary morphology, the intact ring of HAGBs, the pronounced orientation jumps and the negligible intragranular strain unequivocally confirm that these equiaxed grains are produced by DDRX rather than by continuous rotation or geometrical fragmentation [492,493,501]. It should be emphasised that the

intrinsically low SFE of the Al-rich region suppresses dislocation climb and cross-slip, thereby attenuating dislocation annihilation and rearrangement during recovery and consequently heightening the driving force for subsequent recrystallisation [506]. Moreover, the high solute content within the Al-rich zones pins dislocations, further retarding recovery and preserving additional stored energy for the forthcoming recrystallisation [507]. Finally, the reduced thermal conductivity of the Al-rich deposit lowers the local cooling rate, affording sufficient time for the bulging–nucleation–growth sequence and, from both thermal and kinetic perspectives, promoting the formation of DDRX-derived equiaxed grains [455,508].

Continuous dynamic recrystallisation (CDRX) in the Cu-rich region near the crown of the deposit. In the section situated 13–17 mm above the substrate, Fig. 4-10 shows the parent columnar grains contain a dense honeycomb network of LAGBs (fraction ≈ 69 %) that gradually evolve into closed HAGBs (fraction ≈ 31 %). The originally columnar grains are thus refined into sub-micron equiaxed subgrain clusters, and no evidence of boundary bulging or the penetration of new interfaces is observed. This transformation, whereby an intragranular LAGBs network steadily increases its misorientation and converts into HAGBs, meets the canonical criteria for CDRX: (i) a high LAGBs content with orientation gradients permeating the entire grain (see Fig. 4-10); (ii) most new boundaries originate within the grain interior rather than from pre-existing HAGBs; and (iii) the refined grains remain geometrically contiguous with the parent grain, exhibiting no marked orientation jump (Fig. 4-4 (f1),(g1)) [492,509]. Accordingly, this region is judged to have undergone CDRX rather than DDRX.

The evolution of CDRX can be divided into three stages: (i) Dislocation storage and subgrains formation – cyclic loading and cooling cause rapid interaction and rearrangement of dislocations on the slip planes, producing subgrains with misorientations of 2–5°. (ii) Subgrain rotation and boundary sharpening – under the sustained stress-temperature field, subgrains accumulate rotation at a certain rate, raising the LAGBs misorientation to 10–15°. (iii) HAGBs development and equiaxation – once the critical misorientation is exceeded, the subgrains gradually decouple into discrete grains. The network of LAGBs is segmented into closed HAGBs rings, ultimately yielding stable, fine equiaxed grains [504,510]. In Fig. 4-10 (a),(b), fragments of HAGBs have already emerged within the subgrains highlighted by the yellow arrows, indicating that these subgrains are presently

undergoing CDRX.

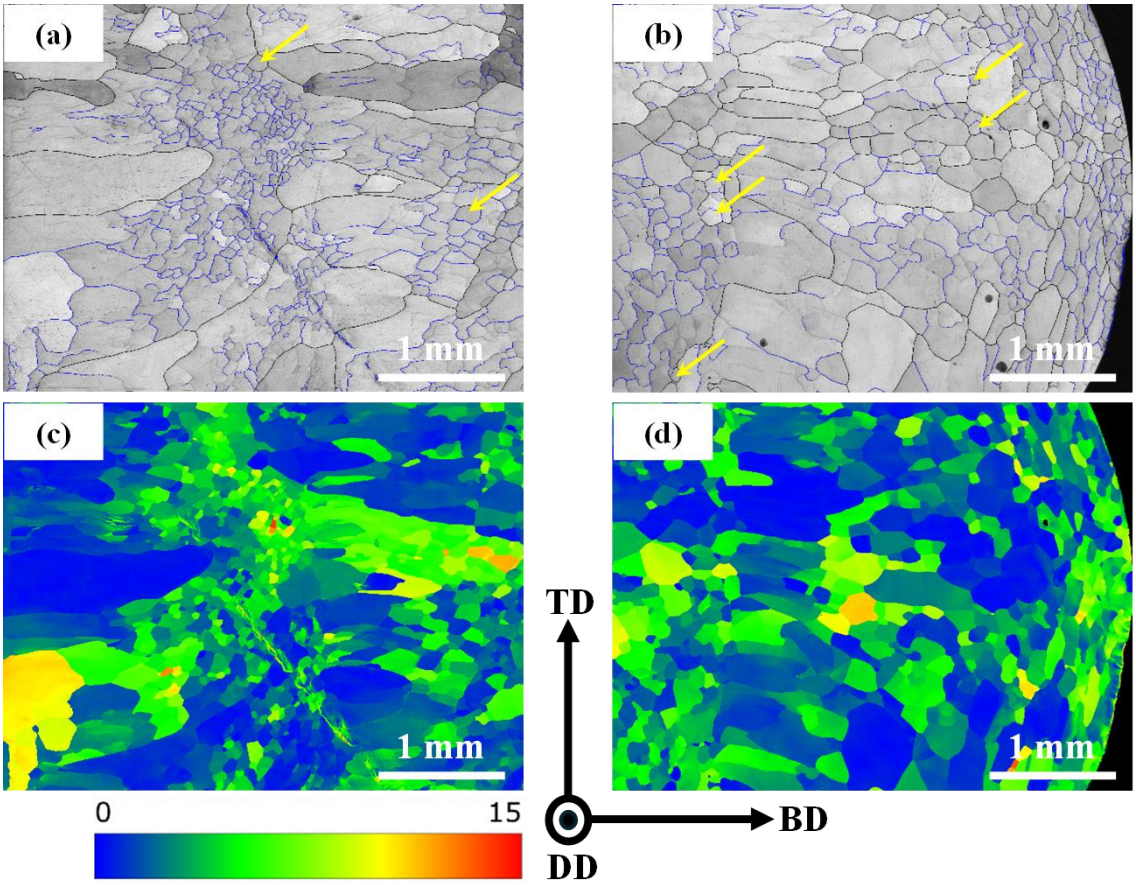

Figure 4-10 CDRX in the Cu-rich regions near the top of the FCG deposit. (a) EBSD IQ + GBs map covering the SCR-2.2 and SCR-0.6 regions. (b) EBSD IQ + GBs map of the SCR-0.2-2 region. Black lines delineate HAGBs, whereas blue lines denote LAGBs. Yellow arrows highlight representative subgrains that are actively undergoing CDRX. (c, d) GROD maps corresponding to (a) and (b), respectively, illustrating the intragranular orientation gradients. Colour scale: 0–15°.

A decrease in Al content markedly elevates the SFE of Cu–Al alloys: at 0.6 at.% the SFE is ≈ 70 mJ · m^{-2}, whereas at 2 at.% it is only ≈ 50 mJ · m^{-2} [511]. In high-SFE systems dislocations cross-slip and climb readily, promoting rapid recovery. The enhanced recovery rate means that dynamic recovery contributes more effectively to dislocation annihilation and acts synergistically with subgrain rotation, thereby favouring the onset of CDRX rather than DDRX [512]. Moreover, near the crown of the deposit both the thermal gradient and the cooling rate are substantially reduced, and the stored-energy density is insufficient to drive boundary bulging for nucleation. Conversely, interlayer heat

accumulation raises the matrix temperature, affording a time–diffusion window that facilitates dislocation climb and rotation, further promoting CDRX [480].

Within the FCG deposit, the successive SCRs display a non-monotonic evolution of grain size and LAGBs fraction along the BD. These trends can be rationalised by the coupled effects of deposition heat cycling and local composition on recrystallisation and grain coarsening mechanisms.

Mechanism for the initial increase and subsequent decrease in grain size with BD. The basal SCR-0.2-1 is directly coupled to the substrate: the thermal gradient is steep and the cooling rate high, while the highly conductive substrate extracts heat so efficiently that very little time is available for grain boundary migration [513]. In WAAM, interlayer reheating occurs when the latent heat from a newly deposited and solidified droplet is conducted and radiated back into the underlying layer, subjecting it to a brief re-heating/re-cooling thermal cycle. The closer a layer lies to the substrate, the greater the cumulative number of such cycles [514]. Under typical WAAM parameters, the first layer is sequentially "re-fired" by the layers above at a frequency of roughly 30–60 s per cycle, categorised here as frequent reheating. Yet the substantial thermal path into the massive substrate limits the peak temperature of each cycle to only 0.4–0.55 T_m (T_m denotes the alloy's melting point) and, within 5–20 s, the temperature rapidly falls owing to vigorous heat conduction [86]. Accordingly, the dwell time at elevated temperature is far below the critical time–temperature integral required for significant static coarsening. According to the kinetics of static grain growth:

$$D^n - D_0^n = K_0 t exp\left(-\frac{Q}{RT}\right) \tag{4.9}$$

where, D is the mean grain diameter after holding for time t; D_0 is the initial mean diameter (commonly taken at the end of recrystallisation); n is the growth exponent, reflecting grain boundary migration geometry ($n \approx 2$ for purely curvature-driven growth and $n > 2$ when pinning or solute drag is present); K_0 is a pre-exponential factor determined by material constants; Q is the apparent activation energy for boundary migration; R is the universal gas constant; and T is the absolute temperature [515].

When the peak temperature remains below 0.6 T_m and the individual dwell time is $t < 30$ s (typical of WAAM bottom-layer thermal cycles), the exponential term $\exp(-Q/RT)$ is

extremely small, so the effective rate constant becomes:

$$K = K_0 exp\left(-\frac{Q}{RT}\right) \lesssim 10^{-21} m^n s^{-1} \tag{4.10}$$

rendering grain boundary migration virtually “frozen” [515]. Significant static coarsening is therefore unlikely, in agreement with experimental observations that Cu–Al and Al alloys held at 300–450 °C for tens of seconds exhibit only negligible grain growth [516].

Repeated yet modest thermal cycles encourage dislocation recovery rather than providing additional driving force, thereby further attenuating static coarsening. Consequently, although the basal region is subjected to frequent interlayer reheating, the combination of low peak temperature, brief dwell time and rapid cooling fails to supply sufficient thermal activation energy or temporal window to trigger appreciable static grain growth, and the mean grain size ultimately remains at only ≈ 387 μm [492].

As the build height increases, heat accumulation in SCR-13.3 leads to concurrent reductions in both the thermal gradient and cooling rate, thereby enhancing the driving force for grain boundary migration while suppressing nucleation. The grains consequently coarsen progressively to ≈ 1100 μm [514]. Upon reaching SCR-2.2, the grain size rises abruptly to its maximum value of 1904 μm for two principal reasons: (i) the local Al content falls, raising the SFE of this region, so that dynamic recovery accelerates and the nucleation of new HAGBs is impeded, allowing existing boundaries to migrate over long distances and engulf neighbouring grains [506]; and (ii) the temperature plateau at this height continues to supply sufficient grain boundary driving force to sustain abnormal grain growth [492]. Approaching the crown of the wall (SCR-0.6 and SCR-0.2-2), convective and radiative heat exchange between the melt pool and the environment becomes dominant. Cooling rate is slightly higher than in the mid-wall, and the number of interlayer thermal cycles falls sharply, shortening the grain growth window. Accordingly, the mean grain size decreases again to ≈ 869 μm [517].

Notably, although the basal and crown regions both contain ≈ 0.2 at.% Al, the initial grains in the crown segment are already markedly coarser owing to cumulative heat input [518]. XRD results presented in Fig. 4-11 show that the basal, mid-height and crown sections of the FCG specimen all display the characteristic FCC reflections of α-Cu, yet their peak positions differ systematically. Because the lattice parameter of a Cu–Al solid solution

expands linearly with increasing Al content [519,520], the (111) peak from the Al-rich mid-section is displaced to lower 2θ values relative to those from the basal and crown regions, indicating alloying-induced lattice expansion and an overall shift towards lower diffraction angles.

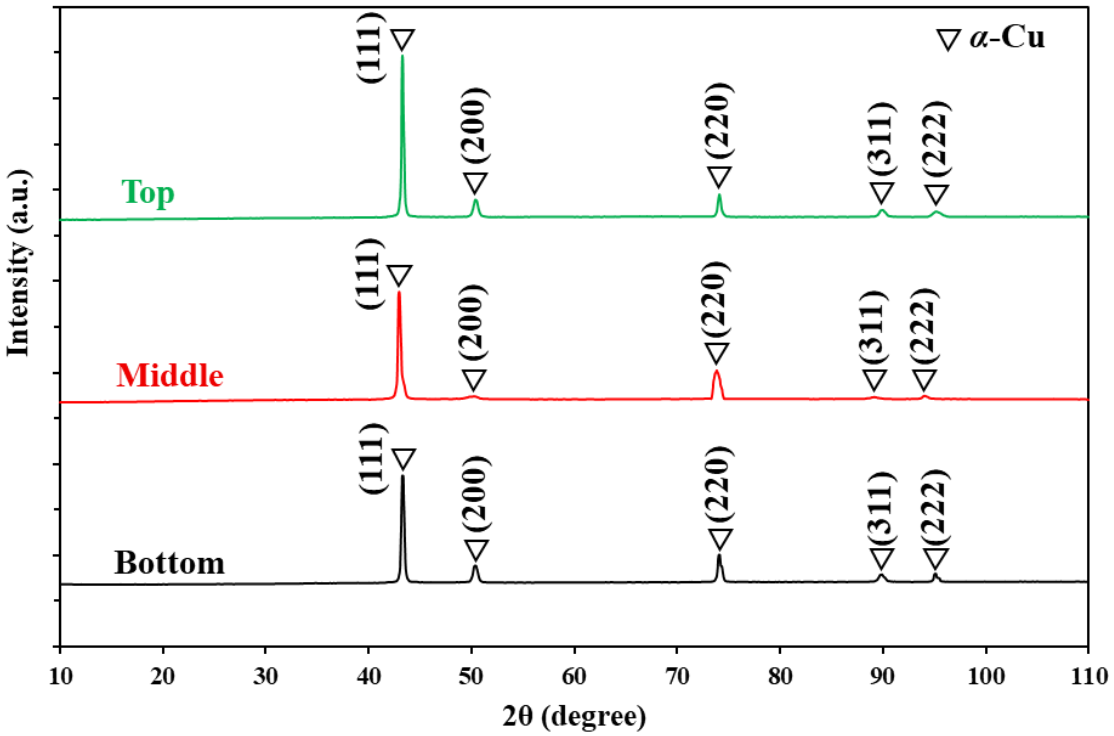

Figure 4-11 XRD analysis of distinct regions within the FCG specimen.

For the basal and crown zones, which share an identical Al level, the alloying-related lattice expansion may therefore be regarded as equivalent. Within the deposit, the maximum (111) diffraction peaks for the basal and crown regions occur at 43.316° and 43.264°, respectively, whereas the reference α-Cu position is 43.297°. The upward shift of the basal peak to higher angle signifies lattice contraction along the diffraction vector, corresponding to compressive residual stress. Conversely, the downward shift of the crown peak denotes tensile stress [521]. Compressive stress raises the apparent activation energy for grain boundary migration and inhibits curvature-driven coarsening, whereas tensile stress lowers the migration barrier and thus promotes abnormal grain growth [522,523]. Accordingly, despite their identical composition, the crown develops larger grains because tensile stress acts synergistically with slow cooling and pronounced thermal accumulation, whilst the substrate-adjacent layers remain comparatively fine grained under the combined influence of compressive stress and rapid interlayer cooling [518].

“Increase–slight decline–sharp surge” evolution of the LAGBs fraction. Along the BD, the LAGBs fraction in the FCG wall exhibits a compound “increase–slight decline–sharp surge” profile (Table 4-5). This reflects the sequential predominance of DDRX in the Al-enriched mid-height segments and CDRX in the Cu-rich upper segments, respectively, each governing the evolution of dislocation structures and grain boundaries.

In the basal SCR-0.2-1 region, rapid solidification and compressive residual stress restrict the transformation of dislocations into walls, so that the LAGBs fraction remains as low as 11.4 %. Upward movement to SCR-11.5 (Al ≈ 11–13 at. %) introduces pronounced thermal accumulation. During the bulging-nucleation and early growth stages of DDRX, dislocation pile-ups generate a dense subgrain network, elevating the LAGBs fraction to approximately 24.2 % [493,509]. In the subsequent SCR-9.1-2 and SCR-4.9 regions, DDRX progresses to subgrain growth and coalescence, converting much of the LAGBs network into newly formed HAGBs, such that the LAGBs proportion temporarily drops below 11 %. Concomitantly, grain growth driven by enhanced boundary mobility yields an average size of 1370 μm, corroborating the “LAGBs-to-HAGBs” transition as the trigger for abnormal coarsening [493,524].

When the Al content decreases to the Cu-rich SCR-2.2 zone, the low SFE and the tensile/slow-cooling stress field suppress HAGBs nucleation but sustain continuous accumulation of dislocation walls; thus, CDRX enters its early "subgrain rotation" phase, in which the LAGBs fraction surges to 77.5 %, whereas only 22.5 % HAGBs are produced. Although the abnormal grain growth reaches 1.90 mm, this results from tensile-stress-assisted curvature-driven migration rather than complete subgrain amalgamation. The capping layers (SCR-0.6 and SCR-0.2-2) undergo merely the final heat cycle; subgrains have insufficient time to rotate and merge, so that the LAGB proportion remains at 52–60 %, corresponding to ~0.87 mm intermediate-sized grains and 39–48 % HAGBs, characteristic of an “immature” CDRX microstructure [506].

Consequently, the multi-peaked LAGB evolution is the direct manifestation of successive DDRX (subgrain generation → HAGB conversion) and CDRX (subgrain accumulation → rotation and coalescence) mechanisms operating within distinct thermal–compositional windows: LAGBs rise during early DDRX, fall upon their conversion to HAGBs, surge again in early CDRX, and remain high when deposition terminates before complete coalescence.

As the Al content continues to decline to SCR-2.2, the combination of residual tensile stress and slow cooling suppresses the nucleation of new HAGBs while promoting the continual accumulation of dislocation walls. CDRX therefore enters an “early subgrain rotation” stage, in which LAGBs fraction rises sharply to 77.5 %, yet, owing to the limited thermal window, only 22.5 % HAGBs are generated [498,509]. The grains nevertheless coarsen abnormally to 1.90 mm, indicating that the tensile-stress–curvature driving force has reduced the resistance to boundary migration.

The terminal crown regions (SCR-0.6 and SCR-0.2-2) undergo merely the final heat cycle. Subgrains have insufficient time to rotate and merge, so that the LAGBs proportion remains at 52–61 % and 39–48 % HAGBs, characteristic of an “immature” CDRX microstructure [498].

Hence, the multi-modal variation in LAGBs fraction reflects the successive dominance of DDRX and CDRX within different thermal–compositional windows: in early DDRX, the LAGBs fraction first increases and then decreases rapidly as LAGBs transform into HAGBs, whereas in early CDRX the LAGBs fraction surges and, if deposition terminates before full rotation and coalescence, the high LAGBs proportion is retained [506,508,509].

4.2.3.2 RCG sample

Fig. 4-12 presents IPF-BD maps together with the corresponding Al EDS maps for each SCR of the RCG specimen, arranged in order of increasing deposition height.

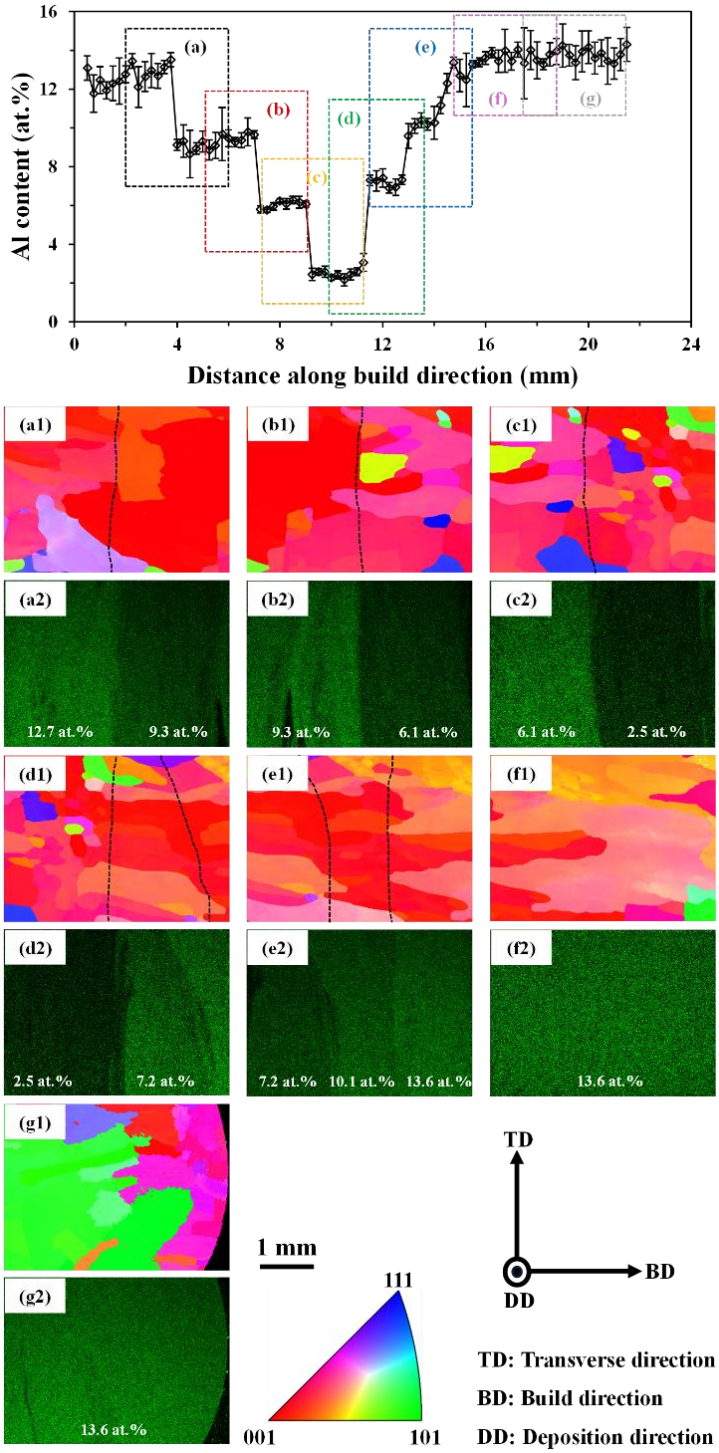

Figure 4-12 Al Microstructural evolution of the RCG sample. An accompanying Al content profile measured along the BD of the RCG wall. Dashed coloured boxes labelled (a)–(g) delineate the heights at which EBSD and EDS analyses were performed. (a1–g1) IPF-BD maps for the transverse section at each boxed position; the colour key corresponds to the stereographic triangle shown bottom-centre. The dashed black line marks the fusion line. (a2–g2) Corresponding Al EDS maps revealing compositional partitioning along the BD. Average Al contents (at.%) for the different regions in each field of view are annotated.

The basal SCR-12.7 region (Fig. 4-12 (a1),(a2)), characterised by an average Al content of ~12.7 at.%, exhibits a typical coarse columnar morphology with a mean grain size of 1193 μm. Grain boundaries are dominated by HAGBs (84.4 %), whereas LAGBs constitute only 15.6 %. Two factors account for this microstructural state: (i) Solid solution of ~12.7 at.% Al markedly lowers the thermal conductivity of the alloy, thereby attenuating lateral heat dissipation within the melt pool and channelling the heat flux primarily towards the massive substrate. A steeper vertical thermal gradient is thus established at the solid–liquid interface [459,525]. Concurrently, Al reduces the thermal diffusivity, impeding the advance of the solidification front [525]. The combined effect elevates the ratio G/R, intensifying columnar grain competitive growth and widening the primary columnar spacing, so millimetre-scale coarse grains are obtained [459,526,527]. (ii) Because the melt pool lies close to the highly conductive substrate, heat is removed rapidly in two dimensions. Although the instantaneous cooling rate is high, viscous flow in the melt pool and the thermal tie to the substrate constrain the actual interface velocity, yielding a high-G, low-R combination that most strongly favours columnar solidification along the heat flow direction (i.e. the BD) [459,471,526].

With further progression along the BD into SCR-9.3 (Fig. 4-12 (a1),(a2),(b1) and (b2)), the coarse columnar grains thicken to an average diameter of 2041 μm, while the fraction of LAGBs surges to 32.7 %. This behaviour may be interpreted in terms of the coupled evolution of alloy thermo-physical properties and WAAM thermal history: (i) Compared with the underlying 12.7 at.% Al layer, the reduced Al content (9.3 at.%) slightly elevates the thermal conductivity of the deposit and raises the liquidus temperature, thereby diminishing the vertical thermal gradient at the solid–liquid interface while allowing the solidification front to advance more rapidly. The resulting decrease in the G/R ratio weakens lateral inhibition between columnar grains, promotes their sideways coarsening and extends the solidification time [459,527,528], facilitating continued millimetre-scale grain growth. (ii) From SCR-9.3 upwards, the underlying microstructure is repeatedly subjected to partial remelting and thermal cycling during subsequent layer deposition. Although the peak temperature is insufficient to fully dissolve the columnar trunks, it is adequate to activate dislocation recovery, rearrangement and subgrain rotation. The extended secondary solidification interval and elevated relaxation temperature enable newly formed subgrain boundaries to subdivide the original HAGBs, causing the LAGBs content to increase dramatically while the HAGBs proportion falls to 67.3 %. In addition,

accumulated heat and a shortened heat dissipation path reduce the interlayer cooling rate. Thermal-stress relaxation therefore proceeds mainly via multidirectional dislocation climb rather than grain boundary migration, further stabilising the subgrain network [492,498,529,530].

Ascending further, the Al content declines to 6.1 at.% in SCR-6.1, where the mean grain size contracts abruptly to 990 μm and a few equiaxed grains emerge adjacent to the fusion line (Fig. 4-12 (b1),(b2),(c1) and (c2)). The proportion of HAGBs attains its maximum at 86.5 %, whereas LAGBs comprise only 13.5 %. The same tendency intensifies in the lowest-Al SCR-2.5 (d = 568 μm), which exhibits the finest equiaxed clusters and an elevated LAGBs fraction of 57.6 % (Fig. 4-12 (c1),(c2),(d1) and (d2)).

The reduction in Al content exerts a dual influence on the thermo-physical solidification conditions. First, the thermal conductivity and diffusivity rise markedly as Al decreases, enabling melt pool heat to dissipate more rapidly into the wall and the surrounding atmosphere, thereby increasing the instantaneous cooling rate and shortening the grain growth window [459,471,525]. Secondly, the liquidus temperature shifts upward and the viscosity diminishes, so the solidification front advances more quickly. Simultaneously, enhanced lateral heat loss attenuates the vertical thermal gradient, causing the overall G/R ratio to collapse and favouring the nucleation of equiaxed grains [459,526–528]. Under this coupled field of "high cooling rate combined with low G/R", heterogeneous nucleation is frequent while grain growth is constrained, so the grain size refines rapidly from the millimetre to the sub-millimetre scale as the Al level falls [527].

In addition, the low-Al regions lie in the mid-height of the component and experience the greatest number of remelting–partial-melting cycles: repeated thermal stresses continually remelt and truncate the original columnar framework, and rapid solidification further regenerates fine equiaxed grains. Concurrently, dislocations undergo recovery, polygonisation and rotation under repeated thermo-mechanical coupling, forming a dense subgrain network that raises the LAGBs fraction to 57.6 % and lowers the HAGBs proportion to 42.4 % [492,498,529].

Beginning in the mid-height of the wall, the Al content rises once more. In SCR-7.2 the mean grain size is 1187 μm and the LAGBs fraction falls slightly to 33.4 %. Further upward, pronounced subgrain refinement occurs in SCR-10.1: although the average grain

size remains ~1135 μm, the LAGBs fraction increases to 61.2 % and the HAGBs fraction declines to 38.8 %, indicating that the coarse grains are subdivided internally into cellular sub-structures formed by dense dislocation–subgrain boundaries [492,498]. At the very crown, within SCR-13.6, the cooling rate is at its lowest and the thermal gradient again favours columnar growth. The grains therefore coarsen to 1991 μm, accompanied by moderate subgrain partitioning (LAGBs 38.2 %) and a recovery of the HAGBs fraction to 61.8 % [459,529,530].

On the one hand, renewed Al solid solution endows the upper layers with a millimetre-scale coarse columnar morphology similar to that observed in the Al-rich zone near the base. On the other hand, despite the nearly symmetrical Al distribution at the bottom and top, the LAGBs fractions differ markedly. Two factors account for this disparity: (i) **Thermal conductivity and heat accumulation effects.** Although high Al content lowers the thermal conductivity in both regions, the basal layers are subject to forced cooling by the substrate. The heat flux is channelled downward, establishing an extreme vertical thermal gradient and a rapid post-solidification temperature drop that precludes significant dislocation recovery and CDRX. By contrast, the crown layers experience pronounced heat accumulation, so the cooling rate is low and the material dwells much longer in the 0.4 to 0.6 Tm regime, known as the "recovery window" in which dislocation glide and subgrain boundary rotation are most active, thereby fostering the formation of a dense LAGBs network within the large grains [459,471,492,527,530]. (ii) **Gradient stress field arising from constrained contraction.** Overall contraction of the component is constrained by the substrate, producing a bottom-to-top gradient in residual stress. As previously noted, the basal region remains under dominant compressive stress. Dislocation slip is inhibited and the stored strain energy is mainly released by glide along existing HAGBs. In the crown, however, tensile stress develops during cooling owing to the thermal-contraction mismatch with the rigid lower wall. Alternating tensile–compressive cycles promote dislocation accumulation and drive the CDRX “dislocation–subgrain rotation” mechanism, accelerating the generation of LAGBs [492,498,513,531]. Table 4-7 lists the mean grain size, and the fractions of LAGBs and HAGBs for every SCR, whilst Fig. 4-13 shows the statistical grain size histograms.

Table 4-7 Quantitative statistics of the mean grain size and the fractions of grain boundaries in the different SCRs of the RCG sample.

Regions	Grain size (μm)	LAGBs (%)	HAGBs (%)
SCR-12.7	1193 ± 327	15.6	84.4
SCR-9.3	2041 ± 573	32.7	67.3
SCR-6.1	990 ± 343	13.5	86.5
SCR-2.5	568 ± 204	57.6	42.4
SCR-7.2	1187 ± 410	33.4	66.6
SCR-10.1	1135 ± 257	61.2	38.8
SCR-13.6	1991 ± 985	38.2	61.8

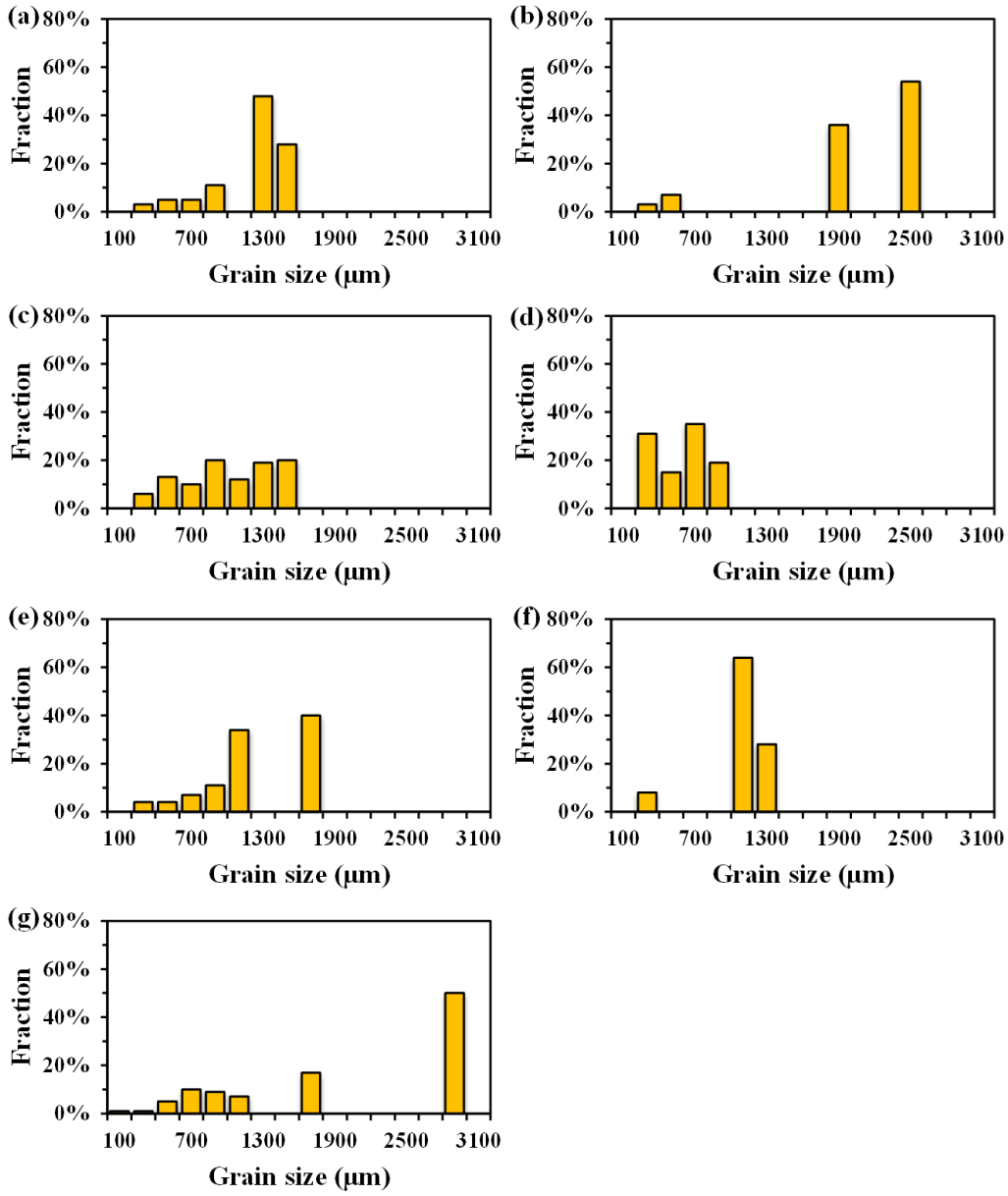

Figure 4-13 Histograms of the grain size distributions for the individual SCRs in the RCG sample: (a) SCR-12.7; (b) SCR-9.3; (c) SCR-6.1; (d) SCR-2.5; (e) SCR-7.2; (f) SCR-10.1; (g) SCR-13.6.

In summary, the microstructural evolution of the RCG specimen is characterised by the following features: (i) **"V-shaped" dependence of grain size on Al content.** Both ends of the compositional spectrum (high-Al regions) exhibit coarse grains, whereas the central low-Al segment displays fine grains, reflecting the influence of Al on the liquidus–solidus separation and the stability of the solidification front. (ii) **Progressive increase in LAGBs content with cumulative thermal cycling.** This trend is particularly pronounced in the upper section, where Al content rises again and the thermal gradient diminishes. (iii) **Complementary variation between HAGBs and LAGBs fractions.** High-Al regions subjected to fewer thermal cycles contain a predominance of HAGBs, whereas zones experiencing intense thermal cycling and cellular sub-structure formation exhibit a higher proportion of LAGBs. (iv) **Sequential change in grain morphology along the BD.** The microstructure evolves through "columnar → columnar-plus-equiaxed mixture → equiaxed → columnar-plus-cellular mixture", governed by the interplay of the imposed thermal history and the compositional gradient.

4.2.4 Crystallographic orientation evolution along the build direction

Fig. 4-14 demonstrates that, in the FCG sample, the Al content initially increases and subsequently decreases along BD from bottom to top, accompanied by a corresponding progressive evolution of crystallographic orientation from a single preferential growth to multivariant competition, and ultimately weakening.

In the low-Al SCR-0.2-1 region at the bottom, the {100} pole figure exhibits a sharp single peak oriented along the DD, indicative of a typical <100> growth fibre with a peak intensity of approximately 22.6 m.u.d. Concurrently, the {110} and {111} pole figures display generally weak and nearly ring-like distributions, suggesting an approximately diffuse distribution of orientations other than <100> (see Fig. 4-14 (a)). With increasing Al content, the single {100} peak gradually weakens and evolves into multipolar discrete spots, fluctuating in intensity within the range of ≈18–22 m.u.d. However, at the high-Al extreme of the SCR-13.3 region, the {100} orientation markedly strengthens again, reclaiming dominance and exhibiting a pronounced increase with a peak intensity reaching approximately 35.4 m.u.d. In contrast, the {111} orientation transforms from an initially near-ring distribution to discrete multivariant spots, yet its peak intensity remains distinctly lower than that of {100}, whilst the {110} orientation remains consistently weak throughout (Fig. 4-14 (b–e)).

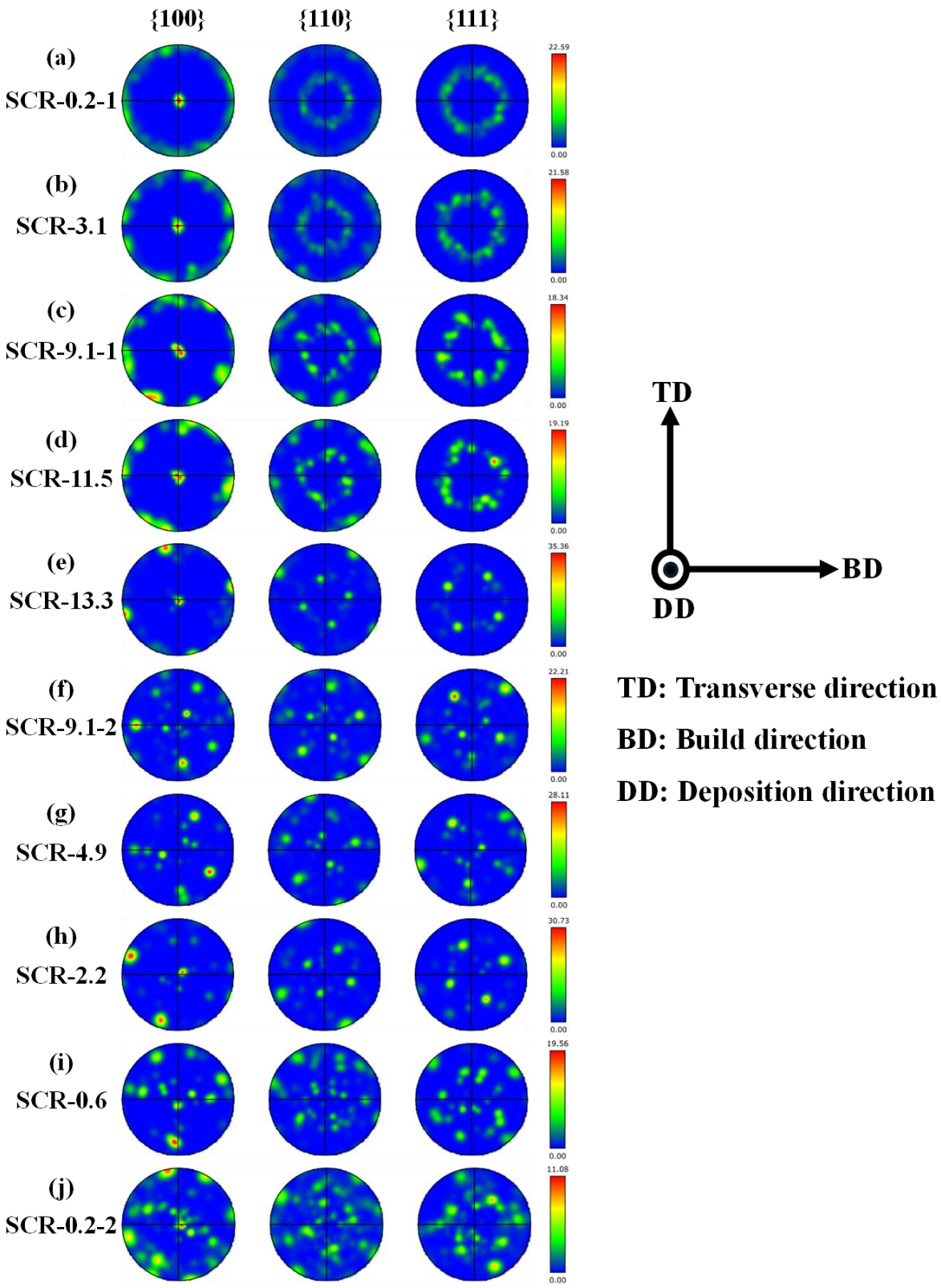

Figure 4-14 {100}, {110} and {111} pole figures of the FCG specimen acquired at successive SCRs along the BD. (a) SCR-0.2-1; (b) SCR-3.1; (c) SCR-9.1-1; (d) SCR-11.5; (e) SCR-13.3; (f) SCR-9.1-2; (g) SCR-4.9; (h) SCR-2.2; (i) SCR-0.6; (j) SCR-0.2-2.

The results indicate that, firstly, the directional solidification kinetics of FCC Cu-based alloys determine <100> as the fastest crystallographic growth direction, given that the isothermal surfaces of the melt pool are approximately aligned with the heat flow direction, which points from the normal of the melt pool surface towards the solidified region [459,532,533]. Consequently, any <100> dendrite trunks approximately collinear with the heat flow direction possess significant configurational advantages during competitive growth [459,532,533]. With increasing Al content, although fine side-branches and misoriented crystals are more readily nucleated, the intensified dendrite coarsening and competitive growth ensure that predominantly only the primary dendrite trunks aligned with the heat flow direction survive. This is manifested by the renewed sharpening of the {100} pole figure in the DD and the formation of a higher intensity peak [459,532,533].

Secondly, as the high-Al region is in the central area of the deposited component, repeated shallow melting and resolidification cycles occur between successive layers during WAAM processing. Consequently, the pre-aligned <100> orientations from previous layers can epitaxially grow across fusion lines, extending into subsequent layers [459,534]. This inheritance, combined with cumulative selection effects, is significantly amplified in regions of high Al content. Although numerous newly nucleated, misoriented grains are initially present, these orientations are more readily truncated during subsequent competitive growth and partial remelting, ultimately resulting in an increased volume fraction of consistently aligned <100> orientations along the DD [459].

Thirdly, {111} orientations primarily originate from twinning, embedding as lamellar or band-like structures within the predominant <100> dendritic matrix. Their geometric continuity and growth anisotropy are inherently weaker than those of the <100> dendrite trunks, and they are prone to partial remelting or obstruction by adjacent <100> dendrites during interlayer thermal cycling, preventing the formation of a continuous, large-scale dendritic framework [459,535]. Therefore, despite the {111} orientations evolving from a ring-like distribution into discrete spots, their peak intensity remains considerably lower than that of {100}, thus playing only a secondary role in modulating the overall texture [535].

Upon entering the segment of decreasing Al content, the pole figures initially maintain relatively high-intensity, discrete hotspots, but subsequently show a progressive decline and reversion to a more dispersed distribution across all orientations. By the uppermost

region with low Al content (SCR-0.2-2), the {100}, {110}, and {111} poles exhibit only weak and scattered spots, marking the most pronounced attenuation in overall texture, with peak intensities declining to as low as 11.1 m.u.d (Fig. 4-14 (j)). The mechanisms underlying this evolution can be elucidated through coupling three primary factors:

Firstly, the decreasing Al content results in a rapid elevation of the SFE of the Cu–Al alloy, thereby enhancing the probabilities of dislocation cross-slip and climb, and accelerating the recovery processes of dislocation cell walls and subgrain polygonisation. Driven by repetitive thermal-mechanical cycling between deposition layers, the initially strongly oriented columnar grains are progressively fragmented into rotated and widened subgrains. CDRX, through incremental misorientation accumulation, systematically converts LAGBs into HAGBs, thus generating randomly oriented fine equiaxed grains and consequently diluting the peak intensities observed in the {100}, {110}, and {111} pole figures [492,506,536–539].

Secondly, with increasing build height, both the melt pool thermal gradient and cooling rates decline synchronously, leading to a significant enhancement of cyclic tensile stresses induced by repeated contraction–reheating–re-contraction at the top region. These tensile stresses not only augment the accumulation of high temperature plastic strain but also encourage the geometrically necessary rotation of dislocation-rich regions, driven by interlayer stress gradients. This accelerates subgrain orientation drift and the randomisation of orientations intrinsic to the CDRX mechanism [459,538–542].

Lastly, a reduction in Al content diminishes solute drag effects and solute shielding provided by dendritic trunks, resulting in rapid dissipation of the solute fields previously anchored around the <100> dendrites. Consequently, the prior competitive advantage of <100> dendrites, which relied upon coupled solute–thermal interactions to engulf adjacent misorientations, is substantially weakened. Concurrently, the reduction in grain boundary migration barriers promotes rapid growth and orientation realignment of subgrains that have already undergone misorientation-induced diffusion, further driven by stress-induced grain boundary migration [532,533,540,543].

Taken together, these factors comprehensively explain the texture evolution in the Al-decreasing segment, culminating in the significantly weakened and dispersed texture observed in the uppermost low-Al region.

Fig. 4-15 illustrates the distinctly non-monotonic texture evolution along the BD from bottom to top in the RCG sample.

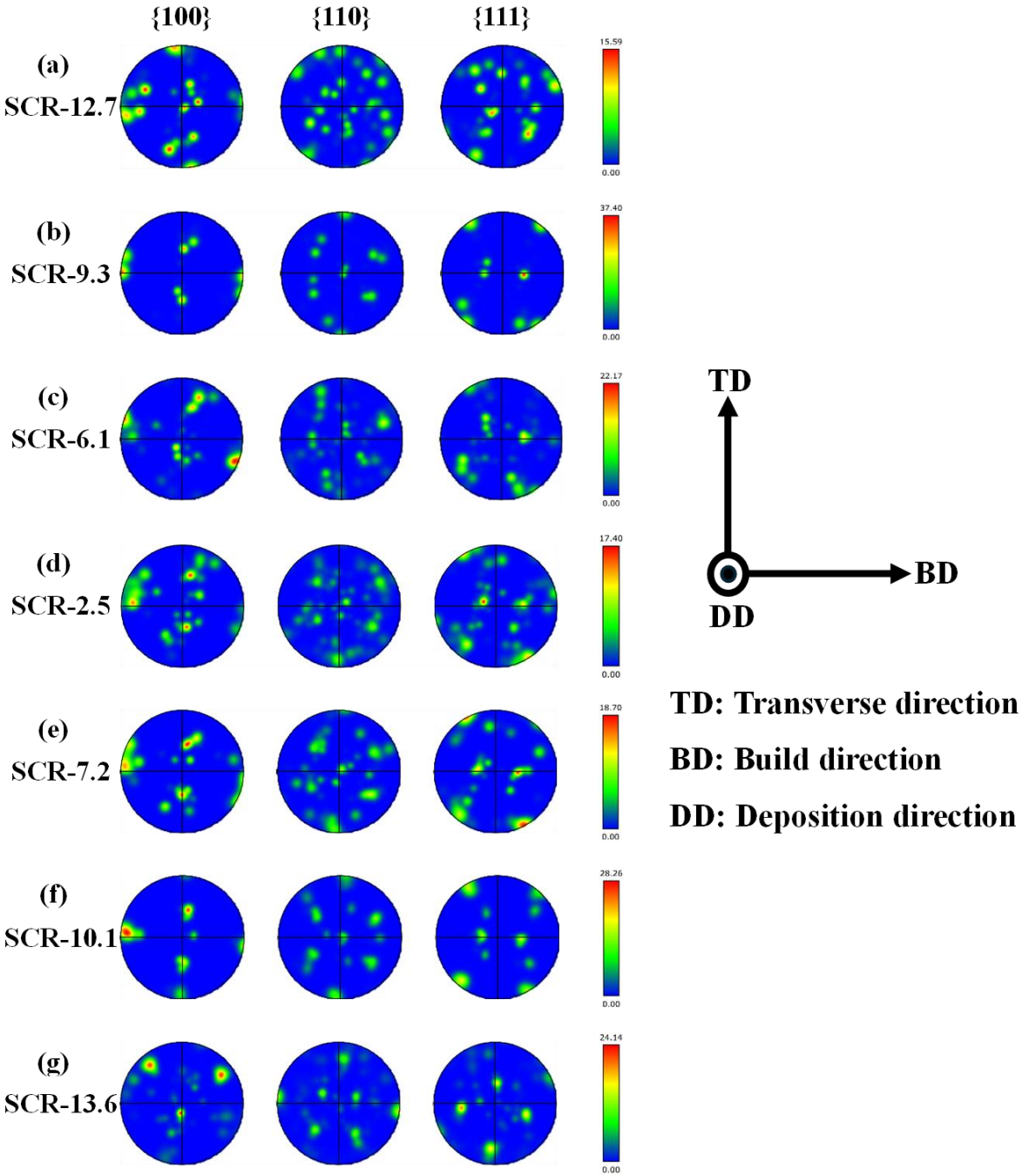

Figure 4-15 {100}, {110} and {111} pole figures of the RCG specimen acquired at successive SCRs along the BD. (a) SCR-12.7; (b) SCR-9.3; (c) SCR-6.1; (d) SCR-2.5; (e) SCR-7.2; (f) SCR-10.1; (g) SCR-13.6.

In the high-Al region at the bottom (Fig. 4-15(a)), the {100} pole exhibits only moderate-intensity hotspots aligned along the DD, whereas the {110} and {111} orientations appear

dispersed and relatively weak. This distribution suggests that, although the dendritic <100> fibre has already been established, it has not yet undergone sufficient competitive selection. With the reduction in Al content towards the central Cu-rich region, particularly at SCR-2.5 (Fig. 4-15(d)), the SFE rapidly increases, facilitating enhanced dislocation cross-slip and climb. This transition promotes CDRX as the dominant microstructural evolution mechanism, causing the original columnar structure to be progressively replaced by rotated and widened subgrains. Consequently, the {100}, {110}, and {111} poles all manifest as multipoint, dispersed patterns, resulting in an overall weakening of texture intensity [492,506,536–539]. It is noteworthy that, within the transitional segments of SCR-9.3 and SCR-6.1, thermo-mechanical cycling still imposes orientation-based selection pressures upon residual columnar grains, resulting in a transient rise in texture intensity peaks [459].

Further along the BD, as Al content increases again towards the top Al-rich region (Fig. 4-15(e–g)), the SFE declines once more, coinciding with reduced cooling rates. Concurrently, the activity of dislocation accumulation and twinning significantly intensifies, leading to DDRX synergistically coupled with repeated thermal cycling. This coupling results in the formation of localised intense peaks of the {110} and {111} poles on the BD–TD plane, thereby restoring the overall texture intensity within the SCR-10.1 and SCR-13.6 regions [459,512,535,541,542].

Thus, the crystallographic orientations observed in the RCG sample exhibit an overall pattern wherein the top Al-rich zone, governed by DDRX, possesses relatively concentrated and moderate-to-high intensity orientations, whereas the central Cu-rich region, dominated by CDRX, shows a tendency towards orientation dispersion and weakened texture. This characteristic evolution is intrinsically correlated to the synergistic modulation arising from Al-induced fluctuations in SFE, transitions between recrystallisation mechanisms, and local differences in thermal history [459,492,506,512,535–543].

4.2.5 Hardness profile along the build direction

Fig. 4-16 depicts the microhardness profiles of the FCG and RCG specimens along the BD. For reference, Fig. 4-16 also includes the experimentally measured composition distribution, shown as black lines, while the microhardness values are plotted as orange lines. A pronounced first-order correlation between hardness and the imposed

compositional gradient is evident, whereas the Hall–Petch effect of grain size and residual stresses generated by the thermal history act as second-order modifiers.

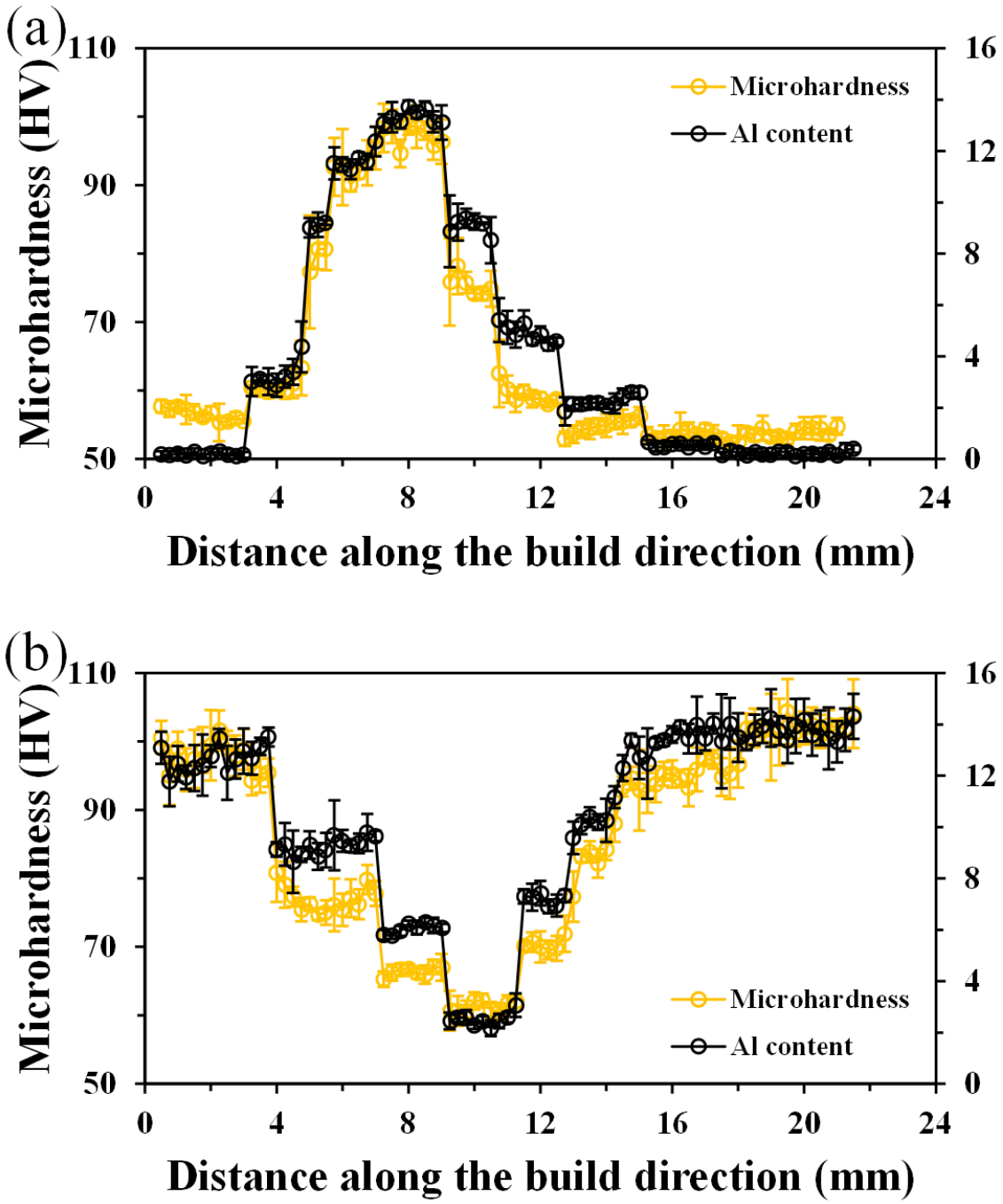

Figure 4-16 Microhardness and composition distribution along the BD. (a) FCG sample. (b) RCG sample. The black lines indicate the experimentally measured composition, and the orange lines indicate the microhardness.

The FCG specimen exhibits a characteristic inverted-V-shaped profile (Fig. 4-16 (a)). At the basal Cu-rich regions, the presence of 0.4–0.5 mm fine grains is counter-balanced by

an almost negligible solid solution contribution, so the hardness remains at ≈ 56 HV [544,545]. As the deposition height increases towards the Al-rich mid-section, the Al concentration rises sharply and the grain size also enlarges. Although grain coarsening attenuates Hall–Petch strengthening, the increase in Al-induced solid solution strengthening predominates, elevating the hardness peak to ≈ 100 HV [544–546]. Near the crown, a steep drop in Al content, further grain coarsening, and the development of significant tensile residual stress owing to free contraction of the final layer combine to reduce the hardness to ≈ 53 HV [544,545].

By contrast, the RCG specimen displays a mirror-image U-shaped profile (Fig. 4-16 (b)). In the initial Al-rich regions, coarse grains coexist with strong compressive residual stress imposed by the substrate, together with high Al solid solution strengthening, this keeps the hardness at ≈ 100 HV [531,547–553]. In the mid-height zones, despite grain refinement, repeated thermal cycling and brief annealing relieve part of the compressive stress, and the reduced Al content diminishes solid solution strengthening, producing a pronounced hardness trough at ≈ 60 HV [552,553]. Further upwards, Al content rises again, and solid solution strengthening is restored. Notwithstanding renewed grain coarsening, the hardness climbs back to ≈ 100 HV [552,553].

In summary, Al solid solution strengthening dictates the positions of the hardness maxima and minima [552,553]. Compressive residual stress at the base and tensile residual stress at the crown respectively amplify or mitigate the combined effects of solid solution and Hall–Petch strengthening, ultimately producing “soft–hard–soft” (FCG) or “hard–soft–hard” (RCG) hardness gradients along the BD [531,544–551].

4.3 Summary

WAAM-fabricated Cu–Al walls with forward (FCG) and reverse (RCG) compositional gradients were systematically compared across geometry, composition, microstructure, texture and microhardness, showing that gradient sequence controls the coupling of thermal history, structure and properties.

Along the build direction, FCG forms an S-shaped wall whereas RCG forms an hourglass. In both, Cu-rich tracks are narrow and deep while Al-rich tracks are shallow and wide, reflecting higher thermal conductivity, a higher liquidus temperature and centripetal Marangoni flow in Cu-rich pools versus thermo-solutal outward flow in Al-rich pools.

FCG contains ten stable compositional zones with a steep Al-ascending and gentle descending segment, while RCG contains seven zones with a minimum Al ≈ 2.5 at.%. This asymmetry arises from deep remelting and vigorous natural convection when a Cu-rich pool overlays an Al-rich substrate, which elevates the lowest attainable Al and suppresses ultra-low-Al regions in RCG. In FCG, a high-to-low *G/R* transition near the substrate triggers CET. Low SFE and thermal cycling in the mid-height Al-rich zone cause intermittent DDRX with fine equiaxed islands, and higher SFE with tensile residual stress in the upper Cu-rich zone drives CDRX-mediated subgrain refinement, with grain size first increasing then decreasing. In RCG, grain size varies in a V-shaped manner with Al content. The Cu-rich mid-section is CDRX-dominated with weakened texture, whereas the Al-rich ends, insufficiently thermo-mechanically cycled, retain coarse columnar <100> fibre texture and the top Al-rich zone shows more LAGBs due to heat build-up and tensile stress. Texture reflects these pathways: in FCG, the <100> growth fibre strengthens during Al ascent and attenuates during Al descent via CDRX, while in RCG overall intensity fluctuates, with dispersed poles in the Cu-rich mid-section and local <110>/<111> hotspots at the top Al-rich zone via cooperative DDRX and twinning.

Microhardness profiles diverge accordingly: FCG shows an inverted-V “soft–hard–soft” trend and RCG shows a U-shaped “hard–soft–hard” trend, with Al solid-solution strengthening setting the extrema and Hall–Petch plus residual stresses providing secondary modulation.

Taken together, the gradient sequence determines how thermal, flow and solute fields overlap in space and time. FCG favours a mid-wall peak in composition and hardness, whereas RCG gives more symmetric ends with a gentle central transition. Using thermophysical contrasts enables control of melt-pool convection, interlayer mixing and recrystallisation to refine grains or strengthen texture where needed. These insights provide a benchmark and mechanistic basis for process–structure–property optimisation of large Cu-based functional-structural gradient components and they guide multiscale gradient-strengthening strategies.

Chapter 5. Microstructure and texture induced by post-printing processes

5.1 Introduction

CGMs, constructed by WAAM, enable spatially tunable properties and functions within a single component and constitute an important materials strategy for integrated manufacturing under increasingly complex service conditions [287,459,513]. Owing to the combined action of a moving heat source and repeated interlayer thermal cycling, WAAM produces pronounced macro- and micro-scale heterogeneity: along the BD there are gradients in thermal history and stress, and the solidification microstructure is commonly characterised by epitaxially grown columnar grains that bear a strong solidification texture [459,513]. Applying subsequent plastic deformation and heat treatment to such graded materials is a routine route to attenuate the as-printed inherited microstructure, homogenise defects, remodel texture and establish deliberately designed property gradients, with CR followed by annealing representing a generally applicable and engineering-feasible process [554,555]. However, the compositional gradient itself, by altering local phase stability, SFE, the level of solid solution strengthening and diffusion kinetics, profoundly modulates the operative deformation mechanisms and recrystallisation behaviour, leading to microstructural and textural evolution that is strongly coupled and highly heterogeneous in space [459,556,557]. Systematically elucidating how CR and annealing regulate the microstructure and texture of WAAM-fabricated CGMs is therefore essential for gradient design and manufacture aimed at integrated structural and functional performance, and it is particularly critical for the subsequent concurrent enhancement of strength and ductility [176,554,555].

This chapter focuses on the microstructural and textural evolution of FCG samples produced by WAAM during CR and annealing. The RCG sample is not considered for the following reasons. First, the finite element model employed here uses composition-dependent constitutive parameters together with a geometrically realistic gradient to predict the spatial distributions of equivalent plastic strain and stored energy. Model calibration and sensitivity analysis have been established on a reproducible FCG data set. Introducing a comparison before completing parameter identification for RCG at a comparable scale would not be rigorous. Second, as a matter of research strategy, this

chapter adopts FCG as a minimal-variable model system to establish the causal chain and operative criteria linking composition, strain, stored energy, recrystallisation and texture. The distinct regularities of RCG will be addressed separately in future work within a complete experimental and modelling framework. These choices enable the present chapter to deliver mechanism-based conclusions of general applicability while maintaining control of variables and statistical reliability.

Regarding research data and methods, this chapter draws on two complementary sources of information. First, EBSD sampling is carried out across multiple SCRs along the compositional gradient, generating orientation maps, local misorientation, grain size and its distribution, grain boundary character distributions and the twin related fraction, together with texture intensity and evolutionary pathways quantified by orientation volume fractions after CR and annealing. Second, a finite element model is established that incorporates composition dependent flow stress and elastoplastic parameters and simulates the spatial distributions of equivalent plastic strain and stress triaxiality under plane strain rolling, to interpret the texture evolution observed by EBSD. The two data sets are paired one to one within each SCR to build a closed loop chain of evidence linking experiment and simulation.

Building on the above framework, this chapter advances the following working hypothesis. During CR, because the yield strength and the work hardening rate vary monotonically with composition, the specimen will exhibit non-uniform strain partitioning across compositional regions together with local gradients in stored energy [558,559]. These gradients will produce systematic spatial differences in subgrain morphology, orientation rotation pathways and the sets of rolling textures [389,492]. During subsequent annealing, the nucleation sites and the sequence in which recrystallisation fronts advance are jointly controlled by the stored energy and the mobility of interfaces [492,536]. Recrystallisation therefore proceeds along the gradient in a defined order and generates zonation in grain size, while orientation selection yields distinct recrystallisation textures [389,492,536]. The central objective of this chapter is to verify and to quantify this hypothesis.

5.2 Results and discussion

Since the non-steady-state characteristics of the initial and terminal layers produced by WAAM can markedly perturb the subsequent deformation and annealing behaviour, the

FCG specimen was sectioned along the BD before CR [459,560]. In the bottom region there is strong dilution and diffusion coupling with the substrate, which drives the local composition away from the designed gradient [471]. The top region is affected by heat accumulation and end-layer effects, and it exhibits geometrical fluctuations in bead morphology together with texture anomalies induced by torch retraction and arc extinction [459,471,560]. To eliminate the compositional and thermal history disturbances associated with these upper and lower boundary zones, several layers adjacent to the substrate and several uppermost layers of the deposit were removed. Only the central segment, within which WAAM processing conditions are stable, melt pool geometry and interlayer temperature fluctuations are minimal, and the compositional profile is approximately symmetric about the geometric mid-plane, was retained for CR and subsequent annealing [459,560]. This ensured that the EBSD and FEM analysis results are statistically representative and mutually comparable. To facilitate understanding of the sectioning workflow, the compositional profile of the WAAM-fabricated FCG specimen along the BD is schematically shown here. Fig. 5-1 shows the Al-content profile along the BD. The red dashed rectangle marks the steady-state window used for CR. The SCR labels match the regions listed in Fig. 5-2 and mark build-direction intervals within this window. The two SCR-9.1 entries denote symmetric locations on the ascending and descending sides. CR comprised seventeen passes, each with a thickness reduction of 0.25–0.5 mm, and the specimen thickness was reduced from the initially sectioned 7.5 mm to a final sheet of 1.5 mm. After rolling, the Al content was measured along the gradient direction (GD) and combined with the original thickness of each SCR, prior to rolling to obtain the actual reduction rate for every SCR in the FCG, the results being presented in Fig. 5-2. For the spatial position of each region, see Fig. 5-1 where the same SCR labels are marked on the composition profile. The rolled specimen was then annealed at 400 °C for 30 min under air-excluded conditions and was immediately water quenched on completion.

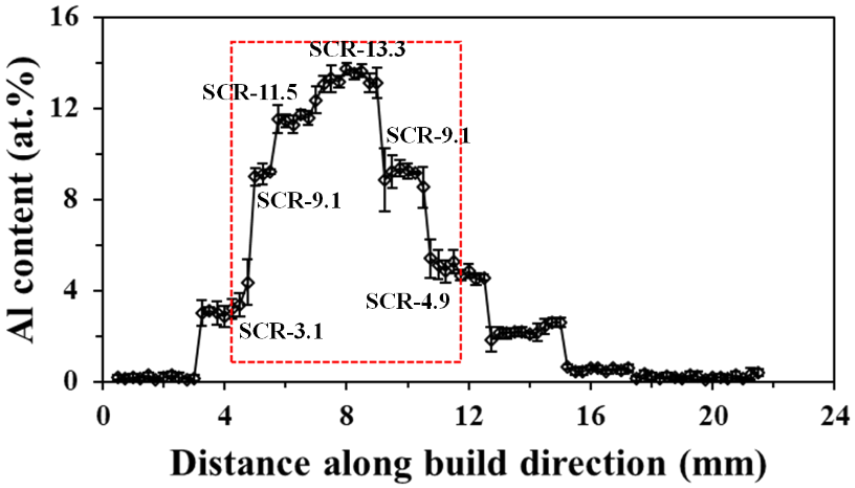

Figure 5-1 Schematic of the sectioning strategy for the WAAM-fabricated FCG specimen. The red dashed rectangle delineates the SCRs retained for CR.

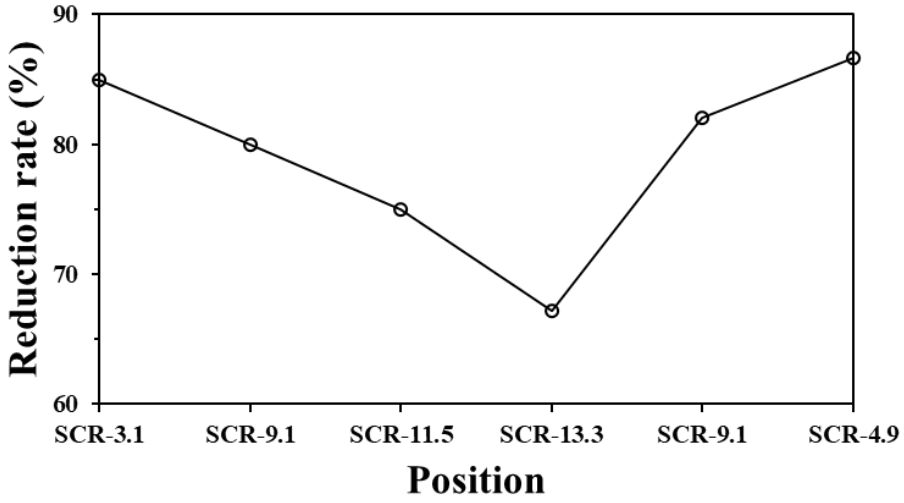

Figure 5-2 Thickness reduction rate after CR for each SCR in the FCG specimen.

The results and discussion in this chapter are structured according to the following structure: First, in Section 5.2.1, post-rolling microstructural characterisation is presented for each SCR, reporting grain and subgrain attributes together with GB character distributions, followed by a systematic exposition and interpretation of the spatial differences. Section 5.2.2 then examines the formation mechanisms of the rolling textures, presents the volume fractions of the principal texture components with their defining characteristics, and analyses the correspondence between orientation-rotation pathways and the operative deformation mechanisms. For the annealing stage, Section 5.2.3 explains, from the temporal and spatial sequence of recrystallisation onset, front advancement, and grain growth, how grain size zonation and GB engineering features in different

compositional regions are jointly governed by stored energy and interfacial mobility. Section 5.2.4 provides the signatures and evolutionary logic of the annealed textures, discusses the contribution of orientation selection to the final texture, and establishes links to the orientational inheritance from the CR stage. Throughout, strain and stress fields from FEM are employed as the interpretive framework and are cross-checked against multiscale EBSD evidence, thereby establishing within the FCG system a verifiable and predictive set of rules for microstructure and texture evolution.

5.2.1 Microstructure induced by cold rolling

In the as-built condition, the WAAM-fabricated FCG exhibits epitaxial columnar grains aligned with the BD and a pronounced solidification texture. Inter-layer reheating gives rise to a cellular and subgrain structure with elevated dislocation density. Comprehensive EBSD results for all SCRs are documented in the earlier chapter on as-built characterisation. The present chapter therefore takes that state as the baseline prior to CR and annealing.

Fig. 5-3 is an image quality (IQ) map overlaid with GBs. Black lines denote HAGBs and blue lines denote LAGBs. The figure reveals the microstructural features of the different SCRs in the FCG sample after CR. The IQ map is a grey scale rendering based on EBSD pattern quality. The grey level correlates positively with the sharpness of the Kikuchi bands. Bright regions indicate sharp patterns, small orientation gradients, low dislocation density and stable indexing. Dark regions correspond to degraded patterns and pronounced local lattice distortion, including areas of high dislocation density, regions with strong orientation gradients, and sites such as shear bands that are prone to mismatch or difficult to index [561,562]. Consequently, the criss-crossing crack-like black network comprises CR-induced microbanding or shear bands together with their junctions. The bands are oriented approximately along the direction of maximum shear stress, they are inclined by about thirty to forty degrees to RD, and they cut across multiple grain boundaries. They cluster and percolate across the RD–GD section, as indicated by the intersecting white lines in Fig. 5-3. Deformation inside the bands is highly localised and the pattern quality is the lowest [562,563].

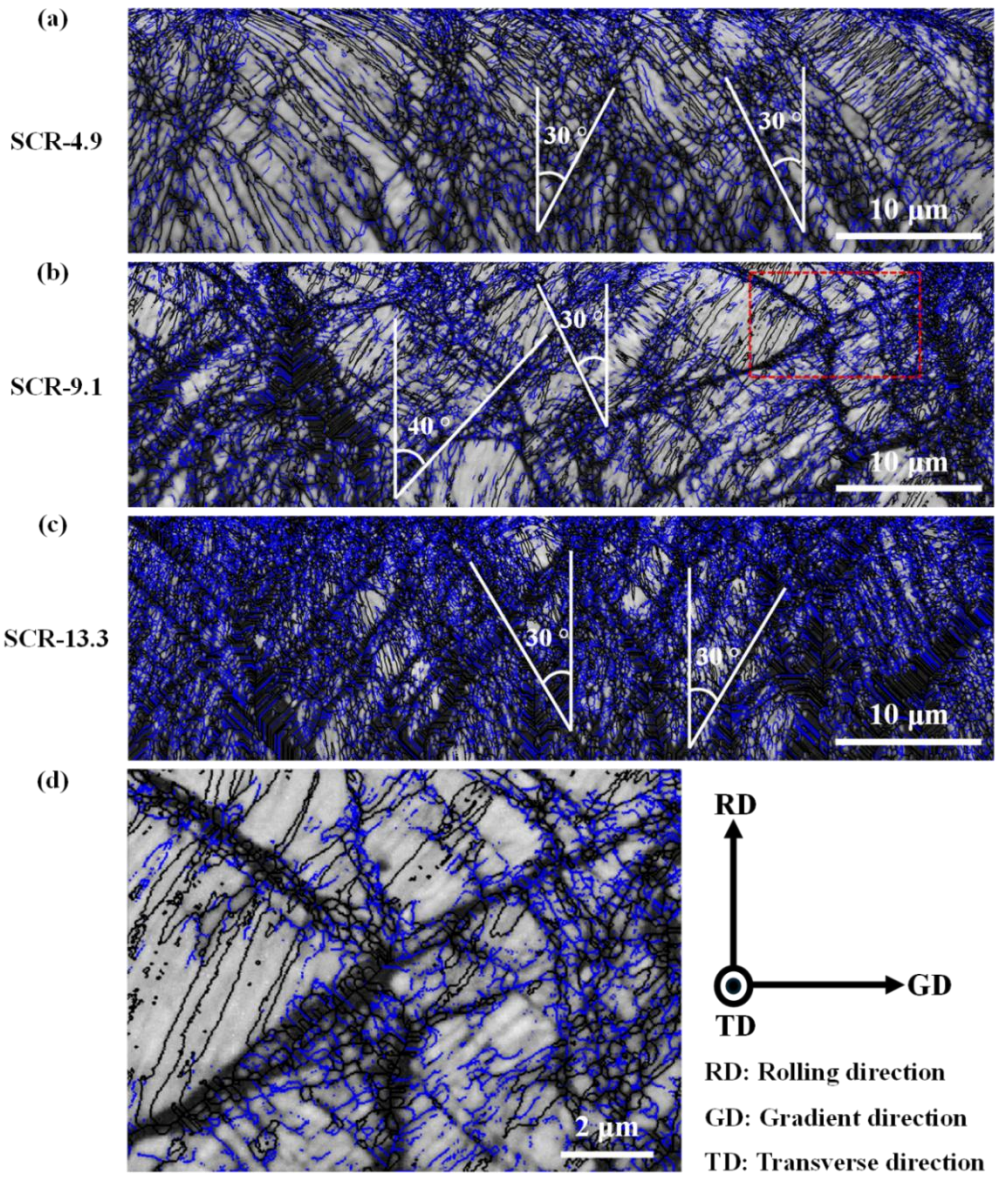

Figure 5-3 EBSD IQ + GBs maps for the different SCRs in the FCG specimen after CR. (a) SCR-4.9; (b) SCR-9.1; (c) SCR-13.3; (d) Enlarged view of the red dashed rectangle in (b). Black lines delineate HAGBs, whereas blue lines denote LAGBs.

In SCR-4.9 (Fig. 5-3 (a)), the band-like features are fine and discontinuous, with diverse inclinations and spacings. Their widths are narrow and the area fraction is small. In SCR-9.1 (Fig. 5-3 (b)), the banded zones become markedly thicker and highly interconnected, often intersecting in multiple orientation sets to form nodal junctions. In SCR-13.3 (Fig. 5-3 (c)), the black banded regions are the coarsest and almost traverse the field of view, giving the highest area fraction and signifying the strongest shear localisation together with severe orientation gradients within the bands. Fig. 5-3 (d) is an enlarged view of the red dashed rectangle in (b). Within the black bands two phenomena are evident: first, equiaxed

ultrafine grains appear within the band core. Second, the band and its enveloping transition zone contain a high density of LAGBs [492,562,564]. Numerous studies show that once deformation localises into a shear band, the lattice undergoes intense orientation rotation and refinement, and equiaxed ultrafine grains frequently develop at the band core. This can occur through CDRX and under very strong shear it can also arise from fragmentation and coalescence of the substructure. Across systems including Cu alloys, stainless steels and Al–Mg alloys, a typical morphology has been observed in which the band core is filled with equiaxed fine grains, and this signature is widely regarded as primary evidence for identifying shear bands [492,564]. Furthermore, a shear band is not a single layer but a hierarchical structure comprising a core, a transition zone and the surrounding matrix. The transition zone outside the core bears a very large gradient in shear strain, dislocation walls and microbands form densely, and a network of LAGBs is produced [492,562]. This accounts for the network-like enrichment of LAGBs around the black bands in Fig. 5-3 (d). The combination of an equiaxed fine-grained core with a transition zone that is rich in LAGBs has been systematically reported as the crystallographic cross-section of a shear band [492,562,564].

The foregoing differences are jointly governed by the SFE and the actual reduction rate of each SCR. Two lines of evidence are first set out. First, increasing the Al content reduces the SFE of Cu–Al alloys. A low SFE suppresses cross-slip and dynamic recovery, renders slip more planar and markedly elevates the activity of faulting and twinning [506,537]. The nucleation threshold for shear bands is thereby lowered and band multiplication and refinement are promoted [492]. Second, during CR a shear gradient exists through the thickness, aligned with the compositional gradient in this study and driven jointly by friction and the roll-bite geometry [565]. This gradient typically manifests as a stronger shear component near the surface, whereas the centre approaches plane strain compression [565]. The gradient increases the propensity for near-surface microbanding or shear banding, yet its influence is subordinate to the intrinsic control exerted by the SFE [492,565]. The through-thickness reduction acts primarily as an amplification factor that shifts initiation sites and alters connectivity, and it is unlikely to overturn the dominant role of a low SFE [506,565].

In the outermost SCR-4.9, although the shear is strong, the relatively high SFE renders cross-slip and recovery active, and dislocations redistribute readily across multiple

systems. The bands are therefore fine and discontinuous, LAGBs string together along the band margins yet are reluctant to coalesce into abundant equiaxed ultrafine-grained cores within the bands [506,565]. The volume fraction of equiaxed ultrafine grains inside the bands is low and the connectivity is poor. In the subsurface SCR-9.1 the SFE has decreased appreciably, planar slip and faulting together with twinning act in concert with the still considerable near-surface shear, the shear band lamellae thicken, their length and connectivity increase, clusters of equiaxed fine grains appear at band intersections, the band contrast darkens further, and both the number density and the degree of maturity take intermediate values [506,565]. Finally, in the central SCR-13.3, although the shear intensity is the lowest in the mid-thickness, the very low SFE minimises the thresholds for shear localisation and refinement. Numerous microbands therefore nucleate in parallel under modest local shear and rapidly coalesce, forming a dense, networked and most mature shear band population, with band cores filled with equiaxed ultrafine grains and the darkest band contrast [565].

Fig. 5-4 presents the grain size distribution histograms for each SCR in the FCG sample after CR, extracted from Fig. 5-3. Following CR, the grain size distributions across the three SCRs evolve stepwise from a bimodal profile with retention of coarse grains to a unimodal profile with pervasive refinement. In SCR-4.9 (Fig. 5-4 (a)), the mean grain size is the smallest, the distribution is broad and bimodal, with multiple bins at the fine-size end and a retained coarse peak at about 20 μm. Compared with SCR-4.9, SCR-9.1 (Fig. 5-4 (b)) exhibits a lower mean grain size, a markedly attenuated coarse mode, and an overall shift towards smaller sizes. In SCR-13.3 the mean grain size decreases further to 1.1 ± 0.3 μm, yielding a narrow, ultrafine, near-unimodal distribution, as shown in (Fig. 5-4 (c)). Studies indicate that, in the Cu–Al system, increasing the Al content lowers the SFE. A reduced SFE suppresses cross-slip and dynamic recovery, renders slip strongly planar, and intensifies faulting and twinning activity, thereby increasing the propensity for strain localisation [506,537]. Further work has shown that low-SFE alloys during cold deformation more readily develop dense and mature shear bands, whose cores contain equiaxed fine grains and whose shells are enriched in LAGBs, reflecting continuous orientation refinement together with subgrain rotation and coalescence [492,506]. As the volume fraction of shear bands increases, the statistical grain size distribution shifts wholesale towards smaller sizes and narrows appreciably [492]. Conversely, at higher SFE, cross-slip and recovery are more active, and deformation is more homogeneous. Coarse

grains that are insufficiently refined are more likely to be retained statistically, producing a bimodal size spectrum, a tendency also summarised in classical recrystallisation and continuous refinement frameworks [492]. In addition, studies have shown that a through-thickness shear gradient arises during CR from the combined action of friction and roll-bite geometry, stronger near the surface and weaker at the centre, although this geometric effect typically modulates rather than overturns the overall trend that low SFE promotes refinement [565]. On this basis, the grain size distributions of the three SCRs in this study can be interpreted as follows. In SCR-4.9 deformation is more homogeneous, coarse grains are retained, and a bimodal spectrum emerges [492,506]. In SCR-9.1 shear banding and refinement intensify and the coarse mode diminishes [492,506]. In SCR-13.3 continuous refinement driven by shear banding is strongest, the size spectrum becomes unimodal and falls within the submicrometre to micrometre range, consistent with literature reports on the coupling pathway from low SFE to shear banding to refinement [492,506,537].

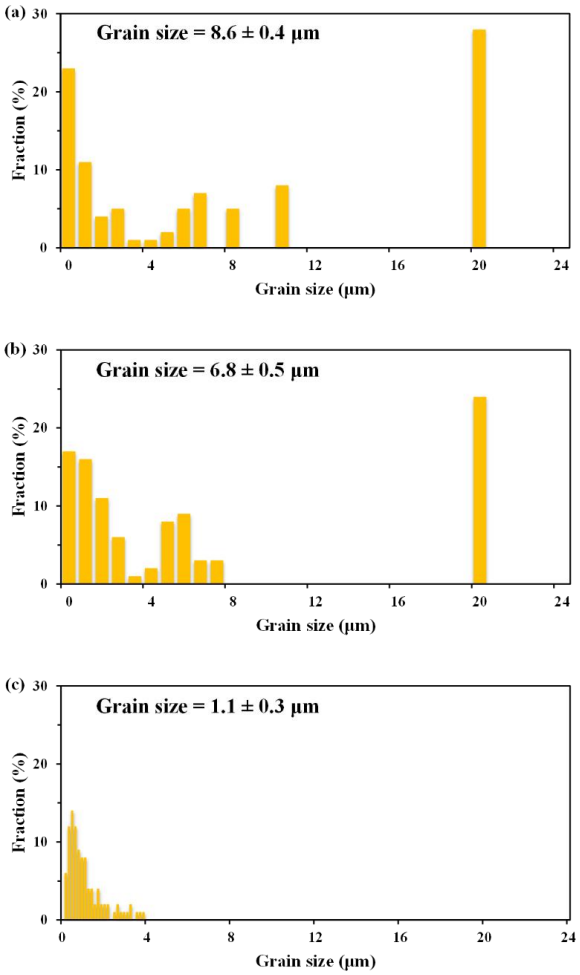

Figure 5-4 Histograms of the grain size distributions for the individual SCRs in the FCG sample after CR. (a) SCR-4.9; (b) SCR-9.1; (c) SCR-13.3.

Table 5-1 summarises the fractions of LAGBs and HAGBs, for each SCR shown in Fig. 5-3. The table shows that as the average Al content in the SCRs increases from 4.9 at.% to 13.3 at.%, the fraction of LAGBs rises continuously whereas the fraction of HAGBs declines. This trend is consistent with the compositional effect whereby the SFE decreases with increasing Al content.

Table 5-1 Quantitative statistics of the fractions of grain boundaries in the different SCRs of the FCG sample after CR.

Regions	LAGBs (%)	HAGBs (%)
SCR-4.9	39.0	61.0
SCR-9.1	41.4	58.6
SCR-13.3	47.6	52.4

Studies demonstrate that lowering SFE in Cu–Al alloys markedly alters deformation micromechanics, promoting more planar slip and intensifying faulting and twinning [506,537]. This raises the propensity for dislocations to pile up and form walls on the same slip system, so that a dense substructure and a network of LAGBs are preferentially generated [566]. More critically, studies have directly shown that a low SFE reduces the capacity for cross-slip and suppresses dynamic recovery, leading to an increase in LAGBs density [506,566]. EBSD statistics reveal that the LAGBs fraction increases approximately linearly with strain, a trend that is particularly pronounced in low-SFE austenitic alloys [564,566].

By contrast, an increase in HAGBs usually depends on continuous refinement through subgrain rotation and coalescence together with a certain extent of recovery through cross-slip or climb to raise the misorientation [492,566]. Under higher SFE or more active recovery the conversion from LAGBs to HAGBs proceeds more fully, hence regions with a higher SFE often display a larger HAGBs fraction [492,506]. In the low-SFE region of the present study, SCR-13.3, although equiaxed fine grains can form within shear band cores and produce local enrichment of HAGBs, the network of LAGBs that is widespread outside and around the bands dominates the area fraction. This drives the overall statistics towards increasing LAGBs and decreasing HAGBs. The coexistence of localised fine-grained band cores together with global proliferation of LAGBs in the surrounding matrix

and band shells accords with the classical metallographic description of shear bands [492,564].

In summary, a reduction in SFE caused by composition limits cross-slip and recovery and promotes planar slip. As a result, the LAGBs network forms more readily and is less likely to transform into HAGBs at a given strain, which together explains the observed statistical trend of rising LAGBs and falling HAGBs with increasing Al content [492,506,537, 566].

Following the geometric and topological characterisation of shear band morphology, grain size distributions and GBs characteristics in each SCR, the EBSD-based intrinsic orientation difference metric, KAM, is now introduced to further quantify the dislocation accumulation and local plastic heterogeneity induced by CR. To ensure comparability between SCRs, KAM is computed using a uniform step size with a consistent neighbourhood definition, HAGBs are masked to eliminate their influence on local misorientation, and an image quality threshold is applied to remove low confidence pixels. The subsequent statistics report both the distributional characteristics of KAM values and representative metrics, thereby enabling a comparative analysis of the differences across the SCRs.

Fig. 5-5 shows the KAM maps of the different SCRs in the FCG sample after CR. KAM quantifies the neighbourhood-scale average misorientation, with colour progressing from blue to yellow as the local orientation gradient increases. Studies have established a quantitative relation between KAM and the density of GNDs, so KAM can serve as a surrogate map of plastic localisation and stored energy [538]. Within the field of view for SCR-4.9 (Fig. 5-5 (a)), high-KAM pixels appear mainly as scattered short traces and the map is dominated by blue, with only faint green outlines along a few bands and at certain grain boundaries. In SCR-9.1, green high-KAM bands increase markedly and interconnect along two inclination sets, forming hotspots at their intersections as indicated by the white arrows in Fig. 5-5 (b). SCR-13.3 exhibits the strongest high-KAM network, with the highest areal fraction and connectivity among the three. Numerous yellow patches are visible within bands and at junctions, as marked by the white arrows in Fig. 5-5 (c), consistent with the dense distribution of shear bands in this region. Shear bands act as conduits for concentrated orientation gradients and both their cores and envelopes commonly show high KAM, a conclusion repeatedly substantiated in EBSD studies [564]. Accordingly, as Al content increases and the SFE decreases, from SCR-4.9 to SCR-13.3

the number, intensity and connectivity of high-KAM bands rise in sequence, in agreement with the general finding that low-SFE FCC alloys more readily develop high densities of shear bands and accumulate larger local misorientation [506,564].

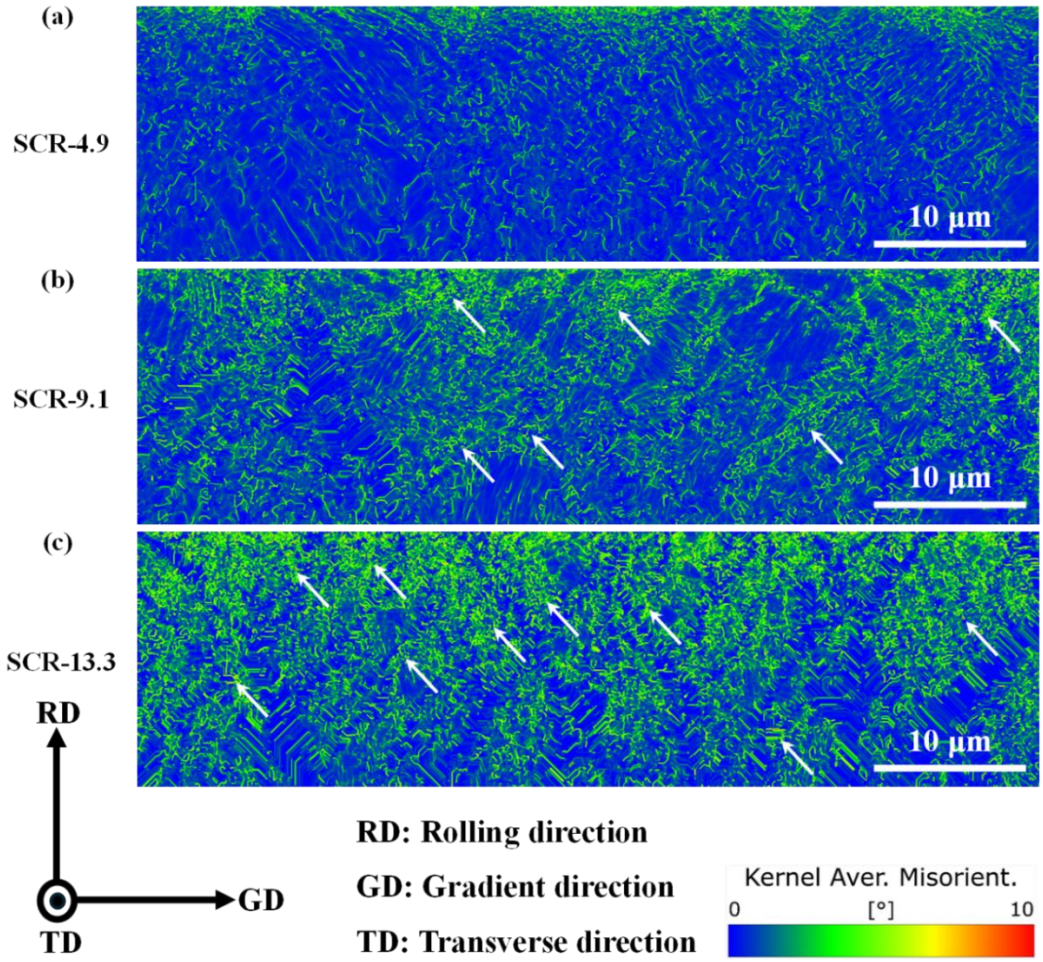

Figure 5-5 KAM maps for different SCRs of the FCG specimen after CR. (a) SCR-4.9; (b) SCR-9.1; (c) SCR-13.3. White arrows indicate hot spots formed within shear bands and at their intersections. Colours indicate the local misorientation angle, from 0 to 10 degrees as shown by the colour bar, with cooler colours denoting lower values and warmer colours higher values.

Fig. 5-6 presents statistical histograms of the KAM value distributions corresponding to Fig. 5-5. The vertical axis labelled “Counts” denotes the frequency. For each bin it gives the number of EBSD measurement points or pixels that were successfully indexed and passed the quality filter, whose KAM value lies within the interval represented by that bin. The sum of counts across all bins equals the total number of valid points included in the statistics [411]. The KAM distribution and mean shift upward and broaden progressively from SCR-4.9 to SCR-9.1 and then to SCR-13.3. In SCR-4.9 (Fig. 5-6 (a)), the principal

KAM peak lies in the low-KAM regime at approximately 0.4–0.6°, with a long tail extending to about 5°, and a mean of 0.87° ± 0.85°. In SCR-9.1 (Fig. 5-6 (b)), the entire distribution translates towards higher KAM, the low-KAM peak diminishes, the long tail persists, and the mean rises to 1.05° ± 0.97°. In SCR-13.3 (Fig. 5-6 (c)), the principal peak shifts further to the right and becomes more pronounced, centred at about 1°, high-KAM pixels increase substantially, the long tail extends to roughly 6°, and the mean attains 1.54° ± 1.12°. This left-to-right peak migration together with tail thickening provides direct quantitative evidence for larger local orientation gradients and a progressive increase in stored energy [538,566].

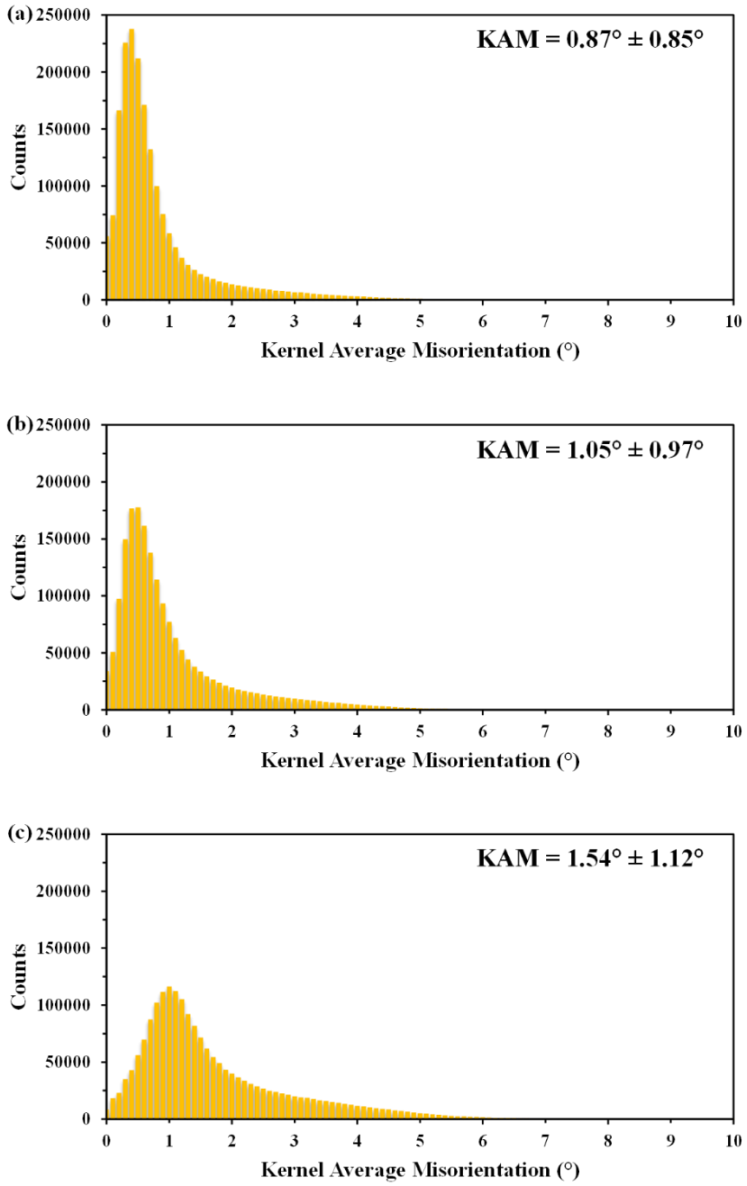

Figure 5-6 Histograms of the KAM distributions for the individual SCRs in the FCG sample after CR. (a) SCR-4.9; (b) SCR-9.1; (c) SCR-13.3.

5.2.2 Texture induced by cold rolling

This section turns to the texture response induced by CR. We first carry out qualitative identification of orientation families from IPF maps and pole figures, using a single projection and a common normalisation scheme to ensure comparability. On this basis, we report the volume fractions of the typical FCC rolling texture components, namely Copper, Brass, S and Goss, together with their twin-related variants, and we assess their evolutionary amplitude and dispersion using a uniform deviation angle criterion and orientation bandwidth. We then combine the distributions of equivalent plastic strain and shear components obtained from finite element simulations to analyse the correspondence between the dominant strain paths within each SCR and the associated orientation rotation trajectories. In doing so, we establish a mechanistic chain that links composition, strain mode and orientation selection, which provides constraints and an interpretive framework for the origin and selectivity of the subsequent recrystallisation textures.

Fig. 5-7 shows IPF-RD maps for the three SCRs of the FCG sample after CR. The colour denotes the crystallographic direction parallel to RD, with the reference IPF triangle shown at the lower right. In SCR-4.9, diagonally oriented banded orientations dominated by red and green are clearly visible. The bands are slender, elongated and continuous, and they often traverse the field of view. Small multicoloured, near-equiaxed fragments are interleaved between the bands. Within many bands the colour is essentially uniform, indicating coherent distribution of the same orientation family over long length scales, as in Fig. 5-7 (a). In SCR-9.1, purple to magenta hues increase markedly. The bands become more uniform and adopt a dense, parallel arrangement. Chevron- or arrow-like interleaving is observed in several areas, and the colours of neighbouring bands alternate frequently over narrow spacings. Near-equiaxed fragments are comparatively fewer, as in Fig. 5-7 (b). In SCR-13.3, long-range parallel bands are much less prevalent. The field of view is filled by a high density of short, multicoloured orientation fragments, giving an overall fine mosaic. Colour changes are more abrupt and occur on finer spatial scales. Only short paired parallel bright bands and sharp reorientations persist locally, and the orientation distribution is more dispersed than in the other two regions, as in Fig. 5-7 (c).

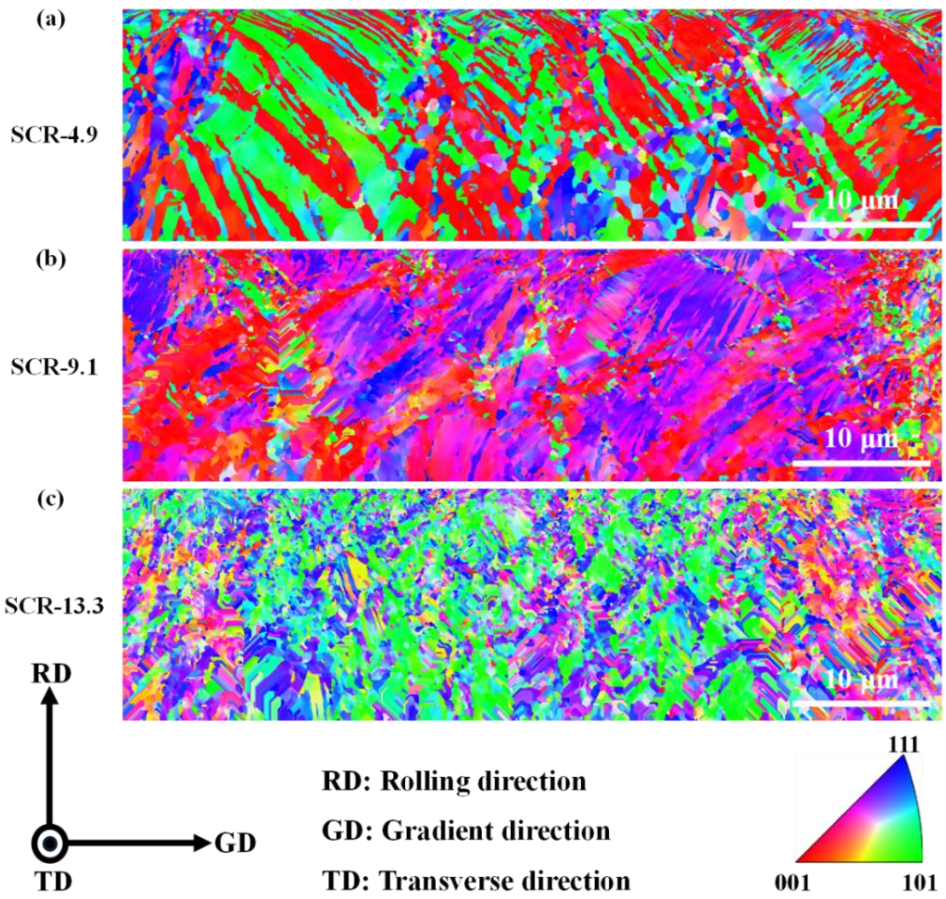

Figure 5-7 IPF-RD maps for different SCRs of the FCG specimen after CR. (a) SCR-4.9; (b) SCR-9.1; (c) SCR-13.3. Colours denote the crystallographic direction parallel to RD according to the colour key.

Fig. 5-8 presents {100}, {110} and {111} pole figures with GD as the projection normal, derived from Fig. 5-7. SCR-4.9 (Fig. 5-8 (a)) shows clear point-like maxima. In the {100} pole figure, symmetric local maxima appear in the four quadrants, and near the perimeter along the RD axis there is one stronger peak above and one below. The {110} pole figure exhibits a regular eight-point symmetric distribution, with the brightest intensities near the TD circumference on the left and right. The {111} pole figure displays strong peaks at the four corners and a pair of enhancements close to the centre along the RD axis.

SCR-9.1 (Fig. 5-8 (b)) retains the same symmetry but the peaks are more concentrated and stronger. The colour scale span of 0 to 14.09 m.u.d. shows that the overall intensity exceeds that of SCR-4.9, which spans 0 to 9.77 m.u.d. In the {100} pole figure two narrower, elongated elliptical bands of enhancement develop along RD. In the {110} pole figure the eight maxima become sharper and the TD sides approach saturation. In the {111} pole

figure both the corner peaks and the RD axis pair become more prominent. This is consistent with the IPF-RD observations for SCR-9.1 in which the parallel bands are denser and the colours more uniform.

SCR-13.3 (Fig. 5-8 (c)) evolves from point-like maxima to continuous diffuse bands and the overall intensity range decreases to 0 to 6.62 m.u.d. In the {100} pole figure two undulating S-shaped enhancement tracks appear rather than discrete poles. In the {110} and {111} pole figures the bright regions broaden markedly. For {111} the local maximum lies near the TD circumference on both sides, while a wide continuous enhancement develops around the RD axis. This diffuse, band-like pole density distribution is consistent with the fine mosaic-like orientation pattern observed previously in the IPF-RD map of SCR-13.3.

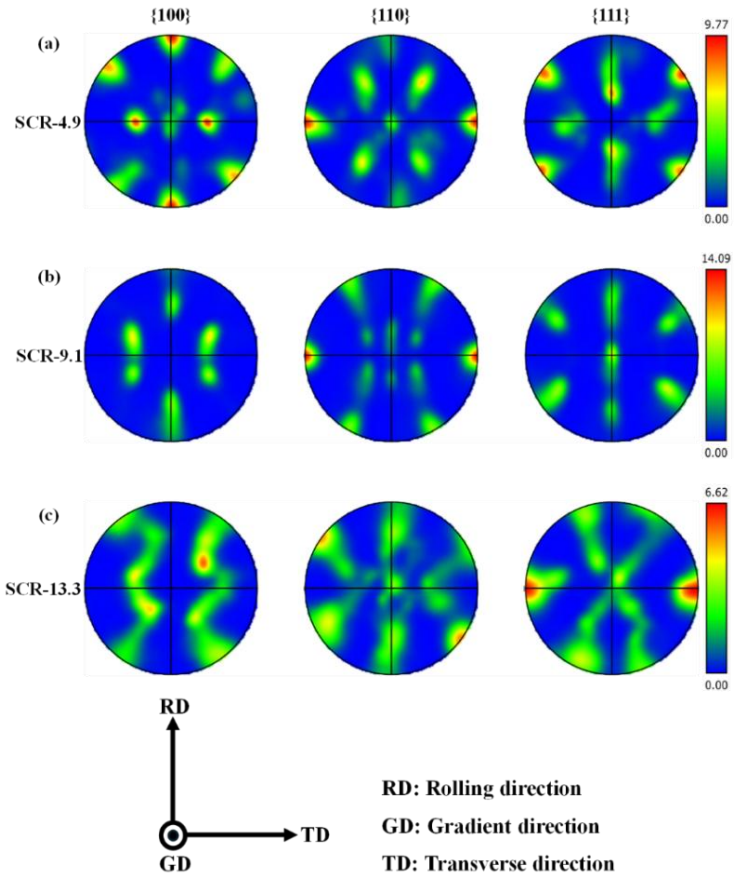

Figure 5-8 {100}, {110} and {111} pole figures of the FCG sample after CR for SCRs: (a) SCR-4.9, (b) SCR-9.1 and (c) SCR-13.3. The projection normal is the gradient direction (GD, out of plane); the in-plane axes are RD (vertical) and TD (horizontal), as indicated at bottom left. Intensities are given in multiples of a uniform distribution (m.u.d.). Colour scales at right apply to each row separately (maxima 9.77, 14.09 and 6.62 m.u.d., respectively).

Fig. 5-9 shows the inverse pole figures along RD, TD and GD, corresponding to Fig. 5-7. In SCR-4.9 (Fig. 5-9 (a)), the RD-IPF exhibits a local bright spot at the <001> vertex. The TD-IPF forms a clear hot spot at the <101> vertex. The GD-IPF is brighter near 101 and weakens progressively along the <101>–<001> edge. In SCR-9.1 (Fig. 5-9 (b)), the RD-IPF evolves from isolated peaks to a narrow band along the <001>–<111> edge. In the TD-IPF the bright spot at <101> becomes sharper and stronger, with an intensity close to the colour scale upper limit of 14.09 for that row. The GD-IPF develops a distinct bright region near the <111> vertex. In SCR-13.3 (Fig. 5-9 (c)), the RD-IPF no longer shows isolated peaks and instead displays a broad, diffuse colour band. In the TD-IPF the strongest bright region shifts to the <111> vertex and locally approaches saturation. In the GD-IPF, intensities are predominantly green along the <101>–<111> edge with a brighter corner at <101>, and the overall intensity across the row is lower.

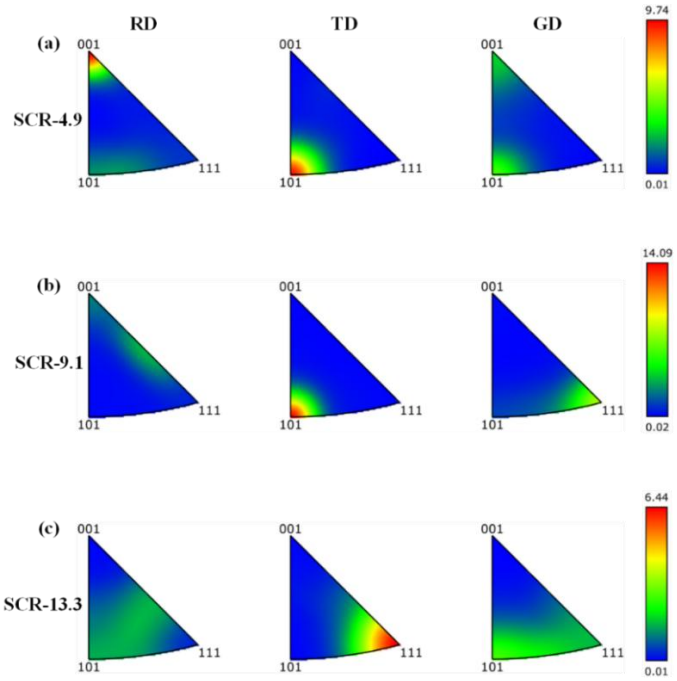

Figure 5-9 Inverse pole figures for the RD, TD and GD of the FCG sample after CR, shown for three SCRs: (a) SCR-4.9, (b) SCR-9.1 and (c) SCR-13.3. Colour indicates orientation density on the cubic fundamental triangle (<001>–<101>–<111>). Intensities are given in multiples of a uniform distribution (m.u.d.). Colour scales at right apply to each row separately (maxima 9.74, 14.09 and 6.44 m.u.d., respectively).

To further quantify the textures of the different SCRs after CR, statistical volume fractions were compiled for each texture component in every SCR, and Table 5-2 lists the Miller

indices for each component. Fig. 5-10 shows clear spatial and compositional differentiation among the three SCRs after CR. In SCR-4.9, the dominant components are Goss and Rotated cube, Copper twin is secondary, Copper is present only in a small amount, and the remaining components are close to zero. In SCR-9.1, the F component rises steeply and becomes dominant, Copper twin increases accordingly, Goss declines markedly, and Rotated cube almost disappears. In SCR-13.3, the texture hierarchy is reordered, with Brass, S and E becoming the principal components, while F, Rotated cube, Copper and Goss all decrease to negligible levels. In trend terms, as the Al content increases from 4.9 to 13.3 at.%, Rotated cube and Goss decay monotonically, F and Copper twin reach a peak in the intermediate composition region SCR-9.1 and then drop rapidly, whereas Brass, S and E rise sharply at the high-Al end and take over as the dominant components.

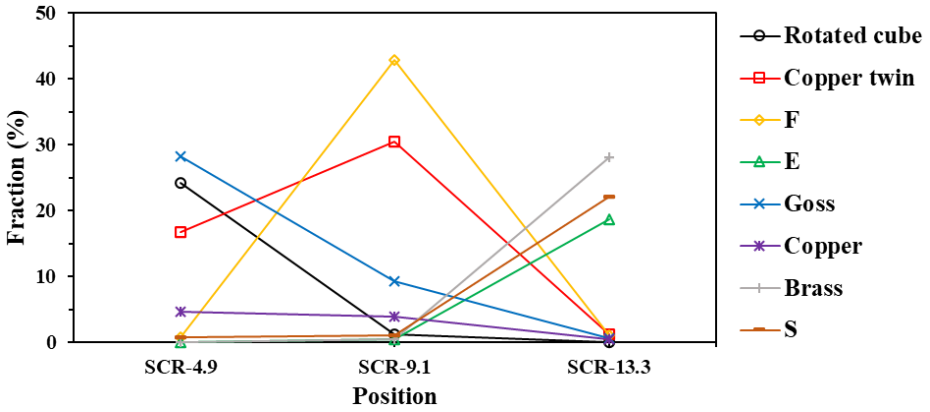

Figure 5-10 Quantified fractions of texture components in the FCG sample after CR, shown for three SCRs (SCR-4.9, SCR-9.1 and SCR-13.3). Components plotted are Rotated cube, Copper twin, F, E, Goss, Copper, Brass and S.

Table 5-2 Miller indices of texture components [482].

Texture component	Miller indices
Rotated cube	{001}<110>
Copper twin	{255}<511>
F	{111}<112>
E	{111}<110>
Goss	{011}<100>
Copper	{112}<111>
Brass	{110}<112>
S	{123}<634>

Building on the texture distributions described above, we now use FEM to elucidate the evolution mechanisms of the CR textures in the FCG sample. Fig. 5-11 (a) shows the finite

element results for the final rolling pass. The map displays the equivalent plastic normal strain ε_n along GD within the GD–TD plane, denoted PE22 in Abaqus. The colour scale from red to blue corresponds to ε_n increasing from values close to zero towards larger compressive magnitudes. The finite element model has a total thickness of 1.5 mm. Along the direction indicated by the white arrow in the figure lie five symmetrically arranged SCRs. In that order their respective thicknesses are 0.2 mm for SCR-4.9, 0.35 mm for SCR-9.1, 0.55 mm for SCR-13.3, 0.2 mm for SCR-9.1, and 0.2 mm for SCR-4.9. The map is evidently symmetric. At both ends, the SCR-4.9 regions are dominated by cool colours. Extensive cyan to blue appears near the roll–strip contact zone, indicating strong compression along the GD. Transitioning inward to SCR-9.1, the colours shift to green to yellow, and the degree of compression diminishes. The central SCR-13.3 is dominated by yellow to red, indicating the smallest compression along GD.

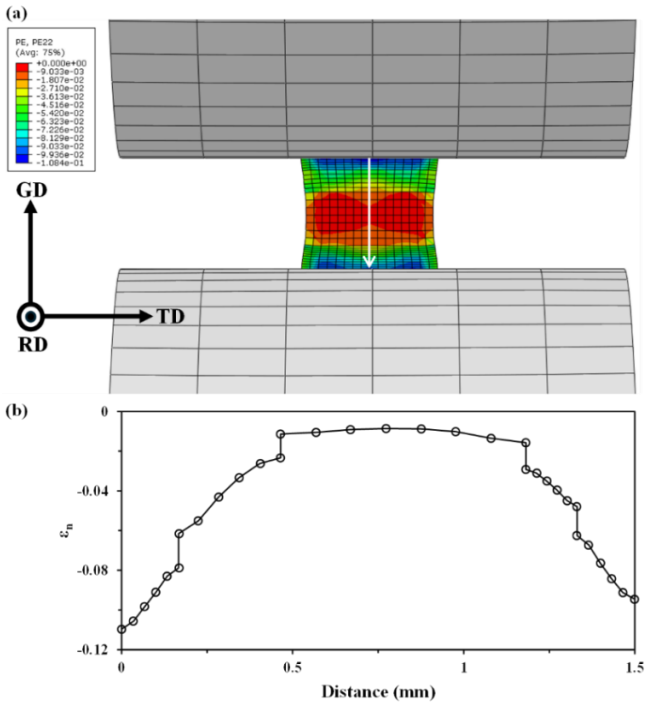

Figure 5-11 Finite element simulation of CR. (a) Contour of the through-thickness equivalent plastic normal strain ε_n, reported as the Abaqus field PE22, in the sheet between the rolls. TD is horizontal, GD is vertical, and RD is out of plane. The white arrow indicates the line along which data were extracted. The colour scale gives equivalent plastic strain, with negative values denoting compression. (b) Through-thickness profile of the plastic normal strain ε_n along the line marked in (a), plotted against distance across the thickness.

Fig. 5-11 (b) shows the ε_n profile along the white arrow. The profile is arch shaped and

approximately symmetric about the midpoint. The largest compression along the GD occurs at both ends, where the strain is close to 0.11. Moving inward, the compressive strain along the GD decreases monotonically, then exhibits two clear steps, and thereafter enters a flat plateau that lies near zero. At the symmetric locations the curve leaves the plateau through the same double-step form and increases to the end maxima. Along the left half, from the edge to just beyond the first step the absolute magnitude of ε_n decreases, and the second step brings the curve onto the plateau. The right half displays a mirror feature. Within the plateau ε_n is only slightly negative, with the centre closest to zero. In conjunction with the compositional layout of the specimen, this magnitude ranking and the step positions directly indicate that the compression along the GD is largest in SCR-4.9 at both ends, intermediate in the adjacent SCR-9.1, and smallest in the central SCR-13.3 [567]. This corroborates the earlier conclusion that the reduction rate is largest in SCR-4.9, intermediate in SCR-9.1, and smallest in SCR-13.3.

Relative to the mid-length at 0.75 mm, the curve is not strictly mirror symmetric. On the left, the rising segment from 0 to 0.55 mm is longer and more gradual, and the two inflections lie clearly at about 0.2 mm and 0.55 mm. On the right, the corresponding falling segment spans only 1.1 to 1.5 mm, the inflections occur near 1.1 mm and 1.3 mm, and the slope is steeper. The plateau extends from 0.55 to 1.1 mm. Its geometric centre is about 0.825 mm, which is shifted to the right of the specimen midpoint. The immediate cause of this left–right difference is the asymmetric thickness allocation of the SCR layers [567]. On the left, SCR-9.1 is 0.35 mm thick and provides a wider transition zone, allowing ε_n to fall from the strong compressive value of the end SCR-4.9 to the weak compression of the central SCR-13.3 over a longer distance. The left slope is therefore extended and shallower. On the right, SCR-9.1 is only 0.2 mm thick, and the transition zone is shorter, so ε_n must rise from the plateau value to the end maximum over a shorter distance, which increases the slope and sharpens the inflections. The two end SCR-4.9 layers are both 0.2 mm thick, hence the magnitudes of the end minima are essentially identical. The plateau width of 0.55 mm matches the thickness of the central SCR-13.3, which indicates that ε_n is approximately stable within this layer and that the compression is minimal.

Next, Fig. 5-12 (a) displays a contour map of the shear strain along RD within the GD–TD plane, denoted as PE12 in Abaqus. Warm colours indicate positive shear, cool colours indicate negative shear, and green corresponds to values near zero. The section exhibits the

typical pattern of opposite signs with positive above and negative below [565,568]. The largest magnitudes are concentrated in the upper and lower surface layers that contact the rolls, whereas the central region is close to zero.

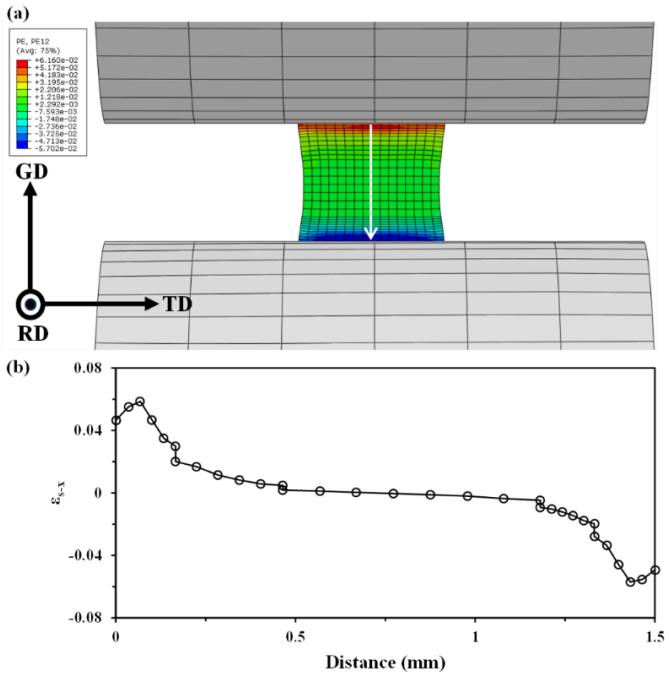

Figure 5-12 Finite element simulation of CR. (a) Contour of the through-thickness RD plastic shear strain $\varepsilon_{s\text{-}x}$, reported as the Abaqus field PE12, in the sheet between the rolls. TD is horizontal, GD is vertical, and RD is out of plane. The white arrow indicates the line along which data were extracted. The colour scale gives shear plastic strain, with negative values denoting compression. (b) Through-thickness profile of $\varepsilon_{s\text{-}x}$ along the line marked in (a), plotted against distance across the thickness.

The RD shear strain profile, $\varepsilon_{s\text{-}x}$, extracted along the white arrow is shown in Fig. 5-12 (b). From 0 to 0.2 mm in the upper surface SCR-4.9, it rises rapidly to a positive peak and then decreases. From 0.2 to 0.55 mm in the upper SCR-9.1, the positive value decays gradually and approaches zero near 0.55 mm. From 0.55 to 1.1 mm in the central SCR-13.3 a flat plateau remains near zero. From 1.1 to 1.3 mm in the lower SCR-9.1, the value becomes negative and its magnitude increases progressively. From 1.3 to 1.5 mm in the lower surface SCR-4.9, it increases rapidly to the most negative shear strain and then diminishes slightly. The inflections near 0.2, 0.55, 1.1 and 1.3 mm correspond one to one to the SCR interfaces. The upper and lower halves are not perfectly mirror symmetric. In the upper half the positive shear decays from the surface to zero over a longer distance with a gentler

slope. In the lower half, the negative shear decreases more steeply. The central 0.55 mm segment corresponding to SCR-13.3 is a neutral zone with shear close to zero.

Fig. 5-13 (a) further presents the shear plastic strain component within the GD–TD plane, reported as the Abaqus output variable PE23. The most salient feature is the appearance of paired high magnitude shear patches at the four corners, whereas shear is lower in the section centre. Along the vertical paths marked by the white lines labelled Line 1 and Line 2, the shear rises rapidly near the upper and lower edges that contact the rolls.

Fig. 5-13 (b) presents the TD shear plastic strain profile, $\varepsilon_{s\text{-}z\text{-}1}$, along Line 1. Although the SCRs along Line 1 are geometrically left–right symmetric, the profile clearly shows an asymmetric distribution with stronger shear on the left and weaker on the right. Given that the absolute magnitude is very small, $|\varepsilon_{s\text{-}z\text{-}1}| \lesssim 10^{-4}$–$10^{-3}$, the TD shear along Line 1 may be treated as zero in subsequent macroscopic analyses and averaging. This approximation does not deny localisation at the edges and corners, it is restricted to the interior traverse defined by Line 1.

Next, Fig. 5-13 (c) shows the TD shear plastic strain profile along Line 2. Comparison with Fig. 5-12 (b) reveals commonalities and marked differences in both trend and magnitude. The commonalities are as follows. Along 0–1.5 mm both profiles display an edge-strong, centre-weak distribution. Near the left starting edge, the shear is initially positive and reaches a peak at about 0.1–0.2 mm, then decays inward and forms a near-zero segment, and towards the right end it becomes negative. Both curves exhibit pronounced inflections or steps where the edge-affected region gives way to the interior. Numerically, the left-hand peaks are of comparable magnitude. In the central interval 0.5–1.1 mm both are small in absolute value, RD shear plastic strain is essentially zero and TD shear plastic strain is slightly negative, with $|\varepsilon|$ usually below 0.01.

The differences appear in three aspects. First, in the degree of asymmetry and in the extrema, the TD profile right-hand trough is deeper, falling abruptly to about −0.08 at 1.25–1.35 mm and then recovering slightly, whereas the RD profile right-hand trough is about −0.06 with a smaller rebound, hence the left–right asymmetry is stronger for TD profile. Second, in the transition cadence and the position of the zero crossing, the TD curve shows two step-like discontinuities at about 0.45 mm and 1.25 mm and crosses zero further inwards at roughly 0.6–0.7 mm, whereas the RD curve decays smoothly on the left and

exhibits only one major discontinuity on the right at about 1.3–1.4 mm, with the zero crossing further to the left at about 0.45–0.5 mm. Third, regarding the flatness of the internal plateau, RD profile lies essentially on the zero axis over 0.5–1.1 mm, while TD profile is slightly negative over the same interval and drifts down slowly.

In summary, both profiles share the feature of edge strengthening with the centre approaching zero, yet TD shear shows more pronounced localisation and stronger left–right asymmetry, with more abrupt changes and a deeper negative shear on the right, whereas RD shear remains closer to zero in the mid-thickness and varies more gently.

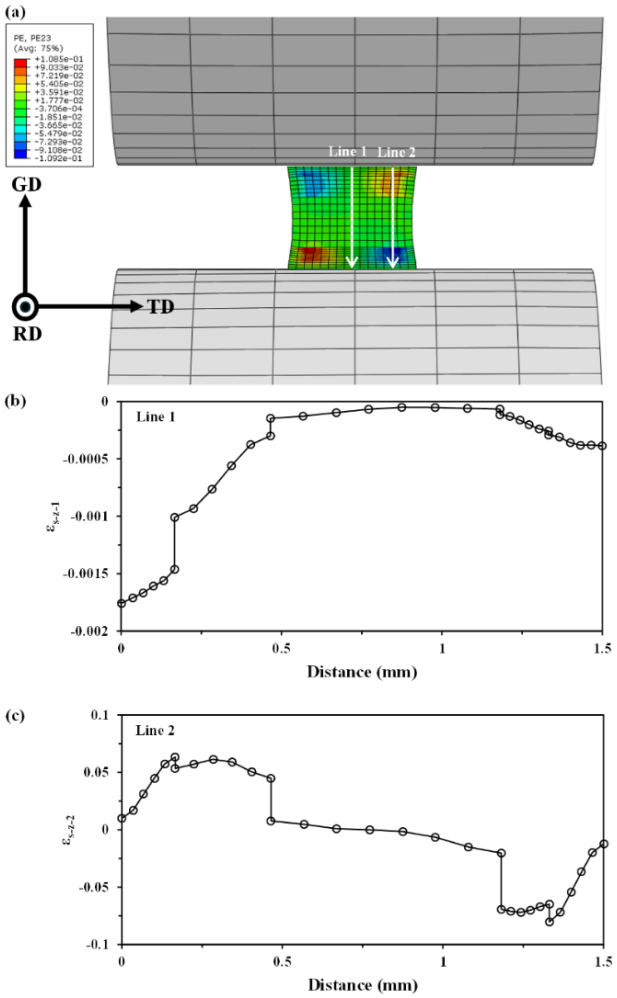

Figure 5-13 Finite element simulation of CR. (a) Contour of the through-thickness TD plastic shear strain $\varepsilon_{s\text{-}z}$, reported as the Abaqus field PE23, in the sheet between the rolls. TD is horizontal, GD is vertical, and RD is out of plane. The white arrows indicate the lines along which data were extracted. The colour scale gives shear plastic strain, with negative values denoting compression. (b,c) Through-thickness profiles of $\varepsilon_{s\text{-}z\text{-}1}$ and $\varepsilon_{s\text{-}z\text{-}2}$ along the lines marked in (a), plotted against distance across the thickness.

The primary cause of the corner localisation is the superposition of geometry and boundary conditions. Contact friction acting along the GD imposes strong tangential constraints on the upper and lower surface layers, which generates a pronounced near-surface shear field [565]. At the same time the two sides of the strip in the TD are free surfaces. Lateral spread occurs during rolling and produces velocity and stress gradients across the width [569]. Fig. 5-14 depicts these stress gradients, whose spatial distribution matches that of the shear strain field in Fig. 5-13 (a). Where these two gradient fields converge at the four corners, which are both near the roll–strip contact and adjacent to the free edges, the shear strain is reinforced by superposition and corner hot spots form [569]. Rolling-modelling studies have explicitly shown the coupling between spread and width-wise stress–strain and have established that plane strain models which neglect spread are inadequate to describe width-wise non-uniformity [565]. Significant three-dimensional shear and normal–tangential coupling must therefore arise in the edge zones, consistent with the high shear distribution at the corners in this figure. Surface layer shear induced by friction is especially pronounced under compressive and rolling type loading and has been directly linked to stress concentration in the contact region and to the initiation and propagation of X-shaped high shear paths [565]. As the junction of the contact zone and the free surface, the corners are more prone to such localisation. If one further considers differences in Al content across the SCRs, the spatial pattern of high corner shear is markedly amplified by compositional heterogeneity [567]. Alternating soft and hard SCR lamellae guide multiaxially driven plastic flow towards the relatively soft low-Al regions, which facilitates shear strain accumulation near SCR boundaries and free edges and in turn strengthens localisation at the four corners. The causal basis is that a spatial gradient in Al content translates into spatial gradients of strength and hardness and manifests under load as non-uniform and localised strain fields [567].

It is important to note that the map itself shows PE23 enhanced mainly at the edges and the four corners, with weaker values in the section centre. This reflects a width-wise shear mechanism governed by lateral spread. The centre is close to plane strain, whereas TD-direction shear is concentrated near the free edges and the corners [569]. By contrast, shear along RD is driven primarily by friction at the roll–strip interface and by the velocity difference about the neutral point. It is typically symmetric about the mid-thickness, strong in the surface layers, weak in the centre, and reverses sign between entry and exit [565]. Experimental and numerical studies have shown that, in symmetric rolling, the material

centre is essentially in a plane strain state, while the intensity and penetration depth of surface layer shear are controlled by the friction coefficient and the contact length [565,569]. This explains the spatial contrast between RD shear, strong at the surface and decaying with depth, and TD shear, strong at the edges and decaying towards the width-wise centre. In addition, the rolled FCG strip exhibits in-plane anisotropy arising from texture, which yields different responses in RD and TD for both yielding and plastic flow. This constitutive difference amplifies the disparity between RD and TD shear strain distributions under identical external boundary conditions [570]. The RD–TD differences observed here are consistent with such anisotropic behaviour [570].

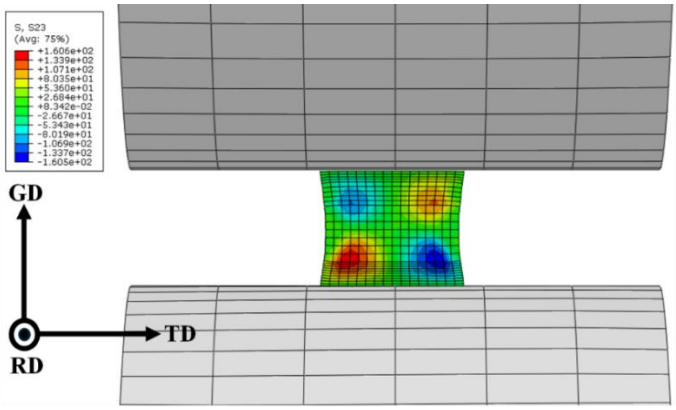

Figure 5-14 Finite element simulation of CR: shear stress field. Contour of the through-thickness TD shear stress, reported as the Abaqus field S23, in the sheet between the rolls. TD is horizontal, GD is vertical, and RD is out of plane. The colour scale gives shear stress, with positive and negative lobes indicating opposite senses of TD shear.

Shear strain asymmetry and the Rotated cube texture. Cu–Al alloys produced by WAAM exhibit pronounced non-uniformity of strain paths during CR. Because of friction at the roll–material interface and heterogeneity in the mechanical response, the through-thickness profile develops shear components of opposite sign in the upper and lower surface layers, as shown in Fig. 5-12 (b) and Fig. 5-13 (c). The shear strain maps show that pronounced shear deformation occurs near the outer regions of the specimen along the RD and the TD, whereas the shear components approach zero near the plane of symmetry. Under these conditions the outer regions SCR-4.9 with low Al content sustain RD and TD shear deformation, which induces the Rotated cube texture component with orientation {001}<110> [571]. The Rotated cube texture is a characteristic shear texture component that commonly forms in surface layers of sheet during rolling where frictional shear is

active [571]. In the present study, the strong shear in the outer layers rotates grain orientations so that {001} planes become parallel to the rolling plane and crystallographic directions align along <110>, thereby generating a pronounced Rotated cube maximum. The Rotated cube observed at the outer edges can therefore be attributed to the local concentration of orthogonal shear strains together with the relatively high SFE that facilitates easy slip in these regions, and this behaviour is consistent with literature reports of surface shear induced textures [571].

Compositional gradient effects and twinning induced Copper twin texture. The FCG specimen in this study possesses a spatial compositional gradient, which produces regional differences in mechanical behaviour and in SFE. As the Al content increases, the SFE of Cu-based FCC alloys decreases and twinning becomes easier to activate [572]. In the transition region SCR-9.1 with intermediate Al content, plane strain compression superposed with finite shear causes a subset of grains, for example those with the Copper orientation {112}<111>, to undergo twinning. Twinning imposes a mirror-related reorientation and generates the Copper twin texture, that is the {255}<511> orientation [398]. Measurements show a relatively high volume fraction of the Copper twin orientation in SCR-9.1, indicating that many grains have transformed to this state through twinning. This twin texture is essentially the twin-related variant of the classical Copper texture, and it acts as an intermediate waypoint in deformation texture evolution. Accordingly, the Copper twin observed in SCR-9.1 originates from the twinning mechanism promoted by the intermediate SFE in this region. Twinning shifts part of the orientation population from the conventional Copper {112}<111> towards its twin-related {255}<511> variant and it lays the groundwork for subsequent evolution towards the Brass texture [398,573]. This outcome accords with published studies on FCC alloys which show that deformation twinning can markedly alter texture pathways and promote the transition from Copper to Brass [573].

Synergistic twinning and shear banding inducing {111}-oriented textures. In the transition region SCR-9.1 and in the central region SCR-13.3, which has the highest Al content and the lowest SFE, the deformation mechanisms are dominated by dense twinning together with the formation of shear bands. Deformation there is close to symmetric plane strain, yet incompatibility with neighbouring regions produces pronounced local differences in strain partitioning that trigger shear band initiation. The profuse twin

lamellae restrict dislocation slip, promote strain localisation, and favour the development of shear band structures on {111} planes [573]. Grain orientations within the bands deviate strongly from the conventional β fibre and tend towards states in which {111} planes are parallel to the rolling plane and GD is parallel to <111>.

Two unconventional components consequently appear in the centre. F texture {111}<112>, in which {111} is parallel to the rolling plane and the <112> direction aligns with RD, is commonly regarded as a product of shear band deformation and its plane normal coincides with GD [573]. E texture {111}<110>, again with {111} parallel to the sheet plane and the <110> direction along RD, represents an alternative shear band induced rotation of the lattice relative to the rolling frame [573].

These F and E orientations are frequently observed in low-SFE FCC materials after large deformation and are recognised as shear band induced texture components [573]. In the high-Al region like SCR-9.1 and SCR-13.3, the synergy between twinning and shear banding concentrates many grain orientations near states with {111} parallel to the rolling plane, producing pronounced F and E maxima. Frequent twinning also reinforces the classical Brass-type texture. The measured fractions of the Brass component {110}<112> and the S component {123}<634> increase markedly, which indicates a shift towards the characteristic Brass-type deformation texture [573]. Comparable shear band textures have been reported elsewhere. In Al alloys processed by accumulative roll bonding or differential speed rolling, strong shear leads to components approaching <111> parallel to ND [571]. It follows that the unconventional F and E textures observed in SCR-9.1 and SCR-13.3 arise directly from intense twinning coupled with shear band deformation under low SFE, in agreement with published experimental and simulation studies [573].

5.2.3 Microstructure induced by annealing

After annealing at 400 °C for 30 minutes followed by immediate water quenching, the FCG specimen exhibits pronounced microstructural differences at different locations. The EBSD IPF-RD map in Fig. 5-15 (a) shows that the sizes of recrystallised grains are unevenly distributed between the SCRs and the compositional transition regions, TR. In the low-Al region SCR-4.9, the grains are evidently coarser, whereas in the high-Al region SCR-13.3, the grains are fine and uniform. At the interfaces between SCR-4.9 and SCR-9.1 and between SCR-9.1 and SCR-13.3, marked by white dashed rectangles in Fig. 5-15

(a), a continuous fine-grained band is directly observable [574]. This indicates that during CR, the transition region, owing to differences inherited from the initial WAAM microstructure, experienced intense local plastic strain that led to extreme refinement [574]. By comparison, the recrystallised grain size within each SCR is relatively larger and decreases from the surface towards the centre as the Al content rises from 4.9 at.% to 13.3 at.%. The EDS elemental map in Fig. 5-15 (b) confirms a stepwise increase of Al from the surface to the centre across the section, with a symmetric distribution that mirrors the microstructural differences described above.

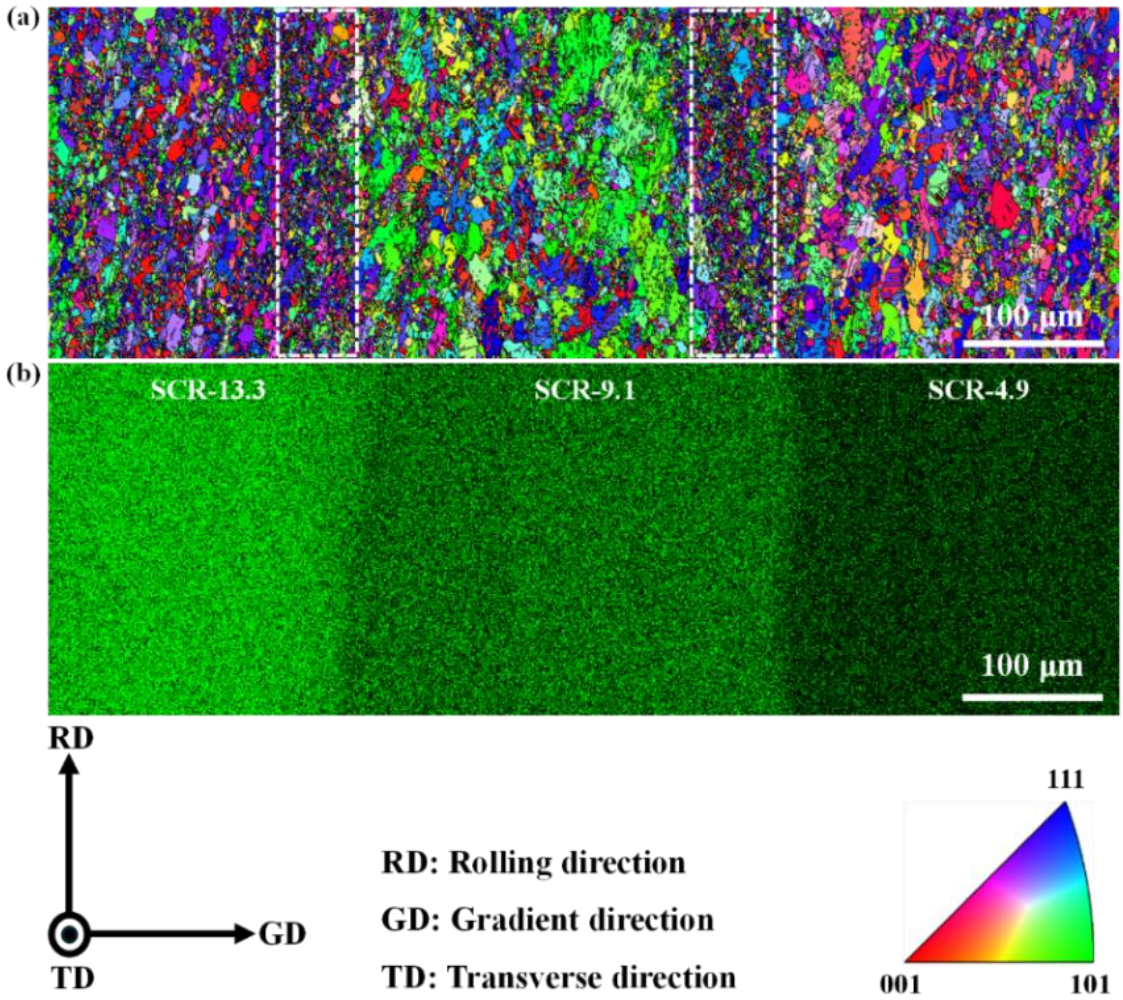

Figure 5-15 (a) EBSD IPF-RD map of the WAAM built FCG Cu–Al alloy after cold rolling and annealing. (b) Corresponding Al-EDS map. White dashed rectangles mark fine-grained bands located in the compositional transition regions. RD, TD and GD denote rolling, transverse and gradient directions, respectively. The IPF colour key is shown.

The grain size distribution histograms in Fig. 5-16 further quantify the regional contrasts. Fig. 5-16 (a) shows that SCR-4.9 exhibits the broadest distribution and is distinctly

bimodal. The principal peak lies in the fine to medium size range and is accompanied by a separate coarse-grain peak. The coarse-grain tail extends to approximately 40–50 μm, which drives both the mean and the standard deviation to larger values, namely 19 ± 5.7 μm. Fig. 5-16 (b) indicates that TR-4.9-9.1 is refined overall. The principal peak is concentrated at about 3–8 μm, and a secondary peak appears near 10–15 μm. The distribution is thus bimodal within the fine-grain regime and lacks any coarse-grain tail above 20 μm. From Fig. 5-16 (c), SCR-9.1 remains relatively broad yet no longer contains extremely coarse grains. The distribution is predominantly unimodal with a slight shoulder, the peak lying in the fine to medium range, and the mean size decreasing to 14.7 ± 4.6 μm. Fig. 5-16 (d) shows that TR-9.1-13.3 resembles the preceding transition region. The principal peak lies at about 3–7 μm and a secondary peak emerges at 10–14 μm, yielding a bimodal distribution within the fine-grain range. The overall spread is very narrow and again there is no coarse-grain tail. Fig. 5-16 (e) demonstrates that SCR-13.3 exhibits a narrowly peaked quasi-unimodal distribution with the peak below 10 μm. Coarse-grain populations are suppressed and the mean size is 9.9 ± 3.0 μm.

It is important to emphasise that, besides SCR-4.9, both TRs also display bimodal distributions, yet their bimodality differs fundamentally from that of SCR-4.9. In SCR-4.9 the bimodality comprises a principal peak in the fine to medium range together with a well-separated coarse-grain peak, typically expressed as a pronounced right-hand coarse-grain tail and a step-like separation. In contrast, the bimodality in both TRs is confined to the fine-grain scale. The secondary peak represents a minor population at 10–15 μm that sits adjacent to the principal peak with small separation and without any trailing tail of very large grains. Progressing from SCR-4.9 to SCR-9.1 to SCR-13.3, both the mean grain size and the distribution width decrease overall. The two TRs are the finest and most uniform across the section, exhibiting a fine plus sub-fine bimodality rather than a fine plus coarse bimodality.

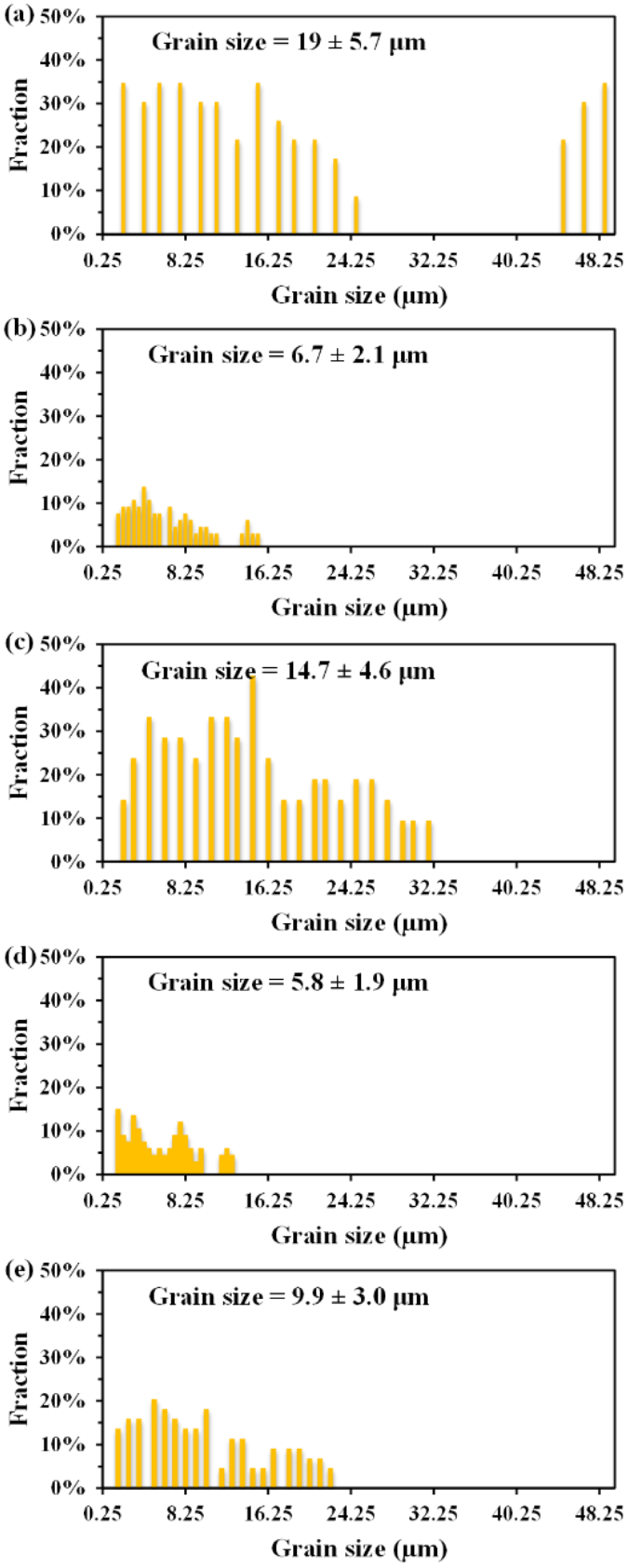

Figure 5-16 Grain size distributions for SCRs and TRs after annealing. Histograms derived from EBSD quantify the grain size statistics in: (a) SCR-4.9, (b) TR-4.9-9.1, (c) SCR-9.1, (d) TR-9.1-13.3 and (e) SCR-13.3.

The evolution of microstructure and grain size distributions with increasing Al content is closely linked to the deformation state prior to annealing. First, owing to differences in mechanical properties, during CR, the low-Al region SCR-4.9 carried the largest plastic strain, with a thickness reduction of approximately 87%, whereas the high-Al region SCR-13.3 experienced a smaller deformation of about 67%, as shown in Fig. 5-2. In addition, Al as a solute in Cu lowers the SFE, promotes deformation twinning and increases dislocation density [536,572]. Consequently, high-Al regions can accumulate large numbers of dislocations and form twins more readily even at smaller strains, thereby providing abundant nucleation sites for recrystallisation [536,575]. During annealing, the readily formed twin boundaries facilitate the release of stored deformation energy and reduce the driving force for boundary migration, which hinders grain coalescence and growth [575]. As a result, after recrystallisation, the grain size in high-Al regions tends to remain fine and uniform through pinning by twin boundaries [575]. In low-Al regions, by contrast, the higher SFE weakens twinning propensity, dislocations more readily undergo recovery and rearrangement into substructures during cold deformation, and the nucleation density of new grains is relatively limited [536,572]. With fewer constraints from twin boundaries, some recrystallised grains can grow, which favours the appearance of coarse grains and a bimodal size distribution [536]. Taken together, as the Al content increases from 4.9% to 13.3%, the mean grain size after annealing decreases markedly from about 19 μm to around 10 μm, and the grain size distribution evolves from bimodal to a narrow unimodal form. This pattern of microstructural evolution in the gradient material reflects the influence of stored deformation energy and twinning propensity on recrystallisation behaviour [536,575] and is also consistent with literature reports of the coexistence of fine and coarse grains after high strain annealing [536]. The experimental results clearly show that after recrystallisation the low-Al region tends to contain a small fraction of abnormally grown grains, whereas the high-Al regions and the transition zones are fully recrystallised into uniform fine-grained structures [574,575].

5.2.4 Texture induced by annealing

As shown in Fig. 5-17, the FCG-structured Cu–Al alloy after CR and annealing exhibits a systematic evolution of crystallographic orientations across regions. Along RD, the orientation rotates from <111> parallel to RD at the low-Al end in SCR-4.9, proceeds along the <101>-<111> edge towards <101> parallel to RD in the intermediate SCR-9.1 region,

and finally concentrates at <001> parallel to RD and <223> parallel to RD at the high-Al end in SCR-13.3. Along TD, the orientation migrates from <102> parallel to TD in SCR-4.9 along the <101>-<001> edge to <001> parallel to TD in SCR-9.1, then shifts towards <113> parallel to TD, forming an arcuate trajectory in the IPF triangle that connects the <101>-<001> and <111>-<001> edges. Along GD, the orientation moves from <001> parallel to GD in SCR-4.9 along the <101>-<001> edge to concentrate near <101> parallel to GD in SCR-9.1 and subsequently transforms to <102> parallel to GD in SCR-13.3. This sequence of orientation migrations indicates continuous texture rotation along the compositional gradient.

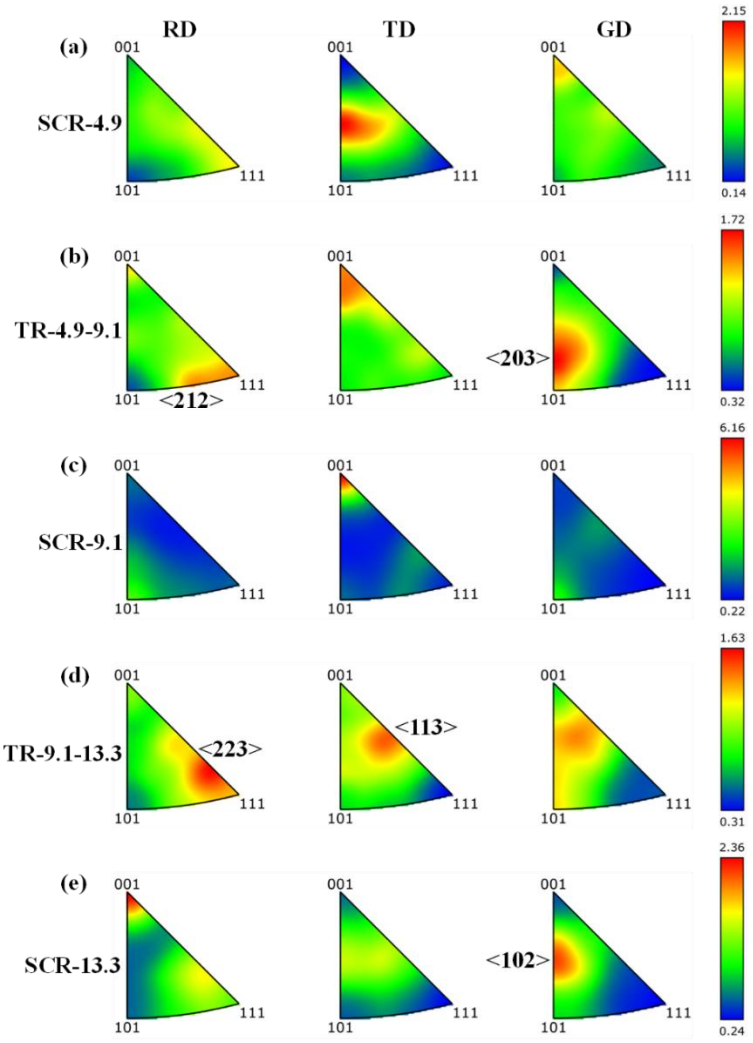

Figure 5-17 Inverse pole figures along RD, TD and GD showing orientation evolution across the composition gradient. (a) SCR-4.9, (b) TR-4.9-9.1, (c) SCR-9.1, (d) TR-9.1-13.3 and (e) SCR-13.3.

Differences in the initial textures after CR govern the preferential growth and attenuation

of orientations during recrystallisation annealing. In the high-SFE region SCR-4.9, dynamic recovery is extensive, and the stored energy is low, so recrystallisation proceeds predominantly in a continuous manner [536]. The rolling texture therefore weakens uniformly after annealing and no new strong components emerge. For example, the previously dominant Goss orientation diminishes markedly and the overall orientation distribution becomes more diffuse.

By contrast, in the intermediate-SFE region SCR-9.1, twins coexist with matrix orientations, and oriented nucleation may occur during annealing [575]. Parent-orientation grains adjacent to twin boundaries, where stored energy is high, tend to nucleate first, and recrystallisation twins may also form, so that certain orientations are strengthened [575]. In SCR-9.1, the abundant Copper twin orientation present in the rolled state is reduced after annealing, whereas its related Rotated cube orientation may be enhanced through oriented nucleation [576].

In the low-SFE region SCR-13.3, recrystallisation often involves reorganisation of orientations [575]. New grains can grow as twin-related variants of the deformation texture. The concentration of orientations with <001> parallel to RD observed after annealing in SCR-13.3 can thus be attributed to new grains nucleated at twin boundaries that grow towards Cube or Goss type, with RD close to <001> [575]. Similarly, the arc of <223> parallel to RD suggests that recrystallisation twins drive further extension of orientations along the <111>–<001> edge, linking the orientation families before and after twinning [575].

Overall, the post-anneal changes in orientation arise from the combined effects of stored energy within the constituent rolling texture components and the spatial distribution of twins [536,575]. In high-SFE regions, continuous recrystallisation weakens the prior texture and reduces anisotropy. In low-SFE regions, discontinuous recrystallisation together with oriented nucleation and twinning tends to reorganise the orientation distribution. These mechanisms are consistent with the orientation evolution trends observed in the gradient material and they reveal the strong influence of SFE and deformation conditions on texture development [536,575].

5.3 Summary

This chapter establishes a closed-loop, one-to-one evidence chain linking EBSD and FEM,

and it systematically elucidates the microstructural and textural evolution of WAAM-fabricated FCG during CR and annealing. It also validates the causal chain from composition to strain to stored energy to recrystallisation to texture.

During CR, a rise in Al content lowers the SFE, slip changes from diffuse to strongly localised shear, and a hierarchical shear band network develops that consists of equiaxed ultrafine cores, LAGBs-rich shells and the surrounding matrix. The volume fraction of LAGBs increases along the gradient while HAGBs decrease. KAM indicates a monotonic rise in stored energy. The grain size distribution shifts from a bimodal form with retained coarse grains to a narrow unimodal distribution in the submicrometre to micrometre range. The finite element analysis reveals pronounced RD shear at the surfaces and TD shear concentrated at the edges and corners, together with compression along GD that is greatest in the low-Al region. These fields drive selective texture development: Rotated cube and Goss in the outer layers, strengthening of F and Copper twin in the mid-region, and a transition to Brass, S and E in the centre under the combined action of shear banding and twinning.

During annealing, recrystallisation advances along the gradient in an order set by the distribution of stored energy and by boundary mobility. The transition regions are fully refined. The high-Al region attains a uniform fine grain size through pinning by twin boundaries, whereas the low-Al region, limited by a lower nucleation density, exhibits abnormal grain growth and a bimodal size spectrum. Texture reorganisation reflects an SFE-controlled bifurcation of mechanisms. In high-SFE regions, continuous recrystallisation tends to attenuate the rolling texture uniformly. In low-SFE regions, oriented nucleation together with inheritance through twinning more readily drives reorganisation, causing RD to approach <001> while the <223> family of orientations is retained.

In sum, the compositional gradient, through its coupling to SFE and to the operative deformation mode, fixes the density of shear bands, the distribution of stored energy and the selection of recrystallisation orientations. The result is a set of verifiable and predictive rules that can be used to design gradient materials for synergistic strength and ductility and for integrated functionality.

Chapter 6. Impact of gradient structures on mechanical properties

6.1 Introduction

The strengthening of metallic materials has long been constrained by the trade-off between strength and ductility. In recent years, gradient-structured materials, whose properties and microstructures are tunable in space, have been shown to deliver macroscopic synergy of high strength and high ductility. The essential mechanism is the plastic incompatibility between heterogeneous regions, which triggers HDI stress of opposite sign together with additional work hardening. These effects delay strain localisation and enlarge the window of uniform plasticity [120,174]. This phenomenon accords with strain gradient theory. When plasticity is distributed non-uniformly in space, the material necessarily generates GNDs characterised by lattice curvature. Long-range back stress and continuous lattice rotation are thereby produced, and together they modulate yielding, hardening and instability behaviour [75]. Studies based on EBSD and its high precision variants further demonstrate a quantitative link between lattice curvature and GND density, which provides an experimental pathway for tracking strain gradients and internal stress distributions across scales [577].

There are at least two independent yet potentially coupled dimensions by which "gradients" can be realised. The first is a compositional gradient. Spatially varying solute content systematically alters the level of solid solution strengthening and the SFE, which in turn changes the separation of partial dislocations, the facility for cross-slip, and the threshold and characteristic scale for deformation twinning. Near a compositional transition interface, solute segregation and mismatch in SFE impart pronounced barrier-versus-transparency selectivity to dislocation transmission and pile-up [506,537,578,579]. The second is a structural gradient. Directional gradients in grain size, dislocation density, residual stress and texture strength can, under load, induce multiaxial stress and strain states together with strong strain partitioning, thereby producing significant HDI strengthening and HDI strain hardening [120,174]. From a fracture mechanics perspective, internal layered or transitional interfaces can also cause crack deflection and twisting, which act as extrinsic shielding and raise the effective driving force required for crack propagation [251,580].

Although the foregoing single dimension gradient effects have been verified individually, the synergy and competition between compositional and structural gradients within one material system still lack systematic and directly comparable experimental evidence. Most studies either concentrate on the macroscopic tensile response of gradient nanocrystalline or layered structures or confine themselves to post-mortem microscale analyses of dislocation–interface interactions. Few investigations combine full-field strain measurement, in-situ tracking of failure paths, and direct characterisation of compositional gradients, to disentangle the specific contributions of different gradients to plasticity partitioning, strain gradients and crack–interface interactions [581].

Building on these insights and on the materials and processing platform established in earlier chapters, this chapter constructs three directly comparable specimens within a single alloy system. The first possesses a single compositional gradient, SCG. The second contains a single structural gradient, SSG. The third exhibits dual gradients in both composition and structure, DG. These specimens will be tested and analysed using an approach in which the methods corroborate one another, namely DIC under uniaxial tension to obtain full field strain together with corresponding finite element simulations, examination of the fracture surfaces, in-situ tracking of the evolution of specimen surface morphology, and characterisation and analysis of structural gradient layers and compositional transition regions by SEM and TEM.

6.2 Results and discussion

This section first reports the uniaxial tensile responses, microhardness distributions, and associated statistical metrics for the different specimens. We then use DIC to provide full-field strains and strain trajectories throughout the tests, thereby probing strain partitioning and strain gradients under the various gradient architectures, and we cross-validate these observations against finite element analysis. Subsequently, fracture surface morphology is examined to identify crack deflection and branching near compositional transition interfaces or across structural gradient transitions. Next, in-situ optical time-series of surface morphology are employed to reveal the evolution of multiaxial stress states and multiaxial strain states under macroscopic loading. Finally, SEM and TEM are used to characterise the structural gradient layer within the dual gradient architecture together with the compositional transition regions, to elucidate the overall advantages of the dual gradient design in achieving synergy between strength and ductility over single structural

gradient, single compositional gradient, and homogeneous counterparts.

6.2.1 Mechanical properties

In this section, uniaxial tensile testing is used as the basis for a side-by-side assessment of the mechanical properties of all specimens under identical test conditions. First, the abbreviations are defined. DG, SCG, SSG and Hom denote the dual gradient, single compositional gradient, single structural gradient and homogeneous reference specimens respectively. They have the same average Al content (9.1 at.%). σ_y denotes the yield strength, σ_{UTS} the ultimate tensile strength, ε_u the uniform elongation, ε_f the elongation to failure, and $\varepsilon_f - \varepsilon_u$ the post-necking elongation.

Fig. 6-1 (a) shows engineering stress–strain curves indicating that at comparable composition different gradient architectures produce pronounced mechanical differences. The DG specimen achieves the highest strength and ductility simultaneously. The Hom specimen has the lowest strength, the SSG specimen shows markedly limited ductility, and although the SCG specimen exhibits ductility comparable to DG its strength is lower than that of DG.

Fig. 6-1 (b) presents the evolution of strain-hardening rate as a function of true strain. The DG specimen maintains a high strain-hardening rate throughout the uniform deformation regime, and the reduction in hardening rate is smooth and slow. This delays the onset of deformation localisation and ensures a large uniform elongation [591]. By comparison, the SCG specimen shows a pronounced early peak in hardening rate followed by a rapid decline. The SSG and Hom specimens possess more limited hardening capability, especially SSG. It is evident that the superior strain-hardening ability of DG is the key factor that enables the concurrent achievement of high strength and high ductility [115,120].

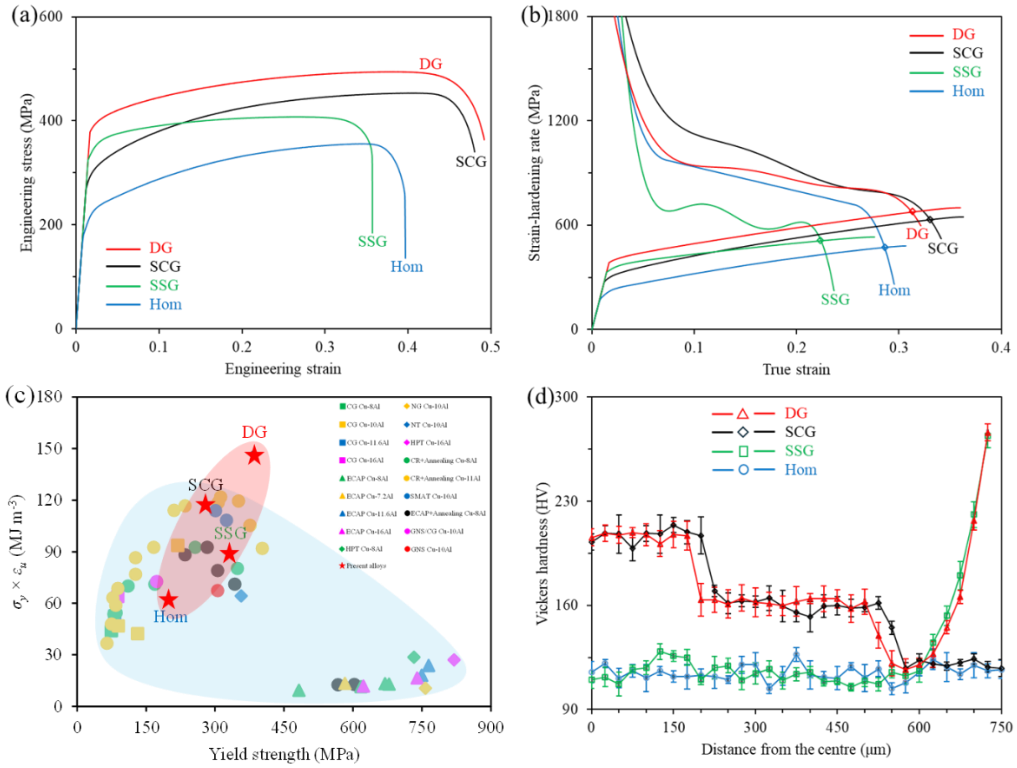

Figure 6-1 (a) Engineering stress–strain curves for DG, SCG, SSG and Hom specimens with the same average Al content. (b) Strain-hardening rate versus true strain. (c) Strength–ductility index, $\sigma_y \times \varepsilon_u$, plotted against σ_y. The light blue shaded envelope compiles literature data for Cu–Al alloys of similar average Al contents [217,582–590]. The red star marks the present DG Cu–Al, which lies above the envelope, indicating superior combined performance. (d) Vickers hardness along the thickness of different Cu–Al alloys before tensile testing.

To contextualise performance, Fig. 6-1 (c) benchmarks the present Cu–Al compositional gradient materials against conventional Cu–Al alloys and against gradient structured systems reported in the literature. Red stars mark our four states labelled Hom, SSG, SCG and DG. The present alloys shift progressively towards the upper right as gradient design is introduced, and the DG state lies at the upper bound of the envelope. Fig. 6-1 (c) plots the product $\sigma_y \times \varepsilon_u$ against the yield strength σ_y. The quantity $\sigma_y \times \varepsilon_u$ serves as an indicator of combined strength–ductility performance, a larger value signifying higher strength while maintaining substantial ductility [115]. The blue shaded region compiles data for Cu–Al alloys of similar SFE from the literature, where $\sigma_y \times \varepsilon_u$ is generally constrained by the strength–ductility trade-off and does not exceed about 120 MJ m^{-3} [591]. The DG specimen exceeds 140 MJ m^{-3} and at a yield strength of about 385 MPa achieves a property combination far superior to the literature alloys, demonstrating unprecedented strength–

ductility synergy.

Fig. 6-1 (d) shows Vickers microhardness profiles across the thickness. The Hom specimen is essentially constant through thickness and exhibits no hardness gradient. The SSG specimen displays a steep near-surface gradient within about 125 μm, the surface hardness rises rapidly, and the thickness of the structural gradient layer is therefore about 125 μm [120,299]. The SCG specimen exhibits a characteristic stepwise distribution, with a harder centre and softer surfaces, consistent with its compositional gradient in which the central region has a higher Al content and correspondingly higher hardness. The DG specimen integrates the features of SCG and SSG, retaining a high core hardness and showing a further marked rise within about 175 μm of the surface [120,299]. Notably, the surface hardness maxima of DG and SSG are very close, which highlights the contribution of the surface structural gradient to the hardness increase.

To elucidate the strain-hardening behaviour triggered by different gradient types, microhardness after tensile fracture was measured systematically along the thickness on gauge sections away from the necked region, as shown in Fig. 6-2 (a), and the hardness change ΔH between the pre- and post-tension states was calculated, as shown in Fig. 6-2 (b). Relative to the pre-tension hardness profiles in Fig. 6-1 (d), the overall shapes are retained for all specimens: Hom is nearly constant across the thickness, SSG rises steeply at the surface, SCG is stepwise, and DG exhibits a composite dual gradient profile. There is, however, a key difference. Before deformation, the outermost hardness of DG is like that of SSG, whereas after deformation, the outermost hardness of DG exceeds SSG, indicating that the dual gradient confers stronger residual hardening and greater dislocation storage capacity at the surface.

Figure 6-2 (b) further quantifies this residual hardening. In Hom, ΔH is about 50 HV throughout the thickness, characteristic of a homogeneous material with limited residual hardening. In SSG, within the structural gradient layer, ΔH falls sharply towards the surface, which indicates that the shot peened prehardened layer leaves little capacity for additional hardening during tensile loading. In the region that is not affected by shot peening, ΔH is about 66 HV, higher than the 50 HV in Hom, demonstrating that a single surface structural gradient can transmit heterogeneous constraint into the interior and thereby enhance residual hardening.

SCG exhibits clear layering. In the central SCR-13.3, ΔH is about 70 HV. In the intermediate SCR-9.1, ΔH is about 58 HV. Because the average Al content in SCR-9.1 is close to that of the corresponding regions in Hom and SSG, its ΔH lies between those two cases. This shows that with composition alone the residual hardening level is limited and does not match that of a single structural gradient.

DG reveals the synergistic advantage of combining gradients. In the same SCR-13.3 region as in SCG, ΔH is about 80 HV, distinctly higher than the 70 HV of SCG, indicating that in the high-Al core, the synergy between structure and composition further promotes dislocation accumulation and subsequent hardening. In the same SCR-9.1 region as in SCG, ΔH is about 71 HV, the highest among all four specimens at comparable Al content, which shows that the dual gradient most effectively activates residual hardening in the medium-Al layer as well. Notably, within the structural gradient layer of DG, the decline of ΔH with proximity to the surface is much less steep than in the corresponding layer of SSG. This implies that after tensile loading, the DG surface maintains a more stable hardening distribution with a weaker softening tendency, evidencing mutual buffering and cooperative load sharing between the surface structural gradient and the interior compositional gradient.

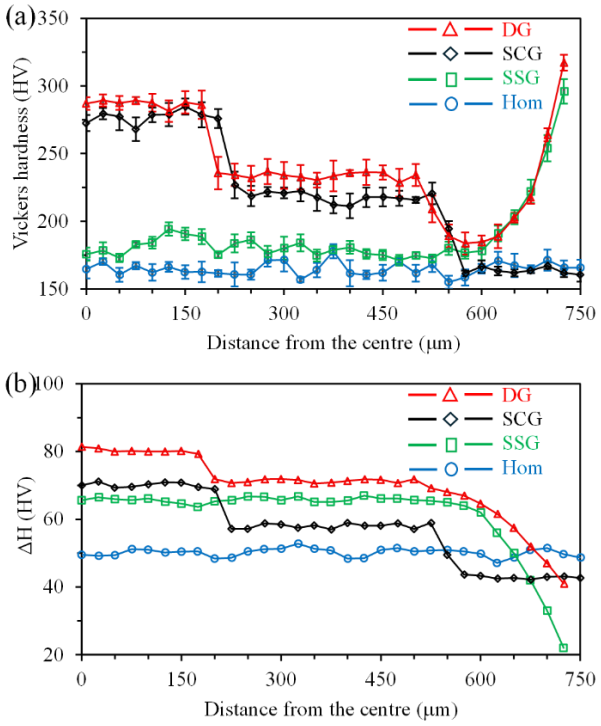

Figure 6-2 (a) Microhardness distribution after tensile test and (b) variation of microhardness before and after tensile test for Hom, SSG, SCG and DG samples.

Fig. 6-3 compares the tensile responses of Hom and SSG specimens at average Al contents of 4.9, 9.1 and 13.3 at.% together with the performance of a reverse single compositional gradient (RSCG) specimen. As the Al content increases from 4.9 to 13.3 at.%, the Hom specimens exhibit a marked rise in both yield strength and ultimate tensile strength. The yield strength increases from approximately 101 MPa to approximately 311 MPa, while the uniform elongation shows a slight increase. At a fixed Al content, introducing a single structural gradient SSG further elevates strength. For example, at 9.1 at.% Al the yield strength increases from approximately 182 MPa to approximately 334 MPa, accompanied by a reduction in ductility, with the uniform elongation decreasing from 34% to 27%. This trend is evident across all compositions examined. It should be emphasised that this outcome arises because the shot peening process parameters were not optimised in the present study, and consequently the introduced structural gradients did not realise its full potential to raise strength and ductility simultaneously. Notably, the RSCG specimen, indicated by the yellow curve in Fig. 6-3, performs poorly, with both strength and ductility inferior to those of the Hom and SSG specimens at the same composition, namely an average Al content of 9.1 at.%. The RSCG scheme is therefore not effective and is not pursued further in this study. Henceforth, SCG refers exclusively to the forward compositional gradient design.

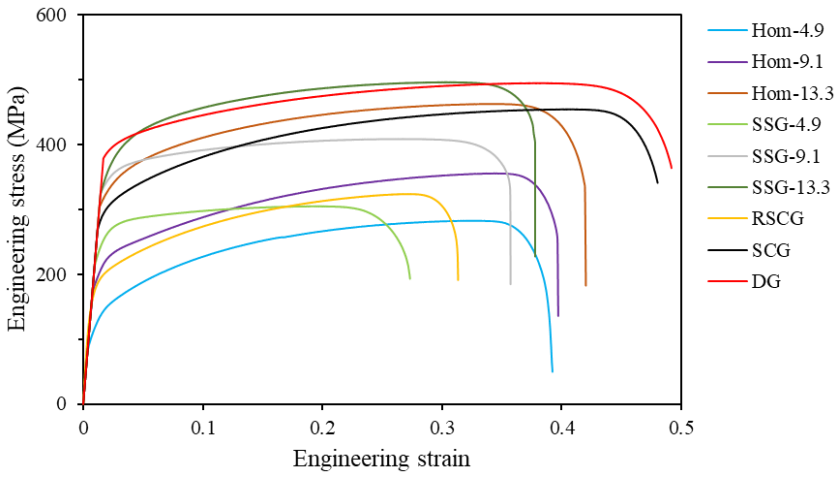

Figure 6-3 Engineering stress–strain response of homogeneous and gradient Cu–Al alloys.

Table 6-1 summarises the mechanical property data for all specimens. The difference $\varepsilon_f - \varepsilon_u$ is used to quantify the material's plastic deformation capacity in the post-necking regime. A larger value indicates that the material continues to deform after necking rather than fracturing immediately. For the DG specimen, $\varepsilon_f - \varepsilon_u$ is approximately 11%, markedly

higher than the values for the other alloys, which mostly lie between 4% and 9%. This demonstrates that DG sustains plastic deformation beyond the end of uniform deformation without premature fracture, further underscoring its superiority in combined mechanical performance.

Table 6-1 Tensile properties of homogeneous and gradient Cu–Al alloys.

	σ_y (MPa)	σ_{UTS} (MPa)	ε_u (%)	ε_f (%)	$\varepsilon_f - \varepsilon_u$ (%)
DG	385 ± 7	495 ± 9	38 ± 0.6	49 ± 1.1	11
SCG	284 ± 8	454 ± 10	41 ± 0.4	48 ± 0.9	7
SSG-9.1	334 ± 9	408 ± 10	27 ± 2.1	36 ± 2.6	9
Hom-9.1	182 ± 6	355 ± 7	34 ± 1.1	40 ± 1.7	6
SSG-13.3	341 ± 10	496 ± 11	30 ± 1.9	38 ± 2.7	8
Hom-13.3	311 ± 5	462 ± 9	34 ± 0.9	42 ± 1.6	8
SSG-4.9	230 ± 13	305 ± 15	20 ± 2.2	27 ± 2.5	7
Hom-4.9	101 ± 6	282 ± 9	32 ± 1.5	39 ± 1.8	7
RSCG	175 ± 12	324 ± 13	27 ± 0.9	31 ± 1.5	4

6.2.2 Strain gradients and gradient transitions

Having established the macroscopic mechanical differences in section 6.2.1, this section turns to the spatial distribution of plastic strain. Fig. 6-4 shows the evolution of the ε_x strain contour maps along the thickness direction with increasing plastic strain. The X axis denotes the thickness direction and coincides with the gradient direction. Blue indicates greater thickness contraction and red indicates lower contraction. The in-situ DIC fields reveal sharply contrasting deformation characteristics across the four specimen types.

In the Hom specimen, Fig. 6-4 (a), a deep blue nucleus appears at the same geometric location from 2.1% onward as indicated by the white arrow. This indicates that localised strain zones, abbreviated as LSZs, first initiate at a local site along the thickness. By 10.1% to 19.9% this evolves into a deep blue band that traverses the thickness, while large surrounding areas remain yellow and green. The deformation uniformity is therefore very poor. The density of LSZs is low yet they are highly concentrated, so thickness contraction is dominated by a single band and most of the volume is not effectively engaged. This phenomenon fundamentally arises from the absence of intrinsic gradients and interfacial constraints that can suppress local instability [592]. In a homogeneous microstructure, the yield strength and strain-hardening capacity are nearly isotropic. Under uniaxial tension, a slightly softer region first develops greater thickness contraction, that is, a more negative ε_x. Local thinning raises the true stress and reduces the effective load bearing area,

establishing a feedback loop of thinning, stress concentration and further thinning. When the strain-hardening rate does not satisfy the Considère criterion, the initial blue strain nucleus rapidly propagates along the thickness and loading directions and merges into a single through-thickness band of localised strain, while the surrounding regions remain yellow and green with low contraction for an extended period [592]. The consequence is very poor deformation uniformity, a low density of LSZs that are nevertheless strongly concentrated, thickness contraction dominated by a single band, and a large fraction of the volume not effectively mobilised to participate in plastic deformation.

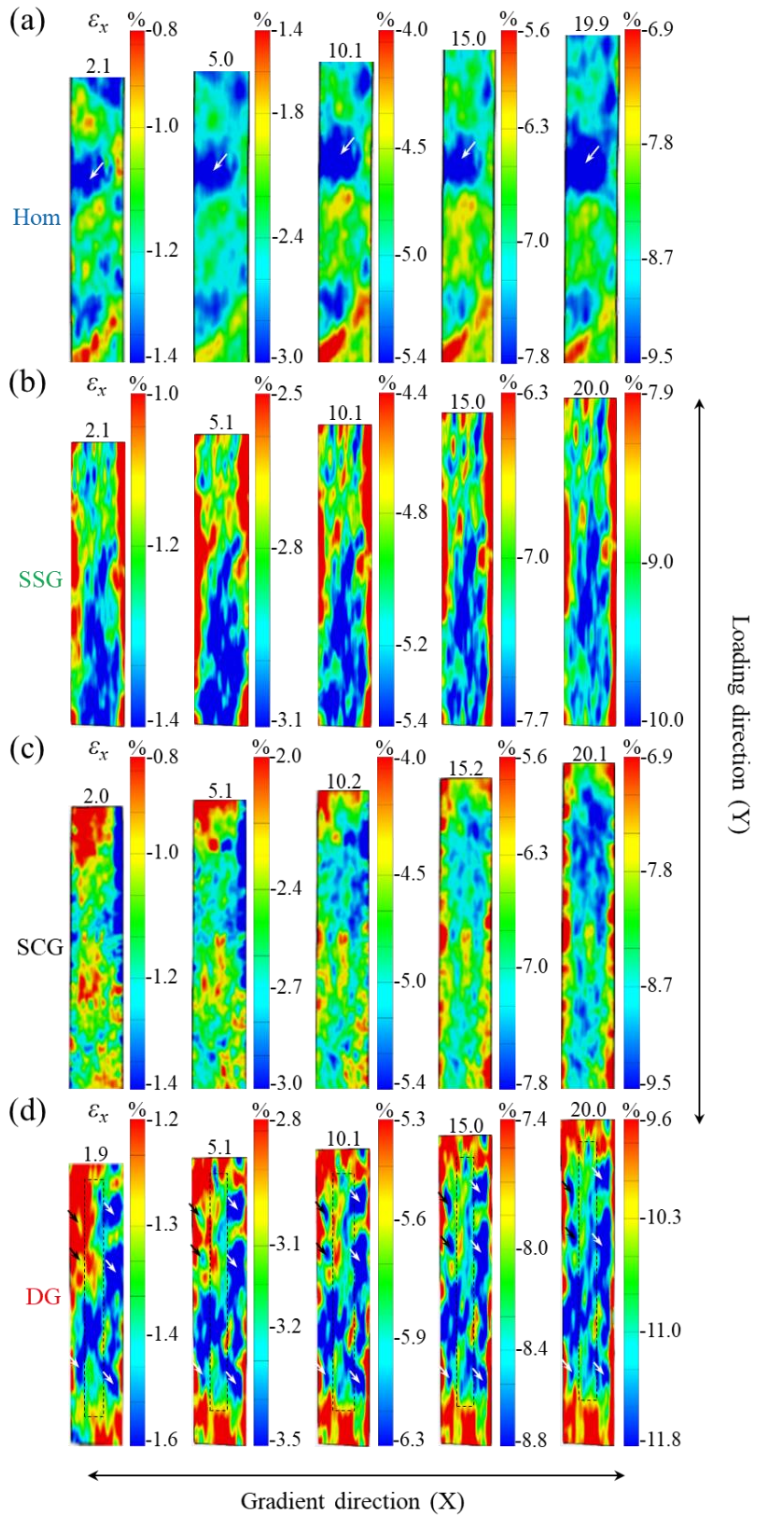

Figure 6-4 DIC maps of thickness-direction strain ε_x under uniaxial tension. (a) Hom. (b) SSG. (c) SCG. (d) DG. Colour represents ε_x along the gradient direction (X), which coincides with the thickness direction. Blue indicates more negative ε_x and therefore greater contraction in X, red indicates less negative ε_x and therefore smaller contraction. The loading direction is Y. Numbers above each map give the applied engineering strain ε_{app} in per cent. The colour bar beside each column gives the scale for that strain step.

In the SSG specimen, Fig. 6-4 (b), a stable sandwich-like colour sequence of red near both surfaces and blue at the centre persists from 2.1% to 20.0%. This demonstrates that the imposed structural gradient sustains a persistent through-thickness strain gradient. Contraction near the surfaces is constrained and the centre continuously carries the strain. LSZs reside mainly within the central blue band. Their density and dispersion are moderate, and the utilisation of material is non-uniform. The root cause lies in the SSG produced by shot peening [299]. The nanocrystalline and ultrafine-grained surface layer has a higher yield strength than the coarse-grained core, so under uniaxial tension, the core enters plasticity deformation first. Once the core yields, it bears the major share of plastic deformation and undergoes greater thickness contraction, with ε_x becoming more negative and the map turning blue. The high strength surface layer requires a higher stress to yield, so it plastically deforms later and for an extended period retains smaller contraction, appearing red on the map. This strong then weak then strong stratification stably channels strain into the core and establishes a persistent through-thickness strain gradient. LSZs develop predominantly within the central blue band, slender and aligned with the loading direction, with only moderate density and dispersion. At the same time, the surface layer dissipates little energy and contributes little to thickness contraction during plastic flow, which biases material utilisation towards the core and results in non-uniform utilisation [299].

The SCG specimen, Fig. 6-4 (c), exhibits a pronounced gradient transition. At early strains below 10%, the near-surface regions are bluer, and the centre is redder. After 10% to 15%, the pattern reverses to a bluer centre and redder surfaces. The exchange of colour domains between the early strain set at 2.0% and 5.1% and the later set at 10.2%, 15.2% and 20.1% is direct evidence of this reversal. The density of LSZs is moderate and the zones migrate as deformation proceeds. Different SCRs take turns to bear plasticity at different stages, which leads to relatively full utilisation of the material. The strain gradient transition observed in the SCG specimen arises because the SCG introduces an initial strength contrast and a difference in strain-hardening rate, which triggers interlayer mechanical incompatibility and stress redistribution [115,592]. At low strain below 10%, the near-surface region yields first owing to its lower Al content and hence lower yield strength [594], and it exhibits greater thickness contraction with ε_x more negative and therefore blue, while the centre responds predominantly elastically or with weak plasticity and remains red. The incompatibility between SCRs generates strain gradients that must be

accommodated by GNDs. These GNDs usually pile up near the interfaces between SCRs and reside within the softer domain, namely the surface SCR-4.9 region, which elevates the instantaneous strain-hardening rate at the surface above that of the centre [592]. As strain increases to about 10% to 15%, the surface strengthens rapidly through hardening and back stress from HDI incompatibility [115,592]. The effective flow stress of the surface then exceeds that of the centre and the plastic load is progressively transferred to the central SCR-13.3 region. The DIC colour map reverses accordingly to a bluer centre and redder surfaces. Thus, the gradient transition in SCG is the synergistic outcome of the initial yield disparity, in which the surface yields before the centre, combined with a disparity in strain-hardening rate, in which the accumulation of GNDs at the surface accelerates hardening [115,592,594]. This manifests as a moderate density of LSZs that migrate along the thickness as deformation proceeds, with different SCRs taking turns to bear plasticity at different stages, which delays single band localisation and improves overall material utilisation.

The DG specimen, Fig. 6-4 (d), shows the most uniform distribution and the highest utilisation. From 1.9% to 20.0% the maps display fine, closely spaced, alternating blue and red lamellae without any single deep blue band running through the thickness. The LSZs indicated by white arrows and the ε_x surge regions indicated by black arrows are numerous and widely dispersed. Crucially, all ε_x surge regions marked by black arrows lie within SCR-9.1 and are halted at the boundary of the dashed rectangle. They do not penetrate into SCR-13.3. This provides direct evidence that the compositional transition interface pins and segments LSZs and suppresses their coalescence and spread along the gradient direction [592].

In summary, deformation uniformity and material utilisation rank as DG greater than SCG greater than SSG greater than Hom. The density and dispersion of LSZs are highest and most diffuse in DG, and lowest and most concentrated in Hom.

To clarify the physical nature of the strain gradient and the gradient transition in the SCG specimen, finite element simulations were conducted to exclude the influence of experimental noise and surface effects. Under controlled constitutive laws and boundary conditions, the simulations quantify the spatial allocation of through-thickness strain within each SCR and its evolution with increasing load. The objectives are twofold. First, to verify whether the surface-to-centre load transfer observed by DIC arises from the

compositional gradient itself rather than from measurement artefacts. Second, to distinguish the relative contributions of the different compositional regions to thickness contraction at different stages of loading, thereby determining whether a transition from surface-dominated to centre-dominated behaviour occurs.

Fig. 6-5 presents the finite element results for SCG. LE33 denotes the strain along the gradient direction, which is the thickness direction and is equivalent to ε_x. More negative values indicate greater thickness contraction. The colour scale shifts from red to blue as contraction increases. The SCG is symmetric and consists of five layers distributed from surface to centre in the order SCR-4.9, SCR-9.1, SCR-13.3, SCR-9.1, SCR-4.9. In the in-plane coordinate system, LD is the loading direction, GD is the gradient direction which coincides with the thickness, and TD is the width direction that is out of plane. Fig. 6-5 (a) corresponds to an applied engineering strain of 1.3% and captures the instantaneous response. Fig. 6-5 (b) corresponds to 14% and represents a stage of large plastic deformation.

At 1.3% applied strain, Fig. 6-5 (a) shows a bluer band in the surface SCR-4.9 and a red dominant band in the central SCR-13.3. The intermediate SCR-9.1 appears green to yellow. The LE33 magnitude ranges from about −0.00349 to −0.00533, and it decreases monotonically from surface to centre along the thickness. The surface therefore accommodates more thickness contraction while the centre deforms less. This distribution indicates that at the onset of yielding the surface enters plasticity first because of composition-induced differences in yield strength, establishing a clear through-thickness strain gradient that is large at the surface and small at the centre.

At 14% applied strain, Fig. 6-5 (b) exhibits a marked reversal. The central SCR-13.3 becomes the dominant yellow band, the two outer SCR-4.9 layers turn orange to red, and SCR-9.1 remains a transition layer. The LE33 magnitude increases overall to about −0.0344 to −0.0663. The distribution now decreases from centre to surface along the thickness, which means that the centre bears more thickness contraction and the surface less. Relative to Fig. 6-5 (a), the principal load bearing layer switches from the surface to the centre. This evidences a load redistribution from surface-dominated to centre-dominated as strain advances.

In summary, Fig. 6-5 (a) provides direct evidence for a strain gradient. At the same load

level, the through-thickness ε_x field is monotonic, with blue at the surface and red at the centre. The swap of dominant colour domains between Fig. 6-5 (b) and Fig. 6-5 (a) constitutes clear proof of a gradient transition, namely a reversal of the strain gradient direction during deformation from surface-large and centre-small to centre-large and surface-small.

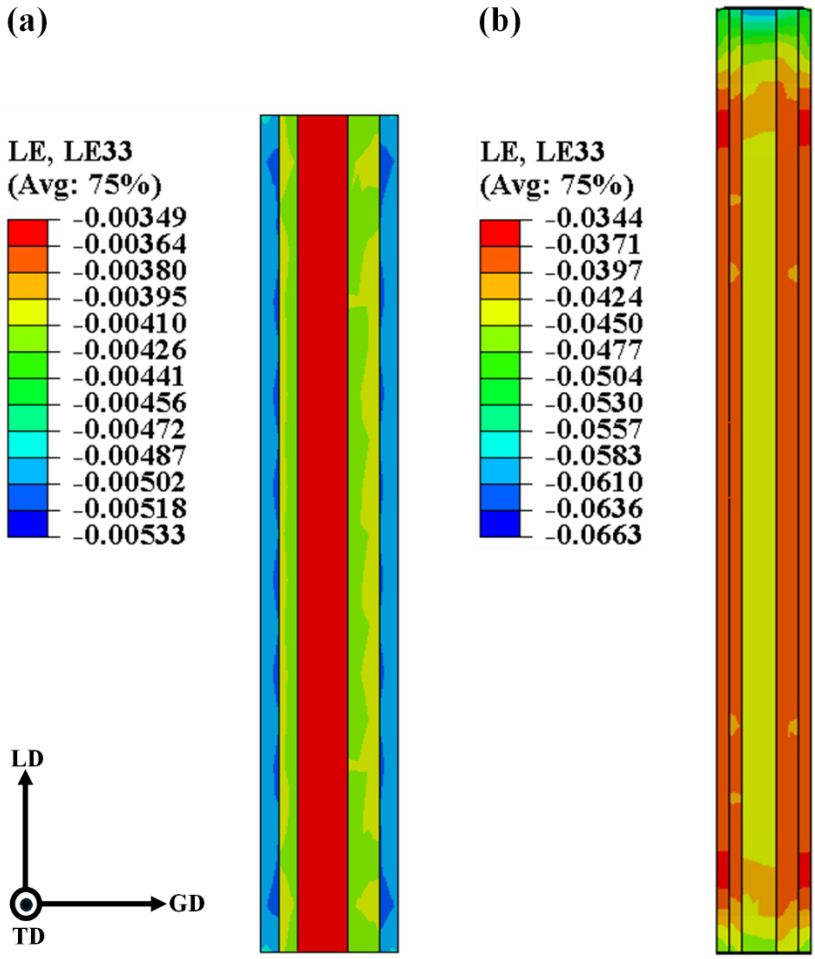

Figure 6-5 Finite element simulation of the SCG specimen showing contours of gradient direction strain ε_x reported as LE33. (a) Applied engineering strain 1.3%. (b) Applied engineering strain 14%. LD is the loading direction in tension, GD is the gradient or thickness direction, and TD is the transverse direction. Colour bars give the ε_x scale for each case.

Mechanistically, in the SSG specimen, the single structural gradient generates and sustains a stable strain gradient, concentrating deformation in the core and stabilising the strength of the surface layer, which is beneficial for strength–ductility synergy yet limited by insufficient utilisation of the surface [115,120]. In the SCG specimen, the single compositional gradient triggers a transformation of the strain gradient as deformation

proceeds, enabling staged alternation between the surface and the core in bearing load, which delays localisation and improves the strength–ductility synergy [115,592]. The DG specimen combines both effects. Its structural gradient establishes, along the gradient, a continuous strength spectrum governed by grain size and dislocation density, so that the local yield strength and the instantaneous strain-hardening rate vary layer by layer [115,120]. Under external loading, multiple relatively soft microdomains are activated in sequence, forming parallel channels for plastic transmission. These channels are continually added and alternated as strain advances, causing LSZs to emerge at high density in a finely dispersed manner with small scale and short correlation length rather than coalescing along a single pathway [593]. In DG, this flow partitioning mechanism is coupled with a pinning and blocking effect at compositional gradient interfaces. Fig. 6-4 (d) shows multiple blue-red lamellae spanning the full thickness. Although the localised zones marked by white arrows appear frequently, every one terminates at the dashed boundary of SCR-13.3 and none links into a principal strain band along the gradient direction. This demonstrates that, while the structural gradient supplies multiple plastic outlets, the compositional interfaces effectively sever channel coalescence [592,593].

The resulting strength and ductility synergy, where one plus one exceeds two, does not arise from simple addition of strength but from extra hardening terms produced by non-linear coupling. First, pronounced HDI incompatibility generated by the structural gradient drives sustained accumulation of GNDs and the HDI stress at numerous interlayer interfaces, maintaining a steep slope of flow stress with strain and markedly elevating strain hardening during the uniform plastic regime [115,592]. Second, the compositional interfaces confine each newly formed LSZ to a limited scale, reduce the correlation length of strain localisation, delay band coalescence and necking, and distribute plastic work across a larger volume fraction [592,593]. Third, phase-wise load redistribution due to the compositional gradient works in concert with the parallel channels provided by the structural gradient. When one layer becomes stronger through rapid hardening, a neighbouring layer that has not yet fully yielded immediately takes over, delivering self-regulating load transfer and sustained uniform elongation [115,592]. As a result, DG attains high initial strength together with persistent strain hardening and ductility, its performance surpasses the linear superposition of the SSG and SCG contributions, and among the four specimen types it achieves the most uniform distribution of plasticity and the most complete utilisation of material [115,592,593].

6.2.3 Crack deflection at the interfaces

Building on the previously established macroscopic performance and strain field characteristics, this section focuses on the interactions between cracks and interfaces. Using fractographic observations by SEM, we reconstruct crack propagation paths in the vicinity of compositional transition interfaces and structural gradient layers to compare the fracture behaviour induced by different gradient architectures.

First, a schematic as shown in Fig. 6-6 is provided to explain the annotation rules and to define the framework for subsequent descriptions of crack initiation, propagation and deflection. As illustrated, the crack initiates at the specimen surface, then advances along the path indicated by the red arrows, and ultimately traverses the GD direction. The locations of crack deflection are marked by black dashed circles and appear as locally raised peaks and recessed valleys within the plane formed by TD and GD. For clarity in the analyses that follow and to enable direct correspondence with the images, the projections of these deflection sites onto the TD–GD plane will be indicated by white dashed lines to delineate the crack deflection trajectory within the specimen.

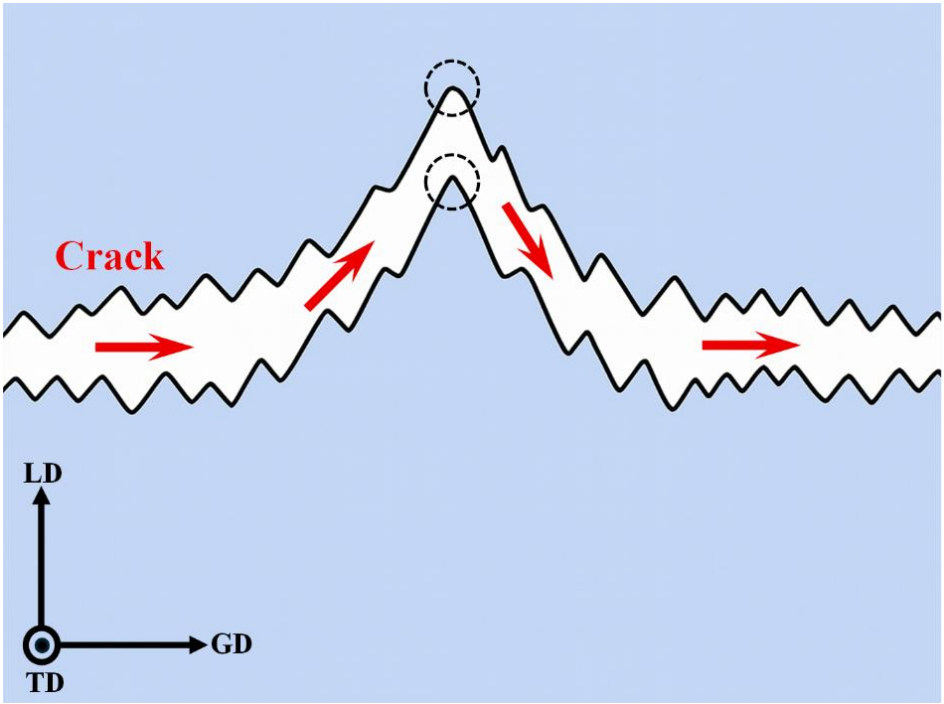

Figure 6-6 Schematic of crack path and notation. LD is the loading direction in tension, GD is the gradient or thickness direction, and TD is the transverse direction. The red arrows indicate the direction of crack propagation. Black dashed circles denote deflection sites that appear as protruding peaks and recessed valleys when viewed in the TD–GD plane.

Fig. 6-7 (a) shows that in Hom only a single white dashed line, approximately parallel to TD, is observed. This indicates that deflection occurs at one dominant site. Its projection extends along TD with very little variation along GD, implying that the crack front advances almost synchronously across the width, the path is close to straight, and plastic participation is limited.

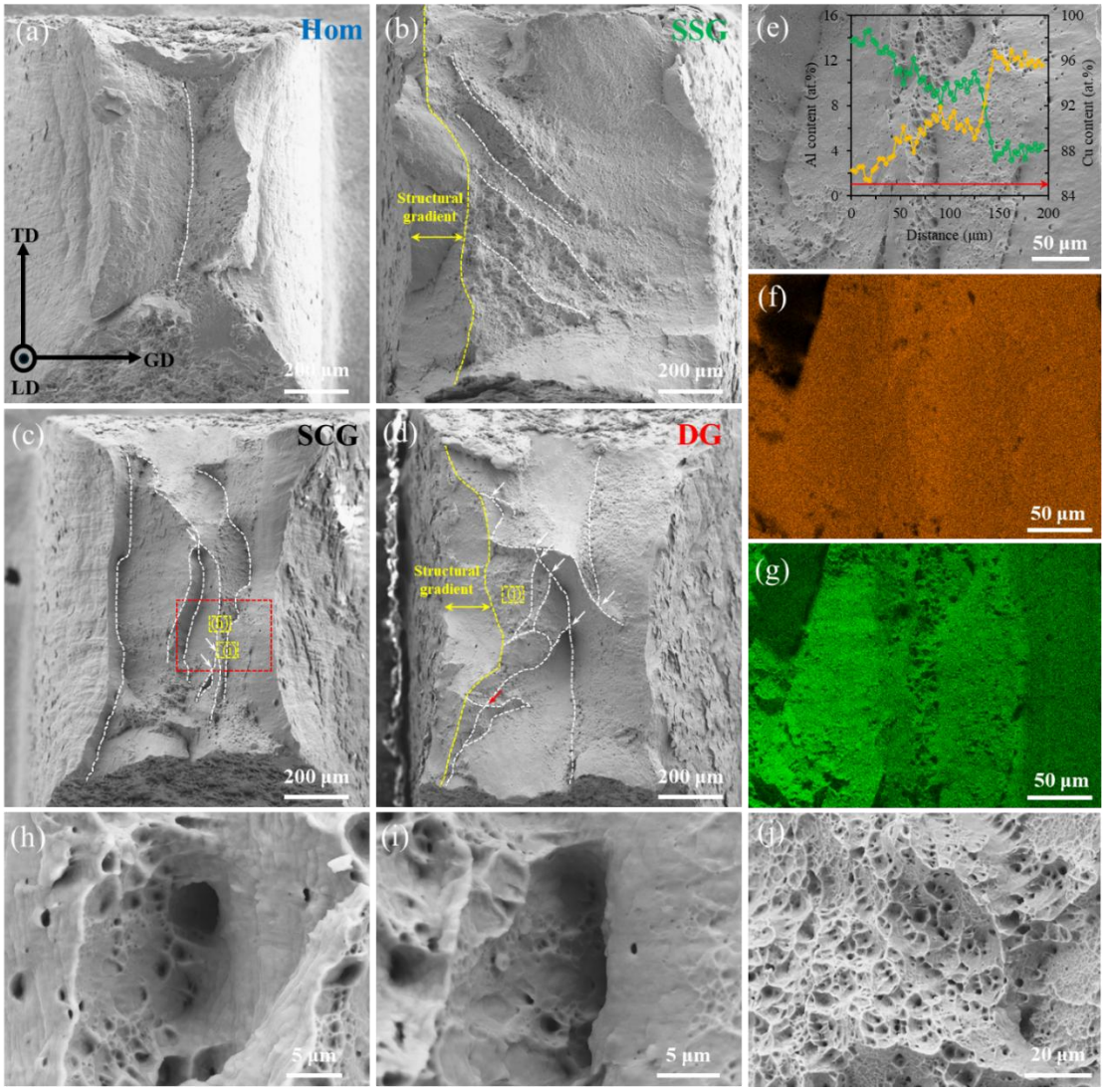

Figure 6-7 Crack path evolution in four samples and compositional evidence for interfacial deflection. (a) Hom. (b) SSG. (c) SCG. (d) DG. (e–g) Magnified views of the red boxed area in (c). (e) SEM image with line profiles taken from (f) and (g). (f) Cu EDS map. (g) Al EDS map. The red arrow gives the line scan path from start to end. (h) and (i) Magnified views of the two yellow boxed areas in (c) located on SCG deflection traces. (j) Magnified view of the yellow boxed area in (d) inside the DG two-dimensional deflection network. The yellow dashed lines with double-headed arrows mark the structural gradient regions. The white dashed lines delineate the crack deflection trajectory within the specimen.

In SSG, Fig. 6-7 (b), the yellow dashed line with the double-headed arrows marks the single structural gradient region. Four white dashed lines appear, each roughly parallel to the others and inclined by about 45° to TD. This arises because the structural gradient along GD imposes a continuous contrast in strength and constraint, which induces laterally increasing strain incompatibility and HDI stress along GD [61,174]. A shear component coupled with the opening mode is therefore generated in the plane spanned by TD and GD, rotating the orientation of the crack deflection trajectory. The near-parallelism of these lines reflects a gradient that is statistically close to linear, with an almost constant ratio between shear- and opening-driven components. The spacing between adjacent dashed lines corresponds to the separation of isosurfaces of equivalent mechanical properties within the gradient. Denser spacing signifies a steeper gradient and more frequent deflection events. All these features are characteristic of a structural gradient. The crack path is consequently more tortuous than in Hom.

Fig. 6-7 (c) shows that SCG contains many more white dashed lines that are approximately parallel to TD. This originates from discrete variations in the density of Al in solid solution along GD caused by the compositional gradient, which forms a series of weakening or strengthening bands across the width. Each crossing of such a band triggers one deflection in the TD–GD plane [595], producing layered multiple dashed lines. The bifurcations marked by white arrows arise from competition between local hard and soft channels, such that the crack partitions between two near-equienergetic routes. This indicates stronger crack shielding and higher energy dissipation. The path length increases further, and plasticity rises markedly.

In DG, Fig. 6-7 (d), the yellow dashed line with double-headed arrows again identifies the structural gradient zone and white arrows again indicate bifurcation. Uniquely, the white dashed lines link through bifurcation and mutual intersection, as indicated by the red arrows, to form fragmented two-dimensional regions rather than isolated lines. This contiguous morphology arises only under dual gradients, because the obliquely oriented deflection bands induced by the structural gradient and the TD-parallel deflection bands produced by the compositional gradient meet in space with comparable scale. Their coupling forms a percolating deflection network [596]. The crack front is repeatedly split and rejoined. The local principal stress direction rotates multiple times. The fracture surface roughness and the effective crack path length increase greatly. The plastic zone

expands widely and the resistance to crack advance is significantly enhanced.

In summary, the crack path in Hom is nearly straight. In SSG, the structural gradient produces strings of oblique deflections. In SCG, multiple TD-parallel deflections with bifurcation further extend the path and increase plasticity. In DG, the interwoven structural and compositional gradients build a unique contiguous two-dimensional deflection network that maximises crack tortuosity and plastic energy dissipation, giving the best overall performance.

Fig. 6-7 (e)–(g) provide a magnified view of the red dashed rectangle in Fig. 6-7 (c) together with compositional evidence. Fig. 6-7 (e) is the SEM micrograph of this region, with overlaid profiles derived from the EDS line scans shown in Fig. 6-7 (f) and Fig. 6-7 (g). The red arrow indicates the start and end points and the direction of the scan path. In the corresponding elemental maps, Fig. 6-7 (f) shows the Cu signal increasing from weak to strong, whereas Fig. 6-7 (g) shows the Al signal decreasing from strong to weak. The line scan results concurrently reveal anti-correlated compositional changes. With increasing distance, the atomic fraction of Al decreases continuously, while that of Cu rises markedly, and a distinct transition band emerges that marks a compositional transition interface. This interface coincides with the crack trace marked by white dashed lines in Fig. 6-7 (c), demonstrating that crack deflection occurs at the compositional transition interface and thereby establishing a direct link between local compositional heterogeneity and the reorientation of the crack path [595].

Fig. 6-7 (h) and Fig. 6-7 (i) show local fracture surfaces from two crack deflection bands in the SCG specimen. Ductile fracture dominated by microvoid nucleation, growth and coalescence is evident [597], yet the plastic response is limited and spatially non-uniform. In Fig. 6-7 (h), large cavities coexist with a dense population of fine equiaxed dimples, indicating strongly localised plasticity with insufficient energy dissipation in neighbouring regions. Fig. 6-7 (i) exhibits more pronouncedly oriented shear dimples together with tear ridges [597]. The number of dimples is greater, but their size distribution remains dispersed, which indicates band-narrowed shear deformation and plastic extension confined to a limited region.

By sharp contrast, the fracture surface of the DG specimen in Fig. 6-7 (j) lies within the two-dimensional contiguous deflection network generated by the interwoven structural and

compositional gradients. The entire field is almost uniformly covered by a high density of fine and deep multiscale dimples, accompanied by continuous bridging and tear ridges. Despite the larger field of view, the dimple number density per unit area is markedly higher than in SCG, while the dimples are further refined and their size distribution more uniform. These features indicate a pronounced expansion of the plastic zone and a multiplication of energy-dissipation pathways [597]. The contiguous deflection network repeatedly reorients the local principal stress by sustained branching and intersection, supplies abundant microvoid nucleation sites and extends the effective crack propagation length, which mechanistically endows DG with the highest ductility and fracture toughness [596].

6.2.4 Multiaxial stress and strain states

This section focuses on the multiaxial stress and multiaxial strain states that arise in gradient architectures during tensile loading and maps them directly to the observed fracture surface morphology to clarify their roles in plastic deformation.

Fig. 6-8 presents, in sequence, the pre- and post-tension morphologies for Hom specimens at different Al contents together with their corresponding SSG specimens, and for SCG and DG specimens. Within each group the left image, numbered 1, is the pre-deformation state and the right image, numbered 2, is the post-deformation state. The viewing plane is LD–GD, with TD normal to the image plane.

In the post-deformation images of Hom-4.9, Hom-9.1 and Hom-13.3, the yellow arrows clearly identify continuous edge flaring along the margins. By contrast, SSG-4.9, SSG-9.1, SSG-13.3, SCG and DG show no edge flaring after deformation, and their side edges remain straight and smooth. Edge flaring is the outward turning of the surface layer produced by coupling between in-plane tension and through-thickness bending. It signifies that the surface is in a plane stress dominated state with strong localisation [598]. It weakens strain hardening and load bearing capacity, drives the migration of strain concentration toward the edges, triggers earlier necking and reduces uniform elongation, which is detrimental to ductility.

From a mechanics standpoint, gradient structures develop multiaxial stress and multiaxial strain during tension. Beyond the tensile stress and tensile strain along LD, non-zero principal stresses and strains arise along GD and TD due to interlayer constraint. These additional loads originate from the mismatch in strength and hardening capacity among the

gradient sublayers and from the coupled deformation required to satisfy displacement continuity, together with HDI stresses induced by strain gradients [61]. In contrast, a homogeneous material lacks strength gradients and interlayer constraints. At the free surface, the lateral stress approaches zero and the deformation is close to uniaxial, so edge flaring occurs more readily [598].

The multiaxial field explains why SSG, SCG and DG do not exhibit edge flaring. In a compositional gradient system, different SCRs contract heterogeneously, with greater contraction in the centre and smaller contraction at the surface. To satisfy compatibility, the surface develops an in-plane compressive internal stress along TD under interlayer constraint [61]. This compression counteracts the bending moment and shear that would otherwise promote outward turning, so the edges remain stable before necking and fracture. This is the direct reason why SCG shows no edge flaring even without any prestress treatment. In SSG and DG, shot peening pre-introduces significant compressive residual stress and a hardened surface layer. During tension, these features further offset local tensile stress and suppress surface crack nucleation and out-of-plane warping, so edges remain straight in these specimens as well [599].

Placing multiaxial stress and multiaxial strain at the centre of the discussion also rationalises the differences in strength and ductility. DG couples the strong interlayer constraints and multiaxial internal stresses provided by the compositional gradient with the surface compressive residual stress and high strength surface layer provided by the structural gradient. Across the full section, this combination sustains HDI stresses and strain partitioning for longer, effectively delaying localisation and necking while improving the damage resistance of the surface, which yields the most favourable strength–ductility synergy [61]. In SSG, the surface compressive stress and the surface strength gradient are present, yet the interior gradient and constraints are weaker and the degree of multiaxial coupling is limited, so high strain hardening cannot be maintained for long. In SCG, the interlayer constraint is pronounced, and compressive stress can be established at the surface along TD to suppress edge flaring, but the absence of shot peening induced surface precompression and multiscale hardening sources leaves the surface more vulnerable and the initial strength relatively lower. The strength–ductility synergies of SSG and SCG are therefore inferior to that of DG.

In summary, the images show directly that edge flaring occurs only in Hom specimens and

is completely suppressed in SSG, SCG and DG. This confirms a stable deformation mechanism that is unique to gradient architectures and governed by multiaxial stresses and strains.

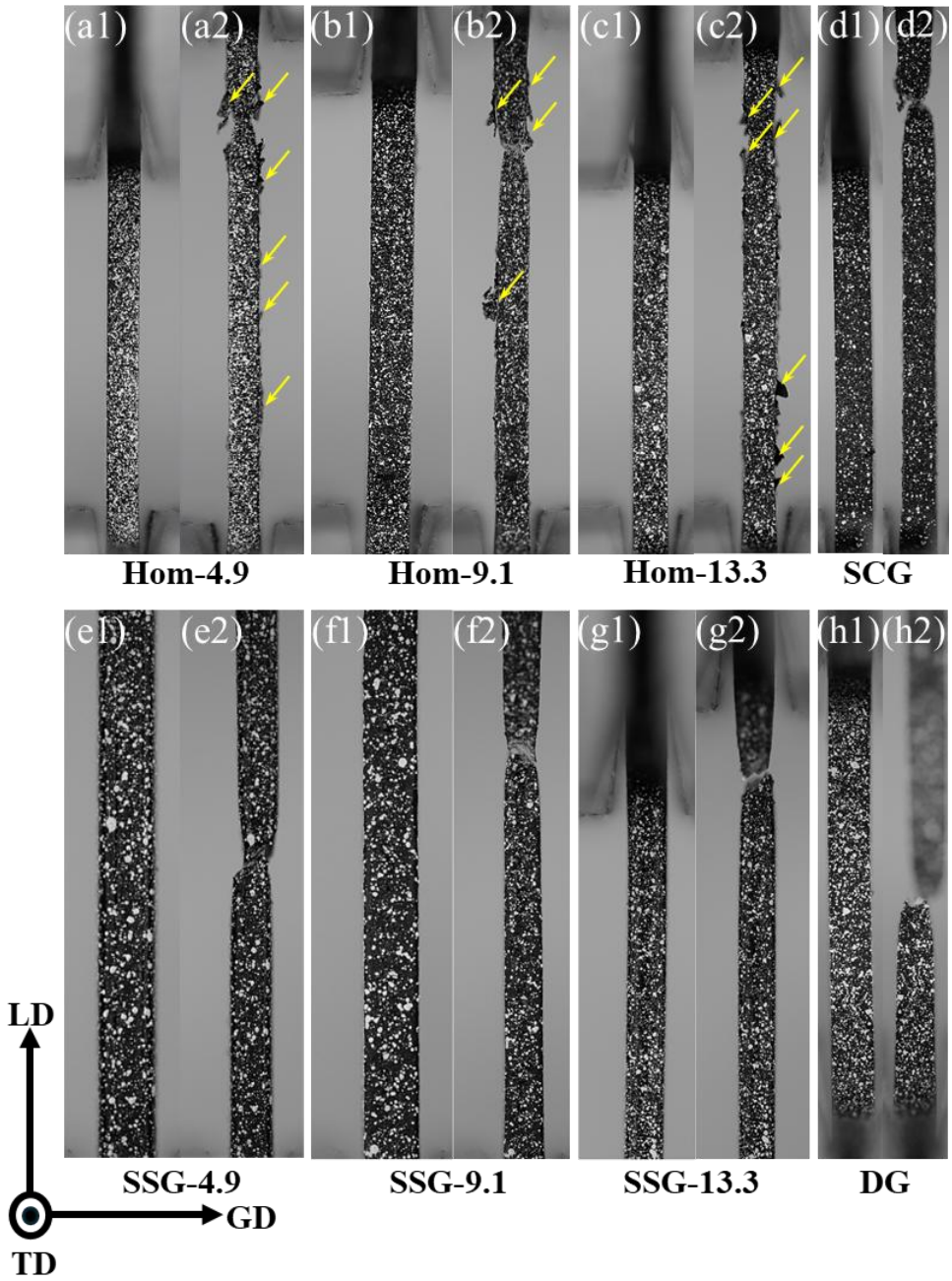

Figure 6-8 Tensile deformation of homogeneous and gradient specimens with varying Al content. Top row from left to right: Hom-4.9, Hom-9.1, Hom-13.3, SCG. Bottom row from left to right: SSG-4.9, SSG-9.1, SSG-13.3, DG. For each specimen, image 1 shows the undeformed state and image 2 shows the state after tensile deformation. Images were taken in the plane defined by the LD and the GD, with the TD perpendicular to the page. Yellow arrows mark edge curling that develops during plastic deformation.

6.2.5 Plasticity induced by lattice rotation

Building on the earlier discussion of the superior mechanical performance of DG, this section moves to microstructural characterisation and further elucidates how the dual gradient architecture contributes to the strength–ductility synergy. Fig. 6-9 (a) presents the IPF-LD map of the SCG specimen prior to tensile deformation from section 5.2.3. Fig. 6-9 (b) shows the corresponding Al EDS map. These two figures are provided here as references that define the initial states of composition and crystallographic orientation. The tonal stratification in Fig. 6-9 (b) clearly confirms a through-thickness compositional gradient and echoes the fine-grained bands at the compositional transition positions visible in Fig. 6-9 (a). Fig. 6-9 (c) gives the line scan results along the GD. The Al content exhibits a stepwise distribution, and the thickness is partitioned from surface to core into five zones, namely SCR-4.9, TR-4.9-9.1, SCR-9.1, TR-9.1-13.3 and SCR-13.3. Combining the fine-grained bands at the transition positions in Fig. 6-9 (a) with the colour steps in Fig. 6-9 (b) enables unambiguous definition of the two transition regions (TRs). Their local compositional gradients are marked as Δ_1 equals 0.21 at.%/μm and Δ_2 equals 0.23 at.%/μm.

Fig. 6-9 (d) shows that shot peening produces an ultrafine-grained near-surface layer in the DG specimen, revealing intense surface plastic deformation [600]. Fig. 6-9 (e) is the IQ + GBs map. Blue lines denote LAGBs, black lines denote HAGBs and red lines denote TBs. The density of LAGBs is markedly elevated at the surface and decays progressively inwards, which indicates a highly developed dislocation substructure and subgrain refinement in the surface layer, while the interior contains abundant twins [561]. Fig. 6-9 (f) presents the KAM distribution. KAM values are highest at the surface and extend towards the centre, reflecting a maximum in dislocation density and residual strain energy at the surface together with a pronounced gradient through the thickness [538].

Taken together, the multiple lines of microstructural evidence consistently demonstrate that a dual gradient structure comprising both compositional and structural gradients has been successfully established.

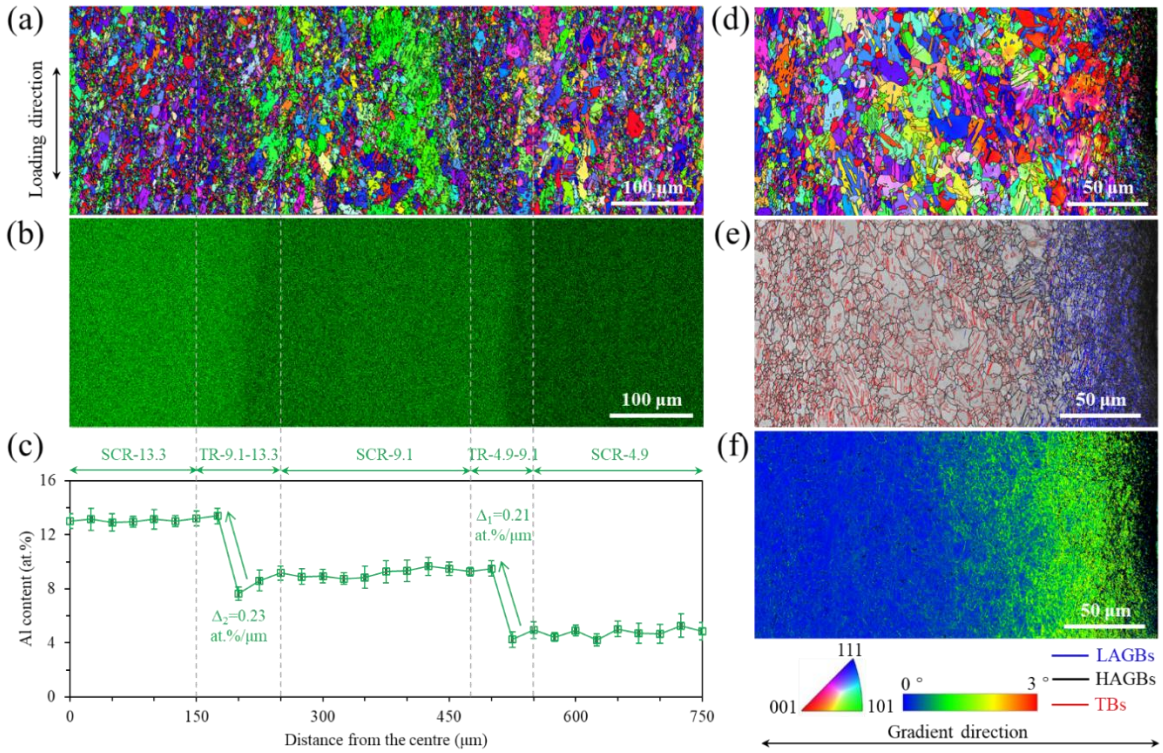

Figure 6-9 Microstructure and composition in SCG and DG samples before tensile deformation. (a) IPF-LD map of the SCG sample before tensile deformation. (b) Corresponding Al EDS map. (c) Line scan of Al content along the gradient direction. (d) IPF-LD map of the DG sample before tensile deformation. (e) IQ + GBs map. Blue lines denote LAGBs, black lines denote HAGBs, and red lines denote twin boundaries. (f) KAM map.

To further interrogate the distinctive deformation mechanism in DG, Fig. 6-10 (a)–(f) present the IPF maps along RD and the texture evolution before and after tensile loading. Fig. 6-10 (a) shows the specimen before deformation. Fig. 6-10 (b) shows the specimen after deformation. Fig. 6-10 (c) and (d) enlarge the ultrafine-grained near-surface layer within the structural gradient. Fig. 6-10 (e) and (f) give the orientation distributions corresponding to Fig. 6-10 (c) and (d). In Fig. 6-10 (c), the ultrafine grains display a pronounced elongated morphology, with long axes inclined by approximately 45° to GD. This indicates that during pre-treatment, near-surface shear dominated the formation process, with the long axes aligned with the direction of maximum resolved shear stress, representing a shear-dominated morphological orientation. The essence is orientation selection driven by lattice rotation induced by intense plastic deformation at the surface. By contrast, in Fig. 6-10 (d) after deformation, the ultrafine grains are further elongated and their long axes are almost coincident with LD, which shows that under uniaxial tension, the orientation evolution is governed by the external load. Through sustained slip and

rotation, the grains evolve towards stable terminal orientations, the <111> axes tend to align with the tensile axis, and the morphological long axes therefore align with LD. Relative to Fig. 6-10 (c), the former reflects orientation selection by the pre-treatment shear field with respect to GD, whereas the latter reflects orientation selection by the tensile field with respect to LD, and the controlling stress states and the associated orientation attractors differ. The orientation distributions also undergo a systematic conversion. Fig. 6-10 (e) shows that before deformation, the <111> direction clusters along GD. Fig. 6-10 (f) shows that after deformation, the <111> direction clusters along LD. This migration from <111> ∥ GD to <111> ∥ LD clearly reveals substantial lattice rotation within the ultrafine-grained layer during plastic deformation. It is important to emphasise that this substantial lattice rotation not only accommodates orientation curvature through the accumulation of GNDs but, under the constraint of interlayer yield mismatch, also generates strong HDI stress and kinematic hardening, thus providing a cooperative plasticity mechanism that couples orientation, curvature and HDI stress [75,559,601,602]. This mechanism sustains an elevated strain-hardening rate and load bearing capacity during necking, delays deformation localisation and enlarges the necking stage elongation $\varepsilon_f - \varepsilon_u$, hence the DG specimen exhibits excellent total ductility [176,179]. In sum, the redirection of the morphological long axis together with the migration of <111> poles from GD to LD jointly demonstrates pronounced lattice rotation within the structural gradient layer, which underpins improved ductility.

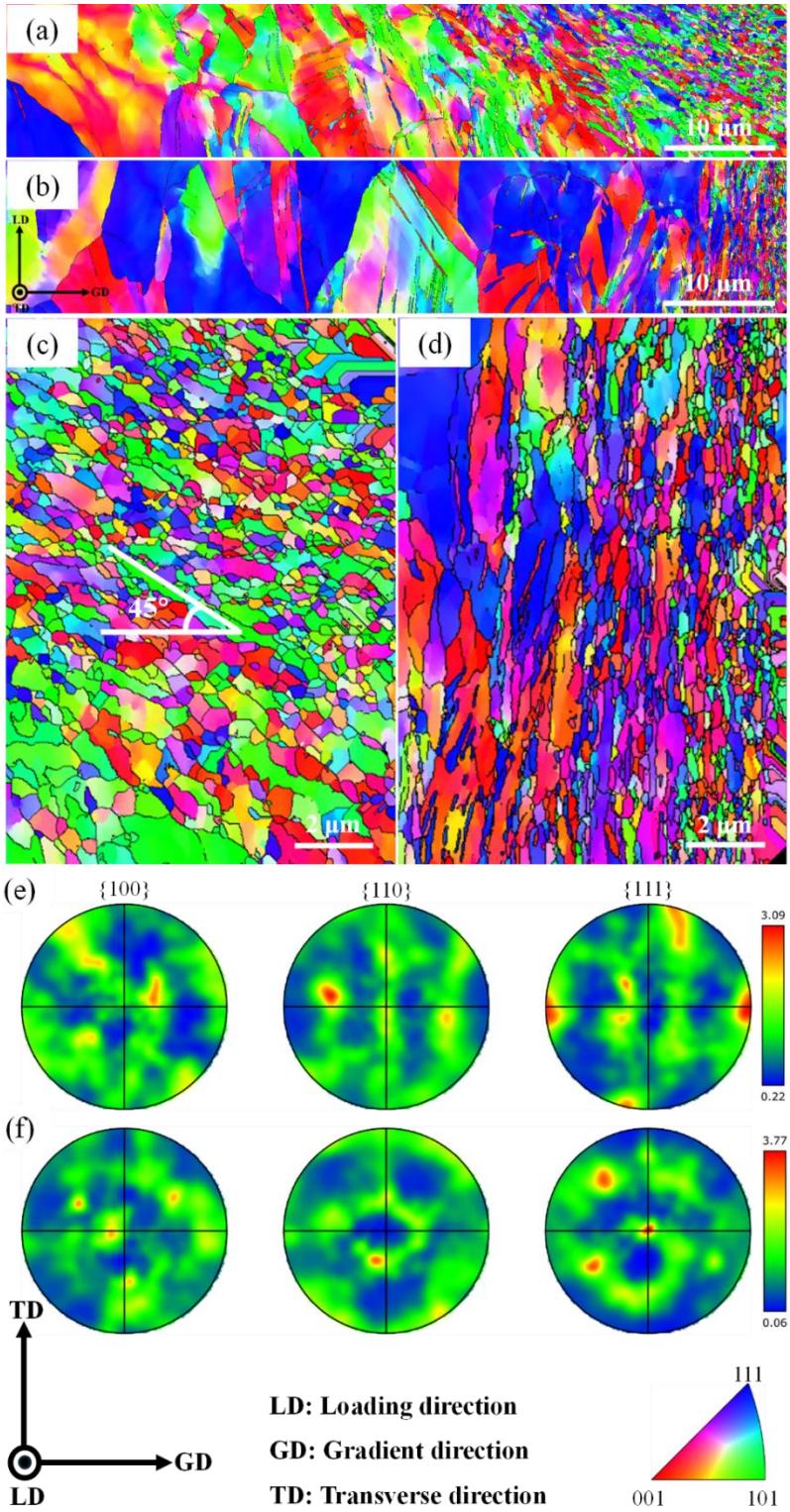

Figure 6-10 Evolution of morphology and crystallographic orientation in the DG sample before and after tension. (a) IPF-RD map of the DG sample before tensile deformation. (b) IPF-RD map of the DG sample after tensile deformation. (c) Magnified view of the outermost ultrafine-grained layer before deformation. (d) Magnified view of the outermost ultrafine-grained layer after deformation. (e,f) Pole figures for {100}, {110} and {111} corresponding to the regions in (c) and (d) respectively.

6.2.6 Strain-hardening behaviour in the compositional transition regions

A comprehensive characterisation and analysis of the compositional transition regions in the DG specimen is presented below. Fig. 6-11 shows the microstructures of two such regions. In TR-4.9-9.1, the IQ + GBs map in Fig. 6-11 (a) uses blue lines for LAGBs, black lines for HAGBs, and red lines for TBs. It shows a high density of boundaries adjacent to the interface together with banded deformation structures. The IPF-RD map in Fig. 6-11 (b) reveals a bimodal grain size distribution with coarse and fine grains coexisting, a feature that has already been described and discussed in detail in section 5.2.3. The KAM map in Fig. 6-11 (c) displays a continuous band of high values near the compositional transition interface. The Al EDS map in Fig. 6-11 (d) clearly marks the position of the compositional jump. In TR-9.1-13.3, Fig. 6-11 (e) and Fig. 6-11 (f) likewise show a heterogeneous microstructure with interleaved coarse and fine grains. In Fig. 6-11 (g), the KAM rises markedly in the vicinity of the interface and then decays progressively towards the low-Al domain. The Al EDS map in Fig. 6-11 (h) is co-registered over the same field.

The consistent occurrence of high KAM near both interfaces indicates a pronounced increase in local lattice curvature and dislocation density [538]. This reflects severe plastic incompatibility and a clear strain gradient driven by contrasts in composition and strength. The origin of the high KAM in the transition zones lies in heterogeneous deformation caused by the bimodal grain size. The relatively more compliant coarse grains yield first and carry plasticity. The fine grains, together with their high density of boundaries, provide strong constraints and suppress slip transfer. Strain gradients therefore arise at the interfaces between coarse and fine grains [112]. To maintain deformation compatibility, a large population of GNDs must accumulate to accommodate these gradients, which produces high KAM at the interfaces and around the peripheries of fine grains [538]. Elevated KAM further points to excellent strain-hardening capacity, since strong mechanical incompatibility between fine and coarse grains induces significant strain gradients that trigger intense HDI strain hardening [174]. Acting together with dislocation multiplication within the coarse grains, this HDI hardening increases the capacity for dislocation storage near the interfaces, sustains a rising flow stress and delays local necking [174]. Accordingly, both compositional transition regions exhibit sustained and robust strain-hardening behaviour during tensile loading.

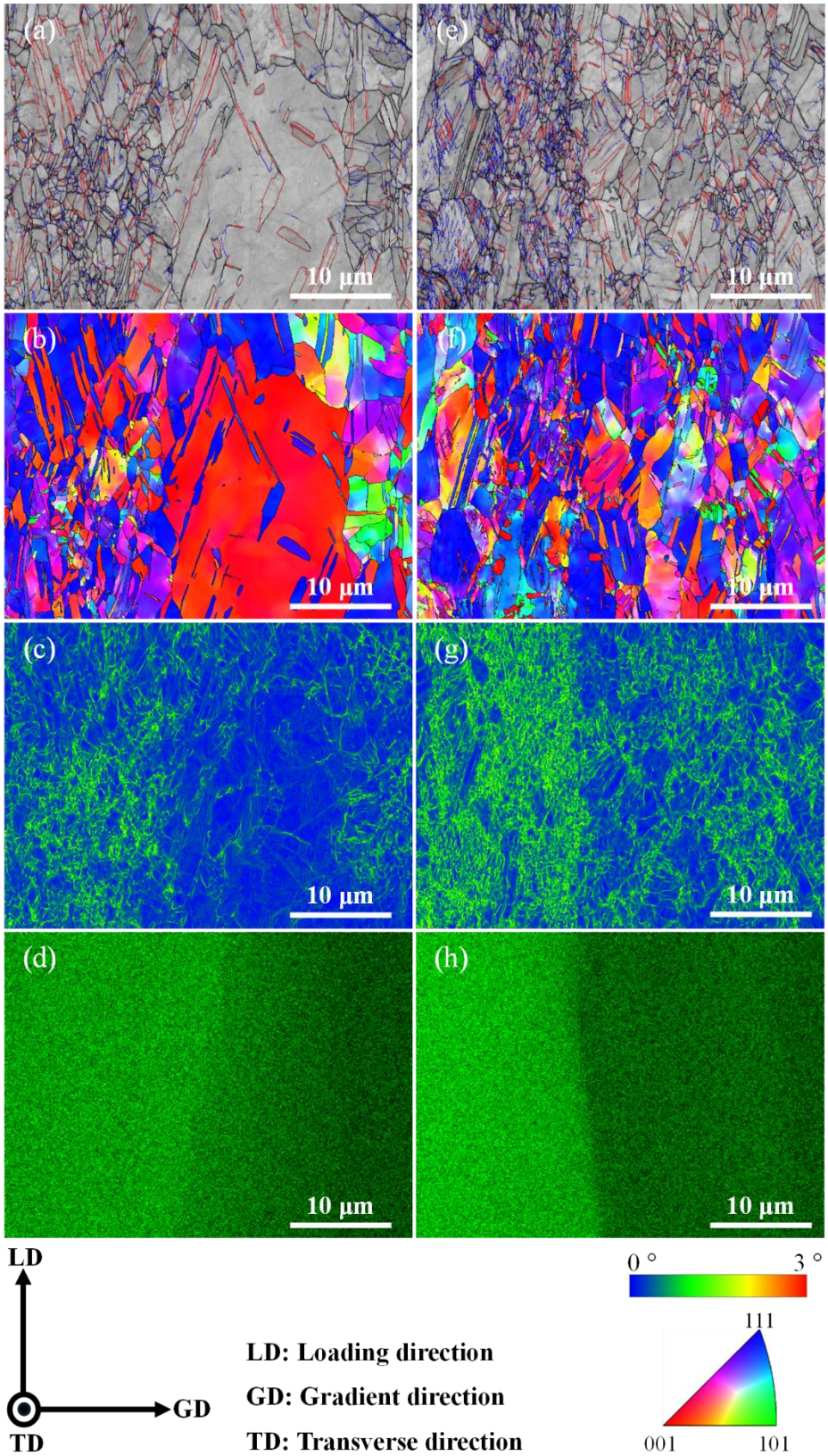

Figure 6-11 Microstructural characterisation of compositional transition regions in the DG specimen after tensile deformation. (a–d) correspond to TR-4.9-9.1, (e–h) correspond to TR-9.1-13.3. (a,e) IQ + GBs maps. Blue lines denote LAGBs, black lines denote HAGBs, and red lines denote twin boundaries. (b,f) IPF-LD maps. (c,g) KAM maps. (d,h) Al EDS maps.

The nanoscale investigation of the compositional transition region of DG is conducted by TEM. Fig. 6-12 (a) is a low magnification TEM image of the TR. Fig. 6-12 (b) is the corresponding Al elemental map, which displays continuous bright bands within the TR and indicates selective Al enrichment along the interface. Fig. 6-12 (c) is a high magnification TEM image of the boxed area in (a), where dense nanotwins interact with grain boundaries. Fig. 6-12 (d) is an HRTEM image of (c). Blue and yellow labels mark the matrix M and the twin T, where they meet at a HAGB indicated by the white dashed line, and local stepwise nucleation and thickening of SF to twin lamellae are visible. Fig. 6-12 (e)–(g) are HAADF-STEM images with Cu and Al EDS maps, which further confirm Al segregation at this HAGB. Fig. 6-12 (h) is the Fast Fourier Transform (FFT) diffraction pattern of (d). The blue and yellow windows index plane (111) of matrix M and plane (111) of twin T and the red window corresponds to a neighbouring grain, revealing the typical twin orientation relationship on the set of planes denoted by braces {111}. These observations collectively indicate that twins originate from HAGBs and extend as lamellae along braces {111}, and that interfacial Al enrichment is highly co-located in space with these twins.

From a mechanistic standpoint, Al segregation at grain boundaries lowers the local SFE through compositional and structural coupling, which promotes preferential nucleation of Shockley partial dislocations at boundaries or interfaces to form SF embryos [603,604]. Successive emission of partials on adjacent braces {111} planes then builds layer upon layer, producing nanotwins that thicken under slip-driven growth [603]. First, theory and experiment have established that in Cu-based alloys Al effectively lowers the SFE and shifts the deformation mode from slip-dominated to twinning-prone [603]. Second, solute segregation at faults or interfaces further depresses the local SFE and the unstable twin barrier, which markedly reduces the nucleation work for partial dislocations [604]. Third, grain boundaries, which possess high free energy and significant free volume, act as dislocation sources and solute sinks and are classic nucleation sites for deformation twins in low-SFE fcc materials [603]. In this work, the bright Al EDS band and the HRTEM identified twin origin coincide at the same HAGB, which provides direct crystallographic evidence for the mechanism outlined above.

The transition region naturally contains strong gradients of chemical potential together with strain and stress gradients. These drive solute segregation to grain boundaries during

deformation and can induce near-interface short-range order or compositional fluctuations, which further decrease the effective SFE at the interface and stabilise fault or twin embryos. This behaviour is consistent with the thermodynamic descriptions of McLean and Lejček [605,606] and with observations of deformation induced grain boundary segregation [124]. The intense compositional waves and fluctuations in the transition region therefore provide both kinetic and thermodynamic channels for Al enrichment at boundaries, so that nanotwins nucleate more readily at interfaces and proliferate rapidly.

This composite interface architecture of grain boundaries and nanotwins confers distinctive advantages for strain hardening. First, dense TBs together with HAGBs form a multilevel blocking network, which greatly shortens the mean free path of dislocations and promotes pile-ups [607]. Second, interactions between TBs and dislocations continuously supply new dislocation sources and interface evolution pathways during plastic flow and sustain a high and persistent strain-hardening rate [607]. Third, when the TR contains spatial gradients in twin thickness or density, coupling between the gradient and the twins amplifies strain gradients, which acts jointly with HDI strengthening and HDI strain hardening to deliver an exceptional cooperative strengthening and hardening response [174]. It follows that this Al segregation induced nanotwinned interface structure in the TR provides unusually strong strain-hardening capacity, markedly delays necking and ultimately enhances ductility [174,607].

Fig. 6-12 systematically demonstrates Al segregation at HAGBs within the TR and the interfacial origin and orientation relationship of deformation twins. Mechanistically, Al enrichment at the interface lowers the local SFE and reduces the nucleation barrier for partial dislocations, which nucleate nanotwins directly at boundaries. The pronounced compositional fluctuations in the TR further intensify this coupling between segregation and twinning. The resulting hierarchical network of grain boundary and nanotwin interfaces stores dislocations and undergoes dynamic evolution of twin boundaries, and together with potential additional contributions from HDI strengthening and HDI strain hardening endows the TR with outstanding strain-hardening capacity and a significant gain in ductility.

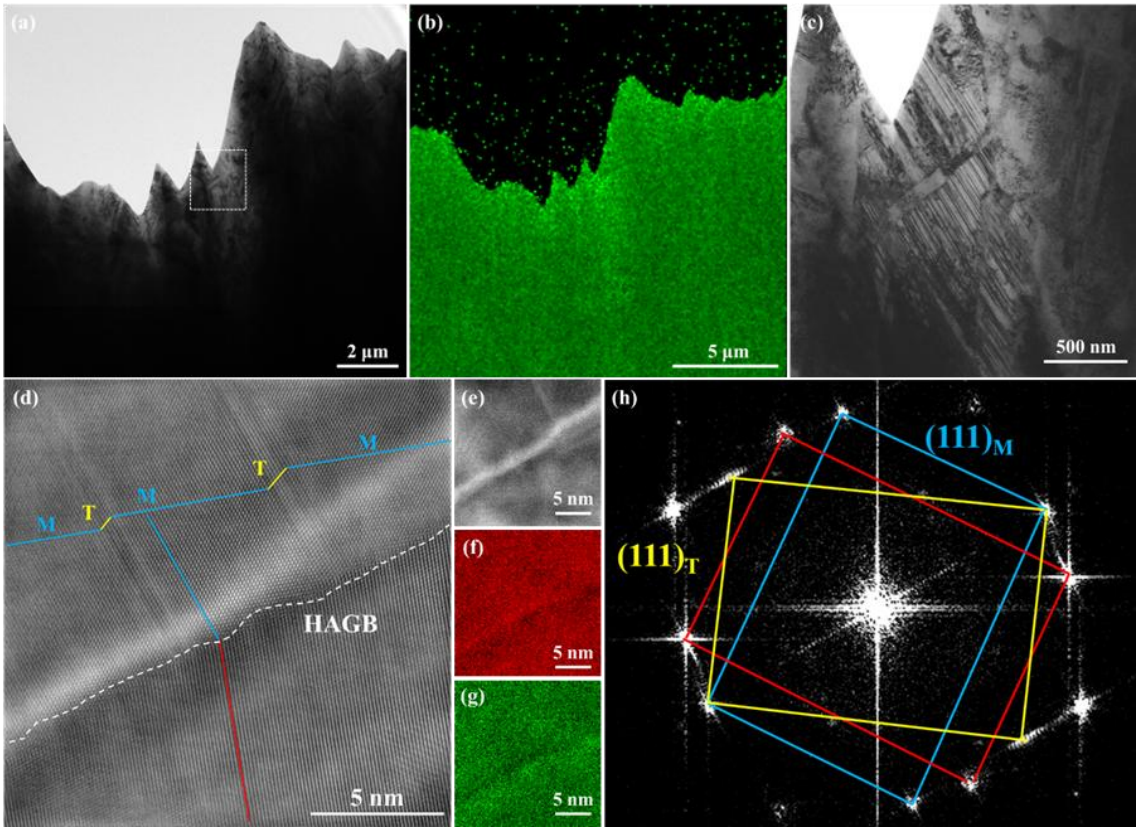

Figure 6-12 TEM characterisation of the compositional transition region. (a) Low magnification TEM image of the transition region. (b) Corresponding Al elemental map from EDS for (a). (c) High magnification TEM image taken from the boxed area in (a). (d) High resolution TEM image from (c). The dashed white line denotes the HAGB. M denotes matrix. T denotes twin. The red line marks a neighbouring grain. (e–g) HAADF-STEM image (e) and the corresponding EDS maps for Cu (f) and Al (g). (h) Fast Fourier Transform (FFT) pattern of (d). Blue box: $(111)_M$ plane of the matrix. Yellow box: $(111)_T$ plane of the twin.

In the compositional transition regions of the DG specimen, the bimodal grain size distribution gives rise to pronounced strain gradients and HDI stresses [61]. At the same time, these regions are architected as a hierarchical interfacial network in which grain boundaries are coupled with a high density of nanotwin boundaries. The two act cooperatively to markedly enhance the strain-hardening capacity of the transition region [61,607]. Accordingly, the ability of the compositional transition interfaces described in section 6.2.2 to arrest the growth and propagation of LSZs can be ascribed to two factors. First, a high strain-hardening rate, consistent with the criterion for stable plastic flow, suppresses local softening and the co-amplification with shear bands, which forces plasticity to disperse more uniformly over a larger volume [61,598]. Second, the

hierarchical interfacial network repeatedly truncates and deflects potential shear bands, so geometric percolation cannot be achieved [61,607]. Furthermore, the crack deflection recorded near compositional interfaces in section 6.2.3 arises from the dense ensembles of GBs and TBs, which impose strong orientation and strength mismatches that drive crack tip mode conversion and path re selection. The result is systematic deflection and blunting together with enhanced fracture resistance [608].

6.3 Summary

This chapter places SCG, SSG and DG in a side-by-side comparison on the same Cu–Al alloy platform. Using full-field strain by DIC with finite element validation, reconstruction of fracture surfaces and crack paths, in situ surface morphology time series, and EBSD, SEM and TEM across multiple length scales, we establish a unified physical picture for how the dual gradient architecture breaks the strength–ductility trade-off. At comparable average composition, DG attains the highest strength and ductility, with $\sigma_y \approx 385$ MPa, $\sigma_{UTS} \approx 495$ MPa, $\varepsilon_u \approx 38\%$ and $\varepsilon_f \approx 49\%$. Its strength–ductility index $\sigma_y \times \varepsilon_u$ exceeds 140 MJ m^{-3}, which markedly surpasses the literature envelope for similar alloys. The post-necking elongation $\varepsilon_f - \varepsilon_u \approx 11\%$ together with the through-thickness ΔH profile demonstrates a stronger capacity for residual hardening and dislocation storage.

Mechanistically, SSG establishes a stable strain gradient with the core as the principal load bearing domain, achieved through a near-surface nano and ultrafine-grained layer combined with residual compressive stress. SCG undergoes a gradient reversal during loading, transferring the principal load bearing role from the surface to the core. DG superposes these effects to generate localised strain zones that are dense, fine in scale and dispersed. Compositional transition interfaces pin and segment these zones, preventing the percolation of a single dominant band, enabling self-regulated load transfer and engaging a larger volume fraction of the material.

With respect to crack behaviour, oblique deflection bands induced by the structural gradient interweave with TD-parallel deflection bands induced by the compositional gradient, forming a spanning two-dimensional deflection network that greatly increases the effective propagation path and the plastic zone volume fraction. At the same time, multiaxial stress and strain states broadly suppress edge flaring, so macroscopic plastic flow remains more uniform and more persistent.

At the microscopic level, the near-surface layer of DG exhibits pronounced lattice rotation and orientation selection, with the <111> axis migrating from GD to LD, accompanied by a steep KAM gradient. Within the compositional transition regions, Al segregation promotes a high density of nanotwins, which together with grain boundaries builds a hierarchical interfacial network. Coupled with GND-driven HDI strengthening and HDI strain hardening, this network both deflects and blunts cracks, and potential shear bands and enhances the strain-hardening capacity.

In summary, DG achieves a toughening gain greater than simple additivity through a non-linear synergy that combines multi-channel parallel plasticity, interface pinning and deflection, self-regulated load transfer and multiaxial coupling. This work proposes a generalisable principle of cross-scale co-design of gradients and interfaces.

Chapter 7. Conclusions and future perspectives

7.1 Conclusions

This study proposes and validates a scalable route to co-construct compositional and structural dual gradients within a single alloy system. Wire arc additive manufacturing is used to programme centimetre scale compositionally graded Cu–Al architectures. Subsequent cold rolling, annealing and rotationally accelerated shot peening introduce a near-surface nano and ultrafine-grained structural gradient. Multiscale characterisation together with DIC and finite element analysis is then used to establish a closed-loop linkage and mechanistic map that connects composition, microstructure and properties. The core conclusions are as follows.

First, the gradient sequence, forward or reverse, governs melt pool coupling between heat transfer, fluid flow and solute transport, and determines the height resolved trajectories of microstructure and hardness. Quantitative analysis based on thermal conductivity contrast and thermal and solutal Marangoni convection explains the narrow and deep geometry of Cu-rich layers and the shallow and wide geometry of Al-rich layers. A forward compositional gradient, FCG, forms ten steady compositional steps and yields an inverted "V" hardness profile, soft then hard then soft. A reverse compositional gradient, RCG, retains seven steps and yields hard then soft then hard, with the minimum Al content raised by remelting induced stirring and buoyancy-driven convection. In FCG, solidification and thermal cycling drive the following microstructural evolution. Near the substrate a columnar-to-equiaxed transition occurs. In the central Al-rich domain, intermittent DDRX generates equiaxed fine grains. At the top Cu-rich domain, CDRX is dominant, and the texture evolves from a strong <100> fibre to a diffuse weakened state.

Second, subsequent cold rolling and annealing establish a one-way chain of evidence linking composition, SFE, deformation mode, stored energy, recrystallisation and texture. During cold rolling, as Al content increases and the SFE decreases, localised shear bands develop into a hierarchical network and both LAGBs and KAM rise monotonically. The rolling texture evolves from Rotated cube and Goss induced by near-surface shear, to F and Copper twin in the interior, and then to the Brass, S and E families in the high-Al region. Finite element analysis confirms the spatial distribution of through-thickness compression and RD and TD shear and its correspondence with the thickness and strength

of each SCR. After annealing at 400 °C, the transition regions are the finest and most uniform. The high-Al region remains fine grains through twin pinning, whereas the low-Al region develops a bimodal population of fine and coarse grains due to limited nucleation density. The texture reorders through competition between stored energy and boundary mobility and retains twin-related orientation inheritance.

Third, the dual gradient architecture delivers a more-than-additive advantage in strength–ductility synergy. Relative to homogeneous, single structural gradient and single compositional gradient counterparts at comparable average composition, the dual gradient specimen attains $\sigma_y \approx 385$ MPa, $\sigma_{UTS} \approx 495$ MPa, $\varepsilon_u \approx 38\%$ and $\varepsilon_f \approx 49\%$. The strength–ductility index $\sigma_y \times \varepsilon_u$ exceeds 140 MJ m^{-3}. The through-thickness ΔH profile after tensile testing shows the greatest residual hardening. DIC reveals that the homogeneous material forms an early through-thickness localised band. The single structural gradient maintains a stable strain gradient with a strong surface and a weak core. The single compositional gradient undergoes a reversal from surface-dominated to core-dominated load bearing. The dual gradient, through multi-channel parallel plasticity combined with pinning at compositional interfaces, produces localised bands that are dense, fine in scale and strongly dispersed, and that are difficult to percolate, which markedly delays necking. In terms of crack behaviour, oblique deflection bands induced by the structural gradient interlock spatially with TD-parallel deflection bands induced by the compositional gradient, forming a spanning two-dimensional deflection network that significantly lengthens the effective propagation path and enlarges the plastic zone volume fraction. At the microscale, the shot peened layer exhibits pronounced lattice rotation, with the <111> axis migrating from GD to LD. The transition regions develop an Al-enriched hierarchical interfacial network of grain boundaries and nanotwin boundaries. Together with GND-driven HDI strengthening and HDI strain hardening, these features constitute the microstructural basis for the high hardening capacity and the high elongation to fracture of the dual gradient material.

7.2 Future perspectives

For engineering deployment and transferable design, we recommend deepening along the following directions:

1. Reversible design and process control. Build a multiscale design map and optimisation framework that links composition, SFE, microstructure and hardening. Incorporate

thermo-fluid-solute coupling, gradient plasticity and crystal plasticity into data-driven inverse design. Develop closed-loop WAAM control with online monitoring of composition and melt pool, suppress unintended remelting and mixing, and tailor step width and gradient steepness on demand.

2. Interface and composition engineering. Use microalloying and thermomechanical pathways to steer the density of grain boundaries and nanotwin boundaries and to promote compositional short-range order. Exploit local SFE tuning in the transition region to realise programmable twinning networks and a hard or soft interlayer strength spectrum, thereby amplifying HDI strengthening and HDI strain hardening in concert with pinning effects.
3. Service and reliability. Systematically evaluate gradient orientation effects and the evolution of fracture toughness under cyclic loading, rate and temperature variation, creep, and corrosion–fatigue coupling. Define compatibility windows and failure thresholds across gradient scale, gradient sequence and load direction, and establish scalable size–property calibration with non-destructive evaluation workflows.
4. Broad-spectrum materials and multifunctional integration. Generalise the principle of dual gradients plus interfacial networks to low and medium SFE FCC alloys, titanium, steels, high-entropy alloys and Cu-based multicomponent systems. Target multifunctional components that combine load bearing with thermal or electrical conductivity and corrosion resistance. Explore three-dimensional multidirectional gradients and in-situ multimaterial transitions to achieve structure–function integration and lifecycle advantages in repairable manufacturing.

Overall, the synergistic paradigm of multi-channel parallel plasticity, interfacial pinning and deflection, adaptive load transfer and multiaxial coupling provides generalisable design rules and process levers for surpassing empirical strength–ductility limits in metallic materials. With the convergence of reversible design, service reliability and digital manufacturing, dual gradient and interface engineering can progress from case-specific optimisation to on-demand customisation, enabling larger scales, more complex geometries and more demanding service conditions.

References

1. Kocich R, Kunčická L. Mechanical properties in progressive mechanically processed metallic materials. Materials 2020;13:4668.
2. Benedetti M, Du Plessis A, Ritchie R O, Dallago M, Razavi N, Berto F. Architected cellular materials: a review on their mechanical properties towards fatigue-tolerant design and fabrication. Mater Sci Eng R, 2021;144:100606.
3. Kogo B, Xu C, Wang B, Chizari M, Reza Kashyzadeh K, Ghorbani S. An experimental analysis to determine the load-bearing capacity of 3D printed metals. Materials 2022;15:4333.
4. Zhang P, Liu J, To A C. Role of anisotropic properties on topology optimisation of additive-manufactured load-bearing structures. Scr Mater 2017;135:148–152.
5. Kruzic J J. Bulk metallic glasses as structural materials: a review. Adv Eng Mater 2016;18:1308–1331.
6. Trzepieciński T, Najm S M. Current trends in metallic materials for body panels and structural members used in the automotive industry. Materials 2024;17:590.
7. Russell A M. Ductility in intermetallic compounds. Adv Eng Mater 2003;5:629–639.
8. Torabi A R. Estimation of tensile load-bearing capacity of ductile metallic materials weakened by a V-notch: the equivalent material concept. Mater Sci Eng A 2012;536:249–255.
9. Xiong Y Z, Gao R N, Zhang H, Dong L L, Li J T, Li X. Rationally designed functionally graded porous Ti-6Al-4V scaffolds with high strength and toughness built via selective laser melting for load-bearing orthopaedic applications. J Mech Behav Biomed Mater 2020;104:103673.
10. Martínez R A. Fracture surfaces and the associated failure mechanisms in ductile iron with different matrices and load bearing. Eng Fract Mech 2010;77:2749–2762.
11. Zhang X Y, Fang G, Leeflang S, Zadpoor A A, Zhou J. Topological design, permeability and mechanical behaviour of additively manufactured functionally graded porous metallic biomaterials. Acta Biomater 2019;84:437–452.
12. Wu S W, Wang G, Wang Q, Jia Y D, Yi J, Zhai Q J, et al. Enhancement of strength-ductility trade-off in a high-entropy alloy through a heterogeneous structure. Acta Mater 2019;165:444–458.
13. Dang B, Zhang X, Chen Y Z, Chen C X, Wang H T, Liu F. Breaking through the

strength-ductility trade-off dilemma in an Al-Si-based casting alloy. Sci Rep 2016;6:30874.

14. Liu J, Jin Y, Fang X, Chen C, Feng Q, Liu X, et al. Dislocation strengthening without ductility trade-off in metastable austenitic steels. Sci Rep 2016;6:35345.
15. Wang H, Chen X, Zhou H, Jiang Y, Liu P. Static recrystallised annealing treatment-induced strength-ductility trade-off in cold-rolled Co36Fe36Cr18Ni10 multi-principal alloy. Mater Charact 2021;179:111254.
16. Wang R, Du C, Zhang Q, Liu J, Ren X. Grain refining mechanism and strength-ductility trade-off of NbC-reinforced FeCoNiCrMn HEA. Mater Sci Eng A 2024;915:147290.
17. Wang X, Ding Y, Gao Y, Ma Y, Chen J, Gan B. Effect of grain refinement and twin structure on the strength and ductility of Inconel 625 alloy. Mater Sci Eng A 2021;823:141739.
18. Li H G, Huang Y J, Zhao W J, Chen T, Sun J F, Wei D Q, et al. Overcoming the strength–ductility trade-off in an additively manufactured CoCrFeMnNi high entropy alloy via deep cryogenic treatment. Addit Manuf 2022;50:102546.
19. Fan J, Zhu L, Lu J, Fu T, Chen A. Theory of designing the gradient microstructured metals for overcoming strength-ductility trade-off. Scr Mater 2020;184:41–45.
20. Su J, Raabe D, Li Z. Hierarchical microstructure design to tune the mechanical behavior of an interstitial TRIP–TWIP high-entropy alloy. Acta Mater 2019;163:40–54.
21. Miyazaki I, Furuta T, Oh-ishi K, Nakagaki T, Kuramoto S, Shibata A, et al. Overcoming the strength–ductility trade-off via a thermally stable and plastically unstable austenitic phase in cold-worked steel. Mater Sci Eng A 2018;721:74–80.
22. Naseri M, Moghaddam A O, Shaburova N, Mikhailov D, Gholami D, Mourad A H, et al. Upgrading the strength–ductility trade-off of Al0.25CoCrFeNiCu and Al0.45CoCrFeNiSi0.45 high-entropy alloys through severe cold rolling. Mater Today Commun 2024;38:108036.
23. Zhu Y, Ameyama K, Anderson P M, Beyerlein I J, Gao H, Kim H S, et al. Heterostructured materials: superior properties from hetero-zone interaction. Mater Res Lett 2021;9:1–31.
24. Wu X, Zhu Y. Gradient and lamellar heterostructures for superior mechanical properties. MRS Bull 2021;46:244–249.
25. Han Z, Liu K, Zhou L, Fang F, Jiang J, Zhou X. Architecting unusual dual-gradient

structures to overcome the strength–ductility trade-off in metallic materials. J Mater Process Technol 2025;335:118670.

26. Li J, Weng G J, Chen S, Wu X. On strain hardening mechanism in gradient nanostructures. Int J Plast 2017;88:89–107.
27. An X, Bao W, Zhang Z, Jiang Z, Yuan S, You Z, et al. Gradient-enhanced strain hardening and tensile deformability in a gradient-nanostructured Ni alloy. Nanomaterials 2021;11:2437.
28. Xu L, Huang Z, Shen Q, Chen F. Atomistic simulations of plasticity heterogeneity in gradient nano-grained FCC metals. Mater Des 2022;221:110929.
29. Liu Y, Lu D, Wu G, Zhang Z, Huang H, Li L, et al. Deformation mechanism and hardening behaviour of gradient heterostructured magnesium alloys prepared by severe shear deformation. J Alloys Compd 2024;985:174099.
30. Shang Z, Sun T, Ding J, Richter N A, Heckman N M, White B C, et al. Gradient nanostructured steel with superior tensile plasticity. Sci Adv 2023;9:eadd9780.
31. He Q, Wei W, Wang M S, Guo F J, Zhai Y, Wang Y F, et al. Gradient microstructure design in stainless steel: a strategy for uniting strength-ductility synergy and corrosion resistance. Nanomaterials 2021;11:2356.
32. Wu X, Zhu Y. Heterostructured metallic materials: plastic deformation and strain hardening. Acta Metall Sin 2022;58:1349–1359.
33. Yang M, Pan Y, Yuan F, Zhu Y, Wu X. Hetero-deformation-induced strengthening and strain hardening in gradient structure. In: Heterostructured Materials. Singapore: Jenny Stanford Publishing; 2021:105–118.
34. Xu L, Huang Z, Shen Q, Chen F. Effect of stacking-fault energy on hetero-deformation in gradient nanograined Cu–Ni alloys. Mech Mater 2024;196:105074.
35. Yuan R. Establishing a quantitative relationship between strain gradient and hetero-deformation-induced stress in gradient-structured metals. Acta Mech 2022;233:961–989.
36. Wei S. Compositionally graded alloys fabricated using the laser powder bed fusion technique [PhD thesis]. Nanyang Technological University; 2023.
37. Kim E S, Park J M, Karthik G M, Kim K T, Yu J H, Lee B J, et al. Local composition detouring for defect-free compositionally graded materials in additive manufacturing. Mater Res Lett 2023;11:586–594.
38. Hue D T H, Lam N V, Dinh V H, Nguyen T G, Bui T Q, Lich L V. Atomic-level analysis of unusual mechanical and failure behaviours in compositionally graded

nanowires: a molecular dynamics study. Vacuum 2024;225:113243.
39. Paul M J. Mechanical anisotropy in additive manufactured materials [PhD thesis]. University of New South Wales; 2023.
40. Santoro L, Boni M. The Reef Ridge supergene non-sulphide zinc mineralisation, Alaska. In: 21st International Mineralogical Association Conference; 2014; Johannesburg.
41. Zhang J. Electrodeposition of novel nanostructured and porous materials for advanced applications: synthesis, structural characterisation and physical/chemical performance [PhD thesis]. Universitat Autònoma de Barcelona; 2016.
42. Fong D D. Stresses in copper thin films and silver/nickel multilayers [PhD thesis]. Harvard University; 2001.
43. Wong K V, Hernandez A. A review of additive manufacturing. Int Sch Res Notices 2012;2012:208760.
44. Abdulhameed O, Al-Ahmari A, Ameen W, Mian S H. Additive manufacturing: challenges, trends and applications. Adv Mech Eng 2019;11:1687814018822880.
45. Gibson I, Rosen D, Stucker B, Khorasani M. Additive Manufacturing Technologies. Cham, Switzerland: Springer; 2021.
46. Dilberoglu U M, Gharehpapagh B, Yaman U, Dolen M. The role of additive manufacturing in the era of Industry 4.0. Procedia Manuf 2017;11:545–554.
47. Bourell D L. Perspectives on additive manufacturing. Annu Rev Mater Res 2016;46:1–18.
48. Frazier W E. Metal additive manufacturing: a review. J Mater Eng Perform 2014;23:1917–1928.
49. Treutler K, Wesling V. The current state of research of wire arc additive manufacturing (WAAM): a review. Appl Sci 2021;11:8619.
50. Derekar K S. A review of wire arc additive manufacturing and advances in wire arc additive manufacturing of aluminium. Mater Sci Technol 2018;34:895–916.
51. Çam G. Prospects of producing aluminium parts by wire arc additive manufacturing (WAAM). Mater Today Proc 2022;62:77–85.
52. Shah A, Aliyev R, Zeidler H, Krinke S. A review of the recent developments and challenges in wire arc additive manufacturing (WAAM) process. J Manuf Mater Process 2023;7:97.
53. Zeng L, Zeng L, Xu P, Liu W, Liang T, Li W, et al. Enhanced strength-ductility synergy in high-entropy alloys via architecting three-level gradient hierarchical nanostructure.

Mater Sci Eng A 2023;885:145597.
54. Pour-Ali S, Kiani-Rashid A R, Babakhani A. Surface nanocrystallization and gradient microstructural evolutions in the surface layers of 321 stainless steel alloy treated via severe shot peening. Vacuum 2017;144:152–159.
55. Grosdidier T, Novelli M. Recent developments in the application of surface mechanical attrition treatments for improved gradient structures: processing parameters and surface reactivity. Mater Trans 2019;60:1344–1355.
56. Bagherifard S, Slawik S, Fernández-Pariente I, Pauly C, Mücklich F, Guagliano M. Nanoscale surface modification of AISI 316L stainless steel by severe shot peening. Mater Des 2016;102:68–77.
57. Wang R. Experimental and numerical investigations of mechanical properties and microstructural evolution of copper processed by accumulative skin pass rolling [PhD thesis]. University of Wollongong; 2021.
58. Qin S, Yang M, Jiang P, Wang J, Wu X, Zhou H, et al. Designing structures with combined gradients of grain size and precipitation in high entropy alloys for simultaneous improvement of strength and ductility. Acta Mater 2022;230:117847.
59. Chen Y, Li D, Xie R, Lu H. Dual precipitates and heterogeneous fine-grain structure induced strength-ductility synergy in a CoCrNi-based medium-entropy alloy. Mater Sci Eng A 2023;867:144504.
60. Jiang J, Chen Z, Ma H, Xing H, Li X. Strength-ductility synergy in heterogeneous-structured metals and alloys. Matter 2022;5:2430–2433.
61. Zhu Y, Wu X. Heterostructured materials. Prog Mater Sci 2023;131:101019.
62. Wang W Z, Jie Z Y, Yu G J, Xiao L F, Fan Y Z. Unified fatigue life calculation of Q460C steel fillet weld cruciform joints considering fatigue crack initiation and propagation. Adv Steel Constr 2024;20:222–231.
63. Zhao Y, Zhu Y, Lavernia E J. Strategies for improving tensile ductility of bulk nanostructured materials. Adv Eng Mater 2010;12:769–778.
64. Faridmehr I, Osman M H, Adnan A B, Nejad A F, Hodjati R, Azimi M. Correlation between engineering stress–strain and true stress–strain curve. Am J Civ Eng Archit 2014;2:53–59.
65. Wu X L, Zhu Y T. Ductility and plasticity of nanostructured metals: differences and issues. Mater Today Nano 2018;2:15–20.
66. Sun P L, Cerreta E K, Bingert J F, Gray G T III, Hundley M F. Enhanced tensile ductility through boundary structure engineering in ultrafine-grained aluminum. Mater

Sci Eng A 2007;464:343–350.
67. Ovid'ko I A, Valiev R Z, Zhu Y T. Review on superior strength and enhanced ductility of metallic nanomaterials. Prog Mater Sci 2018;94:462–540.
68. Vinogradov A, Yasnikov I S, Matsuyama H, Uchida M, Kaneko Y, Estrin Y. Controlling strength and ductility: dislocation-based model of necking instability and its verification for ultrafine grain 316L steel. Acta Mater 2016;106:295–303.
69. Zhao Y H, Guo Y Z, Wei Q, Topping T D, Dangelewicz A M, Zhu Y T, et al. Influence of specimen dimensions and strain measurement methods on tensile stress–strain curves. Mater Sci Eng A 2009;525:68–77.
70. Zhao Y H, Guo Y Z, Wei Q, Dangelewicz A M, Zhu Y T, Langdon T G, et al. Influence of specimen dimensions on the tensile behavior of ultrafine-grained Cu. Scr Mater 2008;59:627–630.
71. Hertzberg R W, Vinci R P, Hertzberg J L. Deformation and fracture mechanics of engineering materials. Hoboken: John Wiley & Sons; 2020.
72. Huda Z. Strengthening mechanisms in metals/alloys. In: Mechanical Behavior of Materials: Fundamentals, Analysis, and Calculations. 2022:63–79.
73. Kostryzhev A G. Strengthening mechanisms in metallic materials. Metals 2021;11:1134.
74. Nag S, Varvenne C, Curtin W A. Solute-strengthening in elastically anisotropic fcc alloys. Model Simul Mater Sci Eng 2020;28:025007.
75. Ashby M F. The deformation of plastically non-homogeneous materials. Philos Mag 1970;21:399–424.
76. Gao H, Huang Y, Nix W D, Hutchinson J. Mechanism-based strain gradient plasticity—I. Theory. J Mech Phys Solids 1999;47:1239–1263.
77. Meyers M A, Chawla K K. Mechanical Behavior of Materials. Cambridge: Cambridge University Press; 2008.
78. Madec R, Kubin L P. Dislocation strengthening in FCC metals and in BCC metals at high temperatures. Acta Mater 2017;126:166–173.
79. Pande C S, Cooper K P. Nanomechanics of Hall–Petch relationship in nanocrystalline materials. Prog Mater Sci 2009;54:689–706.
80. Meyers M A, Mishra A, Benson D J. Mechanical properties of nanocrystalline materials. Prog Mater Sci 2006;51:427–556.
81. Zhu Y T, Liao X Z, Wu X L. Deformation twinning in nanocrystalline materials. Prog Mater Sci 2012;57:1–62.

82. Cheng G M, Jian W W, Xu W Z, Yuan H, Millett P C, Zhu Y T. Grain size effect on deformation mechanisms of nanocrystalline bcc metals. Mater Res Lett 2013;1:26–31.
83. Yamakov V, Wolf D, Phillpot S R, Mukherjee A K, Gleiter H. Deformation-mechanism map for nanocrystalline metals by molecular-dynamics simulation. Nat Mater 2004;3:43–47.
84. Van Swygenhoven H, Derlet P M, Frøseth A G. Stacking fault energies and slip in nanocrystalline metals. Nat Mater 2004;3:399–403.
85. Lu K, Lu L, Suresh S. Strengthening materials by engineering coherent internal boundaries at the nanoscale. Science 2009;324:349–352.
86. Porter D A, Easterling K E. Phase transformations in metals and alloys. Boca Raton: CRC Press; 2009.
87. Li L, Xu W, Saber M, Zhu Y, Koch C C, Scattergood R O. Influence of scandium addition on the high-temperature grain size stabilization of oxide-dispersion-strengthened (ODS) ferritic alloy. Mater Sci Eng A 2015;636:565–571.
88. Saber M, Xu W, Li L, Zhu Y, Koch C C, Scattergood R O. Size effect of primary Y_2O_3 additions on the characteristics of the nanostructured ferritic ODS alloys: comparing as-milled and as-milled/annealed alloys using S/TEM. J Nucl Mater 2014;452:223–229.
89. Clyne T W, Withers P J. An introduction to metal matrix composites. Cambridge: Cambridge University Press; 1993.
90. Gao Y F, Zhang W, Shi P J, Ren W L, Zhong Y B. A mechanistic interpretation of the strength–ductility trade-off and synergy in lamellar microstructures. Mater Today Adv 2020;8:100103.
91. Xu B, Duan H, Chen X, Wang J, Ma Y, Jiang P, et al. Harnessing instability for work hardening in multi-principal element alloys. Nat Mater 2024;23:755–761.
92. Singh D, Yoshinaka F, Takamori S, Emura S, Sawaguchi T. Breaking the strength–ductility trade-off in austenitic stainless steel at cryogenic temperatures: mechanistic insights. J Mater Res Technol 2024;33:600–611.
93. Malygin G A. Analysis of structural factors that control necking during tension of FCC metals and alloys. Phys Solid State 2005;47:246–251.
94. Wu P, Song K, Liu F. Effect of coherent nanoprecipitate on strain hardening of Al alloys: breaking through the strength-ductility trade-off. Materials 2024;17:4197.
95. Gu L, Meng A, Chen X, Zhao Y. Simultaneously enhancing strength and ductility of HCP titanium via multi-modal grain-induced extra <c + a> dislocation hardening. Acta

Mater 2023;252:118949.

96. Shao C W, Zhang P, Zhu Y K, Zhang Z J, Tian Y Z, Zhang Z F. Simultaneous improvement of strength and plasticity: Additional work-hardening from gradient microstructure. Acta Mater 2018;145:413–428.
97. Li Z, Pradeep K G, Deng Y, Raabe D, Tasan C C. Metastable high-entropy dual-phase alloys overcome the strength–ductility trade-off. Nature 2016;534:227–230.
98. Li Z, Wang H, Guo Q, Li Z, Xiong D B, Su Y, et al. Regain strain-hardening in high-strength metals by nanofiller incorporation at grain boundaries. Nano Lett 2018;18:6255–6264.
99. Yang P J, Li Q J, Han W Z, Li J, Ma E. Designing solid-solution hardening to retain uniform ductility while quadrupling yield strength. Acta Mater 2019;179:107–118.
100. Zhao Y H, Liao X Z, Cheng S, Ma E, Zhu Y T. Simultaneously increasing the ductility and strength of nanostructured alloys. Adv Mater 2006;18:2280–2283.
101. Lu L, Shen Y, Chen X, Qian L, Lu K. Ultrahigh strength and high electrical conductivity in copper. Science 2004;304:422–426.
102. Zhu Y T, Wu X L, Liao X Z, Narayan J, Kecskés L J, Mathaudhu S N. Dislocation–twin interactions in nanocrystalline fcc metals. Acta Mater 2011;59:812–821.
103. Zhao Y H, Bingert J F, Liao X Z, Cui B Z, Han K, Sergueeva A V, et al. Simultaneously increasing the ductility and strength of ultra-fine-grained pure copper. Adv Mater 2006;18:2949–2953.
104. Zhao Y H, Zhu Y T, Liao X Z, Horita Z, Langdon T G. Tailoring stacking fault energy for high ductility and high strength in ultrafine grained Cu and its alloy. Appl Phys Lett 2006;89:121906.
105. Zhao Y H, Liao X Z, Zhu Y T, Horita Z, Langdon T G. Influence of stacking fault energy on nanostructure formation under high-pressure torsion. Mater Sci Eng A 2005;410:188–193.
106. Zhao Y H, Liao X Z, Horita Z, Langdon T G, Zhu Y T. Determining the optimal stacking fault energy for achieving high ductility in ultrafine-grained Cu–Zn alloys. Mater Sci Eng A 2008;493:123–129.
107. Zhao Y, Topping T, Bingert J F, Thornton J J, Dangelewicz A M, Li Y, et al. High tensile ductility and strength in bulk nanostructured nickel. Adv Mater 2008;20:3028–3033.
108. Zhao Y H, Bingert J F, Zhu Y T, Liao X Z, Valiev R Z, Horita Z, et al. Tougher ultrafine-grain Cu via high-angle grain boundaries and low dislocation density. Appl

Phys Lett 2008;92:081902.
109. Jian W W, Cheng G M, Xu W Z, Yuan H, Tsai M H, Wang Q D, et al. Ultrastrong Mg alloy via nano-spaced stacking faults. Mater Res Lett 2013;1:61–66.
110. Jian W W, Cheng G M, Xu W Z, Koch C C, Wang Q D, Zhu Y T, et al. Physics and model of strengthening by parallel stacking faults. Appl Phys Lett 2013;103:133108.
111. Liddicoat P V, Liao X Z, Zhao Y, Zhu Y, Murashkin M Y, Lavernia E J, et al. Nanostructural hierarchy increases the strength of aluminium alloys. Nat Commun 2010;1:63.
112. Wang Y, Chen M, Zhou F, Ma E. High tensile ductility in a nanostructured metal. Nature 2002;419:912–915.
113. Tellkamp V L, Lavernia E J, Melmed A. Mechanical behaviour and microstructure of a thermally stable bulk nanostructured Al alloy. Metall Mater Trans A 2001;32:2335–2343.
114. Li X, Lu L, Li J, Zhang X, Gao H. Mechanical properties and deformation mechanisms of gradient nanostructured metals and alloys. Nat Rev Mater 2020;5:706–723.
115. Ma E, Zhu T. Towards strength–ductility synergy through the design of heterogeneous nanostructures in metals. Mater Today 2017;20:323–331.
116. Dong X, Gao B, Xiao L, Hu J, Xu M, Li Z, et al. Heterostructured metallic structural materials: research methods, properties and future perspectives. Adv Funct Mater 2024;34:2410521.
117. Lu K. Making strong nanomaterials ductile with gradients. Science 2014;345:1455–1456.
118. Wu X, Zhu Y, Lu K. Ductility and strain hardening in gradient and lamellar structured materials. Scr Mater 2020;186:321–325.
119. Lu K. Stabilising nanostructures in metals using grain and twin boundary architectures. Nat Rev Mater 2016;1:1–13.
120. Wu X, Jiang P, Chen L, Yuan F, Zhu Y T. Extraordinary strain hardening by gradient structure. Proc Natl Acad Sci USA 2014;111:7197–7201.
121. Fang T H, Li W L, Tao N R, Lu K. Revealing extraordinary intrinsic tensile plasticity in gradient nano-grained copper. Science 2011;331:1587–1590.
122. Liu X C, Zhang H W, Lu K. Formation of nano-laminated structure in nickel by means of surface mechanical grinding treatment. Acta Mater 2015;96:24–36.
123. Xu W, Liu X C, Lu K. Strain-induced microstructure refinement in pure Al below 100 nm in size. Acta Mater 2018;152:138–147.

124. Xu W, Liu X C, Li X Y, Lu K. Deformation induced grain boundary segregation in nanolaminated Al–Cu alloy. Acta Mater 2020;182:207–214.
125. Wei Y, Li Y, Zhu L, Liu Y, Lei X, Wang G, et al. Evading the strength–ductility trade-off dilemma in steel through gradient hierarchical nanotwins. Nat Commun 2014;5:3580.
126. Wang H T, Tao N R, Lu K. Architectured surface layer with a gradient nanotwinned structure in a Fe–Mn austenitic steel. Scr Mater 2013;68:22–27.
127. Chen A, Liu J, Wang H, Lu J, Wang Y M. Gradient twinned 304 stainless steels for high strength and high ductility. Mater Sci Eng A 2016;667:179–188.
128. Chen T T, Wang J, Zhang Y, Jiang P, Yuan F P, Han P D, et al. Twin density gradient induces enhanced yield strength-and-ductility synergy in a S31254 super austenitic stainless steel. Mater Sci Eng A 2022;837:142727.
129. Ding J, Zhang M, Liang Y, Ren Y, Dong C, Lin J. Enhanced high-temperature tensile property by gradient twin structure of duplex high-Nb-containing TiAl alloy. Acta Mater 2018;161:1–11.
130. Mao B, Liao Y, Li B. Gradient twinning microstructure generated by laser shock peening in an AZ31B magnesium alloy. Appl Surf Sci 2018;457:342–351.
131. Chen G, Qiao J W, Jiao Z M, Zhao D, Zhang T W, Ma S G, et al. Strength–ductility synergy of Al0.1CoCrFeNi high-entropy alloys with gradient hierarchical structures. Scr Mater 2019;167:95–100.
132. Ke L, Lu J. Surface nanocrystallisation of metallic materials – presentation of the concept behind a new approach. J Mater Sci Technol 1999;15:193–198.
133. Wang G, Ouyang H, Su Y, Guo Q, Xiong D B, Zhuang Q, et al. Heterostructured bulk aluminium with controllable gradient structure: fabrication strategy and deformation mechanisms. Scr Mater 2021;196:113762.
134. Roumina R, Embury J D, Bouaziz O, Zurob H S. Mechanical behaviour of a compositionally graded 300M steel. Mater Sci Eng A 2013;578:140–149.
135. Ji W, Zhou R, Viveganantha P, Wu M S, Gao H, Zhou K. Recent progress in gradient-structured metals and alloys. Prog Mater Sci 2023;140:101194.
136. Chen W, You Z S, Tao N R, Jin Z H, Lu L. Mechanically-induced grain coarsening in gradient nano-grained copper. Acta Mater 2017;125:255–264.
137. Lee H H, Park H K, Jung J, Amanov A, Kim H S. Multi-layered gradient structure manufactured by single-roll angular-rolling and ultrasonic nanocrystalline surface modification. Scr Mater 2020;186:52–56.

138. Wang Y, Guo F, He Q, Song L, Wang M, Huang A, et al. Synergetic deformation-induced extraordinary softening and hardening in gradient copper. Mater Sci Eng A 2019;752:217–222.
139. Yang L, Chen Z, Ma X, Zhong D, Zhao X, Xiao L, et al. Improvement of strength and ductility in a gradient structured Ni fabricated by severe torsion deformation. Mater Sci Eng A 2021;826:141980.
140. Lin Y, Pan J, Luo Z, Lu Y, Lu K, Li Y. A grain-size-dependent structure evolution in gradient-structured (GS) Ni under tension. Nano Mater Sci 2020;2:39–49.
141. Moering J, Ma X, Chen G, Miao P, Li G, Qian G, et al. The role of shear strain on texture and microstructural gradients in low carbon steel processed by surface mechanical attrition treatment. Scr Mater 2015;108:100–103.
142. Oliaei M, Jamaati R. Improvement of the strength–ductility–toughness balance in interstitial-free steel by gradient microstructure. Mater Sci Eng A 2022;845:143237.
143. Shao C W, Zhang P, Wang X G, Wang Q, Zhang Z F. High-cycle fatigue behavior of TWIP steel with graded grains: breaking the rule of mixture. Mater Res Lett 2019;7:26–32.
144. Wang K, Wei A, Shi Z, Chen X, Lin J, Tong X, et al. The preparation and performance of grain size gradient TWIP steel fabricated by laser heat treatment. Mater Sci Eng A 2019;743:294–300.
145. Huang K, Sun Q, Yu C, Yin H. Deformation behaviors of gradient nanostructured superelastic NiTi shape memory alloy. Mater Sci Eng A 2020;786:139389.
146. Guo F J, Wang Y F, Wang M S, He Q, Ran H, Huang C X, et al. Hetero-deformation induced strengthening and toughening of pure iron with inverse and multi-gradient structures. Mater Sci Eng A 2020;782:139256.
147. Cheng Z, Bu L, Zhang Y, Wu H, Zhu T, Gao H, et al. Unraveling the origin of extra strengthening in gradient nanotwinned metals. Proc Natl Acad Sci USA 2022;119:e2116808119.
148. Sun T, Shang Z, Cho J, Ding J, Niu T, Zhang Y, et al. Ultra-fine-grained and gradient FeCrAl alloys with outstanding work hardening capability. Acta Mater 2021;215:117049.
149. Sun Y T, Kong X, Wang Z B. Superior mechanical properties and deformation mechanisms of a 304 stainless steel plate with gradient nanostructure. Int J Plast 2022;155:103336.
150. Panov D, Chernichenko R, Kudryavtsev E, Klimenko D, Naumov S, Pertcev A. Effect

of cold swaging on the bulk gradient structure formation and mechanical properties of a 316-type austenitic stainless steel. Materials 2022;15:2468.

151. Liu Y, Sun J, Fu Y, Xu B, Li B, Xu S, et al. Tuning strength-ductility combination on selective laser melted 316L stainless steel through gradient heterogeneous structure. Addit Manuf 2021;48:102373.

152. Cheng Z, Zhou H, Lu Q, Gao H, Lu L. Extra strengthening and work hardening in gradient nanotwinned metals. Science 2018;362:eaau1925.

153. Cheng Z, Lu L. The effect of gradient order on mechanical behaviors of gradient nanotwinned Cu. Scr Mater 2019;164:130–134.

154. Wan T, Cheng Z, Bu L, Lu L. Work hardening discrepancy designing to strengthening gradient nanotwinned Cu. Scr Mater 2021;201:113975.

155. Wu B, Fu H, Zhou X, Qian L, Luo J, Zhu J, et al. Severe plastic deformation-produced gradient nanostructured copper with a strengthening–softening transition. Mater Sci Eng A 2021;819:141495.

156. Wang X, Jiang L, Cooper C, Yu K, Zhang D, Rupert T J, et al. Toughening magnesium with gradient twin meshes. Acta Mater 2020;195:468–481.

157. Zhu L, Wen C, Gao C, Guo X, Chen Z, Lu J. Static and dynamic mechanical behaviors of gradient-nanotwinned stainless steel with a composite structure: experiments and modeling. Int J Plast 2019;114:272–288.

158. Jamalian M, Field D P. Effect of gradient microstructures on strengthening and toughening of AZ31. Mater Sci Eng A 2020;771:138615.

159. Miyazaki T. Development of “Macroscopic Composition Gradient Method” and its application to the phase transformation. Prog Mater Sci 2012;57:1010–1060.

160. Paul C G M. Performance and repair applications of 18Ni-300 maraging steel printed with micro-spot laser directed energy deposition [PhD thesis]. University of British Columbia; 2024.

161. Guo N, Zhang Z, Dong Q, Yu H, Song B, Chai L, et al. Strengthening and toughening austenitic steel by introducing gradient martensite via cyclic forward/reverse torsion. Mater Des 2018;143:150–159.

162. Jian S, Wang J, Xu D, Ma R, Huang C, Lei M, et al. Gradient microstructure and mechanical properties of Ti-6Al-4V titanium alloy fabricated by high-frequency induction quenching treatment. Mater Des 2022;222:111031.

163. Fu Y, Chen H, Guo R, Huang Y, Toroghinejad M R. Extraordinary strength–ductility in gradient amorphous structured Zr-based alloy. J Alloys Compd 2021;888:161507.

164. Hu S, Hou L, Wang K, Liao Z, Fautrelle Y, Li W, et al. Formation mechanism of gradient structure of aluminum matrix composite under static magnetic field during directional solidification. J Mater Res Technol 2020;9:4459–4468.
165. Ma P, Liu C, Chen Q, Wang Q, Zhan L, Li J. Natural-ageing-enhanced precipitation near grain boundaries in high-strength aluminum alloy. J Mater Sci Technol 2020;46:107–113.
166. Cerri E, Ghio E, Bolelli G. Effect of the distance from build platform and post-heat treatment of AlSi10Mg alloy manufactured by single- and multi-laser selective laser melting. J Mater Eng Perform 2021;30:4981–4992.
167. Park J, Kim T, Kim G W, Bessonov V, Telegin A, Iliushin I G, et al. Compositional gradient induced enhancement of Dzyaloshinskii–Moriya interaction in Pt/Co/Ta heterostructures modulated by Pt–Co alloy intralayers. Acta Mater 2022;241:118383.
168. Yan L, Chen Y, Liou F. Additive manufacturing of functionally graded metallic materials using laser metal deposition. Addit Manuf 2020;31:100901.
169. Hofmann D C, Kolodziejska J, Roberts S, Otis R, Dillon R P, Suh J O, et al. Compositionally graded metals: a new frontier of additive manufacturing. J Mater Res 2014;29:1899–1910.
170. Mahamood R M, Akinlabi E T. Types of functionally graded materials and their areas of application. In: Functionally Graded Materials. Cham: Springer International Publishing; 2017:9–21.
171. Ahankari S S, Kar K K. Functionally graded composites: processing and applications. In: Composite Materials: Processing, Applications, Characterisations. Berlin, Heidelberg: Springer; 2016:119–168.
172. Parihar R S, Setti S G, Sahu R K. Recent advances in the manufacturing processes of functionally graded materials: a review. Sci Eng Compos Mater 2018;25:309–336.
173. Li N, Cao Y, Fu A, Xie Q, Liu Y, Liu B. Effect of micro-scaled compositional gradient on microstructure of high-strength TiW composites. Mater Charact 2023;195:112523.
174. Zhu Y, Wu X. Perspective on hetero-deformation induced (HDI) hardening and back stress. Mater Res Lett 2019;7:393–398.
175. Nemat-Nasser S, Hori M. Micromechanics: overall properties of heterogeneous materials. Oxford: Elsevier; 2013.
176. Wu X, Zhu Y. Heterogeneous materials: a new class of materials with unprecedented mechanical properties. Mater Res Lett 2017;5:527–532.
177. Yang M, Pan Y, Yuan F, Zhu Y, Wu X. Back stress strengthening and strain hardening

in gradient structure. Mater Res Lett 2016;4:145–151.
178. Wu X L, Jiang P, Chen L, Zhang J F, Yuan F, Zhu Y T. Synergetic strengthening by gradient structure. Mater Res Lett 2014;2:185–191.
179. Wu X, Yang M, Yuan F, Wu G, Wei Y, Huang X, et al. Heterogeneous lamella structure unites ultrafine-grain strength with coarse-grain ductility. Proc Natl Acad Sci USA 2015;112:14501–14505.
180. Park H K, Ameyama K, Yoo J, Hwang H, Kim H S. Additional hardening in harmonic structured materials by strain partitioning and back stress. Mater Res Lett 2018;6:261–267.
181. Han Q, Asgari A, Hodgson P D, Stanford N. Strain partitioning in dual-phase steels containing tempered martensite. Mater Sci Eng A 2014;611:90–99.
182. Huang Y, Gao H, Nix W D, Hutchinson J. Mechanism-based strain gradient plasticity—II. Analysis. J Mech Phys Solids 2000;48:99–128.
183. Pan Q, Zhang L, Feng R, Lu Q, An K, Chuang AC, et al. Gradient cell–structured high-entropy alloy with exceptional strength and ductility. Science 2021;374:984–989.
184. Yang X, Ma X, Moering J, Zhou H, Wang W, Gong Y, et al. Influence of gradient structure volume fraction on the mechanical properties of pure copper. Mater Sci Eng A 2015;645:280–285.
185. Liu H, Gao B, Yang Y, Xu M, Li X, Li C, et al. Strain hardening behaviour and microstructure evolution of gradient-structured Cu-Al alloys with low stack fault energy. J Mater Res Technol 2022;19:220–229.
186. Shi Y, Wang Y, Shang W, Wang L, Zhang X, Liu H, et al. Influence of grain size distribution on mechanical properties and HDI strengthening and work-hardening of gradient-structured materials. Mater Sci Eng A 2021;811:141053.
187. Park K, Nishiyama M, Nakada N, Tsuchiyama T, Takaki S. Effect of the martensite distribution on the strain hardening and ductile fracture behaviors in dual-phase steel. Mater Sci Eng A 2014;604:135–141.
188. Tasan C C, Diehl M, Yan D, Zambaldi C, Shanthraj P, Roters F, et al. Integrated experimental–simulation analysis of stress and strain partitioning in multiphase alloys. Acta Mater 2014;81:386–400.
189. Cong Z H, Jia N, Sun X, Ren Y, Almer J, Wang Y D. Stress and strain partitioning of ferrite and martensite during deformation. Metall Mater Trans A 2009;40:1383–1387.
190. Ryu J H, Kim D I, Kim H S, Bhadeshia H K D H, Suh D W. Strain partitioning and mechanical stability of retained austenite. Scr Mater 2010;63:297–299.

191. Hasan M N, Liu Y F, An X H, Gu J, Song M, Cao Y, et al. Simultaneously enhancing strength and ductility of a high-entropy alloy via gradient hierarchical microstructures. Int J Plast 2019;123:178–195.
192. Zhang X, Gui Y, Lai M, Lu X, Gu J, Wang F, et al. Enhanced strength-ductility synergy of medium-entropy alloys via multiple level gradient structures. Int J Plast 2023;164:103592.
193. Wang F, Li Y, Chen X, Zhao H, Yaqoob K, Du Y, et al. Superior strength–ductility combination in Al alloys via dislocation gradient structure. Mater Res Lett 2023;11:347–353.
194. Han J, Sun J, Song Y, Xu B, Yang Z, Xu S, et al. Achieving gradient heterogeneous structure in Mg alloy for excellent strength-ductility synergy. J Magnes Alloy 2023;11:2392–2403.
195. Zhang X, Jia Z, Liu T, Shi Y, Liu H, Wang X, et al. Enhancing the strength–ductility synergy of medium-Mn steel by introducing multiple gradient structures. Mater Sci Eng A 2022;860:144268.
196. Wang Y, Yang G, Wang W, Wang X, Li Q, Wei Y. Optimal stress and deformation partition in gradient materials for better strength and tensile ductility: A numerical investigation. Sci Rep 2017;7:10954.
197. Zhang Q, Li J, Jiang K, Li P, Li Y, Zhang Y, et al. Gradient structure induced simultaneous enhancement of strength and ductility in AZ31 Mg alloy with twin-twin interactions. J Magnes Alloy 2023;11:2872–2882.
198. He Q, Wang Y F, Wang M S, Guo F J, Wen Y, Huang C X. Improving strength-ductility synergy in 301 stainless steel by combining gradient structure and TRIP effect. Mater Sci Eng A 2020;780:139146.
199. Da Huo P, Li F, Xu H Y, Niu W T, Gao R H. Achieving large-scale gradient structure in the AZ31 magnesium alloys for extraordinary strength-ductility synergy by hard plate rolling. J Alloys Compd 2023;944:169176.
200. Yin Z, Yang X, Ma X, Moering J, Yang J, Gong Y, et al. Strength and ductility of gradient structured copper obtained by surface mechanical attrition treatment. Mater Des 2016;105:89–95.
201. Zhu Y T, Liao X Z, Srinivasan S G, Lavernia E J. Nucleation of deformation twins in nanocrystalline face-centered-cubic metals processed by severe plastic deformation. J Appl Phys 2005;98:034319.
202. Brandes E A, Brook G B. Smithells metals reference book. London Boston:

Butterworth-Heinemann; 1998

203. Ma H, Zhao Y, Feng L, Liu T, Jin B, Yu Z, et al. Synergistic strengthening mechanisms of dual-phase CoCrFeMnNi high-entropy alloys with grain nano-gradient structure. Intermetallics 2024;173:108397.

204. Zhang X, Gai S, Liu T, Shi Y, Wang Y, Zhou Q, et al. Simultaneous improvement of yield strength and ductility in medium Mn steel by combining gradient structure and TRIP effect. Mater Charact 2023;197:112650.

205. Sun L, He X, Lu J. Nanotwinned and hierarchical nanotwinned metals: a review of experimental, computational and theoretical efforts. npj Comput Mater 2018;4:6.

206. Liebig J P, Krauß S, Göken M, Merle B. Influence of stacking fault energy and dislocation character on slip transfer at coherent twin boundaries studied by micropillar compression. Acta Mater 2018;154:261–272.

207. Lu Q, You Z, Huang X, Hansen N, Lu L. Dependence of dislocation structure on orientation and slip systems in highly oriented nanotwinned Cu. Acta Mater 2017;127:85–97.

208. Zhang C, Wang H, Li J, Pang B, Xia Y, Liu Y, et al. The aging-effect-modulated mechanical behavior in U–Nb shape-memory alloys through the modified twinning–detwinning process of the α″ phase. Mater Des 2019;162:94–105.

209. Zhou H, Zhu P, Yang W, Gao H. A gradient Eshelby force on twinning partial dislocations and associated detwinning mechanism in gradient nanotwinned metals. J Mech Phys Solids 2022;159:104746.

210. Ni S, Wang Y B, Liao X Z, Figueiredo R B, Li H Q, Ringer S P, et al. The effect of dislocation density on the interactions between dislocations and twin boundaries in nanocrystalline materials. Acta Mater 2012;60:3181–3189.

211. Cheng Z, Bu L, Zhang Y, Wu H, Zhu T, Lu L. Characterization of gradient plastic deformation in gradient nanotwinned Cu. Acta Mater 2023;246:118673.

212. Cheng Z, Wan T, Bu L, Lu L. Effect of volume fractions of gradient transition layer on mechanical behaviors of nanotwinned Cu. Acta Mater 2023;242:118456.

213. Wu Z X, Zhang Y W, Srolovitz D J. Dislocation–twin interaction mechanisms for ultrahigh strength and ductility in nanotwinned metals. Acta Mater 2009;57:4508–4518.

214. Cheng Z, Wan T, Lu L. Interface strain gradient enabled high strength and hardening in laminated nanotwinned Cu. Acta Mater 2023;256:119138.

215. Zhang Y, Cheng Z, Lu L, Zhu T. Strain gradient plasticity in gradient structured metals. J Mech Phys Solids 2020;140:103946.
216. Fang T H, Tao N R, Lu K. Tension-induced softening and hardening in gradient nanograined surface layer in copper. Scr Mater 2014;77:17–20.
217. Wang J J, Tao N R, Lu K. Revealing the deformation mechanisms of nanograins in gradient nanostructured Cu and CuAl alloys under tension. Acta Mater 2019;180:231–242.
218. Wang Y, Huang C, Li Y, Guo F, He Q, Wang M, et al. Dense dispersed shear bands in gradient-structured Ni. Int J Plast 2020;124:186–198.
219. Zhao P C, Guan B, Tong Y G, Wang R Z, Li X, Zhang X C, et al. A quasi-in-situ EBSD study of the thermal stability and grain growth mechanisms of CoCrNi medium entropy alloy with gradient-nanograined structure. J Mater Sci Technol 2022;109:54–63.
220. Peng H R, Gong M M, Chen Y Z, Liu F. Thermal stability of nanocrystalline materials: thermodynamics and kinetics. Int Mater Rev 2017;62:303–333.
221. Zhou X, Li X, Lu K. Size dependence of grain boundary migration in metals under mechanical loading. Phys Rev Lett 2019;122:126101.
222. Wei J, Feng B, Ishikawa R, Yokoi T, Matsunaga K, Shibata N, et al. Direct imaging of atomistic grain boundary migration. Nat Mater 2021;20:951–955.
223. Hu J, Wang X, Zhang J, Luo J, Zhang Z, Shen Z. A general mechanism of grain growth — Ⅰ. Theory. J Materiomics 2021;7:1007–1013.
224. Fang Z, Xiao J, Tan S, Deng C, Wang G, Mao S X. Atomic-scale observation of dynamic grain boundary structural transformation during shear-mediated migration. Sci Adv 2022;8:eabn3785.
225. Thomas S L, Chen K, Han J, Purohit P K, Srolovitz D J. Reconciling grain growth and shear-coupled grain boundary migration. Nat Commun 2017;8:1764.
226. Homer E R, Foiles S M, Holm E A, Olmsted D L. Phenomenology of shear-coupled grain boundary motion in symmetric tilt and general grain boundaries. Acta Mater 2013;61:1048–1060.
227. Rabkin E, Srolovitz D J. Grain growth stagnation in thin films due to shear-coupled grain boundary migration. Scr Mater 2020;180:83–87.
228. Niu L L, Zhang Y, Shu X, Gao F, Jin S, Zhou H B, et al. Shear-coupled grain boundary migration assisted by unusual atomic shuffling. Sci Rep 2016;6:23602.
229. Zhang Q, Gao Y H, Liu Y J, Xu P, Wu X, Ma J, et al. Enhanced strength–ductility

synergy in pure Al by assembling grain and chemical gradients. Mater Charact 2023;205:113320.

230. Liu C, Rao J, Sun Z, Lu W, Best J P, Li X, et al. Near-theoretical strength and deformation stabilisation achieved via grain boundary segregation and nano-clustering of solutes. Nat Commun 2024;15:9283.

231. Fayik M, El Dhaba A, Awad E. Diffusion-induced stresses due to an impulsive mass source under non-Fickian mass transfer models. 2022.

232. Herring C. Diffusional viscosity of a polycrystalline solid. J Appl Phys 1950;21:437–445.

233. Bardeen J. Diffusion in binary alloys. Phys Rev 1949;76:1403–1404.

234. Li J C M. Physical chemistry of some microstructural phenomena. Reading (MA): Addison-Wesley; 1978.

235. Nouara C, Hakim A A. Unstable plastic flow in the industrial Al-2.5 % Mg alloy: effect of annealing process. Abstr Appl Sci Eng 2016;9:1–19.

236. Zhang F, Curtin W A. Atomistically informed solute drag in Al–Mg. Model Simul Mater Sci Eng 2008;16:055006.

237. Chen X, Guo X, Ren J, Xue H, Ding Y, Lu X. Simulation on shear deformation property of nano-polycrystalline Ni-Co alloy with concentration gradient. Int J Mod Phys B 2023;37:2350259.

238. Luscher D J, Mayeur J R, Mourad H M, Hunter A, Kenamond M A. Coupling continuum dislocation transport with crystal plasticity for application to shock loading conditions. Int J Plast 2016;76:111–129.

239. Garbrecht M, Saha B, Schroeder J L, Hultman L, Sands T D. Dislocation-pipe diffusion in nitride superlattices observed in direct atomic resolution. Sci Rep 2017;7:46092.

240. Pei R, Woo S K, Yi S, Al-Samman T. Effect of solute clusters on plastic instability in magnesium alloys. Mater Sci Eng A 2022;835:142685.

241. Wang H, Dong B S, Chen Z B, Liu J Q, Haghdadi N, Lu R Q, et al. Effect of compositional heterogeneity on the mechanical properties of a single-phase Cu-9Al alloy with different grain sizes. Acta Mater 2024;263:119531.

242. Gu P, Asaro R J. Crack deflection in functionally graded materials. Int J Solids Struct 1997;34:3085–3098.

243. Bezensek B, Banerjee A. A local approach model for cleavage fracture and crack extension direction of functionally graded materials. Eng Fract Mech 2010;77:3394–3407.

244. Schramm B, Richard H A. Crack propagation in fracture mechanical graded structures. Fract Struct Integr 2015;34:280–289.
245. Dibblee K, Richard H A, Kullmer G. Influence of fracture mechanically graded materials on the crack propagation behaviour in 3-dimensional structures. Procedia Struct Integr 2018;13:322–327.
246. Tilbrook M T, Rozenburg K, Steffler E D, Rutgers L, Hoffman M. Crack propagation paths in layered, graded composites. Compos Part B Eng 2006;37:490–498.
247. Anderson T L. Fracture Mechanics: Fundamentals and Applications. Boca Raton: CRC Press; 2005.
248. Broek D. Elementary Engineering Fracture Mechanics. Dordrecht: Springer; 1982.
249. Ritchie R O. Mechanisms of fatigue-crack propagation in ductile and brittle solids. Int J Fract 1999;100:55–83.
250. Evans A G, Faber K T. Crack-growth resistance of microcracking brittle materials. J Am Ceram Soc 1984;67:255–260.
251. Ming-Yuan H, Hutchinson J W. Crack deflection at an interface between dissimilar elastic materials. Int J Solids Struct 1989;25:1053–1067.
252. Cook J, Gordon J E. A mechanism for the control of crack propagation in all-brittle systems. Proc R Soc Lond A 1964;282:508–520.
253. Ritchie R O. Mechanisms of fatigue crack propagation in metals, ceramics and composites: role of crack tip shielding. Mater Sci Eng A 1988;103:15–28.
254. Sun B, Lu W, Gault B, Ding R, Makineni S K, Wan D, et al. Chemical heterogeneity enhances hydrogen resistance in high-strength steels. Nat Mater 2021;20:1629–1634.
255. Gross D, Seelig T. Fracture Mechanics: With an Introduction to Micromechanics. Berlin: Springer; 2017.
256. Niu G, Zurob H S, Misra R D K, Tang Q, Zhang Z, Nguyen M T, et al. Superior fracture toughness in a high-strength austenitic steel with heterogeneous lamellar microstructure. Acta Mater 2022;226:117642.
257. Jin Z H, Paulino G H, Dodds R H Jr. Cohesive fracture modeling of elastic–plastic crack growth in functionally graded materials. Eng Fract Mech 2003;70:1885–1912.
258. Suh J Y. Fracture toughness study on bulk metallic glasses and novel joining method using bulk metallic glass solder [PhD thesis]. California Institute of Technology; 2009.
259. Duan F, Li Q, Jiang Z, Zhou L, Luan J, Shen Z, et al. An order–disorder core-shell strategy for enhanced work-hardening capability and ductility in nanostructured alloys. Nat Commun 2024;15:6832.

260. Xiao B, Chen R, Zhang J, Zhang J, Zhou Y, Ju J, et al. Additively manufactured heterogeneous precipitation-strengthened high-entropy alloys with high strength and ductility. Addit Manuf 2023;77:103795.
261. Huang J, Li W, Yang T, Chou T H, Zhou R, Liu B, et al. An additively manufactured precipitation-hardening medium-entropy alloy with excellent strength–ductility synergy over a wide temperature range. J Mater Sci Technol 2024;197:247–264.
262. Haftlang F, Seol J B, Zargaran A, Moon J, Kim H S. Chemical core-shell metastability-induced large ductility in medium-entropy maraging and reversion alloys. Acta Mater 2023;256:119115.
263. Chai Z, Wang L, Wang Z, Lu Q, Hu J, Sun W, et al. Cr-enriched carbide induced stabilisation of austenite to improve the ductility of a 1.7 GPa press-hardened steel. Scr Mater 2023;224:115108.
264. Zhang X, He Y, Chen T, Bi G, Li Y, Tang D, Wang X. Coordinating the deformation of a low-alloyed magnesium alloy for a superior combination of strength and ductility through core-shell structured reinforcements. Acta Mater 2024;281:120365.
265. Liu J, Wang X, Zong X, Ding X, Xu H, Yang F, Kong F. Superior strength–ductility synergy in novel as-cast L12-type HEI Ni50Co25Cr9.5Al9Ti5Ta1.5 with hierarchical core-shell structure. Acta Mater 2025;120811.
266. Shen J, Wang L, Cao Z, Hu L. Synergistically enhanced strength and ductility in TiAl/Nb composites via core-shell structure design. Mater Sci Eng A 2024;918:147417.
267. Zhang Q, Chen Z, Dong Y, Li C, Wang Y. High strength and ductility eutectic high-entropy alloy with unique core-shell structure. J Alloys Compd 2024;976:173141.
268. Zhang X, Chen T, Ma S, Qin H, Ma J. Overcoming the strength–ductility trade-off of an aluminium matrix composite by novel core-shell structured reinforcing particulates. Compos Part B Eng 2021;206:108541.
269. Cheng J, Wang J, Yun Y, Rui J, Zhao W, Li F. A novel core-shell structure-reinforced Zr-based metallic glass composite with combined high strength and good tensile ductility. J Alloys Compd 2019;803:413–416.
270. Seol J B, Na S H, Gault B, Kim J E, Han J C, Park C G, et al. Core-shell nanoparticle arrays double the strength of steel. Sci Rep 2017;7:42547.
271. He L, Abdolrahim N. Deformation mechanisms and ductility enhancement in core-shell Cu@Ni nanoporous metals. Comput Mater Sci 2018;150:397–404.
272. Liu D, Lu Z, Zhang C, Huang C, Gao Y, Shi C, et al. Simultaneously improving

strength and ductility of NiAl-based composites through two-scale network structures and a core-shell-like structure. Mater Sci Eng A 2022;861:144384.

273. Zhang J Y, Chen T J, Zhang X Z, Gao M, Geng L B. Simultaneously strengthening and toughening a core-shell structured particulate-reinforced aluminium alloy composite by solid solution treatment. J Alloys Compd 2020;842:155765.

274. Lin Y, Pan J, Zhou H F, Gao H J, Li Y. Mechanical properties and optimal grain size distribution profile of gradient grained nickel. Acta Mater 2018;153:279–289.

275. Wu X, Yang M, Yuan F, Chen L, Zhu Y. Combining gradient structure and TRIP effect to produce austenite stainless steel with high strength and ductility. In: Heterostructured Materials; 2021. p. 283–310.

276. Chen A Y, Li D F, Zhang J B, Song H W, Lu J. Make nanostructured metal exceptionally tough by introducing non-localized fracture behaviors. Scr Mater 2008;59:579–582.

277. Kou H, Lu J, Li Y. High-strength and high-ductility nanostructured and amorphous metallic materials. Adv Mater 2014;26:5518–5524.

278. Liu X, Sun L, Zhu L, Liu J, Lu K, Lu J. High-order hierarchical nanotwins with superior strength and ductility. Acta Mater 2018;149:397–406.

279. Yuan F, Yan D, Sun J, Zhou L, Zhu Y, Wu X. Ductility by shear band delocalization in the nano-layer of gradient structure. Mater Res Lett 2019;7:12–17.

280. Zhu Y. Introduction to heterostructured materials: a fast emerging field. Metall Mater Trans A 2021;52:4715–4726.

281. Yang M X, Li R G, Jiang P, Yuan F P, Wang Y D, Zhu Y T, et al. Residual stress provides significant strengthening and ductility in gradient structured materials. Mater Res Lett 2019;7:433–438.

282. Yang J, Xu L, Gao H, Li X, Pan H, Shu B, et al. Effect of global constraint on the mechanical behavior of gradient materials. Mater Sci Eng A 2021;826:141963.

283. Jiang S, Li Y, Zhao Y, Li X, Tong W. Facile route to bulk multi-gradient-structured steel for high strength and toughness. Mater Sci Eng A 2025;923:147749.

284. Kang J Y, Kim J G, Park H W, Kim H S. Multiscale architectured materials with composition and grain size gradients manufactured using high-pressure torsion. Sci Rep 2016;6:26590.

285. Lei Y B, Wang Z B, Zhang B, Luo Z P, Lu J, Lu K. Enhanced mechanical properties and corrosion resistance of 316L stainless steel by pre-forming a gradient nanostructured surface layer and annealing. Acta Mater 2021;208:116773.

286. Wen Y, Zhang B, Narayan R L, Wang P, Song X, Zhao H, et al. Laser powder bed fusion of compositionally graded CoCrMo-Inconel 718. Addit Manuf 2021;40:101926.
287. Zhu Q, Yu X, Yao P, Yue Y, Kang G. Study on optimisation strategy for the composition transition gradient in SS 316L/Inconel 625 functionally graded materials. Materials 2024;17:2910.
288. Zhang Y, Bandyopadhyay A. Influence of compositionally graded interface on microstructure and compressive deformation of 316L stainless steel to Al12Si aluminum alloy bimetallic structures. ACS Appl Mater Interfaces 2021;13:9174–9185.
289. Wen Y, Gao Y, Narayan R L, Cai W, Wang P, Wei X, et al. Tensile behavior of additively manufactured Inconel 718 and stainless steel 316L with compositionally graded joints. Int J Plast 2025;189:104342.
290. Dan X, Ren C, Song Z, Waqar S, Zhang D, Wang M, et al. Exceptional strength and ductility in heterogeneous multi-gradient TiAl alloys through additive manufacturing. Acta Mater 2024;281:120395.
291. Gao Y, Xie Q, Gao T, Yang W, Chen Q, Tian Z, et al. Design of functionally graded Ti–Al alloy with adjustable mechanical properties: a molecular dynamics insights. J Mater Res Technol 2023;23:258–267.
292. Yang Y, Zhang S, Huang P, Wang F. Phase transformation-induced strengthening and multistage strain hardening in double-gradient-structured high-entropy alloys. Appl Phys A 2022;128:258.
293. Saba F, Sun H, Nezhad E G, Cui B, Fan G, Tan Z, et al. Optimising heterostructure parameters towards enhanced toughening in micro/nano-reinforced bimodal-grained Al alloy composites. Compos Part A Appl Sci Manuf 2024;187:108442.
294. Tang Y, Zhou H, Lu H, Wang X, Cao Q, Zhang D, et al. Extra plasticity governed by shear band deflection in gradient metallic glasses. Nat Commun 2022;13:2120.
295. Guan Y, Wang Y, Song W. Modulating mechanical performances of metallic amorphous materials through phase gradient. Int J Mech Sci 2022;234:107680.
296. Li X, Jiang P, Nie M, Liu Z, Liu M, Qiu Y, et al. Enhanced strength–ductility synergy of laser additive manufactured stainless steel/Ni-based superalloy dissimilar materials characterised by bionic mechanical interlocking structures. J Mater Res Technol 2023;26:4770–4783.
297. Li X, Li Q, Nie M, Kong D, Liu Z, Zhang Z. Evading the strength–ductility trade-off dilemma in steel–nickel heterostructured material by bionic crossed-lamellar structures. Virtual Phys Prototyp 2023;18:e2266640.

298. Paul M J, Klein T, Simson C, Niedermayer J, Kruzic J J, Gludovatz B. Strength and fracture resistance of in-situ alloyed compositionally-graded Al-Si processed by dual-wire arc directed energy deposition. Addit Manuf 2022;60:103291.
299. Lu K, Lu J. Nanostructured surface layer on metallic materials induced by surface mechanical attrition treatment. Mater Sci Eng A 2004;375:38–45.
300. Chan HL, Ruan HH, Chen AY, Lu J. Optimization of the strain rate to achieve exceptional mechanical properties of 304 stainless steel using high-speed ultrasonic surface mechanical attrition treatment. Acta Mater 2010;58:5086–5096.
301. Ren X D, Zhou W F, Liu F F, Ren Y P, Yuan S Q, Ren N F, et al. Microstructure evolution and grain refinement of Ti-6Al-4V alloy by laser shock processing. Appl Surf Sci 2016;363:44–49.
302. Lainé S J, Knowles K M, Doorbar P J, Cutts R D, Rugg D. Microstructural characterisation of metallic shot peened and laser shock peened Ti-6Al-4V. Acta Mater 2017;123:350–361.
303. Schulze V, Klemenz M, Zimmermann M. State of the art in shot peening simulation. In: Proc 10th Int Conf Shot Peening; Tokyo (Japan): 2008. p. 15–18.
304. Wang X, Li YS, Zhang Q, Zhao YH, Zhu YT. Gradient structured copper by rotationally accelerated shot peening. J Mater Sci Technol 2017;33:758–761.
305. Saito Y, Utsunomiya H, Tsuji N, Sakai T. Novel ultra-high straining process for bulk materials—development of the accumulative roll-bonding (ARB) process. Acta Mater 1999;47:579–583.
306. Taali S, Toroghinejad M R, Kuglstatter M, Höppel H W. Grain boundary engineering in roll-bonded copper to overcome the strength–ductility dilemma. J Mater Res Technol 2022;17:3198–3204.
307. Wang Q, Zhang S, Zhang C, Wu C, Wang J, Chen J, Sun Z. Microstructure evolution and EBSD analysis of a graded steel fabricated by laser additive manufacturing. Vacuum 2017;141:68–81.
308. Panchenko O, Kladov I, Kurushkin D, Zhabrev L, Ryl'kov E, Zamozdra M. Effect of thermal history on microstructure evolution and mechanical properties in wire arc additive manufacturing of HSLA steel functionally graded components. Mater Sci Eng A 2022;851:143569.
309. Huang J, Liu G, Yu X, Wu H, Huang Y, Yu S, Fan D. Microstructure regulation of titanium alloy functionally gradient materials fabricated by alternating current assisted wire arc additive manufacturing. Mater Des 2022;218:110731.

310. Rodrigues T A, Bairrão N, Farias F W C, Shamsolhodaei A, Shen J, Zhou N, et al. Steel–copper functionally graded material produced by twin-wire and arc additive manufacturing (T-WAAM). Mater Des 2022;213:110270.
311. Li JZ, Alkahari MR, Rosli NAB, Hasan R, Sudin MN, Ramli FR. Review of wire arc additive manufacturing for 3D metal printing. Int J Autom Technol 2019;13:346–353.
312. Ou W, Mukherjee T, Knapp GL, Wei Y, DebRoy T. Fusion zone geometries, cooling rates and solidification parameters during wire arc additive manufacturing. Int J Heat Mass Transf 2018;127:1084–1094.
313. Han C, Fang Q, Shi Y, Tor SB, Chua CK, Zhou K. Recent advances on high-entropy alloys for 3D printing. Adv Mater 2020;32:1903855.
314. Gibson I, Rosen D, Stucker B. Directed energy deposition processes. In: Additive manufacturing technologies: 3D printing, rapid prototyping, and direct digital manufacturing. New York: Springer; 2015:245–268.
315. Cordero PM, Mireles J, Ridwan S, Wicker RB. Evaluation of monitoring methods for electron beam melting powder bed fusion additive manufacturing technology. Prog Addit Manuf 2017;2:1–10.
316. Raghavan N, Simunovic S, Dehoff R, Plotkowski A, Turner J, Kirka M, et al. Localized melt-scan strategy for site specific control of grain size and primary dendrite arm spacing in electron beam additive manufacturing. Acta Mater 2017;140:375–387.
317. Gu D D, Meiners W, Wissenbach K, Poprawe R. Laser additive manufacturing of metallic components: materials, processes and mechanisms. Int Mater Rev 2012;57:133–164.
318. Hu Z, Ma Z, Yu L, Liu Y. Functionally graded materials with grain-size gradients and heterogeneous microstructures achieved by additive manufacturing. Scr Mater 2023;226:115197.
319. Dezfoli A R A, Hwang W S, Huang W C, Tsai T W. Determination and controlling of grain structure of metals after laser incidence: Theoretical approach. Sci Rep 2017;7:41527.
320. Liu Y, Shi J. Epitaxial growth and stray grain control toward single‐crystal metallic materials by additive manufacturing: a review. Adv Eng Mater 2023;25:2201917.
321. Mukherjee T, Elmer J W, Wei H L, Lienert T J, Zhang W, Kou S, et al. Control of grain structure, phases, and defects in additive manufacturing of high-performance metallic components. Prog Mater Sci 2023;138:101153.

322. Yan F, Xiong W, Faierson E J. Grain structure control of additively manufactured metallic materials. Materials 2017;10:1260.
323. Zinovieva O, Zinoviev A, Ploshikhin V. Three-dimensional modeling of the microstructure evolution during metal additive manufacturing. Comput Mater Sci 2018;141:207–220.
324. Koizumi M. FGM activities in Japan. Compos Part B Eng 1997;28:1–4.
325. Miyamoto Y, Kaysser W A, Rabin B H, Kawasaki A, Ford R G, editors. Functionally graded materials: design, processing and applications. New York: Springer; 2013.
326. Suresh S, Mortensen A. Fundamentals of functionally graded materials. London: IOM Communications; 1998.
327. Kieback B, Neubrand A, Riedel H. Processing techniques for functionally graded materials. Mater Sci Eng A 2003;362:81–106.
328. Pasha A, Rajaprakash B M. Functionally graded materials (FGM) fabrication and its potential challenges & applications. Mater Today Proc 2022;52:413–418.
329. Stavroulakis E, Irukuvarghula S, Pickering E, Stewart D, Preuss M. Fundamental aspects of functional grading via powder hot isostatic pressing–Development of microstructure and diffusional processes. Mater Des 2022;215:110437.
330. Sai Charan M, Naik A K, Kota N, Laha T, Roy S. Review on developments of bulk functionally graded composite materials. Int Mater Rev 2022;67:797–863.
331. Angelo P C, Subramanian R, Ravisankar B. Powder metallurgy: science, technology and applications. New Delhi: PHI Learning; 2022.
332. Munir Z A, Anselmi-Tamburini U, Ohyanagi M. The effect of electric field and pressure on the synthesis and consolidation of materials: a review of the spark plasma sintering method. J Mater Sci 2006;41:763–777.
333. Matuła I, Dercz G, Sowa M, Barylski A, Duda P. Fabrication and characterisation of new functional graded material based on Ti, Ta, and Zr by powder metallurgy method. Materials 2021;14:6609.
334. Hardwicke C U, Lau Y C. Advances in thermal spray coatings for gas turbines and energy generation: a review. J Therm Spray Technol 2013;22:564–576.
335. Mittal G, Paul S. Suspension and solution precursor plasma and HVOF spray: a review. J Therm Spray Technol 2022;31:1443–1475.
336. Majumdar J D. Thermal and cold spraying technology in manufacturing. In: Handbook of Manufacturing Engineering and Technology. London: Springer; 2013:1–37.
337. Lokachari S, Leng K, Rincon Romero A, Curry N, Brewster G, Norton A, et al.

Processing–microstructure–properties of columns in thermal barrier coatings: a study of thermo-chemico-mechanical durability. ACS Appl Mater Interfaces 2024;16:10646–10660.

338. Odhiambo J G, Li W, Zhao Y, Li C. Porosity and its significance in plasma-sprayed coatings. Coatings 2019;9:460.

339. Rubino F, Poza P, Pasquino G, Carlone P. Thermal spray processes in concentrating solar power technology. Metals 2021;11:1377.

340. Gildersleeve E J, Vaßen R. Thermally sprayed functional coatings and multilayers: a selection of historical applications and potential pathways for future innovation. J Therm Spray Technol 2023;32:778–817.

341. Prashar G, Vasudev H, Thakur L. Thermal spraying fundamentals: process applications, challenges and future market. In: Thermal Spray Coatings. Boca Raton: CRC Press; 2021:1–36.

342. Ahmed R, Faisal N H, Paradowska A M, Fitzpatrick M E. Residual strain and fracture response of Al_2O_3 coatings deposited via APS and HVOF techniques. J Therm Spray Technol 2012;21:23–40.

343. Boulos M I, Fauchais P L, Heberlein J V. Industrial applications of thermal spray technology. In: Thermal Spray Fundamentals: From Powder to Part. Cham: Springer; 2021:997–1096.

344. Liao T Y, Biesiekierski A, Berndt C C, King P C, Ivanova E P, Thissen H, et al. Multifunctional cold spray coatings for biological and biomedical applications: a review. Prog Surf Sci 2022;97:100654.

345. Thakur L, Vasudev H, editors. Thermal Spray Coatings. Boca Raton: CRC Press; 2021.

346. Karun A S, Hari S, Ebhota W S, Rajan T P D, Pillai U T S, Pai B C. Design and processing of bimetallic aluminium alloys by sequential casting technique. Metall Mater Trans A 2017;48:279–293.

347. Ebhota W S, Karun A S, Inambao F L. Centrifugal casting technique baseline knowledge, applications and processing parameters: overview. Int J Mater Res 2016;107:960–969.

348. Hu L, Kothalkar A, O'Neil M, Karaman I, Radovic M. Current-activated, pressure-assisted infiltration: a novel, versatile route for producing interpenetrating ceramic–metal composites. Mater Res Lett 2014;2:124–130.

349. Tao G, Zheng Z, Liu S. Fabrication of W/Cu functionally graded material and analysis of thermal cycle stress. Acta Mater Compos Sin 2006;23:72–77.

350. Zhang N, Wang Z, Guo L, Meng L, Guo Z. Rapid fabrication of W–Cu composites via low-temperature infiltration in supergravity fields. J Alloys Compd 2019;809:151782.
351. Cook A J, Werner P S. Pressure infiltration casting of metal matrix composites. Mater Sci Eng A 1991;144:189–206.
352. Broxtermann S, Su M M, Hao H, Fiedler T. Comparative study of stir casting and infiltration casting of expanded glass-aluminium syntactic foams. J Alloys Compd 2020;845:155415.
353. Corbin S F, Zhao-Jie X, Henein H, Apte P S. Functionally graded metal/ceramic composites by tape casting, lamination and infiltration. Mater Sci Eng A 1999;262:192–203.
354. Sun L, Yuan G, Gao L, Yang J, Chhowalla M, Gharahcheshmeh M H, et al. Chemical vapour deposition. Nat Rev Methods Primers 2021;1:5.
355. Choy K L. Chemical vapour deposition of coatings. Prog Mater Sci 2003;48:57–170.
356. Bryant W A. The fundamentals of chemical vapour deposition. J Mater Sci 1977;12:1285–1306.
357. Jones A C, Hitchman M L. Overview of chemical vapour deposition. In: Chemical Vapour Deposition: Precursors, Processes and Applications. Cambridge: Royal Society of Chemistry; 2009:1–36.
358. Baptista A, Silva F, Porteiro J, Míguez J, Pinto G. Sputtering physical vapour deposition (PVD) coatings: a critical review on process improvement and market-trend demands. Coatings 2018;8:402.
359. Mundra S S, Pardeshi S S, Bhavikatti S S, Nagras A. Development of an integrated physical vapour deposition and chemical vapour deposition system. Mater Today Proc 2021;46:1229–1234.
360. Mattox D M. Handbook of physical vapour deposition (PVD) processing. Oxford: William Andrew; 2010.
361. Deng Y, Chen W, Li B, Wang C, Kuang T, Li Y. Physical vapour deposition technology for coated cutting tools: a review. Ceram Int 2020;46:18373–18390.
362. Subrahmanyam J, Vijayakumar M. Self-propagating high-temperature synthesis. J Mater Sci 1992;27:6249–6273.
363. Levashov E A, Mukasyan A S, Rogachev A S, Shtansky D V. Self-propagating high-temperature synthesis of advanced materials and coatings. Int Mater Rev 2017;62:203–239.
364. Mossino P J. Some aspects in self-propagating high-temperature synthesis. Ceram Int

2004;30:311–332.

365. Merzhanov A G. The chemistry of self-propagating high-temperature synthesis. J Mater Chem 2004;14:1779–1786.

366. Su X, Fu F, Yan Y, Zheng G, Liang T, Zhang Q, et al. Self-propagating high-temperature synthesis for compound thermoelectrics and new criterion for combustion processing. Nat Commun 2014;5:4908.

367. Biswas A, Roy S K, Gurumurthy K R, Prabhu N, Banerjee S. A study of self-propagating high-temperature synthesis of NiAl in thermal explosion mode. Acta Mater 2002;50:757–773.

368. Bharti S, Ghetiya N D, Patel K M. A review on manufacturing the surface composites by friction stir processing. Mater Manuf Process 2021;36:135–170.

369. Mehta K P, Vilaça P. A review on friction stir-based channeling. Crit Rev Solid State Mater Sci 2022;47:1–45.

370. Kazakov N F, editor. Diffusion bonding of materials. Amsterdam: Elsevier; 2013.

371. Derby B, Wallach E R. Theoretical model for diffusion bonding. Met Sci 1982;16:49–56.

372. Besra L, Liu M. A review on fundamentals and applications of electrophoretic deposition (EPD). Prog Mater Sci 2007;52:1–61.

373. Boccaccini A R, Keim S, Ma R, Li Y, Zhitomirsky I. Electrophoretic deposition of biomaterials. J R Soc Interface 2010;7:S581–S613.

374. Sarkar P, Nicholson P S. Electrophoretic deposition (EPD): mechanisms, kinetics and application to ceramics. J Am Ceram Soc 1996;79:1987–2002.

375. Gardan J. Additive manufacturing technologies: state of the art and trends. In: Additive Manufacturing Handbook. Boca Raton: CRC Press; 2017:149–168.

376. Gibson I, Rosen D, Stucker B, Khorasani M. Design for additive manufacturing. In: Additive Manufacturing Technologies. Cham: Springer International Publishing; 2020:555–607.

377. Prakash K S, Nancharaih T, Rao V S. Additive manufacturing techniques in manufacturing – an overview. Mater Today Proc 2018;5:3873–3882.

378. Vayre B, Vignat F, Villeneuve F. Designing for additive manufacturing. Procedia CIRP 2012;3:632–637.

379. Bourell D, Kruth J P, Leu M, Levy G, Rosen D, Beese A M, et al. Materials for additive manufacturing. CIRP Ann 2017;66:659–681.

380. Gibson I, Rosen D, Stucker B, Khorasani M. Development of additive manufacturing

technology. In: Additive Manufacturing Technologies. Cham: Springer International Publishing; 2020:23–51.

381. Ziaee M, Crane NB. Binder jetting: A review of process, materials and methods. Addit Manuf 2019;28:781–801.

382. Li M, Du W, Elwany A, Pei Z, Ma C. Metal binder jetting additive manufacturing: a literature review. J Manuf Sci Eng 2020;142:090801.

383. Mostafaei A, Elliott AM, Barnes JE, Li F, Tan W, Cramer CL, et al. Binder jet 3D printing—process parameters, materials, properties, modeling and challenges. Prog Mater Sci 2021;119:100707.

384. Gülcan O, Günaydın K, Tamer A. The state of the art of material jetting—a critical review. Polymers 2021;13:2829.

385. Elkaseer A, Chen KJ, Janhsen JC, Refle O, Hagenmeyer V, Scholz SG. Material jetting for advanced applications: a state-of-the-art review, gaps and future directions. Addit Manuf 2022;60:103270.

386. Mora S, Pugno NM, Misseroni D. 3D printed architected lattice structures by material jetting. Mater Today 2022;59:107–132.

387. Kestens L A I, Pirgazi H. Texture formation in metal alloys with cubic crystal structures. Mater Sci Technol 2016;32:1303–1315.

388. Engler O, Hirsch J. Texture control by thermomechanical processing of AA6xxx Al–Mg–Si sheet alloys for automotive applications—a review. Mater Sci Eng A 2002;336:249–262.

389. Hirsch J, Lücke K. Overview No. 76: Mechanism of deformation and development of rolling textures in polycrystalline fcc metals— I . Description of rolling texture development in homogeneous CuZn alloys. Acta Metall 1988;36:2863–2882.

390. Hirsch J, Lücke K. Overview No. 76: Mechanism of deformation and development of rolling textures in polycrystalline fcc metals— II . Simulation and interpretation of experiments on the basis of Taylor-type theories. Acta Metall 1988;36:2883–2904.

391. Hirsch J, Lücke K, Hatherly M. Overview No. 76: Mechanism of deformation and development of rolling textures in polycrystalline fcc metals— III . The influence of slip inhomogeneities and twinning. Acta Metall 1988;36:2905–2927.

392. Dillamore I L, Roberts W T. Rolling textures in fcc and bcc metals. Acta Metall 1964;12:281–293.

393. Vercammen S, Blanpain B, De Cooman B C, Wollants P. Cold rolling behaviour of an austenitic Fe–30Mn–3Al–3Si TWIP-steel: the importance of deformation twinning. Acta Mater 2004;52:2005–2012.
394. Donadille C, Valle R, Dervin P, Penelle R. Development of texture and microstructure during cold-rolling and annealing of FCC alloys: Example of an austenitic stainless steel. Acta Metall 1989;37:1547–1571.
395. Kaushik L, Kim M S, Singh J, Kang J H, Heo Y U, Suh J Y, et al. Deformation mechanisms and texture evolution in high entropy alloy during cold rolling. Int J Plast 2021;141:102989.
396. Zhang J J, Li L J, Liu Z F, Chen Z N, Guo E Y, Kang H J, et al. Microstructure and texture evolution of Cu–Cr–Co–Ti alloys during the two-stage cryorolling. Rare Met 2024;43:4535–4547.
397. Lee C S, Duggan B J, Smallman R E. The texture transition and shear bands in fcc metals. In: Materials Modelling. Boca Raton: CRC Press; 2020. p. 79–84.
398. El-Danaf E, Kalidindi S R, Doherty R D, Necker C. Deformation texture transition in brass: critical role of micro-scale shear bands. Acta Mater 2000;48:2665–2673.
399. Uniwersał A, Wroński M, Wróbel M, Wierzbanowski K, Baczmański A. Texture effects due to asymmetric rolling of polycrystalline copper. Acta Mater 2017;139:30–38.
400. Madhavan R, Ray R K, Suwas S. Micro-mechanical aspects of texture evolution in nickel and nickel–cobalt alloys: role of stacking fault energy. Philos Mag 2016;96:3177–3199.
401. Lee D N. Effect of stacking fault energy on evolution of recrystallization and grain growth textures of metals. Mater Sci Forum 2007;558:93–100.
402. Sathiaraj G D, Bhattacharjee P P. Analysis of microstructure and microtexture during grain growth in low stacking fault energy equiatomic CoCrFeMnNi high entropy and Ni–60 wt.% Co alloys. J Alloys Compd 2015;637:267–276.
403. Dillamore I L. Factors affecting the rolling recrystallisation textures in FCC metals. Acta Metall 1964;12:1005–1014.
404. Caleyo F, Baudin T, Penelle R, Venegas V. EBSD study of the development of cube recrystallization texture in Fe–50% Ni. Scr Mater 2001;45:413–420.
405. Penelle R. Nucleation and growth during primary recrystallization of certain metals and alloys with a face-centered cubic structure: formation of the cube texture. Int J Mater Res 2009;100:1420–1432.

406. Miszczyk M, Paul H, Driver J H, Maurice C. Microstructure and texture evolution during annealing of plane-strain compressed Al and Al–1 % Mn alloy single crystals. Arch Metall Mater 2011;56:933–938.

407. Xiao Y W, Cheng Z, Li S H, Wang S Z, Wu H H, Gao J H, et al. Recrystallization tuning to optimize mechanical properties in heavily rolled CoCrFeNi medium entropy alloy. J Alloys Compd 2023;968:172153.

408. Murphy D B, Davidson M W. Fundamentals of Light Microscopy and Electronic Imaging. Hoboken: John Wiley & Sons; 2012.

409. Williams D B, Carter C B. Transmission Electron Microscopy. 2nd ed. New York: Springer; 2009.

410. Wang H. Microstructural Evolutions in Additively Manufactured Metallic Materials [PhD thesis]. Sydney: The University of Sydney; 2022.

411. Schwartz A J, Kumar M, Adams B L, Field D P. Electron Backscatter Diffraction in Materials Science. New York: Kluwer Academic/Plenum; 2000.

412. Trimby P W. Orientation mapping of nanostructured materials using transmission Kikuchi diffraction in the scanning electron microscope. Ultramicroscopy 2012;120:16–24.

413. Goldstein J I, Newbury D E, Michael J R, Ritchie N W M, Scott J H J, Joy D C. Scanning Electron Microscopy and X-Ray Microanalysis. 4th ed. New York: Springer; 2017.

414. Trimby P W, Cao Y, Chen Z, Han S, Hemker K J, Lian J, et al. Characterizing deformed ultrafine-grained and nanocrystalline materials using transmission Kikuchi diffraction in a scanning electron microscope. Acta Mater 2014;62:69–80.

415. Wall J, Langmore J, Isaacson M, Crewe A V. Scanning transmission electron microscopy at high resolution. Proc Natl Acad Sci USA 1974;71:1–5.

416. Dellby N, Krivanek L, Nellist D, Batson E, Lupini R. Progress in aberration-corrected scanning transmission electron microscopy. Microscopy 2001;50:177–185.

417. Muller D A. Structure and bonding at the atomic scale by scanning transmission electron microscopy. Nat Mater 2009;8:263–270.

418. Shen C, Pan Z, Cuiuri D, Roberts J, Li H. Fabrication of Fe-FeAl functionally graded material using the wire-arc additive manufacturing process. Metall Mater Trans B 2016;47:763–772.

419. Shen C, Pan Z, Ma Y, Cuiuri D, Li H. Fabrication of iron-rich Fe–Al intermetallics

using the wire-arc additive manufacturing process. Addit Manuf 2015;7:20–26.

420. Liu X J, Ohnuma I, Kainuma R, Ishida K. Phase equilibria in the Cu-rich portion of the Cu–Al binary system. J Alloys Compd 1998;264:201–208.

421. Ponweiser N, Lengauer C L, Richter K W. Re-investigation of phase equilibria in the system Al–Cu and structural analysis of the high-temperature phase η1-Al1-δCu. Intermetallics 2011;19:1737–1746.

422. Murray J L. The aluminium–copper system. Int Met Rev 1985;30:211–234.

423. Stráská J, Stráský J, Minárik P, Janeček M, Král R. Microstructure evolution in ultrafine-grained magnesium alloy AZ31 processed by severe plastic deformation. Mod Electron Microsc Phys Life Sci 2016;2:64.

424. Hasan M N. Microstructure and Mechanical Properties of a CrMnFeCoNi High-Entropy Alloy with Gradient Structures [PhD thesis]. Sydney: The University of Sydney; 2020.

425. Callister W D, Rethwisch D G. Materials Science and Engineering: An Introduction. 7th ed. Hoboken: John Wiley & Sons; 2007.

426. Sutton M A, Wolters W J, Peters W H, Ranson W F, McNeill S R. Determination of displacements using an improved digital correlation method. Image Vis Comput 1983;1:133–139.

427. Chu T C, Ranson W F, Sutton M A, Peters W H. Applications of digital-image-correlation techniques to experimental mechanics. Exp Mech 1985;25:232–244.

428. Sutton M A, Orteu J J, Schreier H. Image correlation for shape, motion and deformation measurements: basic concepts, theory and applications. New York: Springer; 2009.

429. Miskdjian I, Hodhod H, Abdeen M, Elshabrawy M. Investigation and optimisation of factors affecting the accuracy of strain measurement via digital image processing. J Eng Appl Sci 2024;71:63.

430. Yang L, Smith L, Gothekar A, Chen X. Measure strain distribution using digital image correlation (DIC) for tensile tests. Rochester (MI): Oakland University; 2010. Technical Report.

431. Dematteis N, Giordan D. Comparison of digital image correlation methods and the impact of noise in geoscience applications. Remote Sens 2021;13:327.

432. Zienkiewicz O C, Taylor R L, Zhu J Z. The Finite Element Method: Its Basis and Fundamentals. 6th ed. Oxford: Butterworth-Heinemann; 2005.

433. Bathe K J. Finite Element Procedures. Englewood Cliffs (NJ): Klaus-Jürgen Bathe; 2006.

434. Johnson G R. A constitutive model and data for metals subjected to large strains, high strain rates and high temperatures. In: Proceedings of the 7th International Symposium on Ballistics; 1983; The Hague (Netherlands).
435. Hughes T J. The Finite Element Method: Linear Static and Dynamic Finite Element Analysis. Mineola (NY): Dover Publications; 2003.
436. Wang Y, Wei Y, Zhao Z, Long H, Lin Z, Guo F, et al. Activating dispersed strain bands in tensioned nanostructure layer for high ductility: the effects of microstructure inhomogeneity. Int J Plast 2022;149:103159.
437. Huang C X, Wang Y F, Ma X L, Yin S, Höppel H W, Göken M, et al. Interface affected zone for optimal strength and ductility in heterogeneous laminate. Mater Today 2018;21:713–719.
438. Zhang J, Song B, Yang L, Liu R, Zhang L, Shi Y. Microstructure evolution and mechanical properties of TiB/Ti6Al4V gradient-material lattice structure fabricated by laser powder bed fusion. Compos Part B Eng 2020;202:108417.
439. Jiang T, Jiao T, Dai G, Shen Z, Guo Y, Sun Z, et al. Microstructure evolution and mechanical properties of 2060 Al–Li alloy via friction stir additive manufacturing. J Alloys Compd 2023;935:168019.
440. Qu S, Gao S, Wang L, Ding J, Lu Y, Wen Y, et al. Full-composition-gradient in-situ alloying of Cu–Ni through laser powder bed fusion. Addit Manuf 2024;85:104166.
441. Zhang R, Jiang F, Xue L, Yu J. Review of additive manufacturing techniques for large-scale metal functionally graded materials. Crystals 2022;12:858.
442. Šket K, Brezočnik M, Karner T, Belšak R, Ficko M, Vuherer T, et al. Predictive modelling of weld bead geometry in wire arc additive manufacturing. J Manuf Mater Process 2025;9:67.
443. Chaudhari R, Parmar H, Vora J, Patel V K. Parametric study and investigations of bead geometries of GMAW-based wire–arc additive manufacturing of 316L stainless steels. Metals 2022;12:1232.
444. Wu B, Pan Z, Ding D, Cuiuri D, Li H, Xu J, et al. A review of the wire arc additive manufacturing of metals: properties, defects and quality improvement. J Manuf Process 2018;35:127–139.
445. Rosenthal D. The theory of moving sources of heat and its application to metal treatments. Trans Am Soc Mech Eng 1946;68:849–865.
446. Eagar T W, Tsai N S. Temperature fields produced by traveling distributed heat sources. Weld J 1983;62:346–355.

447. Shah A, Gupta N K, Aliyev R, Zeidler H. Study of various process parameters on bead penetration and porosity in wire arc additive manufacturing of copper alloy Cu1897. Appl Sci 2024;14:9188.
448. Faber T E, Ziman J M. A theory of the electrical properties of liquid metals: III. The resistivity of binary alloys. Philos Mag 1965;11:153–173.
449. Ziman J M. Electrons and phonons: the theory of transport phenomena in solids. Oxford: Oxford University Press; 2001.
450. Mott N F. The electrical conductivity of transition metals. Proc R Soc Lond A 1936;153:699–717.
451. Rossiter P L. The electrical resistivity of metals and alloys. Cambridge: Cambridge University Press; 1991.
452. Khajil T M A, Tomak M. Electrical resistivities of liquid Al–Mg and Al–Cu alloys. Il Nuovo Cimento D 1989;11:739–744.
453. Vahvaselkä K S. An X-ray investigation of structural properties and electrical resistivities of liquid Al, liquid Cu, and liquid Al–Cu alloys. Phys Status Solidi A 1984;83:103–112.
454. Giordanengo B, Benazzi N, Vinckel J, Gasser J G, Roubi L. Thermal conductivity of liquid metals and metallic alloys. J Non-Cryst Solids 1999;250:377–383.
455. Sun Y, Muta H, Ohishi Y. Thermophysical properties of liquid Al–Cu alloys. Int J Thermophys 2019;40:1–11.
456. Thakore B Y, Khambholja S G, Suthar P H, Jani A R. Electrical transport properties of liquid Al–Cu alloys. AIP Conf Proc 2010;1249:194–197.
457. Mukherjee T, Manvatkar V, De A, DebRoy T. Dimensionless numbers in additive manufacturing. J Appl Phys 2017;121:064901.
458. Kou S, Limmaneevichitr C. Visualization of Marangoni convection in simulated weld pools containing a surface-active agent. Weld J 2000;79:324–330.
459. DebRoy T, Wei H L, Zuback J S, Mukherjee T, Elmer J W, Milewski J O, et al. Additive manufacturing of metallic components – process, structure and properties. Prog Mater Sci 2018;92:112–224.
460. Schmitz J, Brillo J, Egry I, Schmid-Fetzer R. Surface tension of liquid Al–Cu binary alloys. Int J Mater Res 2009;100:1529–1535.
461. Egry I, Lohöfer G, Sauerland S. Measurements of thermophysical properties of liquid metals by noncontact techniques. Int J Thermophys 1993;14:573–584.
462. Konstantinova N Y, Popel' P S, Yagodin D A E. The kinematic viscosity of liquid

copper-aluminum alloys. High Temp 2009;47:336–341.
463. Meyer A. Self-diffusion in liquid copper as seen by quasielastic neutron scattering. Phys Rev B 2010;81:012102.
464. Brillo J, Chathoth S M, Koza M M, Meyer A. Liquid Al80Cu20: atomic diffusion and viscosity. Appl Phys Lett 2008;93:121905.
465. Pearson J R A. On convection cells induced by surface tension. J Fluid Mech 1958;4:489–500.
466. Schatz M F, Neitzel G P. Experiments on thermocapillary instabilities. Annu Rev Fluid Mech 2001;33:93–127.
467. Davis S H. Thermocapillary instabilities. Annu Rev Fluid Mech 1987;19:403–435.
468. Menart J, Malik S. Net emission coefficients for argon–iron thermal plasmas. J Phys D Appl Phys 2002;35:867.
469. Plevachuk Y, Sklyarchuk V, Yakymovych A, Eckert S, Willers B, Eigenfeld K. Density, viscosity, and electrical conductivity of hypoeutectic Al–Cu liquid alloys. Metall Mater Trans A 2008;39:3040–3045.
470. Oreper G M, Eagar T W, Szekely J. Convection in arc weld pools. Weld J 1983;62:307–312.
471. Kou S. Welding metallurgy. Hoboken: Wiley-Interscience; 2003. p 223–225.
472. Massalski T B. The Al–Cu (aluminum–copper) system. Bull Alloy Phase Diagrams 1980;1:27–33.
473. Desai P D. Thermodynamic properties of aluminum. Int J Thermophys 1987;8:621–638.
474. Arblaster J W. Thermodynamic properties of copper. J Phase Equilib Diffus 2015;36:422–444.
475. Derekar K S, Lawrence J, Melton G B, Addison A, Zhang X, Xu L. Influence of interpass temperature on wire arc additive manufacturing of aluminium alloy components. MATEC Web Conf 2019;269:05001.
476. Ajay V, Shrivastava A. Numerical analysis of heat accumulation during wire arc additive manufacturing. In: Proceedings of the TMS Annual Meeting & Exhibition. Cham: Springer Nature Switzerland; 2024. p 235–243.
477. Fan S, Guo X, Li Z, Ma J, Li F, Jiang Q. A review of high-strength aluminum–copper alloys fabricated by wire arc additive manufacturing: microstructure, properties, defects, and post-processing. J Mater Eng Perform 2023;32:8517–8540.
478. Chen J, Sung P K, Tewari S N, Poirier D R. Directional solidification and convection

in small diameter crucibles. Mater Sci Eng A 2003;357:397–405.
479. Akour S N, Jarrah M A. Experimental and numerical analysis of natural convection for Al–5.5 % Cu alloy. J Mater Process Technol 2005;164:1479–1486.
480. Dong B, Pan Z, Shen C, Ma Y, Li H. Fabrication of copper-rich Cu–Al alloy using the wire-arc additive manufacturing process. Metall Mater Trans B 2017;48:3143–3151.
481. Köhler M, Hensel J, Dilger K. Effects of thermal cycling on wire and arc additive manufacturing of Al-5356 components. Metals 2020;10:952.
482. Kishor G, Mugada K K, Mahto R P, Sivanandam A, Digavalli R K, Amirthalingam M. Microstructural evolution, crystallographic texture, grain morphology, and mechanical integrity of wire arc additively manufactured Inconel 625 alloy. Mater Charact 2024;218:114525.
483. Liu K, Yan Z, Wang F, Li K, Lin S, Chen S. Microstructure, texture and mechanical properties of Inconel GH4169 superalloy fabricated by wire arc additive manufacturing with arc oscillation. J Alloys Compd 2023;952:170070.
484. Xu M, Chen Y, Zhang T, Xie J, He P, Wei K. Effect of grain refinement on strain hardening behavior of nickel-based superalloy fabricated by wire arc additive manufacturing. Mater Lett 2022;324:132723.
485. Wang J, Lin X, Wang J, Yang H, Zhou Y, Wang C, et al. Grain morphology evolution and texture characterization of wire and arc additively manufactured Ti-6Al-4V. J Alloys Compd 2018;768:97–113.
486. Wang Z, Lin X, Wang L, Cao Y, Zhou Y, Huang W. Microstructure evolution and mechanical properties of the wire + arc additive manufacturing Al–Cu alloy. Addit Manuf 2021;47:102298.
487. Geng R, Du J, Wei Z, Xu S, Ma N. Modelling and experimental observation of the deposition geometry and microstructure evolution of aluminum alloy fabricated by wire-arc additive manufacturing. J Manuf Process 2021;64:369–378.
488. Wang Z, Lu X, Lin X, Hao Z, Hu C, Feng Z, et al. Porosity control and properties improvement of Al–Cu alloys via solidification condition optimisation in wire and arc additive manufacturing. Virtual Phys Prototyp 2024;19:e2414408.
489. Wieczorowski M, Pereira A, Carou D, Gapinski B, Ramírez I. Characterization of 5356 aluminum walls produced by wire arc additive manufacturing (WAAM). Materials 2023;16:2570.
490. Rodrigues T A, Duarte V, Miranda R M, Santos T G, Oliveira J P. Current status and perspectives on wire and arc additive manufacturing (WAAM). Materials

2019;12:1121.

491. Kannan A R, Pramod R, Prakash K S, Shanmugam N S, Yoon J, Oliveira J P. Understanding the microstructural evolution and fatigue behavior of aluminum 2319 fabricated by wire arc additive manufacturing. Arch Civ Mech Eng 2024;24:110.

492. Humphreys F J, Hatherly M. Recrystallization and related annealing phenomena. Oxford: Elsevier; 2012.

493. Lin Y C, Wu X Y, Chen X M, Chen J, Wen D X, Zhang J L, et al. EBSD study of a hot deformed nickel-based superalloy. J Alloys Compd 2015;640:101–113.

494. Hunt J D. Steady-state columnar and equiaxed growth of dendrites and the origin of the columnar to equiaxed transition. Mater Sci Eng 1984;65:75–83.

495. Zhang D, Prasad A, Bermingham M J, Todaro C J, Benoit M J, Patel M N et al. Grain refinement of alloys in fusion-based additive manufacturing processes. Metall Mater Trans A 2020;51:4341–4359.

496. Davis A E, Wainwright J, Sahu V K, Dreelan D, Chen X, Ding J et al. Achieving a columnar-to-equiaxed transition through dendrite twinning in high deposition rate additively manufactured titanium alloys. Metall Mater Trans A 2024;55:1765–1787.

497. Sakai T, Belyakov A, Kaibyshev R, Miura H, Jonas J J. Dynamic and post-dynamic recrystallization under hot, cold and severe plastic deformation conditions. Prog Mater Sci 2014;60:130–207.

498. Gourdet S, Montheillet F. A model of continuous dynamic recrystallization. Acta Mater 2003;51:2685–2699.

499. Ding D, Pan Z, Van Duin S, Li H, Shen C. Fabricating superior NiAl bronze components through wire arc additive manufacturing. Materials 2016;9:652.

500. Lv J, Zheng J H, Yardley V A, Shi Z, Lin J. A review of microstructural evolution and modelling of aluminium alloys under hot forming conditions. Metals 2020;10:1516.

501. Pölt P, Sommitsch C, Mitsche S, Walter M. Dynamic recrystallization of Ni-base alloys—Experimental results and comparisons with simulations. Mater Sci Eng A 2006;420:306–314.

502. Gandin C A, Rappaz M. A coupled finite element–cellular automaton model for the prediction of dendritic grain structures in solidification processes. Acta Metall Mater 1994;42:2233–2246.

503. Liu J, Chen H. Nucleation and grain boundary evolution in dynamic recrystallization of 316LN steel during hot deformation. Front Mater 2019;6:209.

504. Hadadzadeh A, Mokdad F, Wells M A, Chen D L. A new grain orientation spread

approach to analyze the dynamic recrystallization behavior of a cast-homogenized Mg–Zn–Zr alloy using electron backscattered diffraction. Mater Sci Eng A 2018;709:285–289.

505. Zhong X, Wang L, Huang L, Liu F. Transition of dynamic recrystallization mechanism during hot deformation of Incoloy 028 alloy. J Mater Sci Technol 2020;42:241–253.
506. Rohatgi A, Vecchio K S, Gray G T. The influence of stacking fault energy on the mechanical behavior of Cu and Cu-Al alloys: deformation twinning, work hardening, and dynamic recovery. Metall Mater Trans A 2001;32:135–145.
507. Ånes H W, van Helvoort A T, Marthinsen K. Orientation dependent pinning of (sub)grains by dispersoids during recovery and recrystallization in an Al–Mn alloy. Acta Mater 2023;248:118761.
508. Ponge D, Gottstein G. Necklace formation during dynamic recrystallization: mechanisms and impact on flow behavior. Acta Mater 1998;46:69–80.
509. Huang K E, Logé R E. A review of dynamic recrystallization phenomena in metallic materials. Mater Des 2016;111:548–574.
510. Gourdet S, Montheillet F. An experimental study of the recrystallization mechanism during hot deformation of aluminium. Mater Sci Eng A 2000;283:274–288.
511. Gallagher P C J. The influence of alloying, temperature, and related effects on the stacking fault energy. Metall Trans 1970;1:2429–2461.
512. Sakai T, Jonas J J. Overview no. 35 dynamic recrystallization: mechanical and microstructural considerations. Acta Metall 1984;32:189–209.
513. Williams S W, Martina F, Addison A C, Ding J, Pardal G, Colegrove P. Wire + arc additive manufacturing. Mater Sci Technol 2016;32:641–647.
514. Hackenhaar W, Mazzaferro J A, Montevecchi F, Campatelli G. An experimental–numerical study of active cooling in wire arc additive manufacturing. J Manuf Process 2020;52:58–65.
515. Burke J E, Turnbull D. Recrystallization and grain growth. Prog Met Phys 1952;3:220–292.
516. Fiset M, Braunovic M, Galibois A. The effect of thermal cycling on grain growth in aluminum. Scripta Metall 1971;5:325–328.
517. Rodrigues T A, Duarte V, Avila J A, Santos T G, Miranda R M, Oliveira J P. Wire and arc additive manufacturing of HSLA steel: Effect of thermal cycles on microstructure and mechanical properties. Addit Manuf 2019;27:440–450.
518. Wu B, Ding D, Pan Z, Cuiuri D, Li H, Han J, et al. Effects of heat accumulation on the

arc characteristics and metal transfer behavior in Wire Arc Additive Manufacturing of Ti6Al4V. J Mater Process Technol 2017;250:304–312.

519. Perevalova O B, Konovalova E V, Koneva N A. Effect of aluminum concentration on the lattice parameters and mean-square displacements of atoms in Cu–Al and Ti-6Al-4V alloys. Bull Russ Acad Sci Phys 2019;83:693–696.

520. King H W. Quantitative size-factors for metallic solid solutions. J Mater Sci 1966;1:79–90.

521. Pandit D. Application of high-resolution X-ray diffractometry in measurements of residual stress and strain rate on deformed quartz from Malanjkhand copper deposit, India. J Sci Res 2022;66:1–10.

522. Combe N, Mompiou F, Legros M. Shear-coupled grain-boundary migration dependence on normal strain/stress. Phys Rev Mater 2017;1:033605.

523. Zielinski E M, Vinci R P, Bravman J C. The influence of strain energy on abnormal grain growth in copper thin films. Appl Phys Lett 1995;67:1078–1080.

524. Muñoz J A, Bolmaro R E, Jorge Jr A M, Zhilyaev A, Cabrera J M. Prediction of generation of high- and low-angle grain boundaries (HAGB and LAGB) during severe plastic deformation. Metall Mater Trans A 2020;51:4674–4684.

525. Zhang A, Li Y. Thermal conductivity of aluminum alloys—a review. Materials 2023;16:2972.

526. Wei H L, Elmer J W, DebRoy T. Origin of grain orientation during solidification of an aluminum alloy. Acta Mater 2016;115:123–131.

527. Guo L, Han C, Ren L, Yang W, Yin A. Effect of transient thermal conditions on columnar-to-equiaxed transition during laser welding: a phase-field study. Metals 2022;12:571.

528. Kurz W, Bezençon C, Gäumann M. Columnar to equiaxed transition in solidification processing. Sci Technol Adv Mater 2001;2:185–191.

529. Ding D, Pan Z, Cuiuri D, Li H. Wire-feed additive manufacturing of metal components: technologies, developments and future interests. Int J Adv Manuf Technol 2015;81:465–481.

530. Zhai W, Wu N, Zhou W. Effect of interpass temperature on wire arc additive manufacturing using high-strength metal-cored wire. Metals 2022;12:212.

531. Yuan Q, Liu C, Wang W, Wang M. Residual stress distribution in a large specimen fabricated by wire-arc additive manufacturing. Sci Technol Weld Join 2023;28:137–

144.
532. Kurz W, Fisher D J, Rappaz M. Fundamentals of solidification. Baech: Trans Tech Publications Ltd; 2023. 5th fully revised ed.
533. Glicksman M E. Principles of solidification: an introduction to modern casting and crystal growth concepts. Springer Science & Business Media; 2010.
534. Basak A, Das S. Epitaxy and microstructure evolution in metal additive manufacturing. Annu Rev Mater Res 2016;46:125–149.
535. Bozzolo N, Bernacki M. Viewpoint on the formation and evolution of annealing twins during thermomechanical processing of FCC metals and alloys. Metall Mater Trans A 2020;51:2665–2684.
536. Doherty R D, Hughes D A, Humphreys F J, Jonas J J, Jensen D J, Kassner M E, et al. Current issues in recrystallization: a review. Mater Sci Eng A 1997;238:219–274.
537. Zhang Y, Tao N R, Lu K. Effect of stacking-fault energy on deformation twin thickness in Cu–Al alloys. Scr Mater 2009;60:211–213.
538. Pantleon W. Resolving the geometrically necessary dislocation content by conventional electron backscattering diffraction. Scr Mater 2008;58:994–997.
539. Gurao N P, Suwas S. Generalized scaling of misorientation angle distributions at meso-scale in deformed materials. Sci Rep 2014;4:5641.
540. Cahn J W, Mishin Y, Suzuki A. Coupling grain boundary motion to shear deformation. Acta Mater 2006;54:4953–4975.
541. Huang W, Wang Q, Ma N, Kitano H. Distribution characteristics of residual stresses in typical wall and pipe components built by wire arc additive manufacturing. J Manuf Process 2022;82:434–447.
542. Dash A, Squires L, Avila J D, Bose S, Bandyopadhyay A. Influence of active cooling on microstructure and mechanical properties of wire arc additively manufactured mild steel. Front Mech Eng 2023;9:1130407.
543. Hersent E, Marthinsen K, Nes E. The effect of solute atoms on grain boundary migration: A solute pinning approach. Metall Mater Trans A 2013;44:3364–3375.
544. Hall E O. The deformation and ageing of mild steel: III discussion of results. Proc Phys Soc B 1951;64:747.
545. Petch N J. The cleavage strength of polycrystals. J Iron Steel Inst 1953;174:25–28.
546. Hansen N. Hall–Petch relation and boundary strengthening. Scr Mater 2004;51:801–806.
547. Srivastava S, Garg R K, Sachdeva A, Sharma V S. Distribution of residual stress in

wire-arc additively manufactured small-scale component: single-versus multi-level heat input. J Manuf Sci Eng 2023;145:021008.

548. Giannakopoulos A E. The influence of initial elastic surface stresses on instrumented sharp indentation. J Appl Mech 2003;70:638–643.

549. Suresh S, Giannakopoulos A E. A new method for estimating residual stresses by instrumented sharp indentation. Acta Mater 1998;46:5755–5767.

550. Sun K, Shi J, Ma L. Atomistic insights into the effects of residual stress during nanoindentation. Crystals 2017;7:240.

551. Jang J I. Estimation of residual stress by instrumented indentation: A review. J Ceram Process Res 2009;10:391–400.

552. Maier-Kiener V, An X, Li L, Zhang Z, Pippan R, Durst K. Influence of solid solution strengthening on the local mechanical properties of single crystal and ultrafine-grained binary Cu–AlX solid solutions. J Mater Res 2017;32:4583–4591.

553. Davis J R. Introduction and overview of copper and copper alloys. In: Metals Handbook Desk Edition. ASM International, Materials Park OH, 1998.

554. Xu X, Ganguly S, Ding J, Seow C E, Williams S. Enhancing mechanical properties of wire+ arc additively manufactured INCONEL 718 superalloy through in-process thermomechanical processing. Mater Des 2018;160:1042–1051.

555. Elmer J W, Gibbs G. Mechanical rolling and annealing of wire-arc additively manufactured stainless steel plates. Sci Technol Weld Join 2022;27:14–21.

556. Mehrer H. Diffusion in solids: fundamentals, methods, materials, diffusion-controlled processes. Berlin Heidelberg: Springer, 2007.

557. Allain S, Chateau J P, Bouaziz O, Migot S, Guelton N. Correlations between the calculated stacking fault energy and the plasticity mechanisms in Fe–Mn–C alloys. Mater Sci Eng A 2004;387:158–162.

558. Fleischer R L. Substitutional solution hardening. Acta Metall 1963;11:203–209.

559. Kocks U F, Mecking H. Physics and phenomenology of strain hardening: the FCC case. Prog Mater Sci 2003;48:171–273.

560. Wu B, Pan Z, Ding D, Cuiuri D, Li H. Effects of heat accumulation on microstructure and mechanical properties of Ti6Al4V alloy deposited by wire arc additive manufacturing. Addit Manuf 2018;23:151–160.

561. Wright S I, Nowell M M. EBSD image quality mapping. Microsc Microanal 2006;12:72–84.

562. Dorner D, Zaefferer S, Raabe D. Retention of the Goss orientation between microbands

during cold rolling of an Fe–3%Si single crystal. Acta Mater 2007;55:2519–2530.
563. Ushioda K, Hutchinson W B. Role of shear bands in annealing texture formation in 3%Si–Fe(111)[112] single crystals. ISIJ Int 1989;29:862–867.
564. Wang B F, Liu Z L, Wang X Y, Li Z Z. An EBSD investigation on deformation-induced shear bands in a low nickel austenitic stainless steel under controlled shock-loading conditions. Mater Sci Eng A 2014;610:301–308.
565. Dieter G E, Bacon D. Mechanical metallurgy. New York: McGraw-Hill, 1976:43–53.
566. Hughes D A, Hansen N. High angle boundaries formed by grain subdivision mechanisms. Acta Mater 1997;45:3871–3886.
567. Sun L, Ding J, Zhang J, Li H, Wang G. Numerical simulation and deformation behavior of a Ti/steel clad plate during the rolling process. Metals 2023;13:218.
568. Yang H P, Sha Y, Zhang F, Zuo L. Through-thickness shear strain control in cold rolled silicon steel by the coupling effect of roll gap geometry and friction. J Mater Process Technol 2010;210:1545–1550.
569. Ginzburg V B, Ballas R. Flat Rolling Fundamentals. New York: Marcel Dekker; 2000.
570. Kocks U F, Tomé C N, Wenk H R. Texture and Anisotropy: Preferred Orientations in Polycrystals and their Effect on Materials Properties. Cambridge: Cambridge University Press; 2000.
571. Cho J H, Lee G Y, Lee S H. Dynamic shear texture evolution during the symmetric and differential speed rolling of Al–Si–Mg alloys fabricated by twin roll casting. Materials 2023;17:179.
572. Werner K V, Niessen F, Li W, Lu S, Vitos L, Villa M, et al. Reconciling experimental and theoretical stacking fault energies in face-centered cubic materials with the experimental twinning stress. Materialia 2023;27:101708.
573. Leffers T, Ray R K. The brass-type texture and its deviation from the copper-type texture. Prog Mater Sci 2009;54:351–396.
574. Paul H, Driver J H, Jasieński Z. Shear banding and recrystallization nucleation in a Cu–2%Al alloy single crystal. Acta Mater 2002;50:815–830.
575. Field D P, Bradford L T, Nowell M M, Lillo T M. The role of annealing twins during recrystallization of Cu. Acta Mater 2007;55:4233–4241.
576. Engler O. An EBSD local texture study on the nucleation of recrystallization at shear bands in the alloy Al–3%Mg. Scr Mater 2001;44:229–236.
577. Konijnenberg P J, Zaefferer S, Raabe D. Assessment of geometrically necessary dislocation levels derived by 3D EBSD. Acta Mater 2015;99:402–414.

578. Thornton P R, Mitchell T E, Hirsch P B. The dependence of cross-slip on stacking-fault energy in face-centred cubic metals and alloys. Philos Mag 1962;7:1349–1369.
579. Luster J, Morris M A. Compatibility of deformation in two-phase Ti–Al alloys: dependence on microstructure and orientation relationships. Metall Mater Trans A 1995;26:1745–1756.
580. Ritchie R O. Toughening materials: enhancing resistance to fracture. Philos Trans R Soc A 2021;379:20200437.
581. Pan B, Qian K, Xie H, Asundi A. Two-dimensional digital image correlation for in-plane displacement and strain measurement: a review. Meas Sci Technol 2009;20:062001.
582. Ren C X, Wang Q, Hou J P, Zhang Z J, Zhang Z F, Langdon T G. The nature of the maximum microhardness and thickness of the gradient layer in surface-strengthened Cu-Al alloys. Acta Mater 2021;215:117073.
583. Ren C X, Wang Q, Hou J P, Zhang Z J, Yang H J, Zhang Z F. Exploring the strength and ductility improvement of Cu–Al alloys. Mater Sci Eng A 2020;786:139441.
584. Tian Y Z, Zhao L J, Park N, Liu R, Zhang P, Zhang Z J, et al. Revealing the deformation mechanisms of Cu–Al alloys with high strength and good ductility. Acta Mater 2016;110:61–72.
585. Wu B, Fu H, Luo J, Yang W, Wu H H, Wu X, et al. Excellent strength-ductility synergy of Cu-Al alloy with a gradient nanograined-nanotwinned surface layer. Mater Sci Eng A 2024;901:146524.
586. Huang C X, Hu W, Yang G, Zhang Z F, Wu S D, Wang Q Y, et al. The effect of stacking fault energy on equilibrium grain size and tensile properties of nanostructured copper and copper–aluminum alloys processed by equal channel angular pressing. Mater Sci Eng A 2012;556:638–647.
587. Qu S, An X H, Yang H J, Huang C X, Yang G, Zang Q S, et al. Microstructural evolution and mechanical properties of Cu–Al alloys subjected to equal channel angular pressing. Acta Mater 2009;57:1586–1601.
588. Wang J J, Tao N R. Comparison of tensile properties between nanotwinned and nanograined CuAl alloys. Scr Mater 2018;149:16–20.
589. Yin Z, Sun L, Yang J, Gong Y, Zhu X. Mechanical behavior and deformation kinetics of gradient structured Cu-Al alloys with varying stacking fault energy. J Alloys Compd 2016;687:152–160.
590. Ran H, Jin R R, Wang Y F, Wang M S, He Q, Guo F J, et al. Optimizing the strength

and ductility of Cu–Al alloy by an ideal grain structure. Mater Sci Eng A 2021;807:140906.

591. Zhang Z, Qu Z, Xu L, Liu R, Zhang P, Zhang Z, et al. Relationship between strength and uniform elongation of metals based on an exponential hardening law. Acta Mater 2022;231:117866.

592. Wang Y, Zhu Y, Yu Z, Zhao J, Wei Y. Hetero-zone boundary affected region: A primary microstructural factor controlling extra work hardening in heterostructure. Acta Mater 2022;241:118395.

593. Wang Y F, Huang C X, He Q, Guo F J, Wang M S, Song L Y, et al. Heterostructure induced dispersive shear bands in heterostructured Cu. Scr Mater 2019;170:76–80.

594. An X H, Lin Q Y, Wu S D, Zhang Z F, Figueiredo R B, Gao N, et al. The influence of stacking fault energy on the mechanical properties of nanostructured Cu and Cu–Al alloys processed by high-pressure torsion. Scr Mater 2011;64:954–957.

595. Rousseau C E, Tippur H V. Compositionally graded materials with cracks normal to the elastic gradient. Acta Mater 2000;48:4021–4033.

596. Wu K, Song Z, Liu M, Wang Z, Chen S M, Yu S H, et al. Distorting crack-front geometry for enhanced toughness by manipulating bioinspired heterogeneity. Nat Commun 2025;16:194.

597. Pineau A, Benzerga A A, Pardoen T. Failure of metals I: brittle and ductile fracture. Acta Mater 2016;107:424–483.

598. Stören S, Rice J R. Localized necking in thin sheets. J Mech Phys Solids 1975;23:421–441.

599. Świetlicki A, Szala M, Walczak M. Effects of shot peening and cavitation peening on properties of surface layer of metallic materials—a short review. Materials 2022;15:2476.

600. Singh S, Guo Y, Winiarski B, Burnett T L, Withers P J, De Graef M. High resolution low kV EBSD of heavily deformed and nanocrystalline aluminium by dictionary-based indexing. Sci Rep 2018;8:10991.

601. Nye J F. Some geometrical relations in dislocated crystals. Acta Metall 1953;1:153–162.

602. Fleck N A, Hutchinson J W. A phenomenological theory for strain gradient plasticity. J Mech Phys Solids 1993;41:1825–1857.

603. Kibey S, Liu J B, Johnson D D, Sehitoglu H. Generalized planar fault energies and twinning in Cu–Al alloys. Appl Phys Lett 2006;89:191911.

604. Shih M, Miao J, Mills M, Ghazisaeidi M. Stacking fault energy in concentrated alloys. Nat Commun 2021;12:3590.
605. McLean D. Grain Boundaries in Metals. Oxford: Clarendon Press; 1957.
606. Lejček P. Grain Boundary Segregation in Metals. Berlin: Springer; 2010.
607. Lu L, Chen X, Huang X, Lu K. Revealing the maximum strength in nanotwinned copper. Science 2009;323:607–610.
608. Hutchinson J W, Suo Z. Mixed mode cracking in layered materials. Adv Appl Mech 1992;29:63–191.